UNIVERSITY OF ICELAND

Dissertation submitted in partial fulfillment of a Philosophiae Doctor degree in Chemistry (Physical Chemistry)

Low Energy Electron Induced Dissociation of Potential Gold Containing FEBID Precursor Molecules

Ali Kamali

Supervisor: Oddur Ingólfsson, Professor
June, 2023

FACULTY OF PHYSICAL SCIENCES

SCHOOL OF ENGINEERING AND NATURAL SCIENCES

UNIVERSITY OF ICELAND

Low Energy Electron Induced Dissociation of Potential Gold Containing FEBID Precursor Molecules

Ali Kamali

Dissertation submitted in partial fulfillment of a
Philosophiae Doctor degree in Chemistry (Physical Chemistry)
Supervisor: Oddur Ingólfsson, Professor

Ph.D. Committee
PD. Dr. Hubertus Marbach
Prof. Janina Kopyra

Opponents on Ph.D. dissertation
Prof. Dr. Štefan Matejčík
Dr. Ivo Utke

Faculty of Physical Sciences
School of Engineering and Natural Sciences
University of Iceland
June 2023

Low energy electron induced dissociation of potential gold containing FEBID precursor molecules

Dissertation submitted in partial fulfillment of a Philosophiae Doctor degree in Chemistry (Physical Chemistry)

Abstract

The focused electron beam-induced deposition (FEBID) process, a 3D nanofabrication technique, involves the utilization of a concentrated electron beam of high energy to dissociate precursor molecules that are adsorbed on a substrate, resulting in the creation of both volatile and non-volatile fragments. The former are pumped away and the latter are deposited on the substrate to form the desired 3D nanostructures. Close to any arbitrary form may be generated by a combination of beam movements and its dwell time at the respective locations. As an electron beam collides with a substrate, many interactions can take place, including scattering, secondary electron emission, Auger electron emission, and ionization. The secondary electrons can interact with the deposit and the substrate and induce processes including dissociative ionization, dissociative electron attachment, neutral dissociation, and dipolar dissociation of the precursor molecules. FEBID encounters challenges such as impurities and lateral broadening of deposited structures. These issues arise from the partial decomposition of precursor molecules induced by low energy electrons and the spatial distribution of secondary electrons beyond the focal point of the primary electron beam.

 To address these challenges, gas phase and surface studies of FEBID precursor molecules can aid in understanding electron interactions in the low-energy range of secondary electrons. This thesis focuses on studying gold precursor molecules [$(CH_3)AuP(CH_3)_3$], [$(CH_3)_2AuCl]_2$, and [$CF_3AuCNC(CH_3)_3$], with respect to their fragmentation through dissociative electron attachment (DEA) and dissociative ionization (DI) in the gas phase under single collision condition and the respective deposit formation in FEBID under ultra-high-vacuum. Quantum chemical calculations are conducted at the DFT and coupled cluster levels of theory to support the interpretation of the observations made in the experiments. The results from these studies are discussed with respect to low energy electron induced fragmentation of these precursors in general and how that is reflected in the elemental composition of the deposits formed in FEBID. Specifically, the suitability of these precursor molecules for the creation of high content gold nanostructures in FEBID is discussed in this context.

Útdráttur

Örprentun yfirborða með skörpum rafeindageisla er þrívíddar örtækni sem notar skarpan háorku rafeindageisla til að sundra sameindum sem eru ásogaðar á yfirborð. Til að mynda málmstúktúta með þessari tækni eru notuð girðitengi sem innihalda málm atom umkringd lífrænum og/eða ólírænum tengihópum. Undir kjöraðstæðum rofna tengihóparnir frá málminum þegar sameindin vixlverkar við rafeindir rafeindageislans. Tengihópatnir eru rokgjarnir og fara í gasham og þannig af yfirborðinu, en málmutinn verður eftir og myndar þá örstrútúra sem ætlunin er að byggja. Í raunheimum hinsvegar, brotna þessi girðitengi sjaldan alveg niður og erfitt hefur reynst að byggja hreina málmstrútúra. Það er frekar reglan að strúktúrar sem eru byggðir með þessari tækni innihaldi töluvert af frumefnum tengihópanna. Í ofanálag víxlverka háorkurafeindirnar við undirlagið og vaxandi örstrúktúrana, tapa orku og losa rafeindir úr undirlaginu, rafeindir sem jafnvel hafa litla sem enga hreyfiorku. Þannig nær orkudreifing rafeindanna sem í raun valda tengjarofunum allt frá nokkrum kílórafeindavoltum alveg niður að 0 rafeindavoltum. Þessar rafeindir geta því valdið tengjarofum á margvíslegan máta, þ.e., með rafeindaörfun sameindanna, rjúfandi rafeinda álagningu og í gegnum tengjarjúfandi jónun. Þetta leiðir til þess raunverulegu ferlarnir á bak við tengjarofin eru ekki vel þekktir og það aftur kemur í veg fyrir að hægt sé með marvissum hætti að hanna sameindir sem eru vel til þess fallnar að mynda hreina málmstrútúra með þessarri aðferð. Í þessu verkefni var tekin sú nálgun að rannsaka þrjár sameindir sem ætlaðar eru til að mynda gull strúktúra; $[(CH_3)AuP(CH_3)_3]$, $[(CH_3)_2AuCl]_2$ og $[CF_3AuCNC(CH_3)_3]$. Þessar sameindir voru rannsakaðar með tilliti til rjúfanti rafeinda álagningar og jónandi tengjarofa þegar þær eru í gasham og voru notaðar til að mynda örstrúktúra. Skammtafræðilegir reikningar voru notaðir til að túlka niðustöður tilrananna þar sem tengjarof voru skoðuð í gasham og niðustöður þeirra tilrauna voru bornar saman við frumeindasamsetningu örstrútútanna sem mynduðust þegar þessar sameindir voru notaðar til að mynda slíka undir geislun með háorkurafeindum. Niðurstöðurnar eru sérataklega skoðaðar í samhengi við hvernig niðurbrotsferlin sem eiga sér stað þegar þessar sameindir eru í gasham endurspeglast í samsetningu örstrúktúra sem myndast þegar þær rofna á yfirborðum undir geislun með háorkurafeindum.

Dedication

I dedicate this dissertation to my late parents, who have been my constant source of support and love throughout my entire life. Without their unwavering encouragement and guidance, I would not have been able to reach this point in my academic career. This thesis belongs to them, as a token of my deepest gratitude for everything they have done for me.

تقدیم به پدر و مادر عزیزم

Preface

This thesis is submitted in candidacy for a Ph.D. degree from the University of Iceland. The work has been conducted at the Faculty of Sciences and supervised by Prof. Oddur Ingólfsson.

Table of Contents

List of Figures

List of Tables

Abbreviations

AD	Autodetachment
AE	Appearance energy
AES	Auger electron spectroscopy
AFM	Atomic force microscopy
BDE	Bond dissociation energy
BSE	Backscattered electron
CVD	Chemical vapor deposition
DD	Dipolar dissociation
DEA	Dissociative electron attachment
DFT	Density functional theory
DI	Dissociative ionization
DLPNO	Domain-based local pair natural orbital
EA	Electron affinity
EBL	Electron beam lithography
EDX	Energy dispersive X-ray spectroscopy
FCF	Franck-Condon factor
FEBID	Focused electron beam induced deposition
FWHM	Full-width-at-half-maximum
GGA	Generalized gradient approximation
GIS	Gas inlet system
LEE	Low-energy electron
ND	Neutral dissociation
SE	Secondary electron
SEM	Scanning electron microscope
SIGMA	SImply a Gas-phase MAchine
TEM	Trochoidal electron monochromator

TNI	Transient negative ion
UHV	Ultra-high vacuum
XPS	X-ray photoelectron spectroscopy
ZPE	Zero-point energy

Acknowledgements

I owe a great debt of gratitude to the many individuals in my life who made my PhD experience a personally and professionally rewarding adventure. I would like to thank my supervisor Prof. Oddur Ingólfsson for his effortless conviviality and also for providing me the opportunity to peruse my Ph.D. studies at the University of Iceland. Having such faith in all of us in the group, he allows us a great deal of independence to develop our minds. Many thanks to PD Dr. Hubertus Marbach and Prof. Janina Kopyra, who have been a great help in my PhD endeavor. They always inspired me by engaging in many thought-provoking debates and providing me with constructive feedback and also for taking a role as a member of my Ph.D. committee. I have much gratitude for Dr. Ragnar Björnsson for his help in conducting computational chemistry calculations. A special thanks to Prof. Štefan Matejčík and Dr. Ivo Utke for taking the role of opponents at my doctoral defense. I also thank administrative staff Þuríður, Sandra, Íris, Brynja Dís and Heiður Anna in student housing for always being helpful.

I'd like to extend my gratitude to my colleagues, especially Mr. Reza Tafrishi, who helped to make my time in Iceland the one that I will never forget.

Finally, I would like to extend my sincere gratitude to my dear friends, especially Dr. Milad Ganjalizadeh, Dr. Amini and Pouya, and to my beloved family, Keyvan, Amir, Shideh, Farnaz, and especially my dear nephew Mr. Sepehr Kamali, for their love and support. Thank you to my Raunó friends, for welcoming me and making me feel at home in a country where I had no built-in safety net. I am grateful to Prof. Sirus Javadpour for his consistent support and guidance throughout the past 20 years, which has been crucial in empowering me to advance my career. I would like to express my heartfelt gratitude to my late parents for their constant encouragement and support. I know that I would not have been able to complete this work without them by my side. Though they are no longer with me, their love and guidance have remained with me every step of the way.

1 Introduction

Researchers in the nanofabrication field seek to construct nanoscale structures, which may operate as components, devices, or systems and are preferably suitable for high-volume manufacturing at low cost. One of the main drivers is the miniaturization trend in the contemporary electronics industry[1,2]. Nanofabrication is also a key component of the wider nanotechnology field and is essential for the practical application of nanotechnology in many conventional engineering and scientific disciplines. The scientific disciplines intersecting in nanoscience and nanotechnology include chemistry, physics, biology, engineering, and medicine. Therefore, the economic and social impact of results from nanotechnology may be significant. Diagnostics, therapies, and preventative measures in medicine[3,4], nanoparticles for sustainable energy[5], magnetic memories for computers[6], electronic devices[7], thin films in electronics[8], biosensors[9], and nanostructured catalysts[10] are just a few examples of applications of nanotechnology in engineering, chemistry, and biotechnology. Furthermore, the properties of materials at the nanoscale may differ significantly from those observed at the macroscopic scale, allowing for the investigation of fundamental physical phenomena such as quantum size effects[11]. These, in turn, may pave the way for further novel nanotechnology applications.

Gold nanostructures are a prominent example of nanostructures that have attracted significant interest in recent years. This is because of their unique optoelectronic characteristics and biocompatibility which make possible a wide variety of fascinating applications in medical imaging and therapy[12] as well as in the general field of nanotechnology[13,14]. Among these are the fabrication of electrical interconnects[15], metamaterials[16], growth of substrates for nanowires and nanotubes[17], and the development of intricate 2D[18] and 3D[19] plasmonic structures. However, application of 3D nanostructure for absorption and scattering of light, e.g., in plasmonic structures, require not only mastery of shape but also precise control over elemental composition. Plasmonic nanostructures may be produced using traditional techniques that consists of depositing a thin metal film using electron-sensitive positive or negative resists in Electron Beam Lithography (EBL)[20]. However, multiple fabrication steps[21], a slow manufacturing process[21], high cost[21], limited throughput[22], substrate limitations[23,24], material restrictions[22], and structural defects resulting from radiation damage caused by high-energy electrons[24] are challenges that the EBL technique faces in its real-world applications. The direct deposition of nanostructures on a substrate driven by a focused electron beam, i.e., FEBID is a potential alternative to the EBL [2,25]. In this process, the electron beam irradiation decomposes precursor molecules adsorbed on the substrate's surface, leaving a deposit, from which the nanostructures may be formed by a combination of the beam position and its dwell time. Furthermore, it is a single-step process capable of creating 3D structures directly on flat as well as uneven surfaces. Indeed, eliminating the requirement for resist material will facilitate the fabrication of nanostructures with larger aspect ratios and offers more control over nanopatterning on planar or non-flat surfaces[25]. However, the high energy incident electron beam in FEBID interacts not only within the adsorbed precursor molecules but also with the substrate and the growing deposit[2,26,27], leading to inelastic electron scattering and the generation of secondary electrons. Furthermore, the electron beam current, the substrate material, the conditions within the deposition chamber, and the chemistry of the precursor all play a role in the FEBID technique[25,27].

Historically, FEBID of gold structures has been carried out using a wide range of chemical vapor deposition (CVD) precursors, such as (CH$_3$)$_2$Au(acac)[28], (CH$_3$)$_2$Au(tfac)[29,30], and (CH$_3$)$_2$Au(hfac)[31] and the resulting deposits have been poor in quality, generally consisting of an amorphous matrix of carbon with embedded metal crystallites. For the precursors listed above, as an example, the gold content achieved has been in the range of 8-20 at. %, 10-40 at. %, and 2-3 at. %, respectively. This is not surprising as the deposition process in the FEBID technique is electron driven[25,32,33], as opposed to the thermally-driven CVD. Hence there is no basis for the presumption that a suitable CVD precursor will also perform well in FEBID. Correspondingly, significant effort has been put into designing improved gold precursors for FEBID[34–36], the two most noticeable of these being ClAuI(PF$_3$)[37] and ClAu(CO)[38]. Despite the high gold content of the deposits achieved in FEBID with these precursors, they have not found general application due to their sensitivity to moisture and their thermal instability leading to a limited lifetime at ambient conditions and restricting their handling and applications[34]. In the still ongoing quest for suitable gold precursors in FEBID, it is thus important to be able to combine their complete decomposition under the electron beam and their stability under ambient conditions. To achieve this, a funded understanding of the underlying electron-induced fragmentation of such precursors must be provided and eventually used in the design of better-performing FEBID precursors. This is a complicated task as the FEBID technique involves the decomposition of the precursors through irradiation with a high-energy focused electron beam. Thus inelastic, ionizing scattering, at and within the substrate and the forming deposits plays a significant role. This in turn leads to the formation of a large number of scattered and low-energy secondary electrons at or near the respective surfaces [25,39]. In addition to the primary electrons of the high energy beam, these low-energy electrons induce dissociation of the precursor molecules through various fragmentation mechanisms. The degree of dissociation of the precursor molecules' ligands impacts the purity of the FEBID deposits, as remaining ligands and fragments may stay in the deposits. Furthermore, backscattered and secondary electrons may also cause deposition outside the directly irradiated area, which in turn reduces the resolution. There are four types of electron-induced fragmentation processes; dissociative ionization (DD), dissociative electron attachment (DEA), dipolar dissociation (DD), and neutral dissociation (ND)[39–43]. These are distinctly different with respect to their electron energy dependence and product formation. Evaluating the energy dependence of these diverse dissociation processes and the respective products formed in relation to their roles in the FEBID deposition of different precursors is thus an important element in rational design of new FEBID precursors[44,45]. Understanding the electron-molecule interactions in the FEBID technique requires integrating UHV surface science with HV gas phase experiments[45]. The ultra-high vacuum regime in surface science studies allows for the investigation of the interaction of precursor molecules with the electron beam as well as the effects of surface kinetics, including adsorption, desorption, and diffusion, in application of the FEBID technique[46–48]. Ultra-high vacuum is important in this content as it reduces co-deposition from background gas in the FEBID chamber and allows better judgement of impurities in the deposit that result directly from the respective precursor ligands. Gas phase electron interaction studies are important as these allow deconvolution of the underlying processes and assessment of their electron energy dependence. This combination is important as bond selectivity of certain dissociation pathways presents a challenge in FEBID, as the electron energy spectrum involved encompasses not only the high-energy primary electrons (in the keV range) but also the low-energy secondary and backscattered electrons ranging from few meV to the energy level of the primary electrons[44]. Furthermore, the purity of the FEBID deposit is also determined by the equilibrium between the desorption of the volatile dissociation

2

fragments and their surface interaction, which coincides with the first electron-induced dissociation reaction steps[49].

Understanding the complex surface chemistry behind FEBID can be greatly facilitated by obtaining knowledge about the species generated during the initial stage of deposit formation, which involves the dissociation of the precursor by electrons. It has been shown that conducting HV gas-phase experiments can shed light on the initial electron-induced precursor fragmentation processes[44,45]. Mass spectrometry (MS) is usually utilized in such gas-phase investigations to analyze the fragmentation products under single electron-molecule collision conditions. Such experiments, which commonly use a crossed molecular and electron beam apparatus, can track either the anionic fragments produced by dissociative electron attachment (DEA) or the positively charged fragments produced by dissociative ionization (DI) processes, however, neutral dissociation (ND) cannot be probed by such experiments[44,50–52].

Secondary electrons (SEs) are emitted in significant numbers when electron beams with energies of several keV interact with solid materials. The energy range of these SEs overlaps with the range that is relevant in DEA, which is most efficient close to the 0 eV threshold but may occur up to about 10 to 15 eV, as well as the range relevant in DI, which onset is at or slightly above the ionization energy of the respective molecule[39,44]. In theory, an assessment of the significance of individual electron induced events in FEBID could be obtained by convolving the energy-dependent cross sections for the production of certain fragments with the energy-dependent SE yielding from the material from which a deposit grows. However, neutral species are not only formed in the ND process as DEA and DI also produce neutral counterparts to the charged fragments observed in the mass spectrometric experiments. Generally, neutral fragments are challenging to measure in gas-phase experiments, but exploiting the thermochemistry associated with the formation of the observed charged fragments, determined by quantum chemical calculations of the respective threshold energies, may help in the identification of these fragments. In addition, the surface science experiments conducted under UHV conditions, where the substrates remain clean due to the low adsorption rate of contaminations from the residual gases, are important for gaining an in-depth understanding of surface reactions in conjunction with those conducted in the gas phase studies[39,45].

To better understand the fundamental electron-induced reaction pathway(s) in the deposition of gold, this thesis studies the extent, nature and energy dependence of DI and DEA processes in the gas-phase on isolated precursor molecules developed for FEBID as well as the elemental composition and morphology of deposits generated in FEBID using these precursors under UHV conditions. Neutral fragments and fragmentation routes in DI and DEA to these gold precursors are identified by using quantum chemical calculations of the respective thresholds and are discussed in context with the composition of the deposits formed in FEBID under UHV.

In this thesis, Chapters 2 and 3 provide an overview of the theoretical and experimental principles that form the basis of the methodologies employed in this study, while chapter 4, discusses the results of single-collision gas-phase experiments and UHV deposition studies conducted on three potential organometallic gold precursors.

2 Theoretical Perspective

2.1 Focused Electron Beam Induced Deposition (FEBID)

Focused Electron Beam Induced Deposition (FEBID) is a single step material deposition technique that allows for precise and controlled 3D growth of nanoscale structures composed of a variety of materials, including metals, alloys, and insulators[25,26]. Utilizing a focused electron beam enables the controlled and precise material deposition onto a substrate in a highly-localized manner[25]. As a result, complex nanostructures with a high degree of accuracy and resolution can be created[53]. The unique capabilities of FEBID make it a promising technology for a wide range of applications, including micro- and nanoelectronics[54], biomedical devices[55], and energy storage systems[56].

2.1.1 Principle of FEBID

The origination of the focused electron-beam induced deposition (FEBID) technology may be traced back to the period when researchers discovered undesired deposits of contaminations, most of which were hydrocarbons, that prevented them from exploring substrates in the electron microscope[2,57]. The primary sources of contamination were the diffusion of hydrocarbons from pump oils and the leakage of water molecules through polymeric O-rings as well as vacuum grease and pump oils[58]. In recent years, the adoption of oil-free turbomolecular pumps, plasma decontaminators, UV radiation, and ozone to clean the SEM chambers have all contributed to the decrease in the undesired deposition of impurities[59–61]. In addition, the temperature within the chambers could be reduced, and other gasses like argon, nitrogen, oxygen, and air can be introduced into the chamber to assist in the removal of contaminations from the electron microscope chamber[62,63].

This was, however, also recognized as an opportunity and researchers attempted to use these unintended processes to open a new avenue for fabricating exceptionally high-resolution nanostructures. The high resolution of the nanostructures is determined by the width of the primary electron beam as well as the very short mean free path of secondary and backscattered electrons in the substrate and deposit.[58] In addition, the depth of focus in this method is rather considerable, and it has the potential to be employed in the fabrication of both two and three-dimensional structures[58]. Today it is common practice to use a scanning electron microscope (SEM) for carrying out FEBID experiment, though other instrument types, such as (S)TEM[64] and STM[65], are also utilized.

The principles underlying FEBID involve electron induced molecular fragmentation and fragment desorption, whereby a focused electron beam is utilized to decompose molecular precursor materials at a surface to desorb unwanted components, leaving the desired deposit. A schematic representation of this process is shown in Figure 2.1.
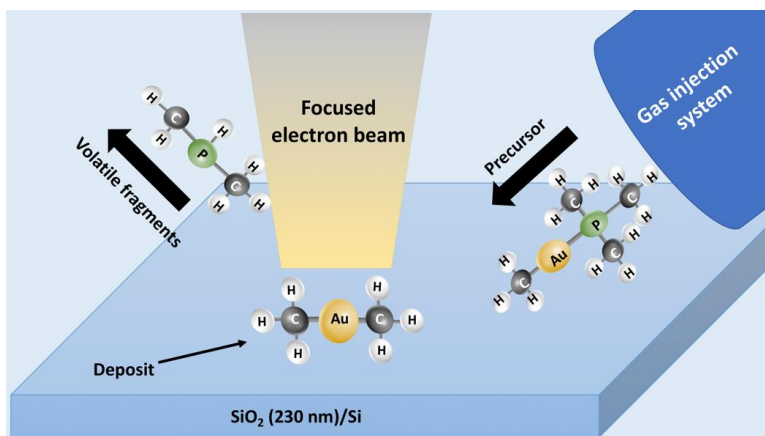
Figure 2.1 Schematic image of the FEBID process. The precursor molecules are introduced to the chamber through GIS and then interact with the electron beam. Upon irradiation, the precursor molecule dissociates into volatile and non-volatile fragments. The volatile fragments are pumped away from the substrate, whereas the non-volatile fragments remain on the substrate and create the deposit. Reprinted with permission from ref. [66]

In FEBID of metallic structures the precursor materials, is typically an organometallic compound with sufficient vapor pressure to be introduced into a vacuum chamber, as shown in Figure 2.1. The precursor compound enters the chamber close to a substrate surface, at which it is subjected to a tightly focused high-energy electron beam. Under the electron beam exposure, the precursor molecules decompose through electrons-induced fragmentation, leading to desorption of the unwanted ligand materials and ideally the deposition of pure metal structures. By moving the electron beam along the surface and varying the dwell time, the spatial material deposition can be controlled, allowing for precise 3D control over the formation of nanoscale structures[25–27].

In this process special Gas Injection Systems (GIS) are commonly used to transfer the gaseous precursor molecules into the gas phase and into the high vacuum chamber in close proximity to the substrate surface[58]. Generally, for metal deposition, the FEBID precursors are organometallic compounds that composed of a metallic core carrying organic ligands, while inorganic precursors include carbon-free ligands are also used[27]. The ligands play a crucial function by increasing the volatility and stability of the precursor molecules, allowing them to pass through the GIS and reach the respective substrates[34]. At the substrate's surface, the precursor molecules are physically adsorbed in dynamic equilibrium with the gas phase, and are subjected to a focused electron beam with an energy of 1, up to 50 keV that impinges on the adsorbate at the surface [25,58]. The molecules of adsorbed precursors on the substrate are decomposed into volatile and non-volatile species while being subjected to the impact of the electron beam[27,58]. The volatile species are pumped away while the non-volatile fragments remain on the substrate, eventually creating well-defined nanostructures from the respective deposits[25,26]. This is a single-step procedure that may be applied on flat or non-flat substrates, and is suitable for the fabrication of 3D structures of significant complexity[67].

However, when a high energy electron beam impinges onto a substrate, secondary electrons (SE) and backscattered electrons (BSE) are generated in close proximity to the irradiated region. For 20 or 30 keV incident electron energies radius for SEs may be on the order of 1 nm and for BSEs it has

been shown to be on the order of 5 μm for 30 keV electrons impinging on a silicon substrate[67,68]. Such backscattered and secondary electrons that are generated close to the surface of the substrate react with the adsorbed precursors and contribute significantly to the deposit formation[67]. For high aspect ratio structures this is also the case for forward scattered electrons. For this reason, the spatial resolution of FEBID-fabricated nanostructures depends not only on the size of the primary electron beam, but rather on the size of the region surrounding the incoming electron beam where scattered and secondary electrons are present[67].

Focused electron beam induced deposition is a versatile single step process with high potential where conventional layer by layer lithographic processes are not suitable. Furthermore, despite the role of scattered and secondary electrons, FEBID is suitable for high precision and high resolution[53,69] fabrication of nanostructures as the high energy electron beam allows for tight focusing and the spread of the secondary electrons is limited. It may be used for the deposition of a wide range of materials[34], including metals, alloys, and insulators, making it a versatile technique for a variety of applications. Furthermore, it offers controlled deposition rate[25], adjustable with the energy and current of the electron beam as well as the delivery of the precursor molecules. And, last but not least, it is compatible with a variety of different substrates[70,71], both with regards to material composition and topography. These parameters make FEBID a versatile technique with high potential for a wide range of potential applications in various fields.

However, although FEBID has several advantages, there are also various challenges and limitations that require attention. One such limitation is the slow deposition rate of FEBID[72], and related to that the technical realization of parallel processing[73]. These are especially of concern for high-volume manufacturing processes. The practical limitations to the range of materials that can be deposited using FEBID are also of concern. This is mainly due to the limited availability of suitable precursors[34]. In practice, the compatibility of FEBID with different substrates can also be challenging, and specialized substrates or surface treatments may be necessary for optimal results[26]. Furthermore, the biggest strength of FEBID is probably in the manufacturing of 3D structures making the stability of high-aspect-ratio nanostructures an intrinsic concern[74]. The cost of equipment and materials required for FEBID, though not high compared to EUV or DUV lithographic manufacturing tools, also limits their access to only few researchers and institutes[25].

Despite these challenges, FEBID is a promising technology with unique capabilities that makes it suitable for a wide range of applications and researchers are working to improve the speed, efficiency, and versatility of this method and to overcome its limitations to making it more accessible and valuable for a broader range of applications in the nanotechnology industry.

To achieve this, both instrumental parameters and parameters of fundamental underlying processes need attention. The important instrumental parameters in the FEBID technique include[25,27,58] the electron beam energy and current as well as control of the precursor delivery. These are important parameters which can affect the deposition rate and the material properties of the deposited nanostructures. The substrate temperature and substrate material are also of importance as well as the cleanliness of the processing environment. Specifically, with respect to the cleanliness, pre-deposition cleaning protocols and background gas contaminations are of importance, i.e., FEBID under high vacuum may produce deposits with considerably higher carbon compared to deposition in ultra-high vacuum. The optimization of these technical and instrumental parameters, along with others not listed here, is crucial for the success of the FEBID

process and the reproducibility in production of high-quality nanostructures with the desired properties.

However, the currently most important parameter to be addressed is the design of suitable FEBID precursors that are stable at ambient conditions, have sufficient vapor pressure and decompose under the electron beam to produce pure deposit and/or allow for their composition control. Hence, the fundamental underlying processes, the electron-molecule interaction mechanisms in FEBID need attention.

2.2 Electron-Molecule Interactions

As the decomposition process in FEBID is not only effectuated by the well-defined primary electrons of the beam, but rather by these, the elastically and inelastically scattered electrons and the secondary electrons resulting from inelastic ionizing processes, precursor molecule dissociation during the FEBID process reflects the energy distribution of the locally available electrons convoluted with the energy-dependent dissociation cross-sections of the respective processes[67].

There are four electron induced dissociation processes that can be brought by the precursor molecules, and these may all proceed within the active electron energy range in FEBID[44]. These electron induced fragmentation processes are dissociative electron attachment (DEA), dissociative ionization (DI), dipolar dissociation (DD), and neutral dissociation (ND), as shown in equations 2.1-2.4, respectively[39]:

$$AB + e^- \rightarrow AB^{-*} \rightarrow A^- + B^. \tag{2.1}$$

$$AB + e^- \rightarrow AB^{+*} + 2e^- \rightarrow A^+ + B^. + 2e^- \tag{2.2}$$

$$AB + e^-(\varepsilon_1) \rightarrow [AB]^{\#} + e^-(\varepsilon_2)(\varepsilon_2 < \varepsilon_1) \rightarrow A^+ + B^- \tag{2.3}$$

$$AB + e^- \rightarrow [AB]^{\#} + e^-(\varepsilon_2 < \varepsilon_1) \rightarrow A^. + B^. \tag{2.4}$$
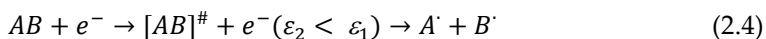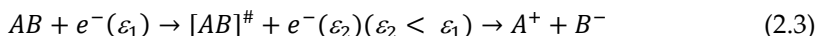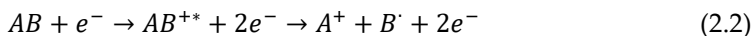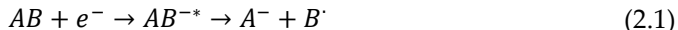
Here, "#" represents the fragment(s) in a vibrationally and/or electronically excited state, "*" indicates electronic excitation, and ε_1 and ε_2 represent the electron's incident energy and the electron's residual energy after the inelastic scattering process, respectively. In principle, the fragments may also be formed in a vibrational or electronically excited state, but that is not specifically indicated in the equations.

2.2.1 Dissociative Ionization

In dissociative ionization, a bonded electron is removed from the target molecule, resulting in the creation of a positively charged parent molecule. This may take place when the energy of the incoming electron is equal to or greater than the ionization energy of the target molecule. The target molecule undergoes a vertical electronic transition from the ground state of the neutral molecule to the ionization continuum of the molecule, which may be the ground state or an excited state of the molecular cation. This is shown in Figure 2.2[39], which shows the cationic ground state and two exclusively repulsive excited cationic states attainable within the Frank-

Condon (FC) region. Dissociative ionization exhibits threshold behavior rather than resonant behavior, hence, it is a non-resonant process. Upon transition from the neutral ground state to one of the possible cationic states within the FC region, the parent cation will be left in a vibrationally and/or electronically excited state. In mass spectrometry, this may result in the observation of the parent cation ($AB^{\#+}$) or cationic fragments resulting from its dissociation (e.g., $A^+ + B$ or $A + B^+$ as shown in Figure 2.2). Fragmentation may be determined by the internal energy of the cation as well as the thermochemical thresholds of the process[44]. As the energy of the impacting electron rises, the fragmentation events evolve from a single bond ruptures to multiple bond ruptures, and the total cross section approaches a maximum at around 50-70 eV. At higher incident electron energies, however, the electron-molecule interaction time becomes shorter, resulting in a reduction of the dissociative ionization cross section[39,44]. Dissociative ionization may result in significant fragmentations since it occurs across an energetic range much beyond the ionization energy of the target molecule. Also, additional energy may be gained through new bond formations in the fragmentation process, i.e., unimolecular rearrangement processes.
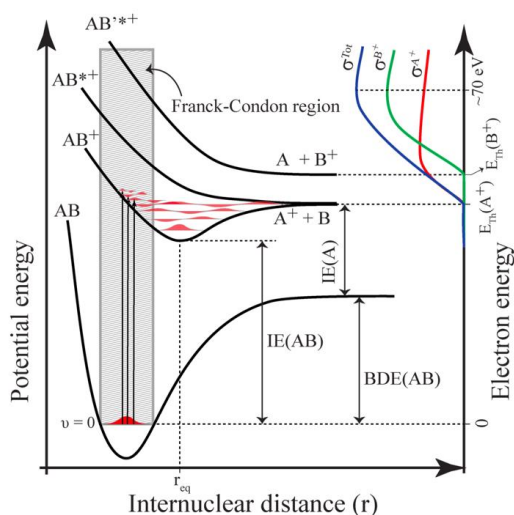
Figure 2.2 Simplified potential energy diagrams for the DI to a diatomic molecule AB. The potential energy curves AB, AB^+, AB^{*+}, and $AB^{'*+}$ depict the ground state of the neutral molecule and its several ionization states. The threshold energies for producing A^+ and B^+ via dissociative ionization of AB are denoted by $E_{th}(A^+)$ and $E_{th}(B^+)$, respectively (adapted with permission from ref. [44]).

The threshold energy (E_{th}) for the formation of a positively charged fragment through the dissociative ionization process in a diatomic molecule can be expressed by equation 2.5;

$$E_{th}(A^+) = BDE(AB) + IE(A) \qquad (2.5)$$

where *IE(A)* is the ionization energy of fragment A *and* $BDE(AB)$ is the bond dissociation energy of AB. For the formation of a fragment in the circumstance of more complicated dissociation mechanisms for a polyatomic molecule where multiple bonds can be broken and formed, equation 2.5 for the threshold energy (E_{th}) takes the form:

$$E_{th} = \sum BDE_{broken} - \sum BDE_{formed} + IE_{(fragment)} \qquad (2.6)$$

In this case, the ionization energy of the fragment is shown as $IE_{(fragment)}$, and BDE_{broken} and BDE_{formed} are the bond dissociation energies of the broken and formed bonds, respectively[40].

2.2.2 Resonant Interactions of Low Energy Electrons

In contrast to DI, the electron attachment mechanism is active across a restricted energy range (less than 10 to 15 eV in most cases). In electron attachment, the impacting electron remains near the target molecule for a longer time, binding to it to form a transient negative ion (TNI), also termed resonance. The lifetime of such a resonance spans from a few vibrational periods (1×10^{-14}s) in the case of N_2 to the 100 μs range in the case of SF_6[75]. Creating a stable anion that can be detected by mass spectrometry requires, from a thermodynamic point of view, a positive value of the electron affinity of the molecule or fragment. However, as the attachment process is a vertical transition, without nuclear displacement, the respective anions are formed in the equilibrium geometry of the neutral state, hence in an excited state. The TNA is thus bound to relax by either re-emitting the electron (autodetachment) or through dissociation (DEA). [76,77]
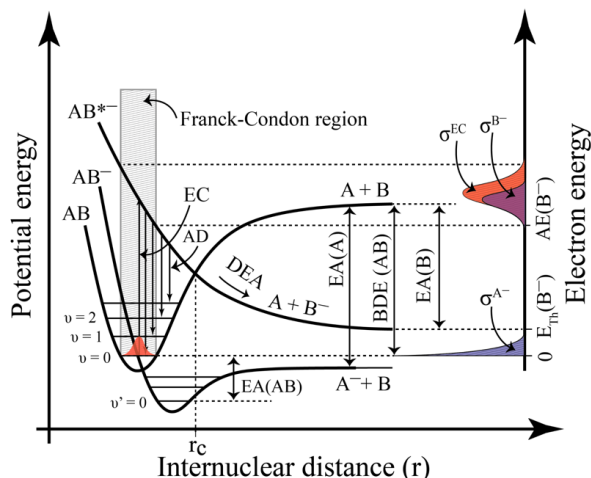
Figure 2.3 Potential energy diagrams for DEA to a diatomic molecule AB, simplified to two dimensions (quasi-diatomic). The electron capture (EC) is depicted with vertical arrows. The neutral and anionic ground states, as well as the anionic excited state of molecule AB are represented by the potential energy curves AB, AB⁻, and AB⁻. The thermochemical threshold for the formation of B⁻ via DEA to AB is shown as $E_{th}(B^-)$. Adapted with permission from ref. [44].*

Because of the complexity of the DEA process, it is often presented in terms of a quasi-diatomic molecule so that the steps may be seen more clearly. This is shown in Figure 2.3, which depicts the electron attachment and the DEA process for a diatomic molecule. In the Franck-Condon region, the vertical transition occurs across a narrow energy window. The Franck-Condon factor, which is defined as the square of the overlap integral between the wave functions of the neutral ground state (Ψ^n) and the resulting electronic state (Ψ^i), is directly proportional to the transition probability (P_{trans}) in the electron attachment process[43].

$$(P_{trans}) \propto |\langle \Psi^n | \Psi^i \rangle|^2 \qquad (2.7)$$

There are two main types of resonances leading to the initial TNI; Feshbach and Shape resonances, which are categorized based on their respective resonance energy compared to the energy of the corresponding parent state[78,79].

Shape resonances

In shape resonances, the attachment of the incoming electron to the molecule is determined by the shape of the potential resulting from the interaction between the molecule and the electron[78]. Suppose a molecule possesses an unoccupied molecular orbital that is energetically favorable and possesses the same symmetry as the angular momentum of the incoming electron, a plane-wave with angular momentum l. In that case, the electron attachment process can occur[78]. Assuming a neutral molecule with non-zero polarizability (α), an approaching electron induces a transient charge induced dipole in the molecule, leading to an attractive long-range polarization potential (V_α) as well as a repulsive centrifugal potential generated between the molecule and electron due to the electron's angular momentum $V_l(r)$ as shown in the following equations:

$$V_\alpha = \frac{-\alpha}{2r^4} \tag{2.8}$$

$$V_l(r) = \frac{l(l+1)}{2r^2} \tag{2.9}$$

Consequently, the sum of the (V_α) and ($V_l(r)$) results in an effective potential as shown in the following equation:

$$V_{\text{effective}} = V_\alpha(r) + V_l(r) = -\frac{\alpha}{2r^4} + \frac{l(l+1)}{2r^2} \tag{2.10}$$

Figure 2.4 shows a representative diagram of the effective potential in dependence of the molecule-electron distance for different angular momentums of the electron. If the centrifugal term is zero for s-wave electrons (l =0), there is no potential barrier owing to the absence of the centrifugal term, and no shape resonances occur. However, for electrons with non-zero angular momentum, there is a potential barrier in the diagram in which the height of the barrier rises by increasing the angular momentum of the electron. The incoming electron can be repelled by the potential barrier, or it can tunnel through it leading to the formation of a TNI[76,80,81].
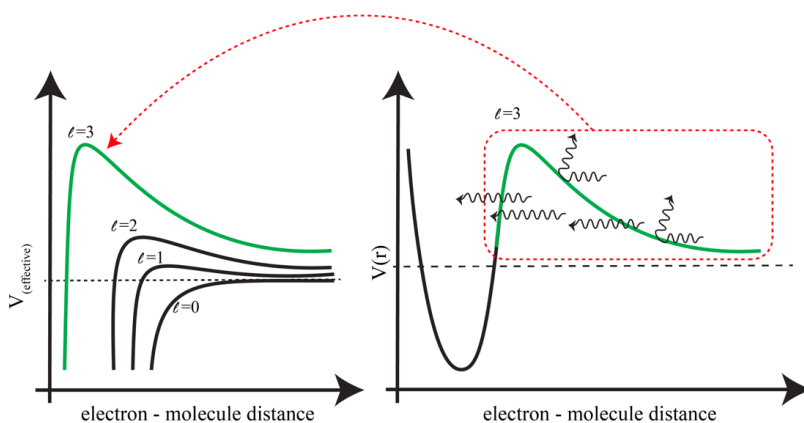
Figure 2.4 An illustration of the effective potential between an incoming electron and its corresponding molecule is shown in the left panel for different angular momentum (l). The total effective potential between the electron and the corresponding molecule, including the electron-electron repulsion) is shown schematically in the right panel. Due to the barrier, the electron may be deflected back (shown with reflecting waves) or tunnel through the potential barrier (shown with straight waves), becoming temporally trapped within the potential barrier. Adapted with permission from ref. [82]*.*

The total effective potential between a molecule and an electron, when their distance becomes very short, is equal to the sum of the short-range repulsive force due to the interaction between the cloud of electrons in the molecule with the incoming electron, and the long-range effective potential.

Similarly, this TNI can decay via auto-detachment when an electron that has tunneled through the potential barrier to form it, tunnels back out. A single-particle shape resonance occurs when this mechanism is active without concomitant electronic excitation. Such resonances are generally restricted to the energy range between 0 to 4 eV and are characterized by the trapped electron occupying a vacant or partially occupied molecular orbital of the ground state parent molecule without altering its electronic structure[76]. At energies at or above the initial electronic excited energy of the neutral parent molecules, electron attachment may trigger electronic excitation. In this case the resonance is termed a two-particle-one-hole shape resonance or core-excited shape resonance. Both of these attachment mechanisms are examples of what is referred to as "open channel resonances" since the electron detachment may proceed through a single particle (electron) transition. This is shown schematically in Figure 2.5 along with the respective electron configurations.
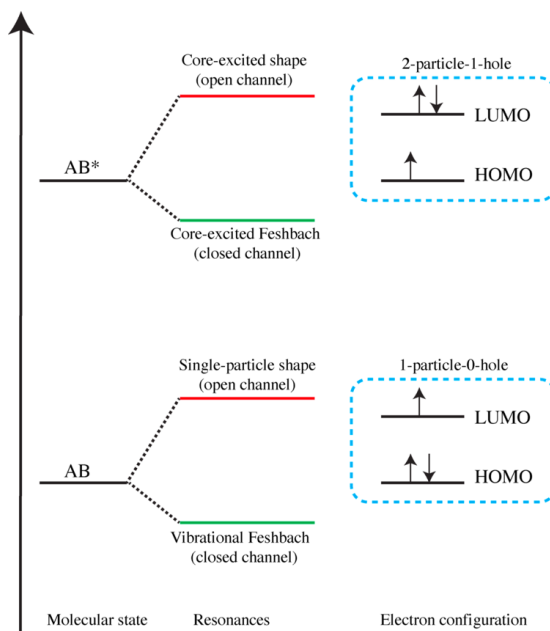
Figure 2.5 An illustration of the four distinct resonance types (vibrational Feshbach, single-particle shape, core-excited Feshbach, and core-excited shape). The neutral molecule AB has two possible states, the ground and the excited one denoted by AB and AB*, respectively. One electron in the LUMO and no hole being generated in the HOMO represented by 1particle-0-hole, while two electrons in the LUMO and one hole being created in the HOMO as a result of electron excitation represented by 2-particle-1-hole. Adapted with permission from ref. [82].

Feshbach resonances

Different to shape resonances, Feshbach resonances are TNIs which are energetically below the corresponding neutral state of the molecule. In this context nuclear-excited (vibrational) Feshbach resonances are lower in energy than their respective vibrational parent states, generally the ground vibrational state of the neutral. Correspondingly, electronically excited Feshbach resonances are energetically below the respective electronically excited parent state. Auto-detachment from theses TNIs is thus not possible in a direct process, which in turn extends their lifetime. Accordingly, these are classified as closed channel resonances [76,78,79]. This is shown schematically in Figure 2.5 along with the respective electronic structures.

2.2.3 Relaxation of TNIs Through Auto-Detachment and Dissociation (DEA)

In principle a TNI, formed through a vertical transition from the ground state neutral, may relax by re-emission of the electron, that is by Auto-detachment (AD) or by dissociation, hence, dissociative electron attachment (DEA). This is shown in equations 2.11 and 2.12:

$$\text{AD: } AB + e^-(\varepsilon_1) \rightarrow AB^{(\#)-} \rightarrow AB^{(\#)} + e^-(\varepsilon_2)(\varepsilon_2 < \varepsilon_1) \tag{2.11}$$

$$\text{DEA: } AB + e^-(\varepsilon_1) \rightarrow AB^{(\#)-} \rightarrow A^{(\#)-} + B^{(\#)} \tag{2.12}$$
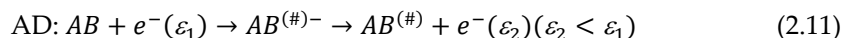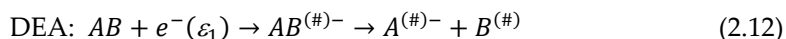
In the Eq. 2.11 and 2.12, "#" denotes a vibrationally and/or electronically excited state. In addition, the ε_1 stands for the energy of the incident electron and ε_2 stands for the energy of the electron after the inelastic scattering process.

In the case of the diatomic molecule AB depicted in Figure 2.3, the TNI is formed via a vertical transition from the ground state of the neutral molecule to either the electronic ground or excited states of the anion. The TNI is initially formed without structural relaxation (vertical transition) and the relaxing process is achievable along the respective, repulsive potential energy surfaces. Auto-detachment can take place anywhere along the nuclear relaxation coordinate before the crossing point, r_c, of the potential energy curve of the TNI with that of the neutral ground state. However, after the crossing the point r_c, the autodetachment process is classically not possible and the TNI will be dissociated, resulting in the production of neutral fragment A and negatively charged fragment B⁻ in Figure 2.3. The equation 2.13 provides the lifetime τ_{AD} of a TNI with respect to auto-detachment where $\hbar$ is the reduced Plank constant, Γ the width of the negative ion state which is given by the Heisenberg uncertainty principle:

$$\tau_{AD} = \frac{\hbar}{\Gamma} \tag{2.13}$$

The DEA cross-section (σ^{DEA}) for this process can be obtained from equation 2.14:

$$\sigma^{DEA} = \sigma_0 \, e^{-\tau_{diss}/\tau_{AD}} \tag{2.14}$$

where σ_0 is the attachment cross section and τ_{diss} the time for relaxation beyond r_c.

Hence, τ_{AD} is inversely proportional to the width of the respective resonance and shorter at high energies, similarly the distance to r_c, is longer at higher transition energies and τ_{diss} thus larger. For this reason, the DEA curve is represented in Figure 2.3 to be red-shifted relative to the electron attachment curve (EA(AB)). Furthermore, at very low energies the attachment cross section is inversely proportional to the square root of the energy and the DEA cross section are generally orders of magnitude higher at the 0 eV threshold, where it is limited to exothermic processes.

With respect to the thermochemistry of the DEA process, the threshold for the formation of A and B⁻ up on electron attachment to AB is given by

$$E_{th} \sim \Delta H_r = BDE(AB) + EA(B) \tag{2.15}$$

where the dissociation energy of the A–B bond is denoted by BDE(AB), while the electron affinity of fragment B is denoted by EA(B). In general terms, the thermochemical threshold energy for DEA to a polyatomic molecule can be written as follows

$$E_{th} = \sum BDE_{(Educt)_i} + \sum BDE_{(Product)_j} - EA(X) \tag{2.16}$$

where the electron affinity of the charge-retaining fragment X is denoted by EA(X), and the bond dissociation energies for all formed and broken bonds are given by $BDE_{(Product)_j}$ and $BDE_{(Educt)_i}$, respectively.

It is also possible that the experimental measurement may record the negative ions produced via the DEA process at energies above their corresponding thermochemical threshold. For one thing, the extra energy can be retained in the neutral and negative ion fragments as internal or translation energy, and it follows that the appearance energy (AE) of the negative ion produced by DEA may be expressed as

$$AE(B^-) = E_{\text{th}} + E^* \tag{2.17}$$

where E^* is the additional energy distributed to the fragments as internal energy or translation energy[43,76,78].

However, DEA is a resonant process and does only occur in the narrow energy ranges of the corresponding vertical transition, which in turn may be well above the threshold for the respective process. Thus, in DEA the appearance energy of individual fragments does only coincide with the corresponding threshold if the energy range of a resonance overlaps with the respective threshold value. Hence, threshold calculations for DEA fragments do only provide a lower limit for the AEs.

In addition to relaxation through AD or dissociation a TNA may also be stabilized through intramolecular vibrational energy distribution (IVR), allowing for mass spectrometric observation of the metastable molecular anion. This is, however, generally limited to very low energies at the 0 eV threshold and enabled by effective coupling of the respective electronic state with the nuclear coordinates through the Jan-Teller or pseudo-Jan-Teller effect. Correspondingly, these observations are mostly restricted to highly symmetric, relatively large molecules, examples being SF_6, C_{60} and C_6F_6.[83,84]

2.3 Neutral Dissociation

Neutral dissociation is a process in which the electron interaction leads to electronic excitation, i.e., inelastic electronic scattering. When the initial electronic excitation energy exceeds the energy required for bond dissociation in a molecule, it has the potential to break apart into two or more neutral fragments. Neutral dissociation is not a resonant process, and its threshold depends on the lowest electronic excitation energy and the bond dissociation energy of the respective molecule. The initial excitation energies of numerous organic and inorganic molecules can be as low as 2 to 5 eV[85]. This makes neutral dissociation active at low electron energies. When a diatomic molecule AB is electronically excited and dissociates to form two neutral fragments the process may be depicted by the equation 2.18

$$AB + e^-(\varepsilon_1) \rightarrow AB^\# + e^-(\varepsilon_2)(\varepsilon_2 < \varepsilon_1) \rightarrow A^\# + B^\# \tag{2.18}$$
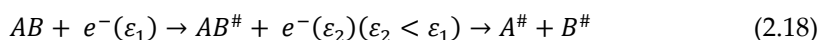
where "#" denotes electronic and/or vibrational excitation. The dissociation of a neutral molecule into fragments can take place solely if the initial electronic excitation energy surpasses the bond dissociation energy (BDE) of AB.

Neutral dissociation may be very efficient, especially for larger molecules with a high density of electronic states. Neutral dissociation can exhibit a significant cross section over a broad range of electron energies, depending on the density of electronically excited states of the molecule and the dissociative nature of these states. As there are no charged fragments produced during

neutral dissociation, it can be a challenge to study this process using a mass spectrometry setup. Nevertheless, electron scattering experiments can be used to measure a molecule's electronic excitation cross section and obtain insights into its potential for neutral dissociation cross sections[86] and quantum mechanical calculation can provide information on the dissociative nature of these states. Moreover, the dissociative excitation process of a $Fe(CO)_5$ was studied with the aid of an electron induced fluorescence apparatus (EIFA)[87,88]. This device can detect photons in the UV/Visible region generated by excited neutral species created by electron-molecule collisions, and its energy-dependent photon efficiency curves can offer useful information about the neutral dissociation process of a molecule.

2.4 Dipolar Dissociation

The process of electron induced dipolar dissociation (DD) involves the formation of an ion-pair resulting from an electronically excited state, depicted as $AB^{\#}$ in Eq. 2.19.

$$AB + e^-(\varepsilon_1) \rightarrow AB^{\#} + e^-(\varepsilon_2)(\varepsilon_2 < \varepsilon_1) \rightarrow A^{(*)+} + B^{(*)-} \qquad (2.19)$$
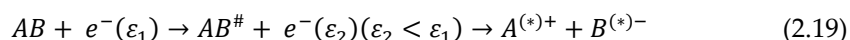
DD and neutral dissociation (ND) are similar, but DD requires overcoming the coulomb interactions between the positively and negatively charged fragments. Non-resonant anion fragment formation may be observed through this process above the excitation energy of the respective molecule. Thus, non-resonant anion formation above the excitation energy of a molecule is a clear indication of DD and can readily be distinguished from DEA, which is a resonant process. The thermochemical threshold for DD of a diatomic molecule AB is given by the equation 2.20

$$E_{\text{th}}(A^+ + B^-) = BDE(AB) + IE(A) - EA(B) \qquad (2.20)$$

However, DD is generally less efficient than DEA, DI, and ND and we did not observe DD process in our studies.

3 Methodology

3.1 Experimental Setups

The part of this thesis that was conducted at the University of Iceland involves high vacuum (HV) gas-phase experiments using a crossed electron-molecular beam apparatus termed SIGMA (SImply a Gas-phase MAchine), that is described in section 3.1. That part of the studies focuses on analyzing the energy dependence and mass spectrometry of the relevant fragments. Quantum chemical calculations are performed at the DFT and coupled cluster level of theory to underpin the interpretation of the gas phase experimental data. These are briefly described in section 3.3. Finally, a scanning electron microscope equipped with a QMS and a hemispherical electron energy analyzer that enables local Auger electron spectroscopy (AES) was used for comparative UHV-FEBID study. The instrument is located at the Friedrich-Alexander-Universität Erlangen-Nürnberg (FAU) in Erlangen, Germany, and a part of this thesis work was conducted during a secondment with PD Dr. Hubertus Marbach at the FAU. This instrumentation is described in section 3.4.

3.1.1 Gas-phase Experiment

In the gas phase experiments, a high-vacuum (HV) crossed electron-molecular beam machine (SIGMA), operating under single collision conditions, was used to conduct the investigations. A schematic representation of the instrument is shown in Figure 3. The chamber housing the instrument is built of non-magnetizable stainless steel and has a base pressure of $1\text{-}3\times10^{-8}$ mbar. The working pressure during experiments was in the range $2\text{-}9\times10^{-7}$ mbar. In SIGMA, an electron beam with a narrow energy distribution intersects with an effusive molecular beam, and the electron-molecule interaction leads to the formation of ions. The ions are extracted into a quadrupole mass spectrometer (QMS) for their analysis and detection. Both negative and positive ions can be analyzed by changing the polarity and voltages of the mass spectrometer, the ion optics and the detection system. The SIGMA instrument comprises three critical components; The first is a trochoidal electron monochromator (TEM), which enables the generation of a monochromatic electron beam. The second is a heatable effusive gas inlet system that enables a controlled supply of the target molecules into the chamber. This is a standard stainless-steel Swagelok inlet system, via which gaseous, liquid or solid, samples may be introduced, directly, through evaporation or through sublimation, respectively. The capillary system transports the vapor to the interaction area, where it is introduced as an effusive beam and crosses the electron beam perpendicular to the quadrupole mass spectrometer. The third component is a HIDEN EPIC 1000 quadrupole mass spectrometer that enables identify and detection of the ions generated in the interaction section.

The TEM was originally introduced by Stamatovic and Schulz[89,90], and it can be operated over a wide range of electron energies and has good energy resolution at comparatively high electron currents, even at very low energies. The trochoidal electron monochromator in our research facility is divided into three primary sections, as shown in Figure 3.1. These sections are designed

to provide a quasi-monoenergetic, collimated electron beam. The first section M1-M3 is composed of a hair-pin tungsten filament followed by a stack of plates with the filament and the progressively smaller apertures of the plates in-line but displaced with respect to the center of the x-axis. The plates are kept electrically isolated from each other using ruby balls and their voltage can be fine-tuned individually. Electrons with a wide energy distribution are emitted from the hairpin tungsten filament (M1) and directed via a series of lenses provided by M2–M4, into the second section of the monochromator. The second section, the deflection section, is provided by two plates M5 and M6 that are perpendicular to the electrical lens components M2-M4 as well as the succeeding components. An electric field is provided between these plates along the y-axis and an orthogonal magnetic field is provided along the z-axis, generated by two Helmholtz coils positioned outside the chamber. Through the M2 and M4 lens components, the electrons move along the z-axis direction and once they enter the deflection section they are subject to the crossed electric and magnetic fields.
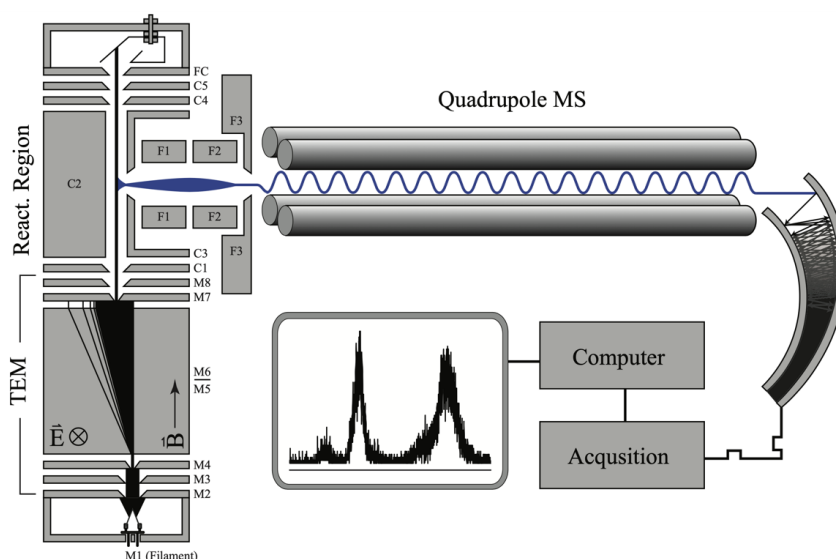
Figure 3.1 Schematic representation of the SIGMA and TEM used in these studies. A tungsten filament serves as the source of the electrons that are then energy-selected by the TEM. The collision region, here denoted by "React. Region," is where electrons and the effusive molecule beam collide; from there, ions are collected by the quadrupole mass spectrometer and directed to an electron multiplier, where the signal is processed. Adapted with permission from ref.[91].

In the deflection section, the crossed electric and magnetic fields force the electrons on a trochoidal trajectory and caused them to drift in the x-axis direction with at a constant velocity v_x.

$$v_x = \frac{E \times B}{|B|^2} \qquad (3.1)$$

Equation 3.1 can be modified to Equation 3.2 due to the fact that E and B are perpendicular.

$$v_x = \frac{E}{B} \qquad (3.2)$$

Hence, the displacement of the electrons in the x-direction is proportional to the time duration they reside in the deflection section and thus their velocity in the z-axis direction. The electrons fan-out along the x-axis as they pass through the deflection area with the faster electrons experiencing less displacement than slower electrons and only a narrow velocity component exits the deflection zone through the centrally placed aperture on the exit plate M7, hence, the exit aperture on M7 is displaces by Δx with respect to the entering aperture on M4. After exiting the deflection section, the electrons are guided through the lens components M7–M8 before entering the collision area where the now quasi monoenergetic electron beam crosses the effusive molecular beam. The electron energy is controlled by the voltage difference between M1-M2 block and the M3-M8 block which can be ramped from 0 up to about 100V. Following their entry into the collision zone through the C1 lens, electrons interact with the target molecules to generate ions, as discussed in detail in Chapter 2. The resulting ions are extracted using a weak electric field and focused onto the quadrupole mass spectrometer using the electrical lens components F1 through F3. To avoid back-scattering of electrons, C4 and C5 guide extra electrons away from the collision area and into the Faraday cup at which the electron current can also be measured. To avoid condensation of the target molecules or background contaminations on the electric lens components during experiments, these are maintained at a temperature of 393 K using two halogen lamps. To obtain the mass spectra, the *m/z* range is scanned at a constant electron energy, while the ion yield curves are recorded by scanning the energy range at a fixed *m/z* [92].

3.1.2 Energy Scale Calibrations and Appearance Energy Determination

The electron energy for the negative ion experiments was calibrated using ion yield of SF_6^- from SF$_6$ that appears through a narrow resonant structure at the 0 eV threshold with a full-width-at-half-maximum (FWHM) of the resonance being less than 1 meV[93,94]. This allows for an energy calibration but also gives a decent estimate of the energy distribution that is reflected in the full width at half maximum (FWHM) of that signal as is shown in Figure 3.2.
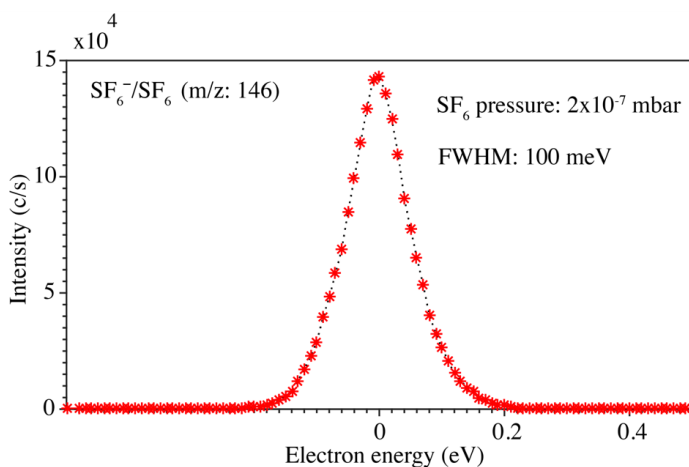
Figure 3.2 A typical ion yield curve for SF$_6^-$/SF$_6$ measured with SIGMA. Adapted with permission from ref.[82].

The energy scale for positively charged fragments was calibrated using the first ionization energy of argon at 15.759 eV[95], i.e., the appearance energy of Ar^+ from Ar.
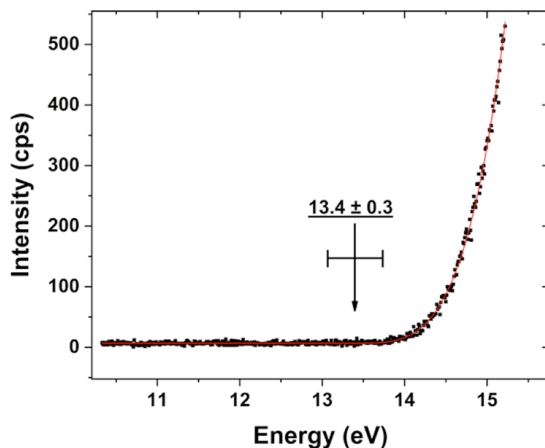
Figure 3.3 An example of a typical DI ion yield curve fitted with the Wannier-type model and measured by SIGMA in the gas phase. Reprinted with permission from ref. 64.

For the determination of the appearance energies (AEs) of individual positive ions, a Wannier-type threshold function[96] was fitted to the experimental threshold region of the respective data. The fitted cross-section dependence as a function of electron energy ($\sigma(E)$) is shown in equations 3.3 and 3.4, and a typical fit to the Ar^+ threshold signal is shown as an example in Figure 3.3. This method was used to calculate the appearance energies of the positively charged fragments[96].

$$\sigma(E) = b \qquad\qquad\qquad\qquad\qquad\qquad\qquad E < AE_1 \qquad\qquad (3.3)$$

$$\sigma(E) = b + a_1(E - IE_1)^{d_1} \qquad\qquad\qquad AE_1 \leq E \qquad\qquad (3.4)$$

In Eq. 3.3 and 3.4, (b) accounts for the baseline signal (a_1) is a scaling factor, (AE_1) the appearance energy, and (d_1) an exponential factor describing the rise of the cross section in the threshold region. For the negative ions, the fit of two Gaussian functions were used to determine the peak position where the negative ion yields were a combination of two contributions[97].

3.1.3 Quantum Chemical Calculation

All quantum chemical calculations can be obtained by solving the Schrödinger equation. Understanding how electrons will be distributed around the nucleus of a molecule allows us to determine the chemical and physical properties of the molecule. The Schrödinger equation can be written in a time-independent form, as shown in equation 3.5

$$H(r, R)\psi(r, R) = E\psi(r, R) \qquad\qquad\qquad\qquad (3.5)$$

where H denotes the Hamiltonian operator (the sum of potential and kinetic energy of the system), E represents the energy eigenvalue, and Ψ is the wave function as a function of nuclear and electronic coordinates. The Hamiltonian operator H can be calculated easily for a system with

a single particle, but it becomes very complicated when multiple particles are involved in the system due to the necessity of considering the kinetic energy of each individual electron ($\hat{T}_e$), as well as nuclei ($\hat{T}_n$), electrostatic repulsion between the nucleus ($\hat{V}_{nn}$), electrostatic repulsion between electrons ($\hat{V}_{ee}$), and coulomb attraction involving nuclei and electrons ($\hat{V}_{ne}$). This is represented in equation 3.6.

$$\hat{H} = \hat{T}_e + \hat{T}_n + \hat{V}_{nn} + \hat{V}_{ee} + \hat{V}_{ne} \tag{3.6}$$

Because of the intrinsic and interrelated complexity of the electrons in the system, which precludes the possibility of an analytical solution, the Schrödinger equation for a complicated system requires several approximations, including Born-Oppenheimer approximation, Hartree approximation, and Hartree-Fock (HF) approximation, prior to being properly solved. The Born-Oppenheimer approximation is based on that the nuclear motion is significantly slower than the electronic motion, as the nucleus is much more massive than the electron. To the extent that this approximation holds, we can disregard the term $\hat{T}_n$ and treat $\hat{V}_{nn}$ as a constant. As a result, we can then calculate the potential energy surface. The Hartree approximation[98] assumes that electrons travel in isolation, such that the wavefunction for multiple electrons may be written as the sum of the wavefunctions for individual electron orbitals. In order to account for the antisymmetric character of orbitals, which is neglected by the Hartree approximation, the whole wavefunction is expressed as a Slater determinant (Hartree-Fock (HF) approximation[99,100]), and these orbitals can be expressed as the linear combination of basis-functions (basis-sets). By substituting trial wavefunctions into the HF energy equation and limiting it in terms of molecular orbital coefficients, one may derive a solution to the HF energy equation from the HF approximation of a many-electron wavefunction. However, post-HF approaches, such as coupled cluster theory, can potentially improve electron correlation, which is currently lacking in the HF method but would greatly increase computing costs.

The Coupled cluster (CC) method is a precise approach within quantum mechanics used for calculating electronic wavefunctions and energies in molecules. This post-Hartree-Fock method accounts for a broad range of electron correlation effects. In CC, the wavefunction is represented as an exponential series of excitation operators, which act on a reference wavefunction. The coefficients of these operators are obtained by solving a set of non-linear equations known as the CC equations. One significant advantage of the CC method is that it provides highly precise and reliable results for molecular properties such as bond lengths, dipole moments, and reaction energies. It is a potent tool for studying chemical dynamics, enabling calculations of excited states and potential energy surfaces for chemical reactions. Furthermore, the CC method is highly parallelizable, allowing for efficient calculations on large systems and parallel computer architectures[101].

Density functional theory (DFT) has emerged as the gold standard in quantum chemistry because it takes a different approach to dealing with the issue of electron correlation. According to the Hohenberg-Kohn (HK) theorems[102], which form the foundation of density functional theory, the actual energy of the system may be represented in the form of electron density. In DFT, accurate energy for the system may be calculated using a functional (a function of electron density); however, finding the proper functional will be the most important challenge. The electron density, in other words, may be calculated using the basis-functions (basis-sets) that characterize the orbitals occupied by the electrons. For the CC calculations in the current thesis, we employed the def2-TZVP basis set (a collection of basis-functions) where TZVP stands for polarized triple

zeta. Kohn-Sham density functional theory energy equation (equation 3.7) allows us to describe the ground state energy of the system if we know the electron density.

$$E[\rho(r)] = T_e^{KS}[\rho(r)] + V_{ek}[\rho(r)] + J[\rho(r)] + E_{xc}[\rho(r)] + V_{kk} \tag{3.7}$$

where $T_e^{KS}[\rho(r)]$ is the non-interacting electron kinetic energy term introduced by the Kohn-Sham equation[103] (i.e., the non-interacting electron kinetic energy term may be derived utilizing orbitals). For electron-nuclear attraction, we have $V_{ek}[\rho(r)]$, for electron-electron Coulomb interaction, we have $J[\rho(r)]$, for electron-electron repulsion exchange-correlation, we have $E_{xc}[\rho(r)]$, and for nuclear-nuclear interaction, we have V_{kk}. We can obtain an accurate solution for the $T_e^{KS}[\rho(r)]$, $V_{ek}[\rho(r)]$, $J[\rho(r)]$, and V_{kk} terms but only an approximation for the $E_{xc}[\rho(r)]$ term. Many DFT functionals diverge in how they express $E_{xc}[\rho(r)]$ exploiting different functionals. There is a plethora of functionals accessible nowadays (PBE0, BP86, B3LYP, etc.). The TPSS and PBE0 functionals were employed in the DFT calculations current thesis. The TPSS is a meta-generalized gradient approximation (meta-GGA) functional that, in addition to density and gradient magnitude, takes into account the kinetic energy density or Laplacian (second derivative) of the density. The hybrid functional, PBE0, combines accurate exchange from Hartree-Fock theory (25%) and DFT exchange (75%). Goel *et al.*[104] and Kepp *et al.*[105] demonstrated that while computing gold clusters, the PBE0 and TPSS functionals yielded the most precise structures and bond energies than other functionals, including B3LYP, M06, etc. The ORCA program, version 4.1, was employed for quantum chemical calculations, utilizing various functionals and basis sets. Detailed information regarding the specific functionals and basis sets used for each precursor molecule can be found in the methods sections of the subsequent chapter. The quantum chemical calculations were employed to aid in interpretation of the gas-phase results and to establish the possible reaction leading to the observed *m/z* ratios for each precursor.

3.2 UHV FEBID Setup

At the University of Erlangen-Nürnberg (FAU), a Multiscanlab commercial UHV system manufactured by Omicron Nanotechnology in Germany was utilized to investigate novel precursor molecules and produce deposits at the nanoscale level. The instrument is divided into two main chambers, analysis and preparation chambers, from which the analysis chambers is shown in Figure 3.4.
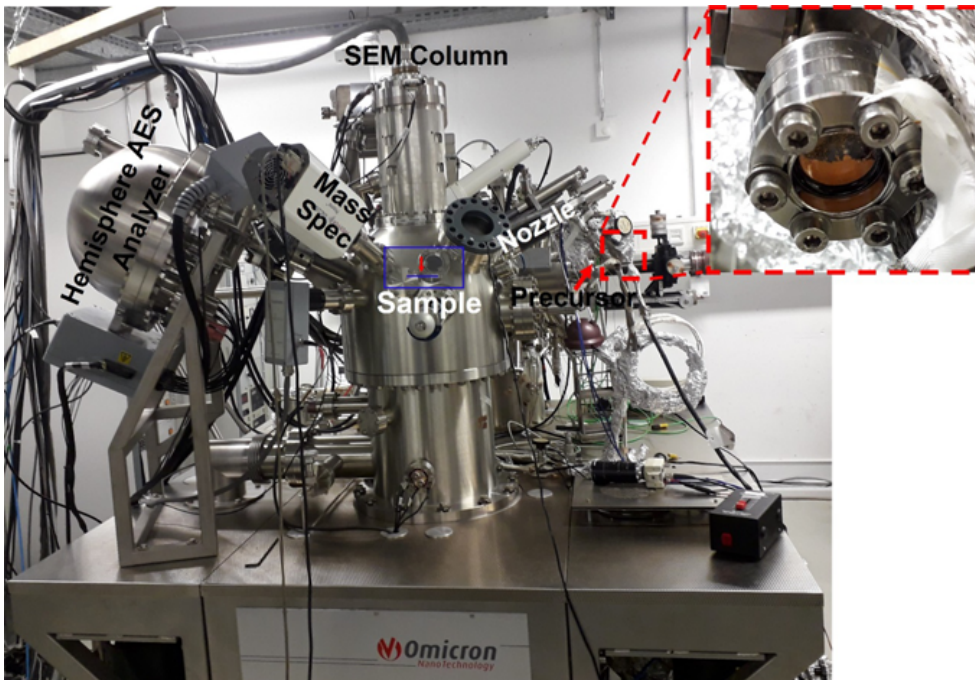
Figure 3.4 Picture of the UHV-FEBID analysis chamber with descriptions of the most important parts. Adapted with permission from ref[106].

Using a sequence of gate valves and linear transfer arms, samples can be transported between the chambers used for sample preparation, analysis, and quick entry. The analysis chamber, equipped with a UHV compatible electron column (Leo Gemini), is utilized for both the creation of nano-scaled structures via FEBID and the imaging of specimens using scanning electron microscopy (SmartSEM/Zeiss, nominal resolution of approximately 3 nm). The chamber background pressure is maintained at 2×10^{-10} mbar. The instrument is further equipped with an Auger electron spectrometer with hemispherical electron energy analyzer combined with the highly focused electron beam (EA 125, Omicron Nanotechnology, NanoSAM).

The precursor gases are delivered through stainless-steel tubing with an inner diameter (capillary) 3 mm at an approximate 12 mm distance to the surface of the substrate. In addition, a QMS (Pfeiffer / Prisma QMS 200M) is used to monitor the purity of the precursor gas. The local vapor pressure at the substrate´s surface was simulated by a Monte Carlo-based method (the GIS Simulator version 1.5[107]) and for comparatively volatile precursors, the pressure at the surface was found to be 30 times greater than the background pressure[106,108]. For example, at the experiment conditions where the target gas pressure in the chamber is 3.0×10^{-7} mbar, the calculated pressure at the surface will be 9.0×10^{-6} mbar. The preparation chamber (base pressure 10^{-9} mbar) is equipped with a sputter gun (Omicron Nanotechnology/ISE10) that is used to clean the substrates before the FEBID studies. These included SiO_x (nat.)/Si(111) and SiO_2 (200 nm)/Si(111) substrates in the current experiments. More information about the UHV system can be found in Thomas Lukasczyk's Ph.D. dissertation[109] and Elif Bilgilisoy's Ph.D. dissertation[106] and more information on the parameters and settings in individual experiments are provided in the respective publications and manuscripts delivered as a part of this thesis work.

4 Results and Discussion

4.1 (CH$_3$)AuP(CH$_3$)$_3$ FEBID Precursor

The fundamental electron-induced dissociation path(s) in gold deposition from (CH$_3$)AuP(CH$_3$)$_3$ as precursor and how these are reflected in the composition of FEBID deposits is best understood by comparing and combining gas-phase studies on the isolated precursor molecules and UHV-FEBID findings with the same precursor. The (CH$_3$)AuP(CH$_3$)$_3$ precursor, as stated in the research paper by Marashdeh *et al*.[110], is an excellent candidate for CVD and FEBID owing to its good volatility under high vacuum and stability at room temperature. The asymmetric crystal structure of (CH$_3$)AuP(CH$_3$)$_3$ is responsible for these features; it contains six molecules per unit cell, of which four have strong aurophillic connections, and two are monomeric. Therefore, under UHV conditions, a number of weakly attached molecules leave the crystal structure. This process weakens the crystal structure of the compound, allowing the "freed" molecules to enter the gas phase. The present experiments, performed in a gas-phase, reflects this and show that the intact precursor molecules can be efficiently delivered into the high vacuum chamber at ambient temperature. The results of a previous FEBID experiment performed under HV conditions demonstrated that 19-25 at. % gold could be deposited from (CH$_3$)AuP(CH$_3$)$_3$, which is highly promising[111]. Prior FEBID study on Co(CO)$_3$NO[112] and Fe(CO)$_5$[113] precursors under UHV conditions resulted in the formation of deposits with more than 80% and 90% metallic purity, respectively. This suggests that the UHV system provides the appropriate environment for minimizing impurity, which may result from the undesirable deposits from residual gases in FEBID the process of creating nanostructures. For comparison, HV experiments on these precursors have given notably lower metal content deposits, with values as low as 70-85 at.% Fe[25,114] and 40-50 at.% Co[115–117], respectively, as compared to the 80% and 90% achieved under UHV conditions.

In the current study, we investigated the fundamental electron induced dissociation pathways of (CH$_3$)AuP(CH$_3$)$_3$ through dissociative ionization experiments in the gas phase, supported by quantum chemical calculations. (CH$_3$)AuP(CH$_3$)$_3$ is a potential FEBID precursor considered for the production of gold nanostructures with high metallic content, and the present work was carried out in conjunction with FEBID experiments with this precursor, using a scanning electron microscope (SEM) operating under ultrahigh vacuum (UHV) conditions. This combined study is at the core of an effort to better understand the electron induced processes underpinning FEBID and link those to the ligand structure of the respective precursors and the resulting composition of the deposits formed in FEBID.

The study was conducted in collaboration with the group of PD. Dr. Hubertus Marbach at the FAU in Erlangen where the FEBID experiments were conducted and the group of Prof. Sjoerd Harder also at the FAU Erlangen which synthesized the precursor under study. The FEBID experiments were conducted by Dr. Elif Bilgilisoy Alperen and constitute a part of her PhD thesis. The gas phase studies, and the quantum mechanical calculations were conducted at the University of Iceland and are submitted as an integral part of the current thesis.

The results of this study were published in Nanomaterials:

4.1.1 Methods

The DI experiments were performed using SIGMA, the electron/molecule crossed apparatus to collide electrons with $(CH_3)AuP(CH_3)_3$ molecules under single collision conditions. Ion fragments were analyzed with a quadrupole mass spectrometer and ion yields were recorded by scanning through electron energy and m/z ranges. Positive ion yields were normalized to the Ar^+ formation cross-section and appearance energies were determined by fitting a model function to the onset of ion yields and calibrated with reference to the first ionization energy of Ar[95]. The gas-phase experiment was conducted at room temperature with base pressure of 2-3 $\times$ 10^{-8} mbar and working pressure of 7-9 $\times$ 10^{-7} mbar.

Threshold energies were calculated using ORCA 4.1 computational chemistry program[118]. The meta-GGA TPSS functional and def2-TZVP basis set were used to optimize the geometries of the primary positively charged fragments and their neutral counterparts, applying the D3(BJ) dispersion correction developed by Grimme *et al.*[119] Harmonic vibrational frequencies were confirmed to be positive, proving that all structures were stationary points on the potential energy surface and were used to compute the thermal and zero-point vibrational energies. Number of alternative fragmentation pathways were considered for each positive fragment observed and compared to the respective AEs. Single-point coupled-cluster computations at the DLPNO-CCSD(T)/QZVPP level of theory were also performed on the optimized geometries as this approach is generally considered more accurate than DFT. The threshold energies for each fragment were calculated by subtracting the sum of the energies of the fragments from the energy of the parent molecule.

4.1.2 Results and Discussion

Dissociative ionization in the gas phase

The electron impact mass spectrum of $(CH_3)AuP(CH_3)_3$ is shown in Figure 4.1; the mass spectrum was collected at 50 eV incoming electron energy and 7×10^{-7} mbar target gas pressure. There are two distinct trends in the mass spectrum. The first is due to the dissociation of the trimethylphosphine ligand, as evident by the predominant contributions of the *m/z* ratios 61 $([P(CH_3)_2]^+)$, 59 $([P(CH_3)CH_2]^+)$, and 45 $([PCH_2]^+)$, as well as the *m/z* ratios at 76 and 75, which are assigned to the $[HP(CH_3)_2CH_2]^+$ and $[P(CH_3)_2CH_2]^+$ fragments, respectively. The second is the removal of one or more methyl ligands which leads to $[AuP(CH_3)_3]^+$, $[AuP(CH_3)_2]^+$, $[AuP(CH_3)]^+$, and $[AuP]^+$, i.e., the observation of the *m/z* ratios 273, 258, 243, and 228, respectively.
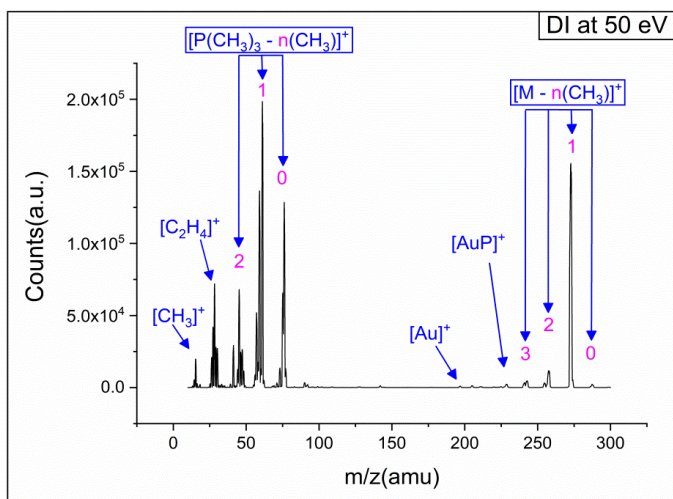
Figure 4.1 The mass spectrum of the positively charged ions produced during dissociative ionization of the $(CH_3)AuP(CH_3)_3$ precursor at an incident electron energy of 50 eV. Adapted with permission from ref [66]*.*

The onset area of the respective ions reflects their appearance energy and thus the thermochemistry of the underlying processes. Figure 4.2 shows the onset of the ion yield curves for the formation of the parent cation (m/z 288) and for the $P(CH_3)_3$ loss with the significant contributions at m/z 76, 75, 61, 59, and 45, as well as the methyl loss at m/z 273. Also shown are the Wannier-type threshold fits that were utilized to determine the AEs and their associated error ranges. The AEs are determined as the mean of three to four separate measurements, and the stated margins of error are the standard deviations from the average values, rounded up to the nearest 100 meV.

Table 4.1 compares the thermally adjusted threshold energies for the corresponding routes calculated at the DLPNO-CCSD(T)/QZVPP and TPSS/def2-TZVP levels of theory with the respective experimentally determined appearance energies.

The experimentally obtained value of 7.5 ± 0.2 eV for the ionization energy of the parent molecule, i.e., the formation of the $[(CH_3)AuP(CH_3)_3]^+$ cation, is in close agreement with the calculated threshold values of 7.58 and 7.45 eV determined at the DLPNO-CCSD(T)/QZVPP and TPSS/def2-TZVP levels of theory, respectively. The methyl loss is one of the dominant fragmentation paths that result in the formation of positively charged gold-containing fragments, as seen by the relatively intense peaks in the mass spectrum in Figure 4.1 in the m/z range of 228 to 288.
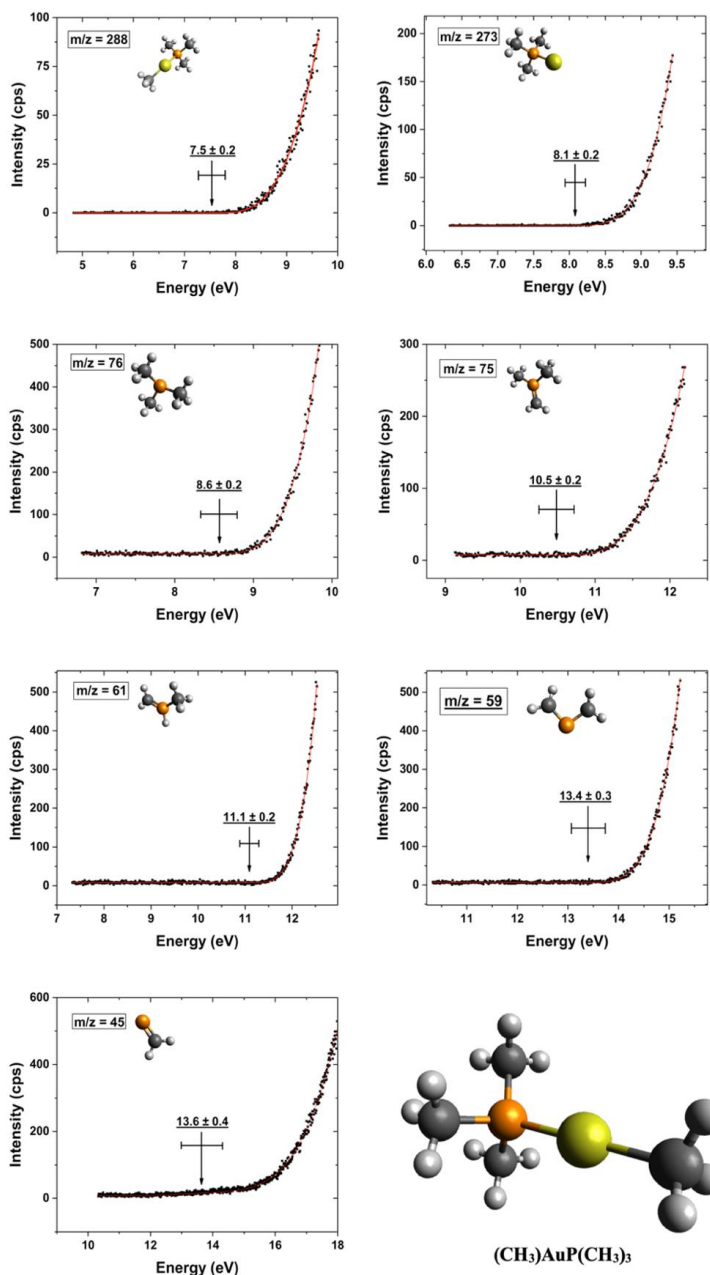
Figure 4.2 Ion yield curves of the parent cation and the most prevalent cations from DI of (CH₃)AuP(CH₃)₃ along with their corresponding Wannier-type threshold fits, appearance energies, and confidence limits. The respective cation structures optimized at the TPSS/def-TZVP level of theory are shown in the respective panels and the structure of the intact neutral (CH₃)AuP(CH₃)₃ is shown in the bottom-right corner. Adapted with permission from ref.[66]

For m/z 288, one possibility is the cleavage of the Au-CH$_3$ bond, whereas another channel is the disruption of one of the P-CH$_3$ bonds in the trimethylphosphine ligand, both of which would release the methyl group. The experimental AE value at m/z 288 is 8.1± 0.2 eV, which is in close accordance with the calculated values of 8.59 and 8.38 eV at the TPSS/def-TZVP and DLPNO-CCSD(T)/QZVPP levels of theory, respectively, for the methyl ligand cleavage from the gold, i.e., the production of [AuP(CH$_3$)$_3$]$^+$. The loss of methyl ligand from trimethylphosphine, in contrast, has computed threshold values of 10.20 and 10.44 eV at the respective theory levels. These values are around 2 eV higher than the experimental AE.

Table 4-1 TPSS/def2-TZVP and DLPNO-CCSD(T)/QZVPP theoretical threshold values for reaction paths leading to the observed m/z ratios in electron impact ionization and dissociation of (CH$_3$)AuP(CH$_3$)$_3$, compared to the respective experimentally determined AEs Experimental and theoretical results that are in best agreement are highlighted bold.

m/z	Product	TPSS-TZVP	DLPNO-CCSD-QZVPP	AE (eV)
288	**[(CH$_3$)AuP(CH$_3$)$_3$]$^+$**	**7.45**	**7.58**	**7.5 ± 0.2**
273	**[AuP(CH$_3$)$_3$]$^+$ + (CH$_3$)**	**8.59**	**8.38**	**8.1 ± 0.2**
	[(CH$_3$)AuP(CH$_3$)$_2$]$^+$ + (CH$_3$)	10.20	10.44	
76	**[P(CH$_3$)$_3$]$^+$ + (CH$_3$)Au**	**9.38**	**9.17**	
	[HP(CH$_3$)$_2$(CH$_2$)]$^+$ + (CH$_3$)Au	9.73	9.61	**8.6 ± 0.2**
	[P(CH$_3$)$_3$]$^+$ + (CH$_3$) + Au	12.04	11.54	
75	**[P(CH$_3$)$_2$(CH$_2$)]$^+$ + (CH$_3$)AuH**	**10.64**	**10.68**	
	[P(CH$_3$)$_2$(CH$_2$)]$^+$ + (CH$_3$)Au + H	12.12	11.86	**10.5 ± 0.2**
	[HP(CH$_3$)(CH$_2$)$_2$]$^+$ + (CH$_3$)AuH	12.62	12.90	
61	**[HP(CH$_3$)(CH$_2$)]$^+$ + (CH$_3$)$_2$Au**	**11.16**	**11.20**	
	[HP(CH$_3$)(CH$_2$)]$^+$ + C$_2$H$_6$ + Au	11.22	10.43	**11.1 ± 0.2**
	[P(CH$_3$)$_2$]$^+$ + (CH$_3$)$_2$Au	11.64	11.62	
59	**[P(CH$_2$)$_2$]$^+$ + (CH$_3$)$_2$Au + H$_2$**	**13.46**	**13.45**	
	[P(CH$_2$)$_2$]$^+$ + (CH$_3$)AuH + CH$_4$	13.18	12.93	
	[P(CH$_2$)$_2$]$^+$ + H$_2$Au + C$_2$H$_6$	13.56	13.07	**13.4 ± 0.3**
	[HP(CH$_2$)CH]$^+$ + (CH$_3$)$_2$Au + H$_2$	15.22	15.61	
45	[PCH$_2$]$^+$ + (CH$_3$)AuH + 2(CH$_3$)	17.50	17.04	
	[PCH$_2$]$^+$ + (CH$_3$)AuH + C$_2$H$_6$	**13.84**	**13.20**	
	[PCH$_2$]$^+$ + Au(CH$_3$) + C$_2$H$_6$ + H	15.32	14.38	
	[PCH$_2$]$^+$ + (CH$_3$)Au(CH$_3$) + CH$_4$	**13.50**	**13.06**	
	[PCH$_2$]$^+$ + Au + (CH$_3$) + C$_2$H$_6$ + H	17.98	16.76	**13.6 ± 0.4**
	[HPCH]$^+$ + (CH$_3$)AuH + C$_2$H$_6$	16.19	15.97	
	[PCH$_2$]$^+$ + AuH + (CH$_3$) + C$_2$H$_6$	14.85	13.75	
	[HPCH]$^+$ + AuH + (CH$_3$) + C$_2$H$_6$	17.19	16.52	

Significant contributions from breakage of the (CH$_3$)Au–P(CH$_3$)$_3$ bond are also observed in the mass spectrum shown in Figure 4.1. These are observed at m/z 76, 75, 61, 59 and 45, representing the trimethylphosphine moieties intact and after the loss of one and two methyl groups as well as

additional hydrogen loss. From these fragments *m/z* 59, 61 and 45 correspond to the loss of hydrogen from $[P(CH_3)_3]^+$, $[P(CH_3)_2]^+$, and $[PCH_3]^+$, respectively.

The calculated threshold energies for the direct fragmentation leading to $[P(CH_3)_3]^+$, at *m/z* 76 are 9.17 and 9.38 eV at the DLPNO-CCSD(T)/QZVPP and TPSS/def-TZVP levels of theory, respectively. We obtained an AE of 8.6 ± 0.2 eV for this *m/z* ratio in our experiments, which is somewhat below the calculated threshold values. Considering a transfer of hydrogen from one of the methyl groups to the phosphor and production of $[HP(CH_3)_2CH_2]^+$, increases the threshold values to 9.61 and 9.73 eV at the DLPNO-CCSD(T)/QZVPP and TPSS/def-TZVP levels of theory, respectively, and considering the formation of the methyl radical and Au as the neutral counterpart (instead of $[AuCH_3]$), raising the corresponding threshold values further by about 2 eV. For the *m/z* ratio 75, the additional loss of one hydrogen, we measured an AE of 10.5 ± 0.2 eV. This value is in close accordance with the calculation values of 10.68 and 10.64 eV at the DLPNO-CCSD(T)/QZVPP and TPSS/def-TZVP levels of theory, respectively, when considering the formation of $[HAuCH_3]$ as the neutral counterpart. Higher threshold values are obtained when the formation of $[HP(CH_2)_2CH_3]^+$ via hydrogen migration inside the cation or generation of $[AuCH_3]$ as well as a hydrogen radical as the neutral counterparts are taken into account (about 1 to 2 eV).

The threshold values for direct loss of one methyl ligand, i.e. the creation of $[P(CH_3)_2]^+$, are 11.64 and 11.62 eV at the TPSS/def-TZVP and DLPNO-CCSD(T)/QZVPP levels of theory, respectively. This is around 0.3 eV over the confidence limits for the measured 11.1 ± 0.2 eV AE of *m/z* 61. In a study on dissociative ionization of trimethylphosphine, Bodi *et al.*[120] examined the production of $[HP(CH_3)(CH_2)]^+$ via transfer of hydrogen atom from a methyl ligand to the phosphor for the *m/z* ratio of 61, rather than a simple methyl loss. For this route they found a stabilization of around 0.43 eV at the CBS-QB3 and G3 levels of theory and based on the kinetic studies and calculations on the reaction path, they conclude that this mechanism could be the dominant channel in the methyl loss from $P(CH_3)_3$ upon DI. Our calculations agree with this and show stabilization through hydrogen transfer of 0.42 and 0.48 eV at the DLPNO-CCSD(T)/QZVPP and TPSS/def2-TZVP levels of theory, respectively. With $(CH_3)_2Au$ as the neutral counterpart, the calculated threshold energies are found to be 11.20 and 11.16 eV, respectively, which agrees well with the measured AE of *m/z* 61, suggesting the formation of $[HP(CH_3)(CH_2)]^+$ rather than the direct methyl loss without further rearrangement. We have also considered the neutral counterparts to be ethane (C_2H_6) as well as atomic Au in this process, yielding threshold values of 10.41 and 11.22 eV at the respective levels of theory. Interestingly the difference between the DFT and coupled cluster results is comparatively large for this channel and we attribute that to overestimation of the atomic energy of Au by DFT meta-GGA TPSS functional, and as the CCSD threshold is much lower than the observed AE we do not consider this path likely. A decrease in mass-to-charge ratio from *m/z* = 61 to 59 represents the loss of two hydrogen atoms from $[P(CH_3)_2]$, which could be related to the formation of the positively charged $[P(CH_2)_2]^+$ fragment and the neutral counterparts H_2Au and C_2H_2, $(CH_3)_2Au$ and H_2, or $(CH_3)AuH$ and CH_4. We find the experimental AE for this fragment to be 13.4 ± 0.3 eV. At the DLPNO-CCSD(T)/QZVPP theoretical level, the calculated values for these reactions are 13.45 eV for H_2 formation, 12.93 eV for CH_4 production, and 13.07 eV for C_2H_6 formation, respectively. Hence, there is excellent agreement between the calculated and experimental results for this *m/z* ratio when assuming the formation of neutral H_2 and $(CH_3)_2Au$ and the positively charged $[P(CH_2)_2]^+$ fragment. Differently, both the $[CH_4]$ and $[C_2H_6]$ formation pathways are below the confidence limits for the experimental AE.

Lastly, a high intensity peak corresponding to the formation of $[PCH_2]^+$ at m/z 45 is observed in the DI mass spectrum of $(CH_3)AuP(CH_3)_3$. As a significant number of combinations of neutral fragments can be assigned to the m/z 45, choosing the appropriate reaction path through comparison of the calculated thresholds with experimental results is not simple. Additional complications arise from the observation that the m/z 45 threshold begins to rise quasi-linearly at 10 eV. This quasi-linear contribution could arise from background gases and we compensate for this by substituting the baseline (d) by a linear function (a + bx) for in the Wannier-type function, as was previously done by Fiegele *et al.*[96] when they determined the DI thresholds. The experimental value for the AE of this fragments was found to be 13.6 ± 0.4 eV. This agrees well with the TPSS/def2-TZVP threshold values of 13.84 and 13.50 eV for the production of the neutral fragments $(CH_3)AuH$ and C_2H_6 and for the production of the neutral fragments $(CH_3)Au(CH_3)$ and CH_4, respectively. As can be seen in Table 1, all of the calculated threshold values for other probable processes are above the confidence limit of the AE. We also find significant contributions at m/z = 28 and m/z = 15 that may represent methyl and ethene from the precursor molecule. However, we have not determined the AEs of these fragments as these are likely to contain significant contributions from residual gases such as pump oil and nitrogen. Also, the complexity which arises from the significant number of reaction paths possible for these m/z ratios, complicates the assignment significantly.
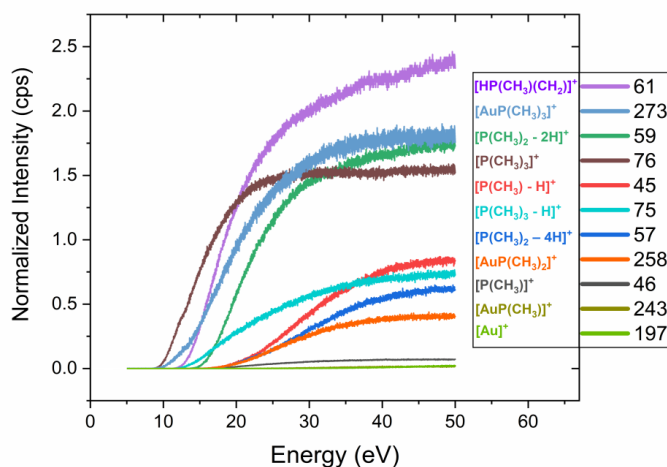
Figure 4.3 Representative curves of the ion yields for the positive ion fragments observed in DI of $(CH_3)AuP(CH_3)_3$. The ion yields are shown in the incidence electron energies range from their threshold to 50 eV and are normalized with respect to the signal intensity and the pressure of Ar^+/Ar at 50 eV incident electron energy. Adapted with permission from ref.[66].

To provide bases for comparison of the fragmentation observed in these DI experiments and the composition of the deposits in the UHV-FEBID experiments, a quantification of ligand loss must be provided. Further, this comparison should preferably be provided for the energy range of the secondary electrons relevant in the FEBID process. Figure 4.3 shows the ion yields of the individual fragments from threshold up to 50 eV electron energy. Table 4.2 compares the integral intensity of these fragments in this energy range with the respective peak heights in the mass

spectrum displayed in Figure 4.1. All the intensities are normalized with respect to the maximum intensity at *m/z* 61, as 100.

Table 4-2 Relative integral intensities of DI fragments from (CH₃)AuP(CH₃)₃ from thresholds to 50 eV derived from the ion yield curves (Figure 4.3), and the relative peak intensities of positively charged fragments from the DI mass spectrum recorded at 50 eV electron incidence energy (Figure 4.1). The compositions of FEBID deposits from both current UHV and earlier HV studies are presented at the bottom of the table.

Fragment	*m/z*	Relative DI Yield (Intensity)	Relative DI Yield (Integration)
$[AuP(CH_3)_3]^+$	273	78.41	79.07
$[AuP(CH_3)_2]^+$	258	5.64	13.30
$[AuP(CH_3)]^+$	243	2.36	0.36
$[Au]^+$	197	0.51	0.29
$[P(CH_3)_3]^+$	76	64.78	78.98
$[P(CH_3)_3 - H]$	75	33.12	28.47
$[HP(CH_3)(CH_2)]^+$	61	100	100
$[P(CH_3)_2 - 2H]^+$	59	68.8	68
$[P(CH_3)_2 - 4H]^+$	57	26.19	17.98
$[P(CH_3)]^+$	46	14.1	2.54
$[P(CH_3) - H]^+$	45	33.7	24.7

Avrg. C loss per incident		1.94	2.01
Avrg. P loss per incident		0.80	0.76
UHV deposit composition	31-34 at. % Au	65-67 at. % C	1-2 at. % P	-
HV deposit composition	19-25 at. % Au	54-62 at. % C	12-16 at. % P	2-7 at. % O

The average phosphor and carbon loss per DI ionization incidence is calculated from the individual contributions and compared to the corresponding results from the UHV- and HV-FEBID studies (bottom of Table 4.2). We attribute the slight difference between the peak values and the integral intensity values for the carbon and phosphor loss mainly to the different AEs of the individual fragments, but also the form of the ion yield curves may play a role.

The mean phosphor and carbon loss per DI incidence in the gas phase are calculated by summing the contributions from all fragments, weighted by their individual phosphor and carbon losses, and dividing by the sum of all DI event intensities. For comparison with the UHV-FEBID results, desorption from the surface is assumed for all fragments that do not contain gold in the assigned

reaction paths given in bold in Table 4.1. The extent of dissociation of the carbon and phosphor in the gas phase is then compared to the stoichiometric ratios of the elements in the unaltered precursor to obtain a hypothetic atomic composition of a deposit that would result from the unaltered DI processes if these alone were determining for the composition of the FEBID deposits. The carbon loss in the DI experiments is found to be on average around 2, while the average phosphor loss is about 0.8 for every ionization incidence. Thus, if the unaltered DI processes are the dominant fragmentation process in FEBID with this precursor, then the Au:P:C deposit ratio would be 1:0.2:2, as compared to the composition ratio of the intact molecule of 1:1:4.

4.1.3 Dissociative Ionization, UHV, and HV FEBID Composition

The mean value of carbon loss in DI experiment was consistent with the results of the present UHV-FEBID study, which showed a Au:C ratio of about 1:2. In the UHV-FEBID investigation, the phosphor, however, was almost completely desorbed, whereas in the gas phase DI experiments, the average loss of phosphor per dissociation incidence was roughly 0.8, thus in 20% of the DI cases, the Au–P ligand survived unchanged. The primary reason for this is through the contribution of the methyl-ligand loss which was linked to the central gold atom, which in the gas phase contributed to the stability of the m/z 273 ([AuP(CH$_3$)$_3$]$^+$ fragment).

However, the EDX results of the HV-FEBID study demonstrated a Au:P ratio of 1:0.63 to 1:0.64 and a Au:C ratio of 1:2.5 to 1:2.8. Although the deposit's carbon content may be slightly higher owing to the contributions of background gases under HV condition, the significantly higher content of phosphor in the HV FEBID study must have its origins in different decomposition/desorption mechanisms in the HV- and UHV-FEBID experiments. Both experiments utilized an electron energy of 5 keV, and in the HV-FEBID experiment, the composition was not considerably affected by the electron current or deposition time. Different substrates or the partial pressure of the background gas in the UHV and HV-FEBID investigations must be the cause of this difference. It is evident from the UHV study that the dissociated phosphor-containing ligands might be freely desorbed from a SiO$_2$ substrate, which is a typical passivated material. The electron-induced decomposition of (CH$_3$)AuP(CH$_3$)$_3$ adsorbed to the SiO$_2$ substrate correlates with the neutral (CH$_3$)$_2$Au formation as well as dissociation channels related to the [P(CH$_n$)$_2$]$^+$ fragment formation observed as significant contributions in the DI experiments. The [AuP(CH$_3$)$_2$]$^+$ fragment was the main fragmentation channel in the DI experiment where the phosphor remained attached to the central gold atom. This channel cannot be active in the UHV-FEBID, as nearly all phosphor desorbed from the SiO$_2$ substrate. However, secondary surface induced reactions or electron induce secondary reactions may also lead to further decomposition of this fragment. Figure 4.4 shows a schematic representation of a possible deposition process that is consistent with the anticipated reaction route of the UHV-FEBID experiment.
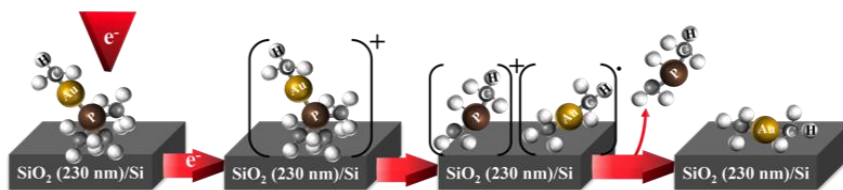
Figure 4.4 A proposed deposition rout for the UHV FEBID, using $(CH_3)Au(CH_3)_3$. As precursor. Positively charged $[(CH_3)Au(CH_3)_3]^+$ is formed during electron-induced ionization of $(CH_3)AuP(CH_3)_3$, which quickly decays into $[P(CH_n)_2]^+$ and $[(CH_3)_2Au]$. The last process involves the desorption of $[P(CH_n)_2]$ from the surface, leaving behind the deposited fragment $[(CH_3)_2Au]$. Adapted with permission from ref.[66].

This does not apply to the FEBID deposition with the $CH_3AuP(CH_3)_3$ precursor on a Si wafer under HV condition, where the deposits still contained significant phosphor with a reported Au:C:P:O compositions of 19–25 at% Au, 54–62 at% C, 12–16 at% P, and 2–7 at% O. Van Dorp *et al*.[111] stated that the dissociation of CH_3–Au ligand and desorption of the methyl group was likely to be the main reaction pathway and that the trimethylphosphine was not a good leaving group for gold precursors. The results of the current UHV-FEBID experiment are contrary to these finding, and it is not straight forward to correlate the different composition of the deposits in these experiments with different surface reactivities in the experiments. However, it is not uncommon for deposition under UHV and HV conditions to result in notably different FEBID compositions, even when comparing the same substrates. In a recent study conducted by Mahgoub *et al*. on the FEBID deposition of $Pt(CO)_2Br_2$ and $Pt(CO)_2Cl_2$[121], it was shown that under HV conditions, halogen desorption was highly efficient, while under UHV conditions, the Pt:Br and Pt:Cl ratios of deposits remained close to 1:1.65 and 1:1.56, respectively. Similar to the electron-induced decomposition of $Pt(NH_3)_2Cl_2$, where efficient Cl elimination occurred via intramolecular reductive HCl production, the desorption of halogen may be attributed to reactions between the precursor molecules with surface water inside the HV chamber. Also, in situ exposure to ammonia during electron irradiation allows for the reductive elimination of HCl from surface-adsorbed (η^3-$C_3H_5)Ru(CO)_3Cl$[122,123]. The purification of deposits by oxidative processes via electron irradiation in the presence of water has proven to be effective in several experiments, both post- and in-situ. For example, under HV conditions, the purity of gold deposits from dimethylgold (III) trifluoroacetylacetonate was increased by 75% by removing carbon residues through oxidation[124] and finally the purity of gold deposits reached 91 at. %.

The oxygen presence in the HV chamber during the FEBID study with the current precursor was reported by van Dorp *et al*[111]. To the same end, it has been suggested that electron-induced reactions of $(CH_3)AuP(CH_3)_3$ in the presence of water might produce non-volatile $OP(CH_3)_3$ or other phosphorous oxides. Although this may help in elucidating the higher phosphor content in the HV-FEBID study compared to the deposit's phosphor content in the current UHV study, the lower O:P ratio in the deposits shows that the presence of water in the chamber could not be the only explanation for the differences between UHV and HV results.

4.2 [(CH$_3$)$_2$AuCl]$_2$ FEBID Precursor

In this study, the feasibility of using [(CH$_3$)$_2$AuCl]$_2$ as a potential FEBID precursor for gold deposition was investigated. Gas-phase fragmentation of this compound through DI and DEA were studied experimentally, FEBID was performed in the UHV setup, and quantum chemical calculations were employed to identify the primary electron induced reaction pathways. The UHV FEBID results were interpreted in light of the observed DI and DEA fragmentation processes and compared to prior FEBID research conducted by van Dorp *et al.*[111] using this precursor under HV. Their previous work demonstrated a promising Au content of 29-41% without any additional purification steps, whereas the current research revealed that the Au content could be further increased to around 50-61 at.% under UHV conditions.

This work was carried out in collaboration with the groups of PD. Dr. Hubertus Marbach, Prof. Dr. Hans-Peter Steinrück, and Prof. Sjoerd Harder, both at the Friedrich Alexander University in Erlangen, Germany (FAU). The UHV FEBID experiments were carried out during a secondment at FAU under the supervision Dr. Elif Bilgilisoy in the group of Dr. Hubertus Marbach. The gas phase experiments, and quantum chemical calculations were carried out at the University of Iceland. The precursor was synthesized and delivered for experiment by the group of Prof. Sjoerd Harder at the FAU. Both the gas phase and surface studies constitute an integral part of this PhD thesis.

The results of this study have been submitted for publication in a peer reviewed Journal:
A combined gas phase dissociative ionization, dissociative electron attachment and deposition study on the potential FEBID precursor [(CH$_3$)$_2$AuCl]$_2$, by Elif Bilgilisoy, Ali Kamali, Thomas Xaver Gentner, Gerd Ballmann, Sjoerd Harder, Hubertus Marbach, Hans-Peter Steinrück[*] and Oddur Ingólfsson[*],
Submitted

4.2.1 Methods

The [(CH$_3$)$_2$AuCl]$_2$ precursor, was synthesized following the protocols outlined by Paul and Schmidbaur[125]. The synthesized precursor was stored in a stainless-steel reservoir at 253 K under nitrogen atmosphere inside a glove box. For visual inspection of purity and potential degradation the reservoir was provided with a small glass window. To avoid photodecomposition during the experiments, the filled reservoir was covered with aluminum foil and directly attached it to the analytical chamber.

For the FEBID deposition experiments, the Multiscanlab UHV equipment (Omicron Nanotechnology, Germany) described in the method section of this thesis was employed. Auger spectra were recorded using 15 kV acceleration voltage and 3 nA beam current (magnification; 100 kX; spectra area; 1.2 × 0.9 µm^2). Electron exposures to 0.4 nA, 1.5 nA, and 3 nA were utilized for FEBID with a beam energy of 5 keV. Lithographic operations were managed using a high-speed DAC PCIe-card and proprietary software written in LabVIEW 8.6 (National Instruments) (M2i.6021-exp, Spectrum GmbH, Germany). For deposition, lithographic step size of 6.2 nm and a sweep number of 10 was used. SEM images were obtained using SmartSEM (Zeiss) at a beam energy of 15 keV and a current of 0.4 nA and were adjusted for contrast and brightness. Mass spectra of the gas phase [(CH$_3$)$_2$AuCl]$_2$ precursor was recorded at ambient temperature (298 K) prior to deposition experiments. The precursor, [(CH$_3$)$_2$AuCl]$_2$, was found to be volatile enough to transfer from the container into the UHV chamber using a gas-injection system where the precursor

container was kept at ambient temperature. The studies were conducted with precursor chamber pressures set between 6.0 and 9.0×10^{-7} mbar. According to calculations using GIS Simulator (version 1.5)[108], the local pressure at the substrate surface was about $2.0–3.0 \times 10^{-5}$ mbar, which is roughly 30 times higher than the chamber pressure. FEBID structures were deposited and studied on two substrates: SiO_2 (500 nm) / Si(111) and thermally cleaned Si (111). The SiO_2 (500 nm) / Si(111) sample was not subjected to any specialized cleaning procedures. AFM studies were conducted using a JPK NanoWizard 4 in noncontact mode.

The crossed election-molecular beam device, discussed in preceding chapters, was used to carry out the gas phase DI and DEA experiments under single collision conditions. These studies were conducted at a constant working pressure of around 4×10^{-7} mbar. The electron energy resolution during the measurements was 140 meV, as measured by the full width at half maximum (FWHM) of the SF_6^- formation from SF_6 at 0 eV incident energy. The incident electron energy for the MS recordings of positive ions was set to 50 eV, whereas those of negative ions ranged from 0 to 10 eV. The SF_6^- formation from SF_6 at 0 eV and the Ar^+ formation from Ar at 50 eV were used to calibrate the electron energy scale in negative ion mode and positive ion mode, respectively. Normalization of the negative ion yields was carried out using the intensity of the SF_6^- signal from SF_6 at 0 eV and the corresponding working pressures, whereas the normalization of the positive ion yields was carried out using the intensity of the Ar^+ signal from Ar at 50 eV.

For quantum chemical calculations, the ORCA program, version 4.1 was employed[118] using the hybrid GGA functional PBE0 with the def2-TZVP basis set and D3BJ dispersion correction developed by Grimme[119] for all geometry optimization. This chose was based on an evaluation by Kang *et al*.[126] on various DFT functionals for gold(I) and gold(III) hydrocarbons where they concluded that the hybrid GGA functional PBE0, with a TZ basis set, was the most effective for optimizing geometry as well as a subsequent study by Kepp *et al*.[105] where they determined that PBE and TPSS functionals, with dispersion corrections, generally provided good results for evaluating gold bond dissociation enthalpies. The restricted Kohn-Sham (RKS) formalism was utilized for closed-shell systems, while the unrestricted (UKS) was employed for open-shell systems. The geometry optimizations were performed using tight SCF settings, and the PBE0/def2-TZVP single point energies were calculated using normal SCF settings. Positivity of the harmonic vibrational frequencies were confirmed at the PBE0/def2-TZVP level of theory and were used to determine the thermal corrections at 298K as well as the zero-point vibrational energies. Single point coupled-cluster computations at the DLPNO-CCSD(T)/TZVP level of theory, using the TZVP/c auxiliary basis set with normal PNO settings were also performed on the optimized geometries. Both levels of theory were used to calculate threshold energies for individual processes by subtracting the single point energies of optimized geometries of the respective fragments from those of the parent molecule, while taking into account the zero-point vibrational energies (ZPVEs) and thermal energy corrections. All fragmentation processes were analyzed by computing various reaction paths, including rearrangement reactions.

4.2.2 Results and Discussion

Surface studies:

Figure 4.5(a) shows a SEM image of a 4×4 μm^2 square FEBID structure deposited with $[(CH_3)_2AuCl]_2$ as precursor and an electron dose of 7.80 C/cm^2 using 5 keV acceleration voltage and 1.5 nA beam current. A green star represents the center of the AES zone in Figure 4.5(a). Figure

4.5(b) depict the AES spectra of the substrate and deposit, shown with black and green lines respectively. Two primary AES signals are observed on the clean SiO_2 (500 nm) /Si (111) substrate's surface and deposit. The peak at 272 eV is attributed to C_{KLL} Auger transitions of carbon[127] while the peaks at 468, 483, and 503 eV are attributed to O_{KLL} and SiO_2 Auger transitions. Following deposition, AES signals are found at 69, 181, 272, and 430 eV[127]. These Auger transitions are attributed to Au_{NOO}, Cl_{LMM}, C_{KLL}, and Sn_{MNN}, respectively (Figure 4.5(b), green spectrum). A broad low intensity signal is apparent at 367 eV[127], which is attributed to residual Sn from the methylation agent $SnMe_4$ used in the synthesis. The deposit of this precursor was found to consist of 51 at.% Au, 2 at.% Cl, 42 at.% C, and 5 at.% Sn. Figure 4.5(c) magnifies a selected section of the SEM image in Figure 4.5(a). Nanoparticles in the deposit are visible in Figure 4.5(c), despite the background signal blurring the image. These are clearer after background subtraction using the ImageJ software[128], shown in Figure 4.5(d). Careful analysis of Figure 4.5(d) reveals nanoparticles of various shapes and sizes on the substrate's surface. Some nanostructures are triangular (yellow circle), rod-shaped (green circle), or hexagonal (red circle), but most of them are spherical shaped (blue-colored circle). These shapes are comparable to gold-based nanoparticles reported in the literature[129,130], which have mostly been investigated by STEM and/or TEM[131].
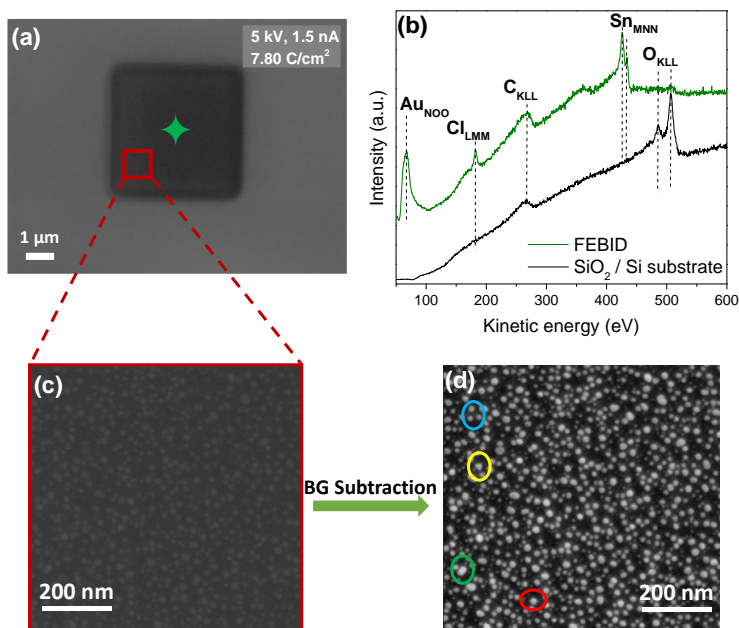
Figure 4.5. (a) SEM images of FEBID deposits with beam current of 1.5 nA, 5 keV and electron dose of 7.80 C/cm². The FEBID structures were deposited on SiO₂ substrate. (b) The results of the AES analysis on the SiO₂ substrate prior deposition (black line) and after deposition (green line). The position where the AES analysis was performed is shown with a green-colored star in (a). (c) The magnified image of the red-colored square in (a). (d) The image of (c) after subtracting the background with different shapes of nanoparticles in red, green, yellow and blue circles.

HAADF-STEM on FEBID (SiO$_2$ (500 nm) / Si (111))

The morphology of the nanoparticles was investigated using HAADF-STEM. Using SiO$_2$ substrates, FEBID structures with 4 × 4 µm^2 dimensions and electron dosages of 7.80 C/cm^2 were created. For HAADF-STEM measurements, a 100-nm-thick, 4 µm-wide lamellae was constructed (Figure S1-paper II). The HAADF-STEM image depicted in Figure 4.6(a) shows a rather regular spatial distribution of nanoparticles smaller than 5 nm and non-uniformly distributed nanoparticles with 15-20 nm sizes in the deposit. Figure 4.6(b) shows a magnification of a nanoparticle from Figure 4.6(a). The particle's fringe spacing is 0.23 nm, which corresponds to the (111) plane spacing of a face-centered cubic (FCC) gold nanoparticles (refs[132,133]). Figure 4.6(c) depicts the selected area electron diffraction (SAED) pattern used to assess the crystallinity of gold nanoparticles. Here, the bright circular patterns reflect polycrystallinity of the particles and the growth planes (111), (200), (220), (133), and (222) correspond to gold's close-packed, face-centered cubic crystal structure lattice spacings (d-spacings) of 2.30 Å, 2.07 Å, 1.42 Å, 1.23 Å, and 1.17 Å[134], respectively (Figure 4.6(c)).
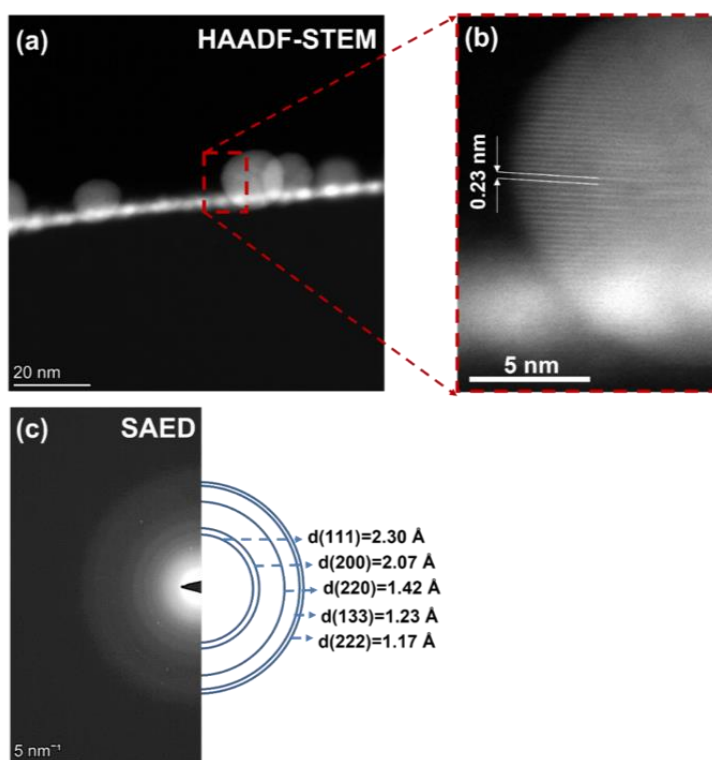
Figure 4.6. (a) HAADF-STEM image of the nanoparticle formed due to FEBID deposition. (b) Magnified image of the red-colored square in (a) which depicts the interplanar distance of 0.23 nm between the {1, 1, 1} planes in the fcc lattice. (c) SAED image of the nanoparticles that match to the fcc gold structure.

FEBID on SiO$_2$ (500 nm)/Si (111) at different beam currents

To create FEBID deposits, the [(CH$_3$)$_2$AuCl]$_2$ precursor was used with beam currents of 0.4 nA (2 × 2 µm^2), 1.5 nA (4 × 4 µm^2), and 3 nA. The remaining deposition parameters (electron dose; 7.80

C/cm^2; acceleration voltage; 5 keV) were not changed across all three experiments. Structures of FEBID deposits were examined by SEM and non-contact AFM. The FEBID deposits and their deposition parameters are shown in Figure 4.7(a). Mega-magnified SEM images are shown in Figure 4.7(b). The effect of the beam current on the composition of these structures was evaluated using Auger electron spectroscopy. The respective spectra are displayed in Figure 4.7(c).

As seen in Figure 4.7(b), particle size decreases with increasing current. Nanoparticle quantities and mean diameters were calculated using ImageJ[128]. Non-round gold nanoparticles are seen in Figure 4.5(d). The average Feret diameter was used was used to measure the size of the nanoparticles since it accounts for all possible orientations (Figure S2- paper II).
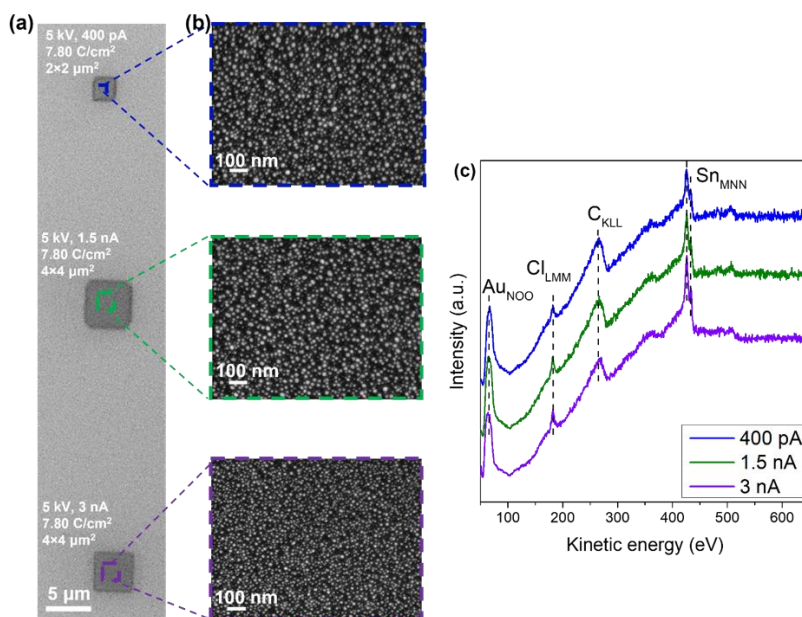
Figure 4.7. (a) SEM image of FEBID structures deposited with different beam currents on SiO$_2$ substrate. (b) Magnified images of FEBID structures from (a), (c) AES analysis of the FEBID structures deposited with 3nA, 1.5 nA, and pA with purple, green, and blue line, respectively.

The average particle size increased from 9.8 to 10.1 to 8.2 nm as the beam current increased from 0.4 nA to 1.5 nA, however, further increase in beam current to 3 nA decreased the particle size to 8.2 nm. The AES diagrams in Figure 4.7(c) were used to calculate the atomic contents of the structures. The composition changed from 45 at.% Au, 1 at.% Cl, 49 at.% C, 5 at.% Sn at 0.4 nA deposition current to 50 at.% Au, 2 at.% Cl, 42 at.% C, 6 at.% Sn at 1.5 nA and 52 at.% Au, 2 at.% Cl, 38 at.% C, 8 at.% Sn at 3 nA. Hence, the gold content rises with increasing current, but carbon content falls. The AES carbon peak areas are 36% smaller when comparing 0.4 nA and 3 nA deposition and by 14% when comparing the depositions with 0.4 nA and 1.5 nA beam current. The deposited gold particle therefore becomes smaller in size as the concentration of carbon decreases with increasing deposition current. This is in line with reported height reduction of gold nanoparticles by 18% due to the elimination of carbon that was reported earlier for FEBID deposits subjected to oxidative purification [135].

AFM of FEBID on (SiO$_2$ (500 nm) / Si (111)) at different beam currents

Non-contact AFM was employed to measure deposit height and particle size to gain additional information on the effect of beam current on the structure of the deposits. Figures 4.8(a) and 4.8(b) show enlarged 2D AFM images and Figure 4.8(c) shows the corresponding height profiles. The magnified 2D AFM images (Fig. 4.8(b)) reveal the same pattern as the SEM images in Figure 4.7(b): the gold nanoparticles are about the same size for FEBID structures written with 0.4 nA and 1.5 nA, but they are smaller in the deposit written with 3 nA beam current. AFM scans show particle diameters of 10.4 nm for 0.4 nA, 9.5 nm for 1.5 nA, and 7.0 nm for 3 nA. (Figure S3b-paper II). These values correlate well with the SEM image values (9.8 nm – 0.4 nA; 10.1 nm – 1.5 nA; 8.2 nm – 3 nA). In Figure 4.8(b), the line profiles for structures formed with 0.4 nA and 1.5 nA show deposit thicknesses of ~17 nm, whereas the thickness of the deposit written with 3 nA is only ~9 nm. Most intriguingly, the beam current changes the deposition height profiles (see also Figure 4.8(b), Figure S4 – paper II).
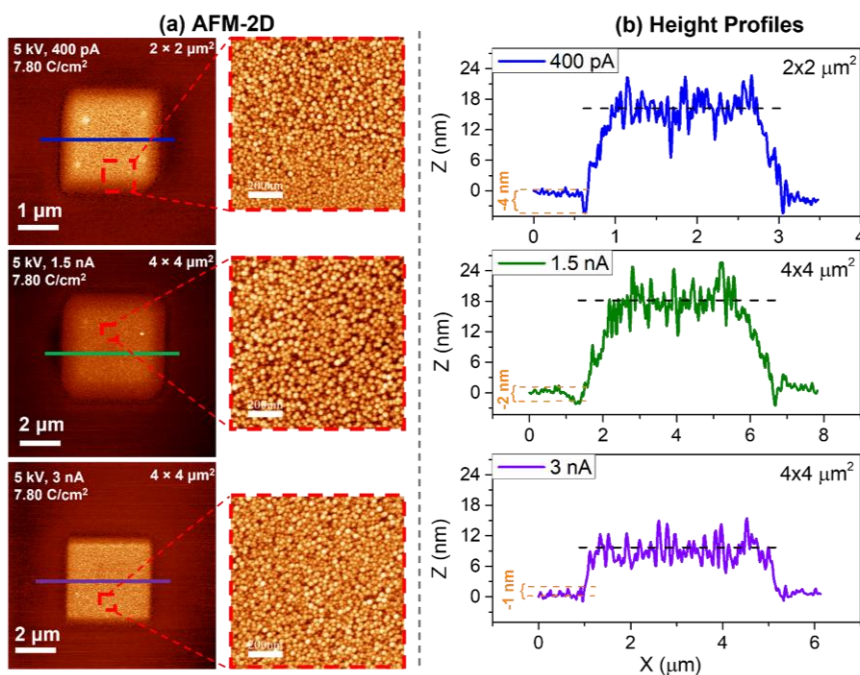
Figure 4.8. (a) Two-dimensional AFM images and magnified AFM images according to the red-dashed squares, (b) related line profiles for the FEBID structures produced with electron dose of 7.80 C/cm^2 using the beam currents of 3 nA (purple line), 1.5 nA (green line), and 400 pA (blue line).

Furthermore, a negative dip at the margin of the height profile of the 0.4 nA deposition (Figure 4.8(b), blue line) is clearly visible (bracketed with orange dashed lines) and this dip is also visible in the depositions with 1.5 nA and 3 nA beam currents (green and purple lines, respectively), though less apparent. Hence, as the beam current increases, the depth of the negative dip diminishes. We attribute this to an etching effect, but for all-beam currents, the etching impact is less significant than the deposition. In the literature, halogen-based precursors were previously shown

40

to cause etching and deposition[38,136] and etching was attributed to halogen ligand release. As demonstrated in Figure 4.7(c), the spectrum produced with 0.4 nA current (blue line), shows 30% lower Cl peak than the structures of deposits with 1.5 and 3 nA beam currents and the combination of scanning electron microscopy (SEM) and atomic force microscopy (AFM), shed light on how the etching process correlates with the Cl content in the deposits and how the carbon content is reflected in the particle size.

FEBID on sputtered and thermally cleaned Si (111)

UHV environment alone is not enough to produce high metal content FEBID structures, as revealed in various UHV-FEBID studies[113,136,137]. A clean and well-defined substrate also enhances metal atomic content. Consequently, to show how surface preparation (reduction of C and O impurities) affects deposition quality, the SiO_2 substrate was sputtered with Ar^+ for 45 minutes and annealed at 823 K in an oxygen environment for 90 minutes before deposition. Following this preparation, AES was used to compare the cleaned surface to the uncleaned surface (Figure S5 – paper II). Figure S5-Paper II demonstrates that the carbon (C_{KLL} at 272 eV) and oxygen peaks (O_{KLL} at 508 eV) were lowered by 17% and 67%, respectively, revealing the Si_{LMM} peak at 92 eV. Utilizing the cleaned sample, a 4×4 μm^2 structures was created in a FEBID experiment with the $[(CH_3)_2AuCl]_2$ precursor using the parameters shown in Figure 4.5. Figure 4.9 shows SEM and AES analysis of this structure, whereby the AES-measured area is represented by a red star.
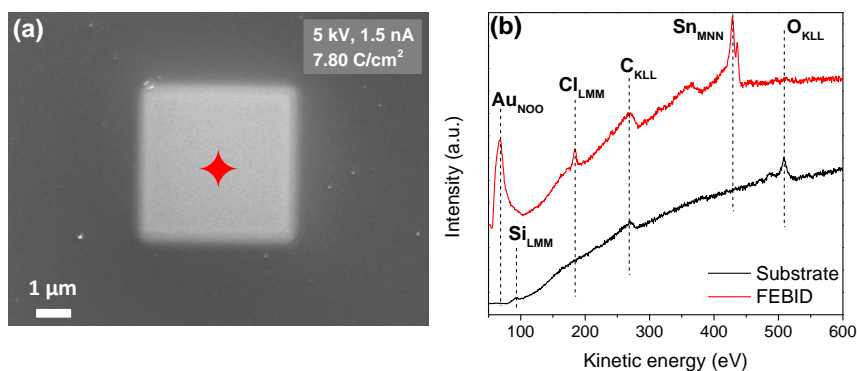
Figure 4.9. (a) SEM image of a FEBID structure with 4 x 4 μm^2 dimension size deposited on SiO_2 with electron beam parameters of 5 keV and 1.5 nA and an electron dose of 7.80 C/cm^2. (b) AES analysis of the SiO_2 substrate prior to deposition (black line) and the result from FEBID structure (red line), from the red-colored star in (a).

The AES data (red line) showed peaks at 69 eV for Au_{NOO}, 181 eV for Cl_{LMM}, 272 eV for C_{KLL}, and 430 eV for Sn_{MNN} yielding atomic quantities of 61 at.% Au, 1 at.% Cl, 35 at.% C, and 3 at.% Sn[127]. Compared to deposition on the untreated substrate shown in Figure 4.5(b), the Au content increased 10 at% while C content decreased 10 at% as result of the cleaning procedure.

In prior research, the same precursor, $[(CH_3)_2AuCl]_2$, was utilized to produce FEBID deposits on SiO_2 substrates under HV conditions with a 5 keV electron beam at beam currents of 0.1 and 0.4 nA.[111] The structures, evaluated with EDX, contained 29–41 at.% Au, 2–6 at.% Cl, and 53–68 at.% C, and the SEM pictures of the deposits showed rough textures. The atomic concentrations of the deposits in this reference study, support full Cl ligand desorption and deposit incorporation of

both (CH$_3$) ligands. Though the current study used UHV and 1.5 nA electron beam current, unlike the HV study and the AES is a surface-sensitive method, unlike the bulk-sensitive EDX technique. It is clear that the electron beam completely desorbs the Cl-ligands in FEBID with [(CH$_3$)$_2$AuCl]$_2$. This has also been the observation for other gold precursors containing the Cl ligand.[37,38]. Noticeably, however, the current UHV-FEBID findings show 10–20% more Au content in the deposits created with [(CH$_3$)$_2$AuCl]$_2$ than the HV FEBID results.

Based on the current study and supported by the previous HV study the following deposition reaction is proposed for FEBID of [(CH$_3$)$_2$AuCl]$_2$:

$$[(CH_3)_2AuCl]_2 + e^- \rightarrow Au_2(CH_3)_x + 2Cl \uparrow + (4-x)(CH_3) \uparrow \qquad (4.1)$$
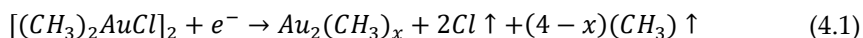
with the AES results shown in Figures 4.5(b) and 4.9(b) indicate that x is 1–2.

Gas-phase studies

Dissociative ionization in the gas phase under single collision conditions

A positive ion mass spectrum of [(CH$_3$)$_2$AuCl]$_2$ recorded at 50 eV electron impact energy is shown in Figure 4.10(a). The loss of methyl groups due to the DI process creates a rich fragmentation pattern from this precursor. In the DI spectrum, the molecular cation at *m/z* 524 is followed by the progressive loss of methyl ligands at *m/z* 509, 494, 479, and 464, with the loss of all four at *m/z* 464 being the most significant channel. At *m/z* 458, 444, and 429, one chlorine atom and two, three, and four methyl ligands are lost in a second progression. From these, *m/z* 458 has lost an extra hydrogen and *m/z* 444 overlaps with smaller contributions from *m/z* 443, which we ascribe to one more hydrogen loss. Similar to the previous progression, the most significant contribution here is through the elimination of all four methyl ligands (*m/z* 429). Both chlorines and two three- and four-methyl ligands are lost in the third progression at *m/z* 422, 408 and 394, respectively. Here, the contributions are comparable, but the loss of three methyl ligands, *m/z* 408, is somewhat stronger. The final progression occurs from the loss of both chlorine atoms, one gold atom and two, three and all four methyl groups at *m/z* 227, 225, 212 and 197, respectively. From these, *m/z* 225 represents the loss of two methyl groups and two hydrogens, while *m/z* 197 represents Au$^+$, the elemental gold. Furthermore, *m/z* 247 is seen with moderate intensity; this fragment is accounted for by the elimination of three methyl ligands, one chlorine atom, and one gold atom, leading to the formation of [(CH$_3$)AuCl]$^+$. The *m/z* 28 and 15 are also noticeable in the DI spectra. The produced [CH$_3$]$^+$ in DI of [(CH$_3$)$_2$AuCl]$_2$ contributes to *m/z* 15. However, also residual gas, including N$_2$, contributes to these signals.
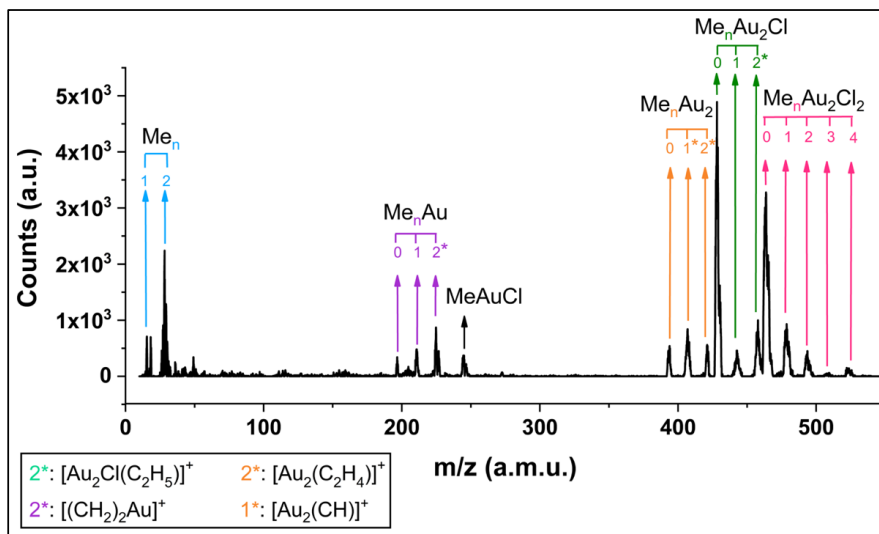
Figure 4.10. Dissociative ionization mass spectrum of cations formed from [(CH₃)₂AuCl]₂ recorded at incident electron energy of 50 eV.

The neutral fragments corresponding to most observed *m/z* ratios may be ascribed to more than one composition, making it difficult to assign the underlying fragmentation process. To further understand the fragmentation process, the corresponding AEs are obtained using a Wannier-type threshold function (see the methodology section) and compared to calculated threshold energies for a number of probable reaction paths.

Figure 4.11 displays the fitted onset-region of typical ion yield curves for the respective fragments with the average AE values derived from 3-4 ion yield curves obtained on different days, the respective geometries, optimized at the PBE0-TZVP level of theory, and are also shown. The computed AE thresholds for several reactions that might produce the relevant fragments are compared in Table 4-3. The best matches of the AEs with the threshold values for single bond ruptures without new bond formations are presented here. The assigned fragmentation reactions in Table 4-3 are in bold, and the thresholds are determined at both the PBE0-TZVP and DLPNO-CCSD(T)-TZVP levels of theory.

For the parent cation $[Au_2Cl_2(CH_3)_4]^+$ the AE, i.e., the ionization energy, is found to be 9.4 ± 0.3 eV. This is in good agreement with the calculated thresholds of 9.23 at the PBE0-TZVP level of theory, while the DLPNO-CCSD(T)-TZVP theory levels, the value is found to be 9.92 eV, which is about 0.2 eV above the higher limit of the experimental AE. For *m/z* 509, loss of one methyl group, the intensity is too low to determine the AE but for *m/z* 494, the removal of two methyl groups, we derive an AE of 9.7 ± 0.2 eV. At the PBE0-TZVP and DLPNO-CCSD(T)-TZVP levels of theory, the threshold values for single bond ruptures, which create two CH_3 radicals, are 13.51 and 14.06 eV, respectively. These exceed the experiment's confidence limits by 4 eV. Considering the formation of ethane CH_3CH_3 in this process, on the other hand, yields threshold values of 9.67 and 10.29 eV at the PBE0-TZVP and DLPNO-CCSD(T)-TZVP levels of theory, respectively. Here the situation is similar to that observed for the formation of the parent ion and at the DFT level of theory the agreement is excellent the threshold value calculated at the DLPNO-CCSD(T)-TZVP levels of theory is about 0.3 eV above the respective confidence limit. This is somewhat surprising as the coupled

43

cluster approach is expected to be more accurate as compared to the DFT calculations and delivers at large good agreement for the other, more complicated, fragmentation processes. Furthermore, using the smaller bases set SVP at the DLPNO-CCSD(T) level, results in good agreement with the experimental AE for these fragments. For the more complicated fragmentation reaction, on the other hand, the SVP basis set generally underestimated the AEs. For comparison, the threshold values calculated with the SVP basis set are shown in Table S7-Paper II in comparison with the experimental AEs and the threshold values calculated with the larger TZVP basis set.

The loss of three methyl ligands, *m/z* 479, has an AE of 11.4 ± 0.2, and the determined threshold for this process without new bond formation is 15.01 and 15.04 eV at the PBE0-TZVP and DLPNO-CCSD(T)-TZVP levels of theory, respectively.
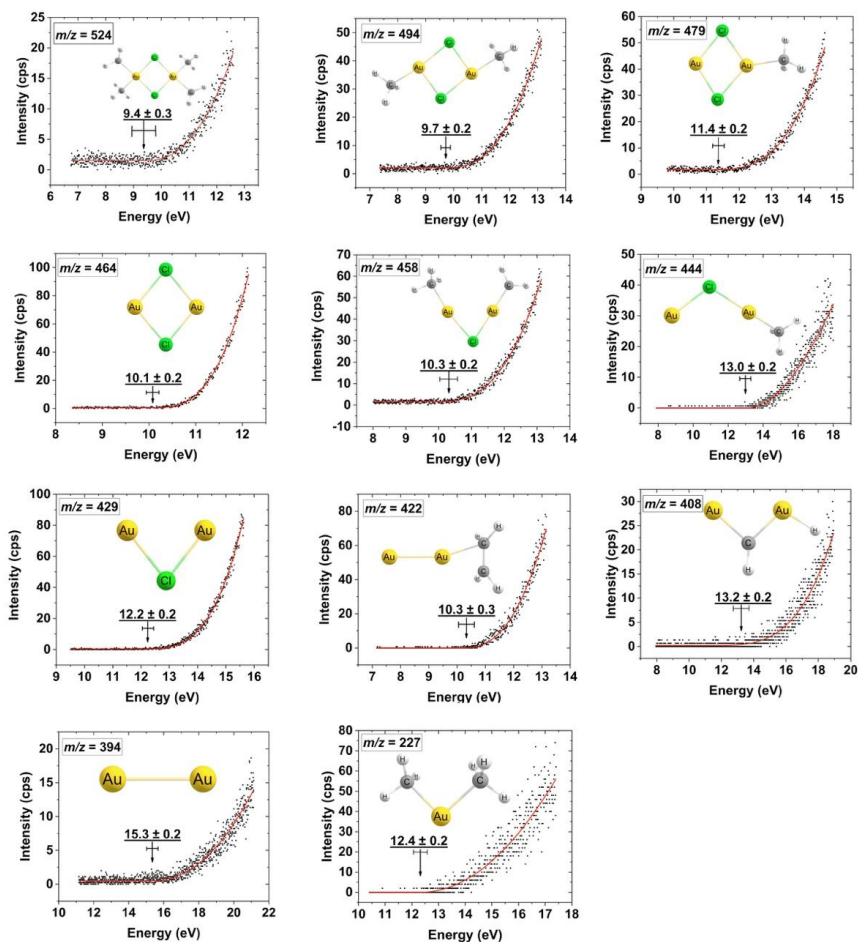
Figure 4.11. Wannier-type fits to the onset region inons formed in electron impact ionisation and dissociation of [(CH₃)₂AuCl]₂ and the respective appearance energies and confidence limits from the average of fits to three curves recorded on different days. The respective structure, optimized at the PBE0-TZVP level of theory, are also shown.

These values are, however, dropped to 11.18 and 11.27 eV if the production of ethane from two of the methyl radicals is considered. This is in both cases in good agreement with the experimental value. For the loss of all four methyl ligands, *m/z* 464, we determine an AE of 10.1 ± 0.2 eV. The threshold values without new bond formations are in this case about 7 eV higher at both levels of theory. When considering the formation of two ethane, these threshold values are lowered to 9.65 and 10.12 eV at the PBE0-TZVP and DLPNO-CCSD(T)-TZVP levels of theory, respectively. Here the DFT value is about 0.25 eV below the confidence limit, but the DLPNO-CCSD(T)-TZVP value is in excellent agreement with the experimental AE. In addition, we considered the formation of ethene (CH_2CH_2), ethane (CH_3CH_3) and molecular hydrogen as the

neutral counterparts to *m/z* 464 but found the threshold for this reaction more than 1 eV higher than the respective AEs.

For the next progression, *m/z* 458, 444, and 429, the AEs are 10.3 ± 0.2, 13.0 ± 0.2, and 12.2 ± 0.2 eV, respectively. Taking into account only single bond ruptures and no new bond formations leads also here to threshold values that are significantly higher than the respective AEs. These *m/z* ratios represent the loss of one chlorine, two methyl groups and a hydrogen (*m/z* 458) and the loss of one chlorine and three and four methyl groups (*m/z* 444 and 429, respectively). Several fragmentation pathways that may lead to the formation of these fragments were investigated, and for *m/z* 458 (AE = 10.3 ± 0.2 eV), the formation of ethane and HCl gives the best agreement with threshold values of 10.46 and 10.41 eV at the PBE0-TZVP and DLPNO-CCSD(T)-TZVP levels of theory, respectively. For *m/z* 444, the loss of chlorine and three methyl groups (AE = 13.0 ± 0.2 eV), the agreement with the calculations is best when assuming the formation of ethane, a methyl radical and atomic chlorine. The threshold values for this reaction at the PBE0-TZVP and DLPNO-CCSD(T)-TZVP levels of theory are 13.58 and 13.52 eV, respectively. These are still 0.3-0.4 eV above the confidence limits of the experimental AE, but considering the formation of chloromethane and two methyl radicals, only rises these values to 13.72 and 13.76 eV, respectively. Considering the formation of chloromethane and ethane, on the other hand, lowers these values to 9.88 and 9.99 eV, i.e., about 3 eV below the experimental AE. Lastly, for the production of $[Au_2Cl]^+$, *m/z* 429 (AE of 12.2 ± 0.2 eV), we find the closest agreement with the observed AE when considering substantial rearrangements to form the neutral counterparts HCl, $2CH_4$, and C_2H_3. This reaction has threshold values of 12.54 and 12.33 eV at the PBE0-TZVP and DLPNO-CCSD(T)-TZVP levels of theory, respectively. Considering the more direct route of the formation of ethane, chloromethane, and the methyl radical, leads to threshold energies of 11.57 and 11.54 eV, at the respective levels of theory. These values are about 0.6 eV below the observed AE. Considering the significant rearrangement, associated with the transfer of three hydrogens is needed for the former path, we consider the direct formation of ethane (along with CH_3 and CH_3Cl) to be the more likely path. These threshold values drop to 11.44 and 11.30 eV, respectively, (about 1 eV below the observed AE) when two ethane molecules and the chlorine radical are considered neutral counterparts. The next progression, constitutes the loss of two chlorine ligands, and two, three, and four methyl ligands (partially associated with additional hydrogen loss) and leads to the formation of the positive ion fragments $[Au_2(C_2H_4)]^+$, $[Au_2(CH_2)]^+$, and $[Au_2]^+$, with *m/z* values of 422, 408, and 394, respectively. For $[Au_2(C_2H_4)]^+$, threshold values of 10.53 and 10.46 eV are calculated at the respective levels of theory when assuming the formation of two chloromethanes and one hydrogen molecule as the neutral fragments. These values match the experimentally determined AE of 10.3 ± 0.3 eV very well, while the calculated threshold for the production of ethane and two HCl as neutral counterparts is found to be 9.51 and 9.44 eV at the respective levels of theory, i.e., 0.79 and 0.86 eV below the observed AE. The production of $[Au_2(CH_2)]^+$ (*m/z* 408) involves the loss of three methyl groups and one hydrogen. This fragment has an AE of 13.2 ± 0.2 eV and we find the DFT and coupled cluster threshold value for the formation of ethene (C_2H_2), 2HCl, and methane as the neutral counterparts to be 13.35 and 13.06 eV respectively, i.e., within the confidence limits in both cases. Considering the more direct formation of ethane (CH_3CH_3), HCl, and chloromethane lowers these values to 12.60 and 12.54 eV, respectively, which is about 0.5 eV below the lower confidence limit of the AE. Lastly, we determine an AE of 15.3 ± 0.2 eV for the formation of $[Au_2]^+$, *m/z* 394. Similar to $[Au_2(CH_2)]^+$, considering the formation of ethene (CH_2CH_2), two HCl, and two methyl radicals yield threshold values of 15.56 and 15.39 eV at the respective theoretical levels, which is in good agreement with the AE at the coupled cluster level and only 0.06 eV above the higher confidence limit at the DFT level.

Table 4-3. Appearance energies (AEs) of the parent ion and the most dominant fragments due to the DI to [(CH₃)₂AuCl]₂ and the respective threshold values calculated at the PBE0/def2-TZVP and DLPNO-CCSD(T)/TZVP levels of theory.

Table 4-3. Appearance energies (AEs) of the parent ion and the most dominant fragments due to the DI to $[(CH_3)_2AuCl]_2$ and the respective threshold values calculated at the PBE0/def2-TZVP and DLPNO-CCSD(T)/TZVP levels of theory.

m/z	Products	AE (eV)	PBE0-TZVP (eV)	DLPNO-CCSD(T)-TZVP (eV)
524	$[Au_2Cl_2(CH_3)_4]^+$	9.4 ± 0.3	<u>9.23</u>	9.92
494	$[Au_2Cl_2(CH_3)_2]^+ + 2(CH_3)$		13.51	14.06
	$[Au_2Cl_2(CH_3)_2]^+ + CH_3CH_3$	**9.7 ± 0.2**	<u>**9.67**</u>	**10.29**
	$[Au_2Cl_2(CH_3)_2]^+ + CH_2CH_2 + H_2$		11.28	11.65
479	$[Au_2Cl_2(CH_3)]^+ + 3(CH_3)$		15.01	15.04
	$[Au_2Cl_2(CH_3)]^+ + (CH_3) + CH_3CH_3$	**11.4 ± 0.2**	<u>**11.18**</u>	**11.27**
	$[Au_2Cl_2(CH_3)]^+ + CH_2CH_2 + H_2 + (CH_3)$		12.78	12.64
464	$[Au_2Cl_2]^+ + 4(CH_3)$		17.32	17.65
	$[Au_2Cl_2]^+ + 2(CH_3CH_3)$	**10.1 ± 0.2**	<u>**9.65**</u>	**10.12**
	$[Au_2Cl_2]^+ + CH_3CH_3 + 2(CH_3)$		13.48	13.89
	$[Au_2Cl_2]^+ + CH_2CH_2 + H_2 + CH_3CH_3$		11.25	11.49
458	$[Au_2Cl(CH_2CH_3)]^+ + 2CH_3 + Cl + H$		18.72	18.50
	$[Au_2Cl(CH_2CH_3)]^+ + CH_3CH_3 + HCl$	**10.3 ± 0.2**	<u>**10.46**</u>	**10.41**
	$[Au_2Cl(CH_2CH_3)]^+ + (CH_4) + CH_3Cl$		**10.64**	**10.60**
	$[Au_2Cl(CH_2CH_3)]^+ + CH_3CH_3 + Cl + H$		14.88	14.73
444	$[Au_2Cl(CH_3)]^+ + Cl + 3(CH_3)$		17.42	17.29
	$[Au_2Cl(CH_3)]^+ + Cl + CH_3CH_3 + (CH_3)$	**13.0 ± 0.2**	**13.58**	**13.52**
	$[Au_2Cl(CH_3)]^+ + Cl(CH_3) + 2(CH_3)$		**13.72**	**13.76**
	$[Au_2Cl(CH_3)]^+ + Cl(CH_3) + CH_3CH_3$		9.88	9.99
429	$[Au_2Cl]^+ + 4(CH_3) + Cl$		19.11	18.84
	$[Au_2Cl]^+ + HCl + 2(CH_4) + CHCH_2$	**12.2 ± 0.2**	<u>**12.54**</u>	**12.33**
	$[Au_2Cl]^+ + (CH_3) + CH_3Cl + CH_3CH_3$		**11.57**	**11.54**
	$[Au_2Cl]^+ + 2 (CH_3CH_3) + Cl$		11.44	11.30
422	$[Au_2(CH_2CH_2)]^+ + 2(CH_3) + 2Cl + 2H$		22.20	21.84
	$[Au_2(CH_2CH_2)]^+ + 2Cl(CH_3) + H_2$	**10.3 ± 0.3**	<u>**10.53**</u>	10.46
	$[Au_2(CH_2CH_2)]^+ + CH_3CH_3 + 2HCl$		9.51	9.44
408	$[Au(CH)AuH]^+ + 3(CH_3) + 2Cl + H$		24.57	24.14
	$[Au(CH)AuH]^+ + CH_2CH_2 + 2HCl + CH_4$	**13.2 ± 0.2**	**13.35**	**13.06**
	$[Au(CH)AuH]^+ + CH_3CH_3 + HCl + Cl(CH_3)$		12.60	12.54
394	$[Au_2]^+ + 4(CH_3) + 2Cl$		22.39	22.09
	$[Au_2]^+ + 2(CH_3) + 2(CH_3Cl)$	**15.3 ± 0.2**	<u>**14.99**</u>	**15.05**
	$[Au_2]^+ + CH_2CH_2 + 2(CH_3) + 2HCl$		<u>**15.56**</u>	**15.39**
	$[Au_2]^+ + 2(CH_3CH_3) + Cl_2$		11.99	12.14
	$[Au_2]^+ + CH_3CH_3 + 2(CH_3Cl)$		11.15	11.28
227	$[(CH_3)Au(CH_3)]^+ + 2(CH_3) + 2Cl + Au$		17.81	18.72
	$[(CH_3)Au(CH_3)]^+ + CH_3CH_3 + Cl_2 + Au$	**12.4 ± 0.2**	**11.24**	**12.54**
	$[(CH_3)Au(CH_3)]^+ + AuCl + CH_3CH_3 + Cl$		**12.46**	**12.20**
	$[(CH_3)Au(CH_3)]^+ + 2Cl(CH_3) + Au$		10.41	11.68
	$[(CH_3)Au(CH_3)]^+ + CH_2CH_2 + 2HCl + Au$		10.98	12.01

Considering the formation of chloromethane and two methyl groups for *m/z* 394, however, gives threshold values of 14.99 and 15.05 eV at the PBE0-TZVP and DLPNO-CCSD(T)-TZVP levels of theory, respectively. This is in both cases only slightly below the lower confidence of the AE. Other alternative reactions were also considered for the formation of this fragment but were found to have thresholds significantly outside the confidence limits of its AE (see table 4-3). The last methyl loss progression constitutes the loss of one of the gold atoms, both chlorine and two, three and four methyl ligands, appearing in the mass spectrum at *m/z* 227/225, 212 and 197, respectively. From these, *m/z* 225 is attributed to additional loss of two hydrogens as compared to *m/z* 227, and *m/z* 197 is attributed to Au^+. The intensities of these ion signals are comparatively low and the number of combinations of neutral fragments is large. We have nonetheless determined the threshold values for m/z 227 and 225 (Table S7- Paper II). For *m/z* 227 we find the AE to be 12.4 ± 0.2 eV which agrees well with the threshold values of 12.24 and 12.54 eV calculated at the respective levels of theory for the formation of ethane, Cl_2 and atomic gold as the neutral counterpart. The agreement is, however, comparable when considering the formation of ethane, AuCl and atomic chlorine, which leads to threshold values of 12.46 and 12.20 eV, respectively.

In addition to the reaction paths discussed here above and listed in Table 4-3, several other alternatives were considered for all *m/z* ratios. A complete list of these can be found in Table S7- Paper II of the supporting material.

It is clear from the considerations here above that DI of $[(CH_3)_2AuCl]_2$ is dominated by rearrangement reactions with multiple bond ruptures and new bond formations. For the loss of the methyl groups, without chlorine loss, the assignment of the neutral counterparts is fairly straight forward and is dominated by ethane formation from the respective methyl groups. For the additional loss of one or two chlorine, which is also in part associated with hydrogen loss, the assignment of the neutral counterparts is more complex. It is, however clear, that the formation of ethane and hydrochloric acid and/or chloromethane plays an important role in these fragmentation processes.

In FEBID the effective damage yield[44,138] for a specific precursor will be a convolution of the energy distribution of the electrons involved, i.e., of the primary, secondary and inelastic scattered electrons, and the energy dependence of the cross sections for the respective electron induced processes. Thus, for more quantitative comparison of the current gas phase and UHV FEBID experiments and the earlier HV experiments on this precursor, the energy dependence of the relative cross sections is important. Figure 4.12 shows these for the most significant DI processes, covering the energy range from below their thresholds to 50 eV. The intensities are normalized to the signal intensity and the pressure of Ar^+ from Ar at 50 eV electron energy.
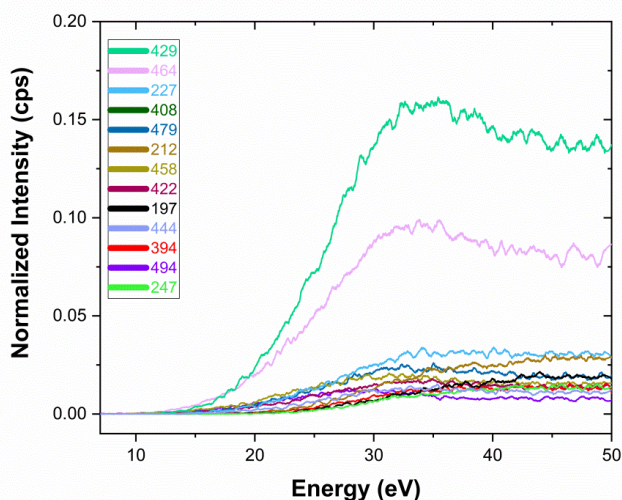
Figure 4.12. Dissociative ionization ion yields for the most dominant fragments from Figure 4.10 over an incident electron energy that extends from below their threshold up to 50 eV. The ion yields are normalized to the signal intensity and pressure of Ar⁺ from Ar at 50 eV.

The relative peak intensities recorded in the mass spectrum, as well as the integral intensities across the energy range shown in Figure 4.12, are listed in Table 4-4. The relative intensities are normalized with respect to that of *m/z* [Au$_2$Cl]⁺ which is set as 100. From these the average chlorine and carbon losses are calculated by adding up the contributions from each fragment weighted by their respective chlorine and carbon losses and dividing by the total intensity of all DI fragments. The average carbon and chlorine loss calculated is given at the bottom of Table 4-4 along with the elemental compositions of the deposits formed in the current UHV experiments and the earlier HV FEBID experiments. As can be seen, the average chlorine loss per DI incident is 0.96 and the average carbon loss is 3.42 per incident when calculated from the integrated intensities of the ion yield curves. The difference between these values and those calculated from the peak intensities in the mass spectra is insignificant and is attributed to the shapes of the ion yield curves and the lower contributions of the higher threshold fragments to the integral intensities. Notwithstanding, if the DI fragmentation as it is observed in the gas phase was the only active mechanism in FEBID, and all fragments that do not contain gold would desorb, a deposit with an elemental composition of 55 at.% Au, 29 at.% Cl, and 16 at.% C would be expected. While the high gold concentration is consistent with that observed for both the UHV and HV deposits, the carbon content is much lower than that reported in FEBID, and in both the UHV and HV depositions. Furthermore, chlorine is nearly completely removed in the deposition experiments, whereas in DI, on average, only half of the chlorine is dissociated. It is evident that the deposit's composition reported in FEBID cannot be explained by the unmodified DI processes, as they are observed in the gas phase under single collision conditions. Thus, other elemental processes must be at play or the deposit's composition must be strongly influenced by surface induced reactions or potentially by electron induced secondary reactions involving further decomposition of fragments formed in the initial process.

Table 4-4. Relative intensities of DI fragments from $Au_2(CH_3)_2Cl_2$ calculated from the peak intensities at 50 eV as they appear in the mass spectrum (Figure 4.12) and from the areas under the respective ion yield curves shown in Figure 4.10. The intensities are normalized with respect to the highest intensity fragment m/z $[Au_2Cl]^+$, that is set as 100. The hypothetical deposit that would be formed if its formation would be governed by DI as observed in the gas phase and the composition of the FEBID deposits from the current UHV and the previous HV experiments are shown at the bottom of the table.

Fragment	m/z	Relative DI Yield (Integration)	Relative DI Yield (intensity)	
494	$[Au_2Cl_2(CH_3)_2]^+$	7.20	9.2	
479	$[Au_2Cl_2(CH_3)]^+$	15.13	19.02	
464	$[Au_2Cl_2]^+$	62.36	67.08	
458	$[Au_2Cl(C_2H_5)]^+$	12.46	20.45	
444	$[Au_2Cl(CH_3)]^+$	8.24	9.41	
429	$[Au_2Cl]^+$	100	100	
422	$[Au_2(C_2H_4)]^+$	10.78	11.45	
408	$[Au_2(CH_2)]^+$	15.69	17.18	
394	$[Au_2]^+$	7.62	11.04	
247	$[(CH_3)AuCl]^+$	6.58	7.57	
227	$[(CH_3)_2Au]^+$	19.97	17.8	
212	$[(CH_3)Au]^+$	13.65	9.82	
197	$[Au]^+$	8.49	6.95	
Chlorine loss		0.96	0.92	
Carbon loss		3.42	3.39	
Expect. comp. from DI	55 at. % Au	29 at. % Cl	16 at. % C	
UHV-FEBID composition	45-61 at. % Au	1-2 at. % Cl	38-49 at. % C	5-8 at. % Sn
HV-FEBID composition	29-41 at. % Au	2-6 at. % Cl	53-68 at. % C	

Dissociative electron attachment

Figure 4.13(a) shows a negative ion mass spectrum of $[(CH_3)_2AuCl]_2$ recorded in the *m/z* range of 10-550. As DEA is generally active below about 10 eV and as it a resonant process, it proceeds within well-defined energy ranges. Thus, to cover the relevant energy range, the mass spectrum

depicted in Figure 4.13(a) is the sum of multiple mass spectra acquired in the electron energy range from around 0 to 10 eV at 1 eV intervals. In Figures 4.13(b) and (c), energy dependence of the ion formation, i.e. the ion yield curves for the two most abundant fragments are shown.
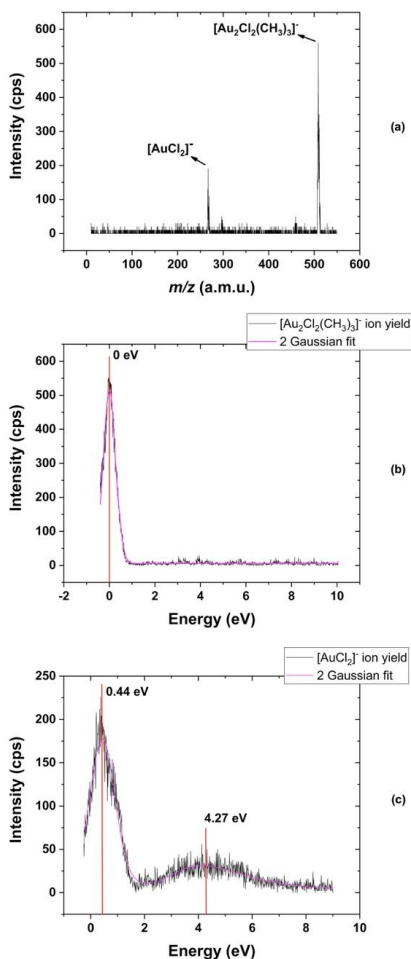
Figure 4.13. a) Cumulative negative ion mass spectrum composed of the sum of individual mass spectra recorded at 1 eV intervals in the energy range from 0 to 8 eV covering the m/z range from about 10 to 550. b) and c) Negative ion yield curves of the most significant fragments observed in DEA to [(CH$_3$)$_2$AuCl]$_2$ in the energy range from about 0 to 10 eV. b) [Au$_2$Cl$_2$(CH$_3$)$_3$]$^-$, m/z 509 and c) AuCl$_2^-$, m/z 267.

Figure 4.13 demonstrates that fragmentation caused by DEA to [(CH$_3$)$_2$AuCl]$_2$ is less extensive than that caused by DI. There are only two major pathways seen in the spectra: the loss of a single methyl group producing [Au$_2$Cl$_2$(CH$_3$)$_3$]$^-$, m/z 509, and the production of [AuCl$_2$]$^-$, m/z 267. The highest attachment cross sections occur near the 0 eV threshold in DEA, as the cross section for the attachment process is inversely proportional to the square root of the electron energy[39]. Hence, DEA reactions that are exothermic and occur at close to 0 eV electron energy are generally

the most effective. This is also the case here, with the production of $[Au_2Cl_2(CH_3)_3]^-$, the loss of a single methyl group, being exothermic by 0.96 and 0.88 eV at the PBE0-TZVP and DLPNO-CCSD(T)-TZVP levels of theory, respectively. Similarly, assuming the production of two neutral ethane molecules and elemental gold, we find that the formation of $[AuCl_2]^-$ is exothermic by about 2 eV at both levels of theory. We also determined the threshold for this product under neutral $AuCH_3$, ethane, and methane formation, as well as when $Au(CH_3)_2$ and one ethane molecule are formed. At both levels of theory, we also find these pathways to be exothermic (Table S7-Paper II of the supplementary material shows all computed thresholds for the generation of negative ions). We anticipate that the contributions of $[Au_2Cl_2(CH_3)_3]^-$ and $[AuCl_2]^-$ close to 0 eV in their ion yield curves result from overlapping resonances associated with single electron occupation of the lowest lying molecular orbitals, and that while the presumably faster loss of a single methyl group dominates at threshold, $[AuCl_2]^-$ is only produced via the high energy flank. In addition, $[AuCl_2]^-$ is produced through a higher lying resonance(s) appearing through a contribution in the ion yield curve that is centered around 4.3 eV. By using the same approach as for the DI products, we can predict the elemental composition of a deposit that would develop if only the unmodified DEA channels observed in the gas phase under single collision conditions would be active in FEBID. In this way, the combined intensities from the ion yield curves in Figure 4.13 lead to a predicted composition of around 32 at.% gold, 32 at.% chlorine, and 36 at.% carbon, assuming that only the gold containing fragments remain on the surface. Hence, whereas both HV and UHV FEBID studies show significant chlorine loss, no such loss is seen in DEA.

4.2.3 Conclusion

The compositions of $[(CH_3)_2AuCl]_2$ FEBID deposits generated under UHV and HV conditions are qualitatively the same, i.e., high gold content, near quantitative elimination of the chlorine, and primarily carbon residues. Nevertheless, the UHV experiments show the expected reduction in residual carbon and, albeit not as pronounced, a more thorough elimination of chlorine. While the overall image shown by deposits made under UHV and HV is similar, it is evident that UHV deposits can lead to substantially higher gold content, and that the deposit's composition is sensitive to both the deposition current and the cleanliness of the substrate. In the current gas phase experiments, we have not taken into account neutral dissociation up on electron excitation; however, it is evident that the electron induced fragmentation of $[(CH_3)_2AuCl]_2$ is significantly influenced in the FEBID experiments compared to single collision conditions in the gas phase. Contrary to what one might assume based only on energy dissipation concerns, the FEBID experiment actually shows more fragmentation than is observed in the gas phase. Instead of direct dissociation without new bond formation, rearrangement reactions are the major fragmentation pathway in DI. Condensed phase or substrate surface modifications are likely to influence the potential energy surfaces along which such rearrangement processes proceed. Electron-induced secondary reactions may also play a role, given the present electron dosage of roughly 5×10^{19} e^-/cm^2 and the volume of the resultant deposits. Considering a molecular diameter of 1 nm and a deposit height of 20 nm, there are approximately 3×10^8 molecules in a 4×4 μm^2 deposit. From the dose, it is estimated that this volume has been exposed to 8×10^{12} electrons. There are 1.5×10^7 molecules in a monolayer, and it has been hit by 4×10^{11} electrons. In terms of electrons, this equates to around 35,000 per molecule. The reactive area of this monolayer is 0.15 μm^2, assuming a general cross section of 10^{-16} cm^2, which is on the order of the DI cross section of the FEBID precursor $Co(CO)_3(NO)$[138], that of the DEA cross section for the same precursor[52,138] and the DEA cross sections for $Pt(PF_3)_4$[139]. If the cross section remains constant, this corresponds

statistically to around 300 reactive occurrences per molecule. While the gas phase experiments only include a single collision. Hence, secondary reactions of immobilized fragments, formed in the primary processes, may play a significant role in FEBID.

Significant number of studies on potential organometallic FEBID precursors containing the higher halogens, chlorine, bromine, and iodine have been conducted. These are mainly carbonyls include $Ru(CO)_4I_2$[47], $(\eta^3\text{-}C_3H_5)Ru(CO)_3X$ (X = Cl, Br)[123,140,141], $Pt(NH_3)_2Cl_2$[122,142], and $Pt(CO)_2X_2$ (X = Cl, Br). Specifically the platinum precursors $Pt(CO)_2X_2$ (X = Cl, Br) have been studied with respect to their low energy electron interaction in the gas phase[97,143], in thin layers under non-steady state conditions[144], in comparative FEBID experiments under HV and UHV conditions,[121,145] and in post-deposition purification studies[146,147]. For these compounds, rapid CO loss was observed in a thin film surface exposure to 500 eV electron up to electron doses of about 10^{16} e^-/cm^2. This led to deposition of a Pt and Cl ratio of around 1:2. A sustained exposure up to levels of about 10^{19} e^-/cm^2, which is on the order of magnitude employed here, resulted in the halogen being nearly completely removed. The first stage showed good agreement with gas-phase observations under single-collision conditions, and the second step showed that pure deposits could be achieved by extended electron exposure of the deposit, i.e., electron induced secondary reactions. Differently, a post deposition purification study on thicker $Pt(CO)_2Cl_2$ deposits using extended electron exposure did not result in effective chlorine removal. In this study, however, atomic hydrogen was shown[148] to be an efficient halogen remover. This might be linked to reduced escape probability of the halogen from the thicker deposit or potentially to the penetration depth of the primary electrons and the secondary electron energy distribution within the deposit as compared to that at the surface.

Intriguingly, a recent study comparing deposition with $Pt(CO)_2Cl_2$ in a scanning electron microscope (SEM) under high vacuum (HV) and in an Auger spectrometer under ultrahigh vacuum (UHV) revealed striking differences in the deposit's composition[121]. While the UHV deposits contained primarily halogen contamination and comparatively low carbon content, the HV deposits contained carbon as the main component, with the halogen content as low as 7.5-8 at.%. It was hypothesized that this was because the halogen was being removed by reductive means in interactions with the more abundant background water in the HV chamber.

In the current study, there are no indications that the higher background water under HV conditions affects the composition of the deposits, despite the fact that HCl production appears to be considerable in DI of $[(CH_3)_2AuCl]_2$ and may be responsible for the etching effects seen. Nevertheless, since the deposit growth rate is very slow, and therefore each monolayer is exposed to a large number of electrons, electron-induced secondary processes are likely to play a role. Non-steady-state experiments, like those described for $Pt(CO)_2X_2$ (X = Cl, Br) and a number of other potential FEBID precursors[144], could be used to investigate this.

4.3 $CF_3AuCNC(CH_3)_3$ FEBID Precursor

In this study gas-phase dissociative ionization and dissociative electron attachment, supported by quantum chemical calculations, are conducted to better understand the fundamental electron-induced dissociation pathways of the potential FEBID precursor, $CF_3AuCNC(CH_3)_3$.

This precursor is chosen for the current study as it was purposely synthesized as a candidate for gold deposition in FEBID and its ligand structure was designed to provide sufficient vapor pressure

and stability at ambient conditions while fragmenting efficiently under electron exposure[35,36]. In this context this compound has recently been tested in electron beam induced deposition in an UHV Auger spectrometer with 3 keV electron energy, resulting in 14 at.% gold content of the deposits. The direct injection probe electron impact (DIP-EI) and negative chemical ionization (DIP-NCI) mass spectrometry were also performed. Specifically, DIP-NCI is conducted under multiple collision conditions making comparison with the current single collision conditions interesting in connection with relaxation mechanisms provided when precursor molecules are physisorbed on the substrate's surface in the deposition experiment.

The current research was conducted in collaboration with the research group of Prof. Lisa McElwee-White at the University of Florida, which synthesized and delivered the compound and contributed the DIP-EI- and DIP-NCIMS. The quantum chemical computations and the crossed beam DI and DEA studies were performed at the University of Iceland and constitute an integral part of the current thesis.

The results of this study have been submitted for publication in a peer reviewed Journal:
Dissociative electron attachment and dissociative ionization of CF₃AuCNC(CH)₃ a potential FEBID precursors for gold deposition, by Ali Kamali, Will G. Carden, Jodie V. Johnson, Lisa McElwee-White, O. Ingólfsson[*]
Submitted

4.3.1 Methods

The precursor was synthesized in the group of Prof. Lisa McElwee-White at the University of Florida as is described in detail in reference[35]. It consists of white granulates that are stable at room temperature (298 K at atmosphere).

The DEA and DI experiments were carried out with the crossed beam apparatus at the University of Iceland. To achieve sufficient vapor pressure the gas injection system was heated to 353 K during experiments to maintain a steady working pressure of 2-4 × 10^{-7} mbar during the experiments. For comparison, mass spectra were also recorded at room temperature and at 333 K. Positive ion mass spectra were recorded at 70 eV impact energy and negative ion mass spectra were recorded in the energy range from about 0 eV to 10 eV with 1 eV intervals. As in previous experiments the zero point of the energy scale was calibrated with the SF_6^- signal from SF_6 at 0 eV for the negative ion experiments and with the first ionization energy of Ar for the positive ion experiment[95]. The electron energy distribution had a full width at half maximum (FWHM) of 190 meV during all experiments. As previously, the determination of appearance energies for positively charged fragments involved fitting a Wannier-type threshold function[96] to the onset region of the corresponding ion yield curves.

The computational chemistry software ORCA[118], version 4.1, was used for all quantum chemical calculations using the hybrid DFT functional PBE0 and the triple-zeta polarization basis set def2-TZVP including the D3BJ dispersion correction by Grimme *et al.*[149] for all geometry optimizations. The optimizations were performed with tight SCF settings and for closed-shell and open-shell systems, the unrestricted Kohn-Sham (UKS) and restricted Kohn-Sham (RKS) formalisms were used, respectively. Harmonic vibrational frequencies were confirmed to be positive for all structures and used to calculate zero-point energies and thermal corrections at 353 K. The PBE0 functional was chosen with reference to Kepp *et al.*[105] and Kang *et al.*[126], which found it to perform better than other functionals they tested on binding energies and structure calculations

of gold complexes. Single point energies were also calculated for the PBE0-TZVP geometries at the coupled cluster DLPNO-CCSD(T) level of theory using the triple-zeta basis set def2-TZVP and the valence triple-zeta auxiliary basis set TZVP/c. The normal PNO setting were used to carry out the calculations. Threshold energies were determined by subtracting the energy of the generated fragments from the energy of the parent molecule with the Zero-point energies and thermal corrections at 353 K included.

4.3.2 Results and Discussion

Positive mass spectra of $CF_3AuCNC(CH_3)_3$, recorded at 70 eV impact energy in the crossed beam experiment under single collision conditions, are shown in Figures 4.14 and 4.15. For clarity and ease of discussion, the low mass range m/z 10-200 and high mass range m/z 200-360 are shown in Figure 4.14 and Figure 4.15, respectively. In both cases these spectra are recorded with the capillary inlet system at 353 K (top panel (a)), 333 K (mid panel (b)), and room temperature (bottom panel (c)). Figure 4.16 displays a direct injection probe (DIP) electron impact mass spectrum of $CF_3AuCNC(CH_3)_3$ for the same m/z ranges (a) m/z 10-200 and (b) m/z 200-360. $CF_3AuCNC(CH_3)_3$ shows a rich fragmentation in dissociative ionization under single collision conditions, whereby the main pathways lead to the observation of m/z 39, 41, 57, 69, which are attributed to the formation of $[H_2CCCH]^+$, $[H_2CCHCH_3]^+$, $[C(CH_3)_3]^+$ and $[CF_3]^+$, respectively, as is discussed here below. In the high m/z range shown in Figure 4.15, the main fragmentation channels lead to the formation of m/z 197, 224, 274, 280, and 349 which are assigned to $[Au]^+$, $[AuCNH]^+$, $[CF_2AuCNH]^+$, $[AuCNC(CH_3)_3]^+$, and $[CF_3AuCNC(CH_3)_3]^+$, respectively. Noticeably, these high mass fragments appear in the crossed beam experiment with significantly lower intensity than the low mass fragments, while this is not the case in the DIP EI mass spectrum (Figure 4.16).
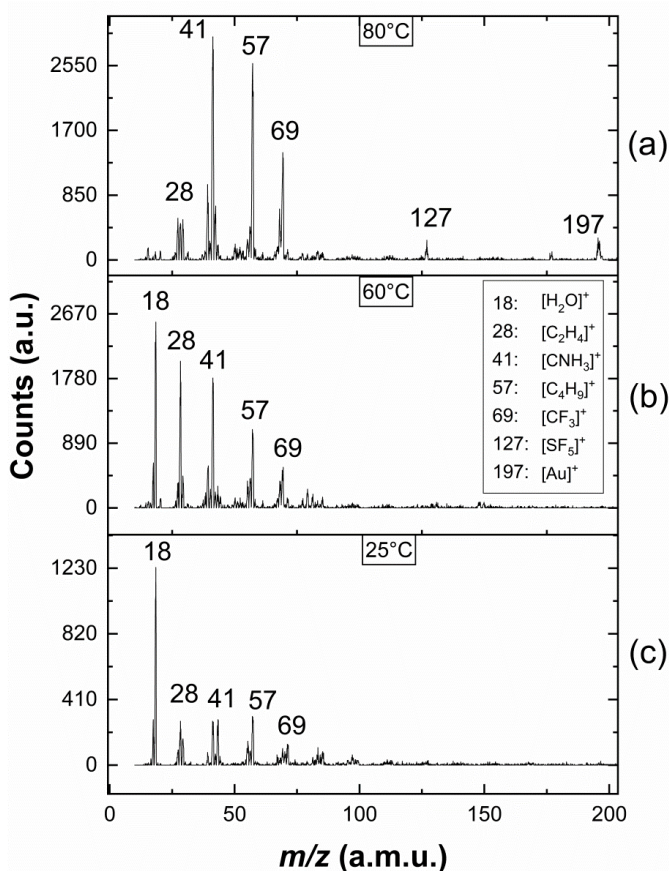
Figure 4.14. Positiveion mass spectrum of $CF_3AuCNC(CH_3)_3$ recorded at 70 eV in the m/z range from about 10-200 with the gas inlet system at (a) 353 K, (b) 333 k, and (c) room temperature. The results show that increasing the temperature resulted in the decrease in intensities of impurities and increase in intensities of DI fragments.

It is clear from Figure 4.14 that the mass spectra recorded at room temperature is dominated by contribution from water and hydrocarbon fragments from the background gas and inlet system that most likely originate from pump oil contaminations. Increasing the temperature to 333 K, the relative intensities of the contributions from impurities decreased, while the relative intensities of fragments we attribute to DI of $CF_3AuCNC(CH_3)_3$ increases and at 353 K these dominate the spectrum. This is consisted with the evolvement of the ion intensities in the high mass range, where significant contributions from DI of $CF_3AuCNC(CH_3)_3$ are only present at 353 K. Comparison between the current crossed beam mass spectra and the DIP EI MS most noticeably shows a significantly higher relative intensities in the low mass range in the former, as well as differences in the relative intensities.
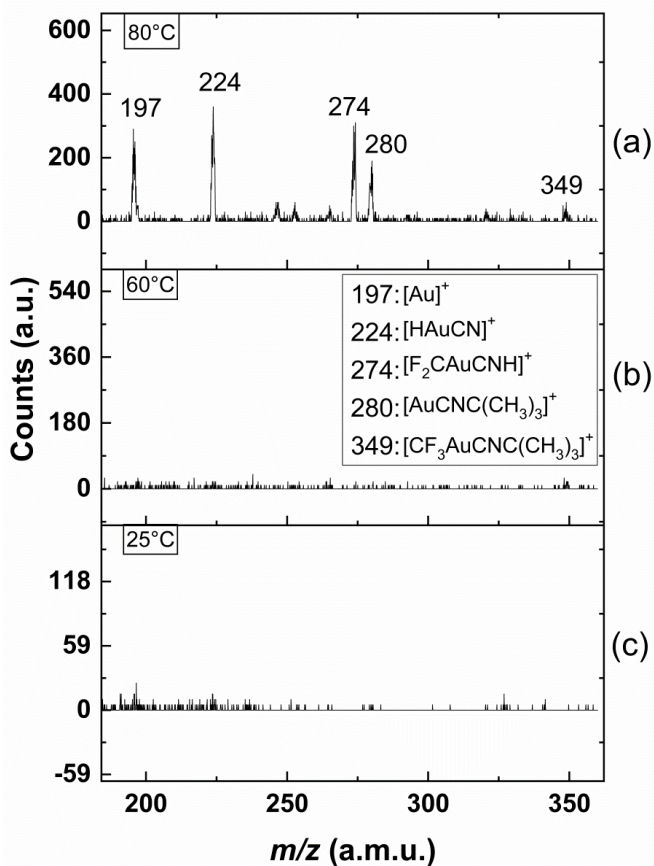
Figure 4.15. Positive mass spectrum of high m/z fragmentations due to DI to CF₃AuCNC(CH₃)₃ *precursor at 70 eV recorded at (a) 353 K, (b) 333 k, and (c) 298 k. The results show that increasing* *the temperature resulted in the decrease in intensities of impurities and increase in intensities of* *DI fragments.*

It is clear that at 333K the signal intensities are mainly because of contamination from the background gas in the crossed beam chamber as well as such evaporated from the inlet system during heating. However, the most abundant ions in the low m/z range at 353 K, i.e., m/z 39, 41, 57, and 69, are certainly derived from the precursor. Potentially, the significantly higher contributions in the low mass range in the crossed beam experiment compared to the DIP EI MS might be from partial decomposition of the compound at the elevated temperatures. We, however, consider that unlikely. Firstly, the decomposition temperature of this compound at ambient conditions has been determined to be 399 K[35], secondly, there are no indicators of decomposition in the negative ion mass spectrum (Figure 4.18). Furthermore, as is discussed here below the appearance energies for these low m/z ratios correlate well with the thermochemical thresholds for their formation through DI of CF₃AuCNC(CH₃)₃. Rather than thermal decomposition in the crossed beam experiment, we anticipate that the local pressure in the ionization zone of the DIP EI mass spectrometer is above the single collision condition regime, hence, that collisional stabilization influences the fragmentation channels in the DIP EI experiment in favor of less

extensive fragmentation. This is especially interesting as such conditions are closer to those in the deposition process in FEBID, where the surface can be expected to provide an effective heat sink.
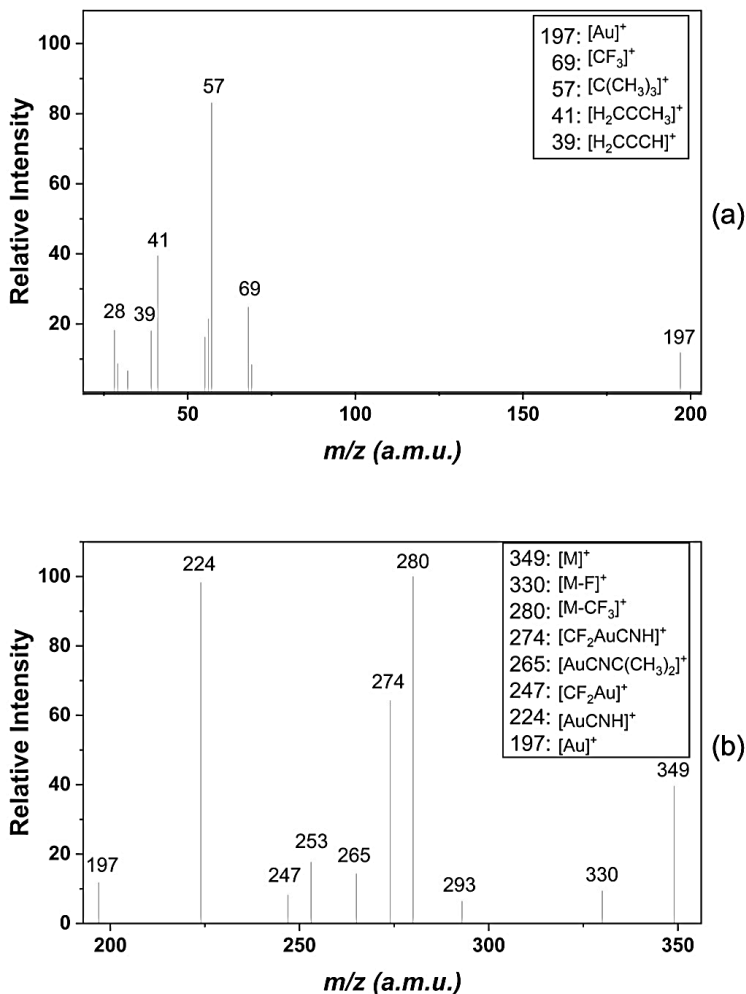
Figure 4.16. Direct injection probe (DIP) electron impact mass of CF₃AuCNC(CH₃)₃ for the m/z range from (a) 25 to 200, and (b)190 to 360.

Figure 4.17 shows the onset area of the ion yield curves for the *m/z* ratios 39, 41, 57 and 69. Also shown are the respective Wannier-type fits as well as the AEs and the respective standard deviations derived from 3 different measurements in each case. The structure of the respective ions, optimized at the PBE0-def2-TZVP level of theory, is shown in each panel.
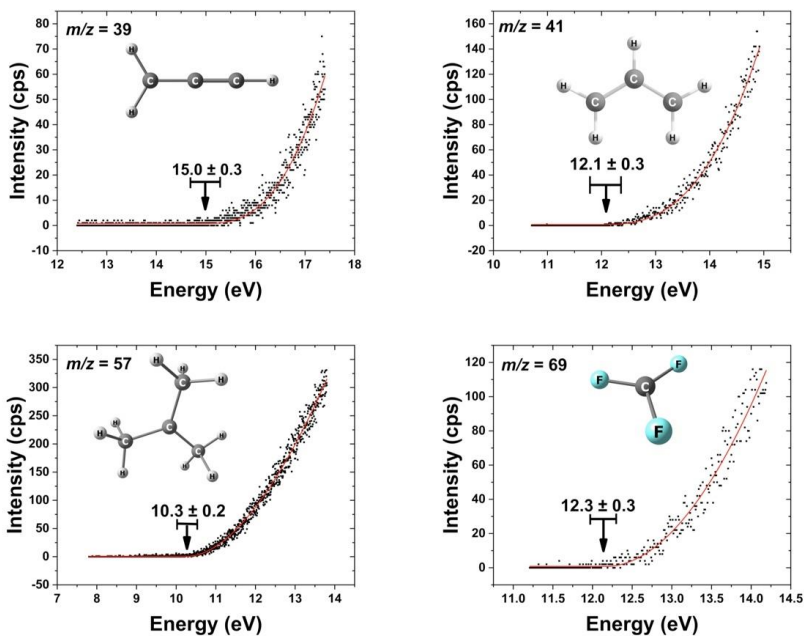
Figure 4.17. Positive ion yield curves as well as Wannier-type threshold fits and appearance energies for the most dominant cations observed in Figure 4.14(a) The respective cationic structures optimized at the XY level of theory are shownn in each panel..

Table 4-5 compares the appearance energies (AEs) to the corresponding threshold energy values adjusted for the thermal energy at 353 K, calculated at the PBE0-def2-TZVP and DLPNO-CCSD(T)/def2-TZVP levels of theory. Also shown is the DEA threshold for the formation of [CF$_3$AuCN]$^-$, that is discussed later in this chapter. Specifically, for *m/z* 39 and 41 the calculated values are shown for a number of possible reactions leading to these *m/z* ratios and the reaction paths that are best aligned to the AEs are highlighted in bold. In general, the DLPNO-CCSD(T)/def2-TZVP approach should provide more accurate energy values and where the results differ between the two approaches, we rather compare to values derived at the coupled cluster level of theory.

Table 4-5. Appearance energy values of the most significant ions in the DI and DEA mass spectra of CF₃AuCNC(CH₃)₃ as well as the calculated threshold energies at the PBE0-TZVP and DLPNO-CCSD(T)-TZVP levels of theory for potential reaction pathways leading to the formation of these fragment .

		CF₃AuCNC(CH₃)₃		
m/z	Products	AE (eV)	PBE0-def2-TZVP (eV)	DLPNO-CCSD(T)-def2-TZVP (eV)
	[CNCH]⁺ + CF₃Au + C₃H₈		15.65	15.48
39	**[H₂CCCH]⁺ + CF₃AuCN + CH₄ + H₂**	15.0 ± 0.3	**15.32**	**14.87**
	[HCCHCH]⁺ + CF₃AuCN + CH₄ + H₂		13.91	13.68
	[CNCH₃]⁺ + CF₃Au + C₃H₆		17.33	17.23
	[CNCH₃]⁺ + CF₃AuC₃H₆		14.67	14.47
41	[HCNCH₂]⁺ + CF₃Au + C₃H₆	12.1 ± 0.3	15.18	15.27
	[HCNCH₂]⁺ + CF₃AuC₃H₆		12.35	12.81
	[H₂CCCH₃]⁺ + CH₄ + CF₃AuCN		12.85	12.82
	[H₂CCHCH₂]⁺ + CH₄ + CF₃AuCN		**12.65**	**12.45**
57	**[C(CH₃)₃]⁺ + CF₃AuCN**	10.3 ± 0.2	**10.61**	**10.82**
	[HCCH₂(CH₃)₂]⁺ + CF₃AuCN		14.54	14.85
69	**[CF₃]⁺ + AuCNC(CH₃)₃**	12.3 ± 0.3	**12.62**	**12.67**
292	**[CF₃AuCN]⁻ + C(CH₃)₃**	0-0.2	**-1.12**	**-1.36**

For *m/z* 39, we find an AE of 15.0 ± 0.3 eV, which agrees with the threshold values of 15.32 and 14.87 eV calculated at the PBE0-def2-TZVP and DLPNO-CCSD(T)/def2-TZVP levels of theory, respectively, for the formation of the [H₂CCCH]⁺ cation and CF₃AuCN, CH₄ and H₂ as neutral fragments. Considering the formation of [HCCHCH]⁺ rather than [H₂CCCH]⁺ lowers these threshold values to 13.91 and 13.68 eV, respectively, which is in both cases more than 1 eV below the experimental AE. Considering the formation of [CNCH]⁺ and the neutrals CF₃Au and C₃H₈, on the other hand, results in threshold values of 15.65 and 15.48 eV at the PBE0-def2-TZVP and DLPNO-CCSD(T)/def2-TZVP levels of theory, respectively. These are in both cases about 0.5 eV above the experimental value. For *m/z* 41 we determine an AE of 12.1 ± 0.3 eV, which is in best agreement with the threshold values for the formation of [H₂CCHCH₂]⁺ and the neutral counterparts CH₄ and CF₃AuCN calculated at the coupled cluster level of theory. The threshold for this reaction is 12.65 eV when calculated with PBE0-def2-TZVP, which is 0.2 eV above the higher confidence limit of the AE, but at the coupled cluster level of theory the threshold is 12.45 eV, which is only 0.05 eV above the upper limit for the experimental AE. Considering the [H₂CCCH₃]⁺ isomer as the positive fragment raises the threshold values to 12.85 and 12.82, respectively. For *m/z* 41 we also considered a number of isomers of the sum formula C₂H₃N as the positively charged fragment as

is shown in Table. 4-5. We found these to be generally well above the experimental AE with the exception of the reaction leading to the formation of [HCNCH$_2$]$^+$ and CF$_3$AuC(CH$_3$)$_2$ as the neutral counterpart. For this reaction we derive a threshold of 12.35 at the DFT level of theory, which agrees with the experimental value, however, at the coupled cluster level the threshold this value is found to be 12.81, i.e., about 0.5 eV above the confidence limits for the AE. For the formation of the *m/z* ratios 57 and 69, we only considered the direct bond cleavage and formation of [C(CH$_3$)$_3$]$^+$ and [CF$_3$]$^+$, respectively. For this reaction channel for *m/z* 57 the calculated threshold values of 10.61 and 10.82 eV are derived at the PBE0-def2-TZVP and DLPNO-CCSD(T)/def2-TZVP levels of theory as compared with the experimentally determined AE value of 10.3 ± 0.2 eV. Hence, 0.1 and 0.3 eV above the confidence limit, respectively. In addition, we analyzed the production of [HC(CH$_2$)(CH$_3$)$_2$]$^+$ by hydrogen transfer from one of the methyl groups to the central carbon, and we found that the threshold for this reaction is more than 4 eV above the observed AE, at both levels of theory. For *m/z* 69, i.e., the formation of [CF$_3$]$^+$ and AuCNC(CH$_3$)$_3$ threshold energies of 12.62 and 12.67 eV are calculated at the PBE0-def2-TZVP and DLPNO-CCSD(T)/def2-TZVP levels of theory, respectively. These values are only marginally higher than the upper confidence limit of the AE, 12.3 ± 0.3 eV.

In most cases, the computed threshold values correspond well with the experimental AEs, but they tend to be slightly higher than the AEs, especially at the DFT level of theory. This is probably due in part to the fact that the thermal energy correction is based on the average rather than the energy distribution at 353K. The high energy tail of the distribution, may thus shifted the AEs to lower energies relative to the actual thermally corrected threshold.

In the crossed beam experiment, the primary gold-containing fragments are seen at m/z 197, 224, 274 and 280, respectively, and correspond to the positive ions [Au]$^+$, [AuCNH]$^+$, [CF$_2$AuCNH]$^+$, and [AuCNC(CH$_3$)$_3$]$^+$. At m/z 247, 253, and 265, smaller contributions are seen, and they are attributed to [AuCF$_2$]$^+$, [AuCN(CH$_3$)$_2$]$^+$, and [AuCNC(CH$_3$)$_2$]$^+$ based on their respective elemental compositions. At m/z 349, the parent cation [CF$_3$AuCNC(CH$_3$)$_3$]$^+$ is also shown to contribute though with very low intensity. Qualitatively, this is consistent with the m/z ratios in the DIP EI spectra displayed in Figure 4.16; however, the relative intensities in these experiments are noticeably different.

For comparison of the current crossed beam DI data and the DIP MS and to put these in relation to the elemental composition found in the deposition experiments with this precursor[35]. Table 4-6 compares the relative intensities of the fragments formed and the average carbon, fluorine and nitrogen loss per incident in these experiments. At the bottom of the table these are translated to atomic compositions that would form if these processes would determine the composition of the deposit. The average element loss is calculated by weighing the contribution of all gold containing fragments with the number of carbons, fluorine or nitrogen lost, and dividing that by the sum of the intensity of all fragments.

Table 4-6. Relative intensities of DI fragments from $CF_3AuCNC(CH_3)_3$ calculated from the peak intensities at 70 eV as they appear in the mass spectra (Figures 4.14, 4.15 and 4.16). The intensities are normalized to the highest intensity fragment set at 100. For the crossed beam experiment this is m/z 41, $[H_2CCHCH_2]^+$ and for the DIP EI MS this is m/z 280, $[AuCNC(CH_3)_3]^+$. For better comparison the relative intensities for the gold containing observed in the crossed beam experiment are also shown normalized with respect to m/z 224 (last column). At the bottom of the table the composition of a hypothetical deposit that would be formed if governed by DI as observed in these gas phase experiments.

m/z	Fragment	Relative Intensity Crossed beam (m/z 224 =100)	Relative Intensity DIP EI	Au-Fragments Crossed beam (m/z 224 =100)
349	$[CF_3AuCNC(CH_3)_3]^+$	2	40	15
330	$[CF_2AuCNC(CH_3)_3]^+$	0	9	0
280	$[AuCNC(CH_3)_3]^+$	2	100	17
274	$[CF_2AuCNH]^+$	11	64	92
265	$[AuCNC(CH_3)_2]^+$	0	14	0
247	$[CF_2Au]^+$	2	8	17
224	$[AuCNH]^+$	12	98	100
197	$[Au]^+$	10	12	83
69	$[CF_3]^+$	48	8	-
57	$[C(CH_3)_3]^+$	88	83	-
41	$[H_2CCHCH_2]^+$	100	40	-
40	$[H_2CCCH_2]^+$	9	0	-
39	$[H_2CCCH]^+$	34	18	-
15	$[CH_3]^+$	5	-	-
Avrg. C loss per incident		3.15	3.30	
Avrg. N loss per incident		0.03	0.04	
Avrg. F loss per incident		0.71	1.71	
Expected composition from DI		14 at.% Au 40 at.% C	32 at.% F	14 at.% N
Expected composition from DIP		17 at.% Au 45 at.% C	22 at.% F	16 at.% N
EBID composition[35]		14 at% Au 80 at% C	0 at% F	6 at% N

For the fragments at *m/z* 39, 41, 57 and 75 the gold containing neutral fragment assigned in table 4-6 is the reference fragment and the hypothetical deposition is formed under the assumption that all fragments that do not contain gold desorb. Also, in the final column, the relative

intensities of the fragments observed in the crossed beam measurements are shown normalized to the most intense gold containing fragment, m/z 224. Notably, the relative intensity of $[Au]^+$, m/z 197 is much higher in the crossed beam experiment compared to the DIP EI MS for the gold-containing fragments. However, in contrast to the mass spectra recorded under single collision conditions, the relative intensity of the parent cation is a significant contributor in the DIP EI MS. In the DIP EI MS experiment, we believe this is due to the impact of collisional stabilization. The absence of m/z 330, $[CF_2AuCNC(CH_3)_3]^+$, and the relatively lower intensity of m/z 280 in the crossed beam experiment under single collision conditions, as compared to DIP EI MS, can be explained by the fact that both of these fragments might undergo further decay to form m/z 274, $[CF_2AuCNH]^+$, m/z 247, $[CF_2Au]^+$, m/z 224, $[AuCNH]^+$ or m/z 197, $[Au]^+$.

From Table 4-6 it can be seen that the average F, N and C loss per incident in DI of $CF_3AuCNC(CH_3)_3$ under single collision conditions is 0.71, 0,03, and 3.15, respectively, while these numbers are 1.71, 0.04, and 3.30 in the DIP EI spectra. Consequently, in a hypothetical scenario where only the DI mechanism, as they occur under single collision conditions, are active for the deposition of this precursor, the resulting deposit would have a composition of 14 at.% Au, 40 at.% C, 32 at.% F, and 14 at.% N. In the DIP experiments, where we expect collisional stabilization to play a role, these would be 17 at.% Au, 45 at.% C, 22 at.% F, and 16 at.% N, respectively.

Negative ion mass spectra of $CF_3AuCNC(CH_3)_3$ recorded at 0 eV incident energy in the m/z range from 10 to 360 are shown in Figure 4.18. These are recorded with the capillary inlet system at 353 K (a), 333 K (b) and room temperature (c), respectively. For comparison, a direct injection probe chemical ionization negative ion mass spectrum, covering the same mass range, is shown in Figure 4.19. In the crossed beam experiment the only significant m/z ratios observed are at 292 and 335, from which m/z 335 is attributed to a synthetic impurity, as has been confirmed by DIPNCI MS of different batches. From the relative intensities at 333 and 353 K in the crossed beam experiment it can be assumed that this impurity has higher vapor pressure than the target compound, but a positive assignment is not possible. Notwithstanding, the absolute dominating negative ion fragment in both the crossed beam experiment and the DIP NCI is m/z 292. In fact this is the only negative ion observed upon electron attachment to $CF_3AuCNC(CH_3)_3$ in both experiments and is assigned to the loss of the t-butyl group and the formation of $[CF_3AuCN]^-$. Applying the same considerations here as for the DI fragmentation channels it can be concluded that DEA to $CF_3AuCNC(CH_3)_3$ leads to the loss of four carbon, but no fluorine and no nitrogen. Thus assuming DEA as it is observed in the gas phase to be the only process leading to the deposit formation in FEBID with $CF_3AuCNC(CH_3)_3$, would result in a Au:C:F:N composition of 1:2:3:1, which translates to about 14 at.% Au, 29 at.% C, 43 at.% F, and 14 at.% N, respectively. Deposits formed under FEBID conditions, on the other hand, were shown to include 14 at.% Au, 80 at.% C, 0 at.% F, and 6 at.% N, using EDX analysis.[35]

In comparison of the DI data provided here with the deposits produced in the UHV Auger spectrometer under exposure to a 3 keV electron beam[35], it is most noticeable that less than 1 fluorine is on average dissociated per incident in the crossed beam DI experiments and 1.7 in the DIP EI, while as good as quantitative removal of the fluorine is observed in the deposition experiment. Furthermore, the main contribution to the fluorine loss in DI and DIP EI is through the dissociation of the CF_3 ligands from the central gold;

$$CF_3AuCNC(CH_3)_3 + e^- \longrightarrow [CF_3]^+ + [AuCNC(CH_3)_3] + 2e^- \qquad (4.2)$$
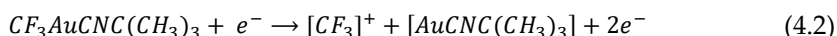
and while this channel is associated with concomitant carbon loss, as good as no carbon removal is observed in the deposition experiment. In fact, more than three carbon atoms are dissociated from the precursor on average per DI incident, while no carbon is removed in the deposition experiment. Furthermore, in DEA no fluorine loss is observed. Though the elemental loss in the gas phase experiments differs significantly from what is reflected in the composition of the deposit, these observations are in line with the interpretation of the deposition experiments. There it was proposed that the fragments formed in the initial dissociation of this precursor are not desorbed, but rather decompose at the surface through further irradiation under fluorine loss forming a carbonaceous deposit retaining the stochiometric Au:C:N ratio of the precursor[35].

With a dose of 1.15×10^{14} e$^-$/μm^2 in the deposition experiment, electron-induced secondary reactions are highly probable. A monolayer of 10^6 molecules covers 1 μm^2 if assuming dense packing and a surface area of 1 nm^2 per molecule. According to the Auger measurements, the thickness of the deposit was greater than 100 nm and assuming 200 nm, then each molecule has been subjected to more than 5×10^5 electrons. The reactive area of this 1 μm^2 is around 0.01 μm^2, when assuming cross section of 10^{-16} cm^2, which is on the order of magnitude for other FEBID precursors[138,139,150]. That means that each molecule may experience around 5,000 reactive incidents. This assumes that the cross section at the surface is the same as in the gas phase and that it stays the same for the secondary and tertiary processes. This does not hold and the cross sections for the secondary and tertiary processes may be orders of magnitude less than those for the initial process. Nonetheless, it is clear that secondary electron-induced processes may play a significant, if not dominating, role in determining the final composition of the deposit in FEBID. This has been discussed in relation to other FEBID precursors[66,151], and is apparent in a variety of non-steady state studies in which thin precursor layers are subjected to 500 eV electrons and the elemental composition change is observed in dependency on the electron dosage. Precursors such as $Ru(CO)_4I_2$[47], cis-$Pt(CO)_2Cl_2$[144], and $(\eta^3\text{-}C_3H_5)Ru(CO)_3Br$[152] are good examples where initial carbonyl loss is observed at surfaces in good agreement with gas phase experiments while prolonged electron exposure causes secondary fragmentation, leading in part to the desorption of the halogens and in part to breakdown of carbon-containing ligands and the incorporation of carbon into the deposit.
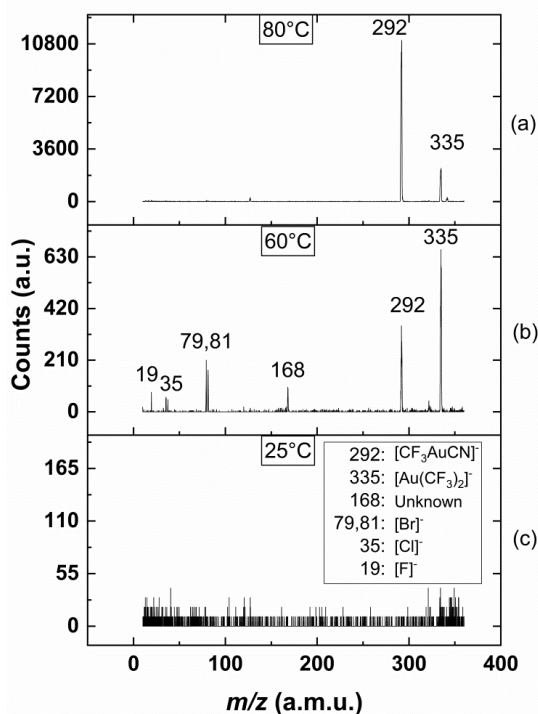
Figure 4.18. Negative ion mass spectra of of CF₃AuCNC(CH₃)₃ recorded at 0 eV incident electron energy and at (a) 353 K, (b) 333 k, and (c) 298 k. The results show that increasing the temperature resulted in the decrease in intensities of impurities and increase in intensities of the DEA from the target molecule.

Figure 4.20(a) displays a [CF₃AuCN]⁻ ion yield curve from 0 to 10 eV, with an expanded inset comparing the normalized [CF₃AuCN]⁻ ion yield curve to that of SF₆⁻ from SF₆, utilized for the corresponding energy calibration. The contour plots of the HOMO (SOMO) of the ground state anion and the LUMO of the neutral molecule are compared in Figure 4.20(b). Chemcraft[153] is used to create the contour plots, with a contour value of 0.05, using the equilibrium geometries optimized at the PBE0-def2-TZVP level of theory. The [CF₃AuCN]⁻ signal is wider (FWHM of 300 meV) and somewhat blue shifted (0.05 eV) compared to the SF₆⁻ ion yield (FWHM190 meV). As discussed above, the prerequisite for the formation of anionic fragments at or close to the 0 eV threshold is that the respective process is exothermic. This is consistent with the calculated threshold values of -1.12 and -1.36 eV at the PBE0-def2-TZVP and DLPNO-CCSD(T)/def2-TZVP levels of theory, respectively, for the direct dissociation process leading to the formation of [CF₃AuCN]⁻ through direct loss of the t-butyl group (see Table 4-5). The observation of such high intensity DEA reactions is not uncommon under single collision conditions, where the only relaxation channels are re-emission of the electron and dissociation. Especially in compounds containing the high higher halogens where the electron affinity of the neutral of the negative ion fragment formed may exceed the bond dissociation energy needed to cleave it from the parent compound. The most prominent example of this is probably the formation of Cl⁻ from CCl₄[154]. The DIP NCI experiments, however, are conducted in the presence of methane as a moderation gas at

about 0.1 torr. As a result, the mean free path in these studies is on the order of 50 nm, which corresponds to a collisional frequency of around 5×10^8 s^{-1} at 333 K.
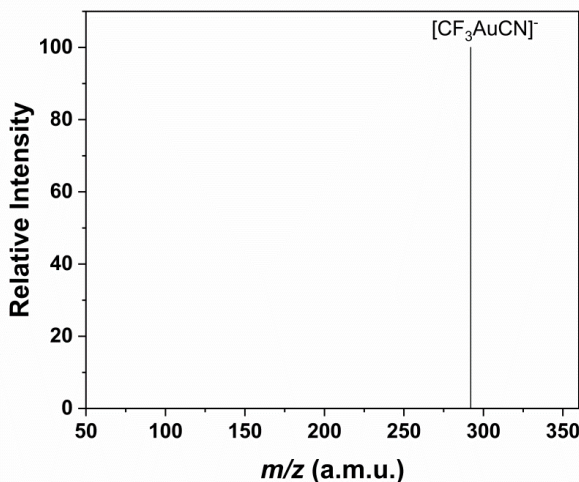
Figure 4.19. Direct injection probe chemical ionization negative ion mass spectrum (DIP-NCI) of CF₃AuCNC(CH₃)₃ recorded in the m/z range from 50 to 360.

Thus, effective collisional stabilization should be provided. Also, at the PBE0-def2-TZVP level of theory we find the adiabatic electron affinity (EA) of CF₃AuCNC(CH₃)₃ to be 0.63 eV, which means that the ground state is stable. Inspecting the contour plots, however, shows that single electron occupancy of the neutral HOMO leads to substantial coupling of this electronic state with the N−C(CH₃)₃ coordinate when compared to the unoccupied LUMO of the anion (Figure 4.20(b)). In the linear ground state, the neutral HOMO is anti-bonding along the AuC−N coordinate with a π* character. However, when occupied by a single electron, this orbital significantly bends the Au−C−N coordinate, stabilizing the molecular anion and reducing the corresponding dihedral angle from 180° to 150°. Hence, while the dissociation, leading to the formation of [CF₃AuCN]⁻, proceeds directly along the N−C(CH₃)₃ bond, the geometrical relaxation of the initially formed TNI to its ground state proceeds along a deformation coordinate. Strong orbital mixing is also observed along the dissociation coordinate, resulting in loss of the anti-bonding π* AuC−N character of the LUMO of the neutral and a relaxed anionic geometry with strong admixture of a σ* character of the N−C(CH₃)₃ bond and an antibonding node at the C atom. We conclude that the vertical transition forming the TNI leads to strong orbital mixing through the bending motion of N−C(CH₃)₃ and that, the dissociation along the repulsive σ* N−C(CH₃)₃ coordinate thus provided occurs on a timescale significantly shorter than collisional stabilization in the DIP NCI experiments. This dynamic problem is intriguing from a purely physical and chemical standpoint, and it demands more investigation at both the experimental and theoretical levels. These dynamics may provide an explanation for the lack of carbon loss from DEA in the deposition studies, whereby the surface provides direct energy dissipated and may dampen the stretch motion, which in turn provides time for reemission of the electron or relaxation to the anionic ground.
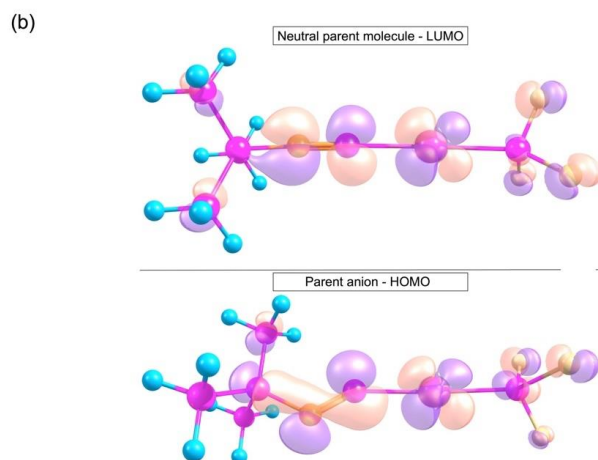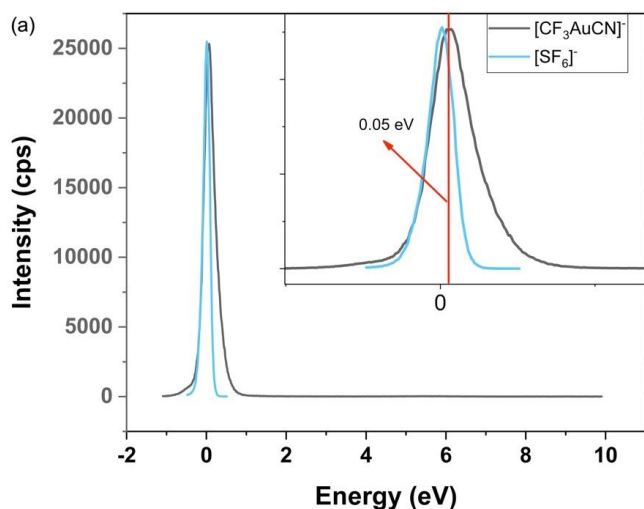
Figure 4.20. (a) Dissociative electron attachment ion yield curve of the [CF$_3$AuCN]$^-$ fragment from CF$_3$AuCNC(CH$_3$)$_3$ recorded in the incident electron energy range from about 0 to 10 eV under single collision conditions. The insert shows a magnification of the energy range from about 0 to 1.5 eV along with the respective [SF$_6$]$^-$ calibration curve. (b) Chemcraft-generated iso-surfaces for the PBE0-def2-TZVP-optimized relaxed geometries of the LUMO of the ground state neutral and the HOMO (SOMO) of the ground-state anion of CF$_3$AuCNC(CH$_3$)$_3$.

4.3.3 Conclusion

Low energy electron induced fragmentation of CF$_3$AuCNC(CH$_3$)$_3$ has been explored in the context of developing molecules favorable to synthesis of gold nanostructures using focused electron beam induced deposition. Both single-collision and collisional-stabilized events for dissociative electron attachment and dissociative ionization were investigated. Dissociative ionization was shown to be more extensive under single collision conditions compared to DIP EI MS, where collisional stabilization was provided, and to be dominated by charged ligand fragments rather

than charged gold containing fragments, as observed in DIP EI MS. Interestingly, the spectra of electron attachments are the same in both cases, and the only detected channel is dissociation to form $[CF_3AuCN]^-$. This is somewhat surprising as we find parent anion to have positive electron affinity and would thus observe collisional stabilization and its detection are more likely in the presence of intermolecular stabilization to lead to observation of the parent anion. When comparing the LUMO of the neutral parent molecule to the HOMO of the relaxed anion, the σ* antibonding character along the respective dissociation coordinate of the TNI suggests a strong π*-σ* coupling in the attachment process and we expect dissociative relaxation along this coordinate to be significantly faster than the collisional stabilization provided. There are significant differences between the gas-phase results and the composition of deposits from this precursor formed by electron-induced deposition in an ultra-high-vacuum Auger spectrometer. The deposition studies show that the deposit retains the parent molecule's carbon and nitrogen stoichiometric content is retained while the fluorine is almost completely eliminated. In contrast, significant carbon loss is observed in the gas phase studies but only a partial removal of fluorine. Furthermore, dissociation of the CF_3 ligand is responsible for the majority of the fluorine loss in gas phase studies, whereas fluorine loss is sequential in the deposition experiments. In line with the deposition experiment, we conclude that this is due to the first electron/molecule interaction leading to immobilization of the partly fragmented molecule on the surface, without ligand desorption. Here, molecular surface interactions and effective energy dissipation work together. With continued exposure to electron irradiation, further fragmentation leads to sequential flour loss and its desorption through electron-induced secondary and tertiary reactions.

We believe that such electron induced secondary and tertiary reactions play an important role in determining deposits compositions in FEBID in general and that these must be considered when approaching a rational design of FEBID precursors and the respective deposition procedures used. Specifically, the immobilized fragments from in the first electron induced dissociation processes must be taken into account and preferably engineered in such a way that they can undergo further electron induced fragmentation and desorption in the corresponding, secondary and tertiary electron induced reactions.

5 Summary and Outlook

Gas phase studies analyzing the interaction of low-energy electrons with organometallic molecules can potentially predict the suitability of certain molecules for use in focused electron beam induced deposition. The two fragmentation processes, termed dissociative electron attachment and dissociative ionization, which are caused by interactions between low-energy electrons and precursor molecules and are important in the FEBID process, have been investigated in this thesis. The single bond ruptures are more common in dissociative electron attachment at incoming electron energies near 0 eV, while multiple bond ruptures are more common in dissociative ionization at higher energies. Deposition in FEBID might be triggered by reactive products from any of these reaction pathways. Molecules that undergo initial deposition stages regulated by DEA may result in deposits containing higher levels of ligand contamination due to the limited number of bond ruptures associated with this process. Nevertheless, tailoring new FEBID precursors in order to cover the intramolecular reactive pathways can facilitate molecular decomposition at low incoming electron energy. More research into optimizing precursors is crucial for advancing FEBID as a nanofabrication technology.

In this thesis, we examined the potential of $(CH_3)AuP(CH_3)_3$ as a gold deposition precursor for FEBID in UHV conditions. Gas-phase DI experiments and quantum chemical calculations were conducted to assist in comprehending the underlying electron-induced reactions. The potential precursor was found to have sufficient volatility and stability for use in FEBID, and under the UHV conditions, a deposit containing 31-34 at.% Au was achieved with a 1:2 Au:C composition. The phosphor was found to be effectively removed in the UHV FEBID experiments, but a small amount of $AuP(CH_3)_2^+$ was formed in the gas phase. Comparisons with a previous HV FEBID study highlighted the differences in deposit compositions and the need for systematic comparisons of UHV and HV deposition experiments. Utilizing a variety of techniques such as UHV-FEBID, gas-phase DI experiments, and quantum chemical calculations, has proven to be an effective strategy for obtaining a comprehensive understanding of electron-induced precursor dissociation mechanisms and the subsequent deposition process.

For the second precursor, we investigated the performance of the $[(CH_3)_2AuCl]_2$ precursor in UHV FEBID and HV gas phase experiments. The composition of deposits generated under UHV and HV conditions were qualitatively similar, with high gold content (about 45-61 at. %) and primarily carbon residues (38-49 at.%). In UHV study, it was shown that the deposit's composition was sensitive to both the deposition current and substrate cleanliness. The DI and DEA experiments yielded different trends in precursor dissociation, with more carbon dissociation and less chlorine dissociation, respectively. Lastly, the study found that higher background water under HV conditions did not affect the deposit's composition, despite the considerable HCl production observed during DI of $[(CH_3)_2AuCl]_2$, and that secondary reactions of immobilized fragments as well as neutral dissociation mechanism may play a significant role in FEBID deposition of this precursor.

For the last study, we presented the results of DI and DEA experiments on $CF_3AuCNC(CH_3)_3$ precursor under single collision conditions and conditions where collisional stabilization is provided and we compared these to. Deposition experiments conducted in an UHV Auger

spectrometer. While collisional stabilization is reflected in less extensive dissociation in the DI experiments these do not influence the negative ion formation, where only one and the same DEA channel is observed under single collision conditions and when collisional stabilization is provided. We attribute this to strong coupling of electronic states in the attachment process and fast dissociation dynamics. Comparison with the composition of the deposits formed under FEBID conditions in the Auger spectrometer does not show direct correlation to the dissociation processes observed in the gas phase and we attribute this in part to more efficient relaxation processes at the surface, but mainly to electron induced secondary and tertiary reactions at the surface, where multiple electron induced fragmentation processes lead to the final composition of the deposit, rather than a single electron molecule collision as it is the case in the gas phase.

In conclusion, the findings of this thesis indicate that the two precursors, $[(CH_3)_2AuCl]_2$ and $(CH_3)AuP(CH_3)_3$, have a high potential for use in FEBID technique. However, additional research on the role of the neutral dissociation process in inducing dissociation into their molecules, as well as the design and implementation of post-purification methods for deposition of these precursors are vital. Furthermore, this study highlights the involvement of electron-driven secondary and tertiary processes, which must be considered in the rational design of FEBID precursors, and for the deposition procedures used. Ideally, the first electron-induced dissociation processes must be engineered in such a way that the immobilized fragments formed can undergo further electron-induced fragmentation, and desorption of ligand material, eventually, as desired, leading to high metal content deposits.

References

(1) Cui, Z. *Nanofabrication: Principles, Capabilities and Limits: Second Edition*; 2017. https://doi.org/10.1007/978-3-319-39361-2.

(2) Ivo Utke, Stanislav Moshkalev, A. P. R. *Nanofabrication Using Focused Ion and Electron Beams*; 2018.

(3) Kumar, C. S. S. R. (Challa S. S. R. .; Hormes, J. (Josef); Leuschner, C. (Carola). *Nanofabrication towards Biomedical Applications : Techniques, Tools, Applications, and Impact*; Wiley-VCH, 2005.

(4) Boisseau, P.; Loubaton, B. Nanomedicine, Nanotechnology in Medicine. *Comptes Rendus Phys.* **2011**, *12* (7), 620–636. https://doi.org/https://doi.org/10.1016/j.crhy.2011.06.001.

(5) Serrano, E.; Rus, G.; García-Martínez, J. Nanotechnology for Sustainable Energy. *Renew. Sustain. Energy Rev.* **2009**, *13* (9), 2373–2384. https://doi.org/https://doi.org/10.1016/j.rser.2009.06.003.

(6) Taha, T. B.; Barzinjy, A. A.; Hussain, F. H. S.; Nurtayeva, T. Nanotechnology and Computer Science: Trends and Advances. *Memories - Mater. Devices, Circuits Syst.* **2022**, *2*, 100011. https://doi.org/https://doi.org/10.1016/j.memori.2022.100011.

(7) Daniels-Race, T. Nanodevices: Fabrication, Prospects for Low Dimensional Devices and Applications. In *Nanolithography: The Art of Fabricating Nanoelectronic and Nanophotonic Devices and Systems*; Feldman, M. B. T.-N., Ed.; Woodhead Publishing, 2013; pp 399–423. https://doi.org/10.1533/9780857098757.399.

(8) Lo Nigro, R.; Fiorenza, P.; Pécz, B.; Eriksson, J. Nanotechnology for Electronic Materials and Devices. *Nanomaterials* **2022**, *12* (19), 3319. https://doi.org/10.3390/nano12193319.

(9) Huang, X.; Zhu, Y.; Kianfar, E. Nano Biosensors: Properties, Applications and Electrochemical Techniques. *J. Mater. Res. Technol.* **2021**, *12*, 1649–1672. https://doi.org/https://doi.org/10.1016/j.jmrt.2021.03.048.

(10) Somwanshi, S. B.; Somvanshi, S. B.; Kharat, P. B. Nanocatalyst: A Brief Review on Synthesis to Applications. *J. Phys. Conf. Ser.* **2020**, *1644* (1). https://doi.org/10.1088/1742-6596/1644/1/012046.

(11) Ghosh, C. K. Quantum Effect on Properties of Nanomaterials BT - Introduction to Nano: Basics to Nanoscience and Nanotechnology; Sengupta, A., Sarkar, C. K., Eds.; Springer Berlin Heidelberg: Berlin, Heidelberg, 2015; pp 73–111. https://doi.org/10.1007/978-3-662-47314-6_5.

(12) Tiwari, P. M.; Bawage, S. S.; Singh, S. R. 13 - Gold Nanoparticles and Their Applications in Photomedicine, Diagnosis and Therapy; Hamblin, M. R., Avci, P. B. T.-A. of N. in P., Eds.; Chandos Publishing: Oxford, 2015; pp 249–266. https://doi.org/https://doi.org/10.1533/9781908818782.249.

(13) Hong, X.; Tan, C.; Chen, J.; Xu, Z.; Zhang, H. Synthesis, Properties and Applications of One- and Two-Dimensional Gold Nanostructures. *Nano Res.* **2015**, *8* (1), 40–55. https://doi.org/10.1007/s12274-014-0636-3.

(14) Hu, M.; Chen, J.; Li, Z.-Y.; Au, L.; Hartland, G. V; Li, X.; Marquez, M.; Xia, Y. Gold Nanostructures: Engineering Their Plasmonic Properties for Biomedical Applications. *Chem. Soc. Rev.* **2006**, *35* (11), 1084–1094. https://doi.org/10.1039/B517615H.

(15) Prima, G. Di; Sachser, R.; Trompenaars, P.; Mulders, H.; Huth, M. Direct-Write Single Electron Transistors by Focused Electron Beam Induced Deposition. *Nano Futur.* **2019**, *3* (2), 25001. https://doi.org/10.1088/2399-1984/ab151c.

(16) Ren, S.; Wang, J.; Song, C.; Li, Q.; Yang, Y.; Teng, N.; Su, S.; Zhu, D.; Huang, W.; Chao, J.; Wang, L.; Fan, C. Single-Step Organization of Plasmonic Gold Metamaterials with Self-Assembled DNA Nanostructures. *Research* **2019**, *2019*, 7403580. https://doi.org/10.34133/2019/7403580.

(17) Homma, Y. Gold Nanoparticles as the Catalyst of Single-Walled Carbon Nanotube Synthesis. *Catalysts* **2014**, *4* (1), 38–48. https://doi.org/10.3390/catal4010038.

(18) Grande, M.; Bianco, G. V; Vincenti, M. A.; de Ceglia, D.; Petruzzelli, V.; Scalora, M.; Bruno, G.; D'Orazio, A.; De Vittorio, M.; Stomeo, T. 2D Plasmonic Gold Nano-Patches for Linear and Nonlinear Applications. *Microelectron. Eng.* **2013**, *111*, 234–237. https://doi.org/https://doi.org/10.1016/j.mee.2013.03.172.

(19) Guo, L.; Chen, G.; Kim, D.-H. Three-Dimensionally Assembled Gold Nanostructures for Plasmonic Biosensors. *Anal. Chem.* **2010**, *82* (12), 5147–5153. https://doi.org/10.1021/ac100346z.

(20) Sharifi, M.; Attar, F.; Saboury, A. A.; Akhtari, K.; Hooshmand, N.; Hasan, A.; El-Sayed, M. A.; Falahati, M. Plasmonic Gold Nanoparticles: Optical Manipulation, Imaging, Drug Delivery and Therapy. *Journal of Controlled Release*. Elsevier B.V. October 1, 2019, pp 170–189. https://doi.org/10.1016/j.jconrel.2019.08.032.

(21) Mpatzaka, T.; Zisis, G.; Raptis, I.; Vamvakas, V.; Kaiser, C.; Mai, T.; Schirmer, M.; Gerngroß, M.; Papageorgiou, G. Process Study and the Lithographic Performance of Commercially Available Silsesquioxane Based Electron Sensitive Resist Medusa 82. *Micro Nano Eng.* **2020**, *8* (December 2019), 100065. https://doi.org/10.1016/j.mne.2020.100065.

(22) Pala, N.; Karabiyik, M. Electron Beam Lithography (EBL) BT - Encyclopedia of Nanotechnology; Bhushan, B., Ed.; Springer Netherlands: Dordrecht, 2012; pp 718–740. https://doi.org/10.1007/978-90-481-9751-4_344.

(23) Zhang, J.; Con, C.; Cui, B. Electron Beam Lithography on Irregular Surfaces Using an Evaporated Resist. *ACS Nano* **2014**, *8* (4), 3483–3489. https://doi.org/10.1021/nn4064659.

(24) Wu, C. S.; Makiuchi, Y.; Chen, C. High-Energy Electron Beam Lithography for Nanoscale Fabrication; Wang, M., Ed.; IntechOpen: Rijeka, 2010; p Ch. 13. https://doi.org/10.5772/8179.

(25) Utke, I.; Hoffmann, P.; Melngailis, J. Gas-Assisted Focused Electron Beam and Ion Beam Processing and Fabrication. *J. Vac. Sci. Technol. B Microelectron. Nanom. Struct.* **2008**, *26* (4), 1197–1276. https://doi.org/10.1116/1.2955728.

(26) Huth, M.; Porrati, F.; Schwalb, C.; Winhold, M.; Sachser, R.; Dukic, M.; Adams, J.; Fantner, G. Focused Electron Beam Induced Deposition: A Perspective. *Beilstein J. Nanotechnol.* **2012**, *3* (1), 597–619. https://doi.org/10.3762/bjnano.3.70.

(27) Van Dorp, W. F.; Hagen, C. W. A Critical Literature Review of Focused Electron Beam Induced Deposition. *J. Appl. Phys.* **2008**, *104* (8). https://doi.org/10.1063/1.2977587.

(28) Wnuk, J. D.; Gorham, J. M.; Rosenberg, S. G.; Van Dorp, W. F.; Madey, T. E.; Hagen, C. W.; Fairbrother, D. H. Electron Beam Irradiation of Dimethyl-(Acetylacetonate) Gold(III) Adsorbed onto Solid Substrates. *J. Appl. Phys.* **2010**, *107* (5). https://doi.org/10.1063/1.3295918.

(29) Jenke, M. G.; Lerose, D.; Niederberger, C.; Michler, J.; Christiansen, S.; Utke, I. Toward Local Growth of Individual Nanowires on Three-Dimensional Microstructures by Using a Minimally Invasive Catalyst Templating Method. *Nano Lett.* **2011**, *11* (10), 4213–4217. https://doi.org/10.1021/nl2021448.

(30) Koops, H. W. P.; Kretz, J.; Rudolph, M.; Weber, M.; Dahm, G.; Lee, K. L. Characterization and Application of Materials Grown by Electron-Beam-Induced Deposition. *Jpn. J. Appl. Phys.* **1994**, *33* (Part 1, No. 12B), 7099–7107. https://doi.org/10.1143/jjap.33.7099.

(31) Folch, A.; Tejada, J.; Peters, C. H.; Wrighton, M. S. Electron Beam Deposition of Gold Nanostructures in a Reactive Environment. *Appl. Phys. Lett.* **1995**, *2080* (1995), 2080–2082. https://doi.org/10.1063/1.113909.

(32) Silvis-Cividjian, N.; Hagen, C. W.; Leunissen, L. H. A.; Kruit, P. The Role of Secondary Electrons in Electron-Beam-Induced-Deposition Spatial Resolution. *Microelectron. Eng.* **2002**, *61–62*, 693–699. https://doi.org/https://doi.org/10.1016/S0167-9317(02)00515-4.

(33) Swiderek, P. Electron-Induced Chemical Reactions for Surface Functionalization. In *Encyclopedia of Interfacial Chemistry: Surface Science and Electrochemistry*; Elsevier, 2018; pp 702–710. https://doi.org/10.1016/B978-0-12-409547-2.13876-4.

(34) Carden, W. G.; Lu, H.; Spencer, J. A.; Fairbrother, D. H.; McElwee-White, L. Mechanism-Based Design of Precursors for Focused Electron Beam-Induced Deposition. *MRS Commun.* **2018**, *8* (2), 343–357. https://doi.org/10.1557/mrc.2018.77.

(35) Carden, W. G.; Thorman, R. M.; Unlu, I.; Abboud, K. A.; Fairbrother, D. H.; McElwee-White, L. Design, Synthesis, and Evaluation of CF3AuCNR Precursors for Focused Electron Beam-Induced Deposition of Gold. *ACS Appl. Mater. Interfaces* **2019**, *11* (12), 11976–11987. https://doi.org/10.1021/acsami.8b18368.

(36) Carden, W. G.; Pedziwiatr, J.; Abboud, K. A.; McElwee-White, L. Halide Effects on the Sublimation Temperature of X-Au-L Complexes: Implications for Their Use as Precursors in Vapor Phase Deposition Methods. *ACS Appl. Mater. Interfaces* **2017**, *9* (46), 40998–41005. https://doi.org/10.1021/acsami.7b12465.

(37) Utke, I.; Hoffmann, P.; Dwir, B.; Leifer, K.; Kapon, E.; Doppelt, P. Focused Electron Beam Induced Deposition of Gold. *J. Vac. Sci. Technol. B Microelectron. Nanom. Struct.* **2000**, *18* (6), 3168. https://doi.org/10.1116/1.1319690.

(38) Mulders, J. J. L.; Veerhoek, J. M.; Bosch, E. G. T.; Trompenaars, P. H. F. Fabrication of Pure Gold Nanostructures by Electron Beam Induced Deposition with Au(CO)Cl Precursor: Deposition Characteristics and Primary Beam Scattering Effects. *J. Phys. D. Appl. Phys.* **2012**, *45* (47), 1–8. https://doi.org/10.1088/0022-3727/45/47/475301.

(39) Ingólfsson, O. *Low-Energy Electrons Fundamentals and Applications*; Pan Stanford Publishing Pte. Ltd.: Singapore, The Republic of Singapore, 2019.

(40) Märk, T. D.; Dunn, G. H. *Electron Impact Ionization*; Springer Science & Business Media: Berlin/Heidelberg, Germany, 1985. https://doi.org/10.1007/978-3-7091-4028-4.

(41) Ingolfsson, O.; Weik, F.; Illenberger, E. *Review The Reactivity of Slow Electrons with Molecules at Different Degrees of Aggregation: Gas Phase, Clusters and Condensed Phase*; 1996; Vol. 155.

(42) Illenberger, E.; Swiderek, P. Electron-Driven Molecular Processes: A General Introduction. *European Physical Journal D*. August 2005, pp 173–176. https://doi.org/10.1140/epjd/e2005-00229-y.

(43) Eugen Illenberger; Momigny, J. *Gaseous Molecular Ions. An Introduction to Elementary Processes Induced by Ionization.*; Darmstadt : Steinkopff Verlag ; New York : Springer-Verlag, 1992.

(44) Thorman, R. M.; Ragesh Kumar, T. P.; Howard Fairbrother, D.; Ingólfsson, O. The Role of Low-Energy Electrons in Focused Electron Beam Induced Deposition: Four Case Studies of Representative Precursors. *Beilstein J. Nanotechnol.* **2015**, *6* (1), 1904–1926. https://doi.org/10.3762/bjnano.6.194.

(45) Utke, I.; Swiderek, P.; Höflich, K.; Madajska, K.; Jurczyk, J.; Martinović, P.; Szymańska, I. B. Coordination and Organometallic Precursors of Group 10 and 11: Focused Electron Beam Induced Deposition of Metals and Insight Gained from Chemical Vapour Deposition, Atomic Layer Deposition, and Fundamental Surface and Gas Phase Studies. *Coord. Chem. Rev.* **2022**, *458*, 213851. https://doi.org/https://doi.org/10.1016/j.ccr.2021.213851.

(46) Wnuk, J. D.; Rosenberg, S. G.; Gorham, J. M.; Van Dorp, W. F.; Hagen, C. W.; Fairbrother, D. H. Electron Beam Deposition for Nanofabrication: Insights from Surface Science. *Surf. Sci.* **2011**, *605* (3–4), 257–266. https://doi.org/10.1016/j.susc.2010.10.035.

(47) Thorman, R. M.; Jensen, P. A.; Yu, J. C.; Matsuda, S. J.; McElwee-White, L.; Ingólfsson, O.; Fairbrother, D. H. Electron-Induced Reactions of Ru(CO)4I2: Gas Phase, Surface, and Electron Beam-Induced Deposition. *J. Phys. Chem. C* **2020**, *124* (19), 10593–10604. https://doi.org/10.1021/acs.jpcc.0c01801.

(48) Spencer, J. A.; Rosenberg, S. G.; Barclay, M.; Wu, Y. C.; McElwee-White, L.; Howard Fairbrother, D. Understanding the Electron-Stimulated Surface Reactions of Organometallic Complexes to Enable Design of Precursors for Electron Beam-Induced Deposition. *Appl. Phys. A Mater. Sci. Process.* **2014**, *117* (4), 1631–1644. https://doi.org/10.1007/s00339-014-8570-5.

(49) Jurczyk, J.; Pillatsch, L.; Berger, L.; Priebe, A.; Madajska, K.; Kapusta, C.; Szymańska, I. B.; Michler, J.; Utke, I. In Situ Time-of-Flight Mass Spectrometry of Ionic Fragments Induced by Focused Electron Beam Irradiation: Investigation of Electron Driven Surface Chemistry inside an SEM under High Vacuum. *Nanomaterials*. 2022. https://doi.org/10.3390/nano12152710.

(50) Bjarnason, E. H.; Ómarsson, B.; Engmann, S.; Ómarsson, F. H.; Ingólfsson, O. Dissociative Electron Attachment to Titatinum Tetrachloride and Titanium Tetraisopropoxide. *Eur. Phys. J. D* **2014**, *68* (5), 121. https://doi.org/10.1140/epjd/e2014-50091-9.

(51) Cipriani, M.; Bjornsson, R.; Barclay, M.; Terfort, A.; Fairbrother, D. H.; Ingólfsson, O. Relative Cross Sections and Appearance Energies in Electron Impact Ionization and Dissociation of Mono-Halogenated Biphenyls. *Int. J. Mass Spectrom.* **2021**, *459*. https://doi.org/10.1016/j.ijms.2020.116452.

(52) Engmann, S.; Stano, M.; Matejčík, Š.; Ingólfsson, O. The Role of Dissociative Electron Attachment in Focused Electron Beam Induced Processing: A Case Study on Cobalt Tricarbonyl Nitrosyl. *Angew. Chemie Int. Ed.* **2011**, *50* (40), 9475–9477. https://doi.org/https://doi.org/10.1002/anie.201103234.

(53) Van Dorp, W. F.; Van Someren, B.; Hagen, C. W.; Kruit, P.; Crozier, P. A. Approaching the Resolution Limit of Nanometer-Scale Electron Beam-Induced Deposition. *Nano Lett.* **2005**, *5* (7), 1303–1307. https://doi.org/10.1021/nl050522i.

(54) Winkler, R.; Fowlkes, J. D.; Rack, P. D.; Plank, H. 3D Nanoprinting via Focused Electron Beams. *J. Appl. Phys.* **2019**, *125* (21). https://doi.org/10.1063/1.5092372.

(55) Schwalb, C. H.; Grimm, C.; Baranowski, M.; Sachser, R.; Porrati, F.; Reith, H.; Das, P.; Müller, J.; Völklein, F.; Kaya, A.; Huth, M. A Tunable Strain Sensor Using Nanogranular Metals. *Sensors (Switzerland)* **2010**, *10* (11), 9847–9856. https://doi.org/10.3390/s101109847.

(56) De Teresa, J. M.; Fernández-Pacheco, A.; Córdoba, R.; Serrano-Ramón, L.; Sangiao, S.; Ibarra, M. R. Review of Magnetic Nanostructures Grown by Focused Electron Beam Induced Deposition (FEBID). *J. Phys. D Appl. Phys.* **2016**, *49* (24), 1–66. https://doi.org/10.1088/0022-3727/49/24/243003.

(57) Ruska, E. The Development of the Electron Microscope and of Electron Microscopy (Nobel Lecture). *Angew. Chemie Int. Ed. English* **1987**, *26* (7), 595–605. https://doi.org/10.1002/anie.198705953.

(58) Utke, I.; Moshkalev, S. A.; Russell, P. E. *NANOFABRICATION USING FOCUSED ION AND ELECTRON BEAMS*; Oxford University Press Inc.: New York, 2012.

(59) Wanzenboeck, H. D.; Roediger, P.; Hochleitner, G.; Bertagnolli, E.; Buehler, W. Novel Method for Cleaning a Vacuum Chamber from Hydrocarbon Contamination. *J. Vac. Sci. Technol. A Vacuum, Surfaces, Film.* **2010**, *28* (6), 1413–1420. https://doi.org/10.1116/1.3484242.

(60) Isabell, T. C.; Fischione, P. E.; O'Keefe, C.; Guruz, M. U.; Dravid, V. P. Plasma Cleaning and Its Applications for Electron Microscopy. *Microsc. Microanal.* **1999**, *5* (2), 126–135. https://doi.org/10.1017/S1431927699000094.

(61) Yoshimura, N. Designing of Evacuation Systems BT - Vacuum Technology: Practice for Scientific Instruments; Yoshimura, N., Ed.; Springer Berlin Heidelberg: Berlin, Heidelberg, 2008; pp 1–34. https://doi.org/10.1007/978-3-540-74433-7_1.

(62) HEIDE, H. G. Electron Microscopic Observation of Specimens under Controlled Gas Pressure. *J. Cell Biol.* **1962**, *13* (1), 147–152. https://doi.org/10.1083/jcb.13.1.147.

(63) Hirsch, P.; Kässens, M.; Püttmann, M.; Reimer, L. Contamination in a Scanning Electron Microscope and the Influence of Specimen Cooling. *Scanning* **1994**, *16* (2), 101–110. https://doi.org/https://doi.org/10.1002/sca.4950160207.

(64) van Dorp, W. F.; Hagen, C. W.; Crozier, P. A.; van Someren, B.; Kruit, P. One Nanometer Structure Fabrication Using Electron Beam Induced Deposition. *Microelectron. Eng.* **2006**, *83* (4-9 SPEC. ISS.), 1468–1470. https://doi.org/10.1016/j.mee.2006.01.155.

(65) MacLeod, J. M.; Lipton-Duffin, J.; Fu, C.; Rosei, F. Inducing Nonlocal Reactions with a Local Probe. *ACS Nano* **2009**, *3* (11), 3347–3351. https://doi.org/10.1021/nn901504m.

(66) Kamali, A.; Bilgilisoy, E.; Wolfram, A.; Gentner, T. X.; Ballmann, G.; Harder, S.; Marbach, H.; Ingólfsson, O. On the Electron-Induced Reactions of (CH3)AuP(CH3)3: A Combined UHV Surface Science and Gas-Phase Study. *Nanomaterials*. 2022. https://doi.org/10.3390/nano12152727.

(67) Hagen, C. W. The Future of Focused Electron Beam-Induced Processing. *Appl. Phys. A Mater. Sci. Process.* **2014**, *117* (4), 1599–1605. https://doi.org/10.1007/s00339-014-8847-8.

(68) Silvis-Cividjian, N.; Hagen, C. W.; Kruit, P. Spatial Resolution Limits in Electron-Beam-Induced Deposition. *J. Appl. Phys.* **2005**, *98* (8). https://doi.org/10.1063/1.2085307.

(69) Van Dorp, W. F.; Zhang, X.; Feringa, B. L.; Hansen, T. W.; Wagner, J. B.; De Hosson, J. T. M. Molecule-by-Molecule Writing Using a Focused Electron Beam. *ACS Nano* **2012**, *6* (11), 10076–10081. https://doi.org/10.1021/nn303793w.

(70) Peinado, P.; Sangiao, S.; De Teresa, J. M. Focused Electron and Ion Beam Induced Deposition on Flexible and Transparent Polycarbonate Substrates. *ACS Nano* **2015**, *9* (6), 6139–6146. https://doi.org/10.1021/acsnano.5b01383.

(71) Drost, M.; Tu, F.; Berger, L.; Preischl, C.; Zhou, W.; Gliemann, H.; Wöll, C.; Marbach, H. Surface-Anchored Metal-Organic Frameworks as Versatile Resists for Gas-Assisted E-Beam Lithography: Fabrication of Sub-10 Nanometer Structures. *ACS Nano* **2018**, *12* (4), 3825–3835. https://doi.org/10.1021/acsnano.8b01071.

(72) Klein, K. L.; Randolph, S. J.; Fowlkes, J. D.; Allard, L. F.; Meyer III, H. M.; Simpson, M. L.; Rack, P. D. Single-Crystal Nanowires Grown via Electron-Beam-Induced Deposition. *Nanotechnology* **2008**, *19* (34), 345705. https://doi.org/10.1088/0957-4484/19/34/345705.

(73) van Dorp, W. F.; Lazar, S.; Hagen, C. W.; Kruit, P. Solutions to a Proximity Effect in High Resolution Electron Beam Induced Deposition. *J. Vac. Sci. Technol. B Microelectron. Nanom. Struct.* **2007**, *25* (5), 1603. https://doi.org/10.1116/1.2775456.

(74) Yuan, P.-S.; Mason, N.; Pintea, M.; István, C.; Fodor, T. Structural Analysis of Si(OEt)4 Deposits on Au(111)/SiO2 Substrates at Nanometer Scale Using Focused Electron Beam Induced Deposition. *{arXiv},* **2022**, *1* (111). https://doi.org/{10.48550/ARXIV.2206.01422},.

(75) Rajput, J.; Lammich, L.; Andersen, L. H. Measured Lifetime of SF6-. *Phys. Rev. Lett.* **2008**, *100* (15), 153001. https://doi.org/10.1103/PhysRevLett.100.153001.

(76) *Electron–Molecule Interactions and Their Applications*; Christophorou, L. G., Ed.; Elsevier, 1984. https://doi.org/10.1016/C2013-0-10496-5.

(77) Gross, J. H. Principles of Ionization and Ion Dissociation. In *Mass Spectrometry: A Textbook*; Springer Berlin Heidelberg: Berlin, Heidelberg, 2011; pp 21–66. https://doi.org/10.1007/978-3-642-10711-5_2.

(78) Schulz, G. J. *Resonances in Electron Impact on Diatomic Molecules" I. Introduction A. Classification of Compound States*; Vol. 4.

(79) Feshbach Resonances. In *Ultracold Quantum Fields*; Springer Netherlands: Dordrecht, 2009; pp 431–473. https://doi.org/10.1007/978-1-4020-8763-9_17.

(80) Morrison, M. A. The Physics of Low-Energy Electron-Molecule Collisions: A Guide for the Perplexed and the Uninitiated. *Aust. J. Phys.* **1983**, *36*, 239–286.

(81) Allan, M. Study of Triplet States and Short-Lived Negative Ions by Means of Electron Impact Spectroscopy. *J. Electron Spectros. Relat. Phenomena* **1989**, *48*, 219–351.

(82) Kumar T.P., R. Low-Energy Electron-Induced Decomposition of Bimetallic and Silicon-Containing FEBID Precursors: HFeCo3(CO)12, H2FeRu3(CO)13, SiC5H10Cl2, SiC5H12 and Si3C3H12, University of Iceland, 2017.

(83) Jaffke, T.; Illenberger, E.; Lezius, M.; Matejcik, S.; Smith, D.; Märk, T. D. Formation of C60– and C70– by Free Electron Capture. Activation Energy and Effect of the Internal Energy on Lifetime. *Chem. Phys. Lett.* **1994**, *226* (1), 213–218. https://doi.org/https://doi.org/10.1016/0009-2614(94)00704-7.

(84) Ingólfsson, O.; Illenberger, E. Effective Intermolecular Relaxation in (C6F6)N– Clusters: Mechanism of C6F6– Formation on Low Energy Electron Impact. *Int. J. Mass Spectrom. Ion Process.* **1995**, *149–150*, 79–86. https://doi.org/https://doi.org/10.1016/0168-1176(95)04243-E.

(85) Send, R.; Kühn, M.; Furche, F. Assessing Excited State Methods by Adiabatic Excitation Energies. *J. Chem. Theory Comput.* **2011**, *7* (8), 2376–2386. https://doi.org/10.1021/ct200272b.

(86) Allan, M. Electron Scattering in Pt(PF3)4: Elastic Scattering, Vibrational, and Electronic Excitation. *J. Chem. Phys.* **2011**, *134* (20), 204309. https://doi.org/10.1063/1.3594206.

(87) Országh, J.; Danko, M.; Ribar, A.; Matejčík, Š. Nitrogen Second Positive System Studied by Electron Induced Fluorescence. *Nucl. Instruments Methods Phys. Res. Sect. B Beam Interact. with Mater. Atoms* **2012**, *279*, 76–79. https://doi.org/10.1016/j.nimb.2011.10.031.

(88) Ribar, A.; Danko, M.; Országh, J.; Ferreira Da Silva, F.; Utke, I.; Matejčík, Š. Dissociative Excitation Study of Iron Pentacarbonyl Molecule. *Eur. Phys. J. D* **2015**, *69* (4), 1–10. https://doi.org/10.1140/epjd/e2015-50755-x.

(89) Stamatovic, A.; Schulz, G. J. Trochoidal Electron Monochromator. *Rev. Sci. Instrum.* **1968**, *39* (11), 1752–1753. https://doi.org/10.1063/1.1683220.

(90) Stamatovic, A.; Schulz, G. J. Characteristics of the Trochoidal Electron Monochromator. *Rev. Sci. Instrum.* **1970**, *41* (3), 423–427. https://doi.org/10.1063/1.1684534.

(91) Ómarsson, B. Promoting Reaction Channels in Dissociative Electron Attachment through Bond Formation and Rearrangement . University of Iceland, School of Engineering and Natural Sciences, Faculty of Physical Sciences: Reykjavík 2013.

(92) Bjarnason, E. H.; Ómarsson, B.; Engmann, S.; Ómarsson, F. H.; Ingólfsson, O. Dissociative Electron Attachment to Titatinum Tetrachloride and Titanium Tetraisopropoxide. *Eur. Phys. J. D* **2014**, *68* (5). https://doi.org/10.1140/epjd/e2014-50091-9.

(93) Harland, P. W.; Thynne, J. C. J. Autodetachment Lifetimes, Attachment Cross Sections, and Negative Ions Formed by Sulfur Hexafluoride and Sulfur Tetrafluoride. *J. Phys. Chem.* **1971**, *75* (23), 3517–3523. https://doi.org/10.1021/j100692a005.

(94) Klar, D.; Ruf, M.-W.; Hotop, H. Attachment of Electrons to Molecules at Submillielectronvolt Resolution. *Chem. Phys. Lett.* **1992**, *189* (4), 448–454. https://doi.org/https://doi.org/10.1016/0009-2614(92)85230-8.

(95) Wetzel, R. C.; Baiocchi, F. A.; Hayes, T. R.; Freund, R. S. Absolute Cross Sections for Electron-Impact Ionization of the Rare-Gas Atoms by the Fast-Neutral-Beam Method. *Phys. Rev. A* **1987**, *35* (2), 559–577. https://doi.org/10.1103/PhysRevA.35.559.

(96) Fiegele, T.; Hanel, G.; Torres, I.; Lezius, M.; Märk, T. D. Threshold Electron Impact Ionization of Carbon Tetrafluoride, Trifluoromethane, Methane and Propane. *J. Phys. B At. Mol. Opt. Phys.* **2000**, *33* (20), 4263–4283. https://doi.org/10.1088/0953-4075/33/20/306.

(97) Cipriani, M.; Svavarsson, S.; da Silva, F. F.; Lu, H.; McElwee-White, L.; Ingólfsson, O. The Role of Low-Energy Electron Interactions in Cis-Pt(Co)2 Br2 Fragmentation. *Int. J. Mol. Sci.* **2021**, *22* (16). https://doi.org/10.3390/ijms22168984.

(98) Hartree, D. R. The Wave Mechanics of an Atom with a Non-Coulomb Central Field. Part I. Theory and Methods. *Math. Proc. Cambridge Philos. Soc.* **1928**, *24* (1), 89–110. https://doi.org/DOI: 10.1017/S0305004100011919.

(99) Fock, V. Näherungsmethode Zur Lösung Des Quantenmechanischen Mehrkörperproblems. *Zeitschrift für Phys. 61*, 126–148.

(100) Slater, J. C. Atomic Shielding Constants. *Phys. Rev.* **1930**, *36* (1), 57–64. https://doi.org/10.1103/PhysRev.36.57.

(101)   Hofmann, M.; Schaefer, H. F. Computational Chemistry; Meyers, R. A. B. T.-E. of P. S. and T. (Third E., Ed.; Academic Press: New York, 2003; pp 487–506. https://doi.org/https://doi.org/10.1016/B0-12-227410-5/00129-0.

(102)   Hohenberg, P.; Kohn, W. Inhomogeneous Electron Gas. *Phys. Rev.* **1964**, *136* (3B), B864–B871. https://doi.org/10.1103/PhysRev.136.B864.

(103)   Kohn, W.; Sham, L. J. Self-Consistent Equations Including Exchange and Correlation Effects. *Phys. Rev.* **1965**, *140* (4A), A1133–A1138. https://doi.org/10.1103/PhysRev.140.A1133.

(104)   Goel, S.; A.Velizhanin, K.; Piryatinski, A.; Tretiak, S.; Ivanov, S. A. DFT Study of Ligand Binding to Small Gold Clusters Satyende. *J. Phys. Chem. Lett.* **2010**, *1* (6), 927–931. https://doi.org/10.1021/jz1000193.

(105)   Kepp, K. P. Benchmarking Density Functionals for Chemical Bonds of Gold. *J. Phys. Chem. A* **2017**, *121* (9), 2022–2034. https://doi.org/10.1021/acs.jpca.6b12086.

(106)   Bilgilisoy, E. Untersuchung von Metallorganischen Precursors Für Elektronen-/Ionen-Induzierte Prozessierung Im UHV, 2022.

(107)   Friedli, V.; Utke, I. Optimized Molecule Supply from Nozzle-Based Gas Injection Systems for Focused Electron- and Ion-Beam Induced Deposition and Etching: Simulation and Experiment. *J. Phys. D. Appl. Phys.* **2009**, *42* (12). https://doi.org/10.1088/0022-3727/42/12/125305.

(108)   Friedli, V.; Utke, I. Optimized Molecule Supply from Nozzle-Based Gas Injection Systems for Focused Electron- and Ion-Beam Induced Deposition and Etching: Simulation and Experiment. *J. Phys. D. Appl. Phys.* **2009**, *42* (12), 125305. https://doi.org/10.1088/0022-3727/42/12/125305.

(109)   Lukasczyk, T. Generation of Pure Iron Nanostructures via Electron-Beam Induced Deposition in UHV. *Vacuum*.

(110)   Marashdeh, A.; Tiesma, T.; van Velzen, N. J. C.; Harder, S.; Havenith, R. W. A.; De Hosson, J. T. M.; van Dorp, W. F. The Rational Design of a Au(I) Precursor for Focused Electron Beam Induced Deposition. *Beilstein J. Nanotechnol.* **2017**, *8* (1), 2753–2765. https://doi.org/10.3762/bjnano.8.274.

(111)   Van Dorp, W. F.; Wu, X.; Mulders, J. J. L.; Harder, S.; Rudolf, P.; De Hosson, J. T. M. Gold Complexes for Focused-Electron-Beam-Induced Deposition. *Langmuir* **2014**, *30* (40), 12097–12105. https://doi.org/10.1021/la502618t.

(112)   Vollnhals, F.; Drost, M.; Tu, F.; Carrasco, E.; Späth, A.; Fink, R. H.; Steinrück, H. P.; Marbach, H. Electron-Beam Induced Deposition and Autocatalytic Decomposition of Co(CO)3NO. *Beilstein J. Nanotechnol.* **2014**, *5* (1), 1175–1185. https://doi.org/10.3762/bjnano.5.129.

(113)   Lukasczyk, T.; Schirmer, M.; Steinrück, H. P.; Marbach, H. Electron-Beam-Induced Deposition in Ultrahigh Vacuum: Lithographic Fabrication of Clean Iron Nanostructures. *Small* **2008**, *4* (6), 841–846. https://doi.org/10.1002/smll.200701095.

(114)   Gavagnin, M.; Wanzenboeck, H. D.; Shawrav, M. M.; Belic, D.; Wachter, S.; Waid, S.; Stoeger-Pollach, M.; Bertagnolli, E. Focused Electron Beam-Induced CVD of Iron: A Practical Guide for Direct Writing. *Chem. Vap. Depos.* **2014**, *20* (7–9), 243–250. https://doi.org/10.1002/cvde.201407118.

(115)   Gazzadi, G. C.; Mulders, J. J. L.; Trompenaars, P.; Ghirri, A.; Rota, A.; Affronte, M.; Frabboni, S. Characterization of a New Cobalt Precursor for Focused Beam Deposition of Magnetic Nanostructures. In *Microelectronic Engineering*; 2011; Vol. 88, pp 1955–1958. https://doi.org/10.1016/j.mee.2010.12.031.

(116)   Gazzadi, G. C.; Mulders, H.; Trompenaars, P.; Ghirri, A.; Affronte, M.; Grillo, V.; Frabboni, S. Focused Electron Beam Deposition of Nanowires from Cobalt Tricarbonyl Nitrosyl (Co(CO)3NO) Precursor. *J. Phys. Chem. C* **2011**, *115* (40), 19606–19611. https://doi.org/10.1021/jp206562h.

(117)   Mulders, J. J. L.; Belova, L. M.; Riazanova, A. Electron Beam Induced Deposition at Elevated Temperatures: Compositional Changes and Purity Improvement. *Nanotechnology* **2011**, *22* (5). https://doi.org/10.1088/0957-4484/22/5/055302.

(118)   Neese, F. Software Update: The ORCA Program System, Version 4.0. *Wiley Interdiscip. Rev. Comput. Mol. Sci.* **2018**, *8* (1). https://doi.org/10.1002/wcms.1327.

(119)   Grimme, S.; Ehrlich, S.; Goerigk, L. Effect of the Damping Function in Dispersion Corrected Density Functional Theory. *J. Comput. Chem.* **2011**, *32* (7), 1456–1465. https://doi.org/https://doi.org/10.1002/jcc.21759.

(120)   Bodi, A.; Kercher, J. P.; Baer, T.; Sztáray, B. On the Parallel Mechanism of the Dissociation of Energy-Selected P(CH 3) 3+ Ions. *J. Phys. Chem. B* **2005**, *109* (17), 8393–8399. https://doi.org/10.1021/jp046353s.

(121)   Mahgoub, A.; Lu, H.; Thorman, R. M.; Preradovic, K.; Jurca, T.; McElwee-White, L.; Fairbrother, H.; Hagen, C. W. Electron Beam-Induced Deposition of Platinum from Pt(CO)2Cl2 and Pt(CO)2Br2. *Beilstein J. Nanotechnol.* **2020**, *11*, 1789–1800. https://doi.org/10.3762/BJNANO.11.161.

(122)   Warneke, J.; Rohdenburg, M.; Zhang, Y.; Orszagh, J.; Vaz, A.; Utke, I.; De Hosson, J. T. M.; van Dorp, W. F.; Swiderek, P. Role of NH3 in the Electron-Induced Reactions of Adsorbed and Solid Cisplatin. *J. Phys. Chem. C* **2016**, *120* (7), 4112–4120. https://doi.org/10.1021/acs.jpcc.5b12184.

(123)   Rohdenburg, M.; Boeckers, H.; Brewer, C. R.; McElwee-White, L.; Swiderek, P. Efficient NH3-Based Process to Remove Chlorine from Electron Beam Deposited Ruthenium Produced from (H3-C3H5)Ru(CO)3Cl. *Sci. Rep.* **2020**, *10* (1), 10901. https://doi.org/10.1038/s41598-020-67803-y.

(124)   Shawrav, M. M.; Taus, P.; Wanzenboeck, H. D.; Schinnerl, M.; Stöger-Pollach, M.; Schwarz, S.; Steiger-Thirsfeld, A.; Bertagnolli, E. Highly Conductive and Pure Gold Nanostructures Grown by Electron Beam Induced Deposition. *Sci. Rep.* **2016**, *6* (September), 1–10. https://doi.org/10.1038/srep34003.

(125)   Paul, M.; Schmidbaur, H. A New Synthesis of Dimethylgold(III) Chloride Using Tetramethyltin. *Zeitschrift fur Naturforsch. - Sect. B J. Chem. Sci.* **1994**, *49* (5), 647–649. https://doi.org/10.1515/znb-1994-0513.

(126)   Kang, R.; Chen, H.; Shaik, S.; Yao, J. Assessment of Theoretical Methods for Complexes of Gold(I) and Gold(III) with Unsaturated Aliphatic Hydrocarbon: Which Density Functional Should We Choose? *J. Chem. Theory Comput.* **2011**, *7* (12), 4002–4011. https://doi.org/10.1021/ct200656p.

(127)   Davis, L. E.; MacDonald, N. C.; P.W., P.; Riach, G. E.; Weber, R. E. *Handbook of Auger Electron Spectroscopy*; Physical Electronics Division, Perkin·Elmer Corporation: Minnesota, USA, 1976.

(128)   Schneider, C. A.; Rasband, W. S.; Eliceiri, K. W. NIH Image to ImageJ: 25 Years of Image Analysis. *Nat. Methods* **2012**, *9* (7), 671–675. https://doi.org/10.1038/nmeth.2089.

(129)   Grzelczak, M.; Pérez-Juste, J.; Mulvaney, P.; Liz-Marzán, L. M. Shape Control in Gold Nanoparticle Synthesis. In *Colloidal Synthesis of Plasmonic Nanometals*; Liz-Marzán, L. M., Ed.; Jenny Stanford Publishing: New York, 2020; p 24. https://doi.org/https://doi.org/10.1201/9780429295188.

(130)   Chen, Y.; Gu, X.; Nie, C.-G.; Jiang, Z.-Y.; Xie, Z.-X.; Lin, C.-J. Shape Controlled Growth of Gold Nanoparticles by a Solution Synthesis. *Chem. Commun.* **2005**, No. 33, 4181–4183. https://doi.org/10.1039/B504911C.

(131)   Georgiev, P.; Bojinova, A.; Kostova, B.; Momekova, D.; Bjornholm, T.; Balashev, K. Implementing Atomic Force Microscopy (AFM) for Studying Kinetics of Gold Nanoparticle's Growth. *Colloids Surfaces A Physicochem. Eng. Asp.* **2013**, *434* (Complete), 154–163. https://doi.org/10.1016/j.colsurfa.2013.05.064.

(132)   Yu, H.; Chen, M.; Rice, P. M.; Wang, S. X.; White, R. L.; Sun, S. Dumbbell-like Bifunctional Au−Fe3O4 Nanoparticles. *Nano Lett.* **2005**, *5* (2), 379–382. https://doi.org/10.1021/nl047955q.

(133)   Belić, D.; Shawrav, M. M.; Gavagnin, M.; Stöger-Pollach, M.; Wanzenboeck, H. D.; Bertagnolli, E. Direct-Write Deposition and Focused-Electron-Beam-Induced Purification of Gold Nanostructures. *ACS Appl. Mater. Interfaces* **2015**, *7* (4), 2467–2479. https://doi.org/10.1021/am507327y.

(134)   Weng, C.-H.; Huang, C.-C.; Yeh, C.-S.; Lei, H.-Y.; Lee, G.-B. Synthesis of Hexagonal Gold Nanoparticles Using a Microfluidic Reaction System*. *J. Micromechanics Microengineering* **2008**, *18* (3), 35019. https://doi.org/10.1088/0960-1317/18/3/035019.

(135)   Wnuk, J. D.; Gorham, J. M.; Rosenberg, S. G.; Madey, T. E.; Hagen, C. W.; Fairbrother, D. H. Atomic Radical Abatement of Organic Impurities from Electron Beam Deposited Metallic Structures. *J. Vac. Sci. Technol. B* **2010**, *28* (3), 527–537. https://doi.org/10.1116/1.3378142.

(136)   Bilgilisoy, E.; Yu, J.-C.; Preischl, C.; McElwee-White, L.; Steinrück, H.-P.; Marbach, H. Nanoscale Ruthenium-Containing Deposits from Ru(CO)4I2 via Simultaneous Focused Electron Beam-Induced Deposition and Etching in Ultrahigh Vacuum: Mask Repair in Extreme Ultraviolet Lithography and Beyond. *ACS Appl. Nano Mater.* **2022**, *5* (3), 3855–3865. https://doi.org/10.1021/acsanm.1c04481.

(137)   Lukasczyk, T.; Schirmer, M.; Steinrück, H.-P.; Marbach, H. Generation of Clean Iron Structures by Electron-Beam-Induced Deposition and Selective Catalytic Decomposition of Iron Pentacarbonyl on Rh(110). *Langmuir* **2009**, *25* (19), 11930–11939. https://doi.org/10.1021/la901612u.

(138)   Engmann, S.; Stano, M.; Papp, P.; Brunger, M. J.; Matejčík, Š.; Ingólfsson, O. Absolute Cross Sections for Dissociative Electron Attachment and Dissociative Ionization of Cobalt Tricarbonyl Nitrosyl in the Energy Range from 0 EV to 140 EV. *J. Chem. Phys.* **2013**, *138* (4), 0–7. https://doi.org/10.1063/1.4776756.

(139)   May, O.; Kubala, D.; Allan, M. Dissociative Electron Attachment to Pt(PF3)4—a Precursor for Focused Electron Beam Induced Processing (FEBIP). *Phys. Chem. Chem. Phys.* **2012**, *14* (9), 2979–2982. https://doi.org/10.1039/C2CP23268E.

(140)   Cipriani, M.; Thorman, R. M.; Brewer, C. R.; McElwee-White, L.; Ingólfsson, O. Dissociative Ionization of the Potential Focused Electron Beam Induced Deposition Precursor π-Allyl Ruthenium(II) Tricarbonyl Bromide, a Combined Theoretical and Experimental Study. *Eur. Phys. J. D* **2019**, *73* (10), 1–7. https://doi.org/10.1140/epjd/e2019-100151-9.

(141)   Thorman, R. M.; Brannaka, J. A.; McElwee-White, L.; Ingólfsson, O. Low Energy Electron-Induced Decomposition of (H3-C3H5)Ru(CO)3Br, a Potential Focused Electron Beam Induced Deposition Precursor with a Heteroleptic Ligand Set. *Phys. Chem. Chem. Phys.* **2017**, *19* (20), 13264–13271. https://doi.org/10.1039/c7cp01696d.

(142)   Rohdenburg, M.; Martinović, P.; Ahlenhoff, K.; Koch, S.; Emmrich, D.; Gölzhäuser, A.; Swiderek, P. Cisplatin as a Potential Platinum Focused Electron Beam Induced Deposition Precursor: NH3 Ligands Enhance the Electron-Induced Removal of Chlorine. *J. Phys. Chem. C* **2019**, *123* (35), 21774–21787. https://doi.org/10.1021/acs.jpcc.9b05756.

(143)   Ferreira Da Silva, F.; Thorman, R. M.; Bjornsson, R.; Lu, H.; Mcelwee-White, L.; Ingólfsson, O. Dissociation of the FEBID Precursor: Cis-Pt(CO)2Cl2 Driven by Low-Energy Electrons. *Phys. Chem. Chem. Phys.* **2020**, *22* (11), 6100–6108. https://doi.org/10.1039/c9cp06633k.

(144)   Spencer, J. A.; Wu, Y.-C.; McElwee-White, L.; Fairbrother, D. H. Electron Induced Surface Reactions of Cis-Pt(CO)2Cl2: A Route to Focused Electron Beam Induced Deposition of Pure Pt Nanostructures. *J. Am. Chem. Soc.* **2016**, *138* (29), 9172–9182. https://doi.org/10.1021/jacs.6b04156.

(145)   Ragesh Kumar, T. P.; Weirich, P.; Hrachowina, L.; Hanefeld, M.; Bjornsson, R.; Hrodmarsson, H. R.; Barth, S.; Howard Fairbrother, D.; Huth, M.; Ingólfsson, O. Electron Interactions with the Heteronuclear Carbonyl Precursor H2FeRu3(CO)13 and Comparison with HFeCo3(CO)12: From Fundamental Gas Phase and Surface Science Studies to Focused Electron Beam Induced Deposition. *Beilstein J. Nanotechnol.* **2018**, *9* (1), 555–579. https://doi.org/10.3762/bjnano.9.53.

(146)   Botman, A.; Mulders, J. J. L.; Weemaes, R.; Mentink, S. Purification of Platinum and Gold Structures after Electron-Beam-Induced Deposition. *Nanotechnology* **2006**, *17* (15), 3779–3785. https://doi.org/10.1088/0957-4484/17/15/028.

(147)   Frabboni, S.; Gazzadi, G. C.; Spessot, A. TEM Study of Annealed Pt Nanostructures Grown by Electron Beam-Induced Deposition. *Phys. E Low-dimensional Syst. Nanostructures* **2007**, *37* (1), 265–269. https://doi.org/https://doi.org/10.1016/j.physe.2006.06.018.

(148)   Spencer, J. A.; Barclay, M.; Gallagher, M. J.; Winkler, R.; Unlu, I.; Wu, Y. C.; Plank, H.; McElwee-White, L.; Fairbrother, D. H. Comparing Postdeposition Reactions of Electrons and Radicals with Pt Nanostructures Created by Focused Electron Beam Induced Deposition. *Beilstein J. Nanotechnol.* **2017**, *8* (1), 2410–2424. https://doi.org/10.3762/bjnano.8.240.

(149)   Grimme, S.; Huenerbein, R.; Ehrlich, S. On the Importance of the Dispersion Energy for the Thermodynamic Stability of Molecules. *ChemPhysChem* **2011**, *12* (7), 1258–1261. https://doi.org/10.1002/cphc.201100127.

(150)   Engmann, S.; Stano, M.; Matejčík, Š.; Ingólfsson, O. The Role of Dissociative Electron Attachment in Focused Electron Beam Induced Processing: A Case Study on Cobalt Tricarbonyl Nitrosyl. *Angew. Chemie - Int. Ed.* **2011**, *50* (40), 9475–9477. https://doi.org/10.1002/anie.201103234.

(151)   Shih, P. Y.; Tafrishi, R.; Cipriani, M.; Hermanns, C. F.; Oster, J.; Gölzhäuser, A.; Edinger, K.; Ingólfsson, O. Dissociative Ionization and Electron Beam Induced Deposition of Tetrakis(Dimethylamino)Silane, a Precursor for Silicon Nitride Deposition. *Phys. Chem. Chem. Phys.* **2022**, *24* (16), 9564–9575. https://doi.org/10.1039/d2cp00257d.

(152)   Spencer, J. A.; Brannaka, J. A.; Barclay, M.; McElwee-White, L.; Fairbrother, D. H. Electron-Induced Surface Reactions of H3-Allyl Ruthenium Tricarbonyl Bromide [(H3-C3H5)Ru(CO)3Br]: Contrasting the Behavior of Different Ligands. *J. Phys. Chem. C* **2015**, *119* (27), 15349–15359. https://doi.org/10.1021/acs.jpcc.5b03775.

(153)   Chemcraft - graphical software for visualization of quantum chemistry computations. https://www.chemcraftprog.com. No Title.

(154)   Klar, D.; Ruf, M.-W.; Hotop, H. Dissociative Electron Attachment to CCl4 Molecules at Low Electron Energies with MeV Resolution11Dedicated to Professor Aleksandar Stamatovic on the Occasion of His 60th Birthday. *Int. J. Mass Spectrom.* **2001**, *205* (1), 93–110. https://doi.org/https://doi.org/10.1016/S1387-3806(00)00271-2.

Paper I

On the electron-induced reactions of $(CH_3)AuP(CH_3)_3$: A combined UHV surface science and gas-phase study

Ali Kamali [1], Elif Bilgilisoy [2], Alexander Wolfram [2], Thomas Gentner [3], Gerd Ballmann [3], Sjoerd Harder [3], Hubertus Marbach [2,*], Oddur Ingólfsson [1,*]

Ali Kamali carried out the gas-phase experiment using HV equipment, performed quantum chemical calculations, contributed to the UHV FEBID deposition and AES analysis, and wrote the manuscript in collaboration with Dr. Elif Bilgilisoy.

Article

On the Electron-Induced Reactions of (CH₃)AuP(CH₃)₃: A Combined UHV Surface Science and Gas-Phase Study

Ali Kamali [1,†] , Elif Bilgilisoy [2,†] , Alexander Wolfram [2] , Thomas Xaver Gentner [3], Gerd Ballmann [3], Sjoerd Harder [3], Hubertus Marbach [2,4,*] and Oddur Ingólfsson [1,*]

[1] Department of Chemistry and Science Institute, University of Iceland, Dunhagi 3, 107 Reykjavik, Iceland
[2] Physikalische Chemie II, Friedrich-Alexander Universität Erlangen-Nürnberg, 91058 Erlangen, Germany
[3] Inorganic and Organometallic Chemistry, Universität Erlangen-Nürnberg, 91058 Erlangen, Germany
[4] Carl Zeiss SMT GmbH, 64380 Roßdorf, Germany
[*] Correspondence: hubertus.marbach@fau.de (H.M.); odduring@hi.is (O.I.)
[†] These authors contributed equally to this work.

Abstract: Focused-electron-beam-induced deposition (FEBID) is a powerful nanopatterning technique where electrons trigger the local dissociation of precursor molecules, leaving a deposit of non-volatile dissociation products. The fabrication of high-purity gold deposits via FEBID has significant potential to expand the scope of this method. For this, gold precursors that are stable under ambient conditions but fragment selectively under electron exposure are essential. Here, we investigated the potential gold precursor (CH₃)AuP(CH₃)₃ using FEBID under ultra-high vacuum (UHV) and spectroscopic characterization of the corresponding metal-containing deposits. For a detailed insight into electron-induced fragmentation, the deposit's composition was compared with the fragmentation pathways of this compound through dissociative ionization (DI) under single-collision conditions using quantum chemical calculations to aid the interpretation of these data. Further comparison was made with a previous high-vacuum (HV) FEBID study of this precursor. The average loss of about 2 carbon and 0.8 phosphor per incident was found in DI, which agreed well with the carbon content of the UHV FEBID deposits. However, the UHV deposits were found to be as good as free of phosphor, indicating that the trimethyl phosphate is a good leaving group. Differently, the HV FEBID experiments showed significant phosphor content in the deposits.

Keywords: focused-electron-beam-induced deposition (FEBID); dissociative ionization; ultra-high vacuum; gold deposits; Auger electron spectroscopy (AES); HV gas-phase study; quantum chemical calculation; low-energy electrons; electron-induced mechanism

1. Introduction

The need for ever-smaller and precisely manufactured nanostructures in fields such as plasmonics [1], the semiconductor industry [2,3], and in nanoelectronics [4] is one of the drivers in the current development of new and emerging nanofabrication techniques. Focused-electron-beam-induced deposition (FEBID) has high potential in this regard since it is capable of creating nanostructures with precise shapes and position control on basically any substrate. In FEBID, a highly focused electron beam of a scanning electron microscope, in ultra-high vacuum (UHV) or high vacuum (HV), is utilized to induce the fragmentation of adsorbed precursor molecules. The desired structures are built up from non-volatile fragments, while the volatile ones are pumped away [5–7].

Controlled localized electron exposure enables the lithographic patterning of practically any shape through direct-write, maskless, and resist-free material deposition. Furthermore, such deposition may be realized on both planar (e.g., Si, SiO₂) and non-planar substrates (e.g., cantilevers) [7]. FEBID is not only of interest in fundamental research but also in industrial applications [8]. The ability to repair UV and EUV lithography masks [8–10], the generation of magnetic nanostructures for magnetic logic circuits [11],

and tip fabrication on cantilevers for scanning probe microscopy [7,12–14] are examples of industrially relevant applications.

One major challenge in FEBID is that deposits created from organometallic precursors are rarely exclusively composed of the targeted metal (i.e., 100 at.% metal purity). This limits the range of applications for nanostructures created via FEBID [1,15,16]. The purity of the deposition depends strongly on the utilized precursor and the writing parameters such as primary beam energy/current, beam diameter, and replenishment time [17]. It has been shown that it is possible to obtain almost pure iron [18] structures from $Fe(CO)_5$ (>95 at.%) or tungsten [19] from WF_6 (>97 at.%). For gold, however, which has gained high interest, especially in the field of plasmonics [1,20,21], it has been challenging to find a suitable precursor [22–25]. The most successful gold-based precursors reported in the literature are ClAuCO and $ClAuPF_3$ [26,27]. In these studies, it is reported that using these two Au-based precursors, it is possible to obtain pure gold structures on standard SiO_2 substrates by varying the writing parameters (i.e., primary beam energy, beam current, or dwell time). However, these precursors are difficult to handle due to their pronounced air and water sensitivity and thermal instability. The most investigated precursors for FEBID of gold in the literature are dimethyl gold acetylacetonate [$(Me)_2Au(acac)$] [28] and its fluorinated derivatives, dimethyl gold trifluoroacetylacetonate [$(Me)_2Au(tfac)$] [29,30] and dimethyl gold hexafluoroacetylacetonate [$(Me)_2Au(hfac)$] [31]. The corresponding deposits consist of gold cores embedded in a carbonaceous matrix [32]. The co-injection of water as an oxidative enhancer, on the other hand, has been shown to lead to pure gold structures from $(Me)_2Au(tfac)$ as a precursor [33]. Nonetheless, it would be more convenient to have stable, high-vapor pressure precursors, yielding high-purity deposits in one step, rendering the use of additional purification methods unnecessary.

The electron-induced decomposition mechanisms of FEBID-relevant precursor molecules have been investigated in combined gas-phase and surface science studies [17,34–36]. The corresponding results suggest that deposition is mainly initiated by reactions between precursor molecules and low-energy electrons [35,36]. In FEBID, these low-energy electrons are secondary electrons resulting from the interaction of the primary electron beam with the substrate. In general, the electron-induced dissociation of precursor molecules can proceed through four different processes [37]: dissociative electron attachment (DEA), dissociative ionization (DI), neutral dissociation (ND), and dipolar dissociation (DD).

In dissociative ionization [37,38], the focus of the gas-phase section of the current study, electrons with energies equal to or larger than the ionization energy impinge on the parent molecules, leading to their ionization. As a result, the parent ion may undergo dissociation, yielding positively charged and neutral fragments. The DI process can be represented by Equation (1):

$$AB + e^- \rightarrow AB^{+*} + 2e^- \rightarrow A^+ + B^{\cdot} + 2e^- \tag{1}$$
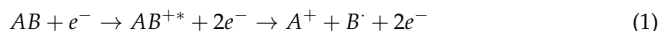
where "*" denotes that the fragments may be in vibrationally and/or electronically excited states. The DI process is a direct, non-resonant scattering process with an interaction time in the order of ~10^{-16} s and starts at or above the ionization energy of a parent molecule (~6–8 eV). The thermochemical threshold for the formation of cations in dissociative ionization can have effects on the extent of fragmentation and, in the simplified case of a diatomic molecule, it can be formulated as:

$$E_{th}(A^+) = BDE(AB) + IE(A) \tag{2}$$

where $BDE(AB)$ is the bond dissociation energy of AB, and $IE(A)$ is the ionization energy of the fragment A. For more complex fragmentation processes of polyatomic molecules, where multiple bonds may be broken and new bonds may be formed, the threshold energy E_{th} for the formation of a given fragment is:

$$E_{th} = \sum BDE_{broken} - \sum BDE_{formed} + IE_{(fragment)} \tag{3}$$

Here, BDE_{broken} and BDE_{formed} are the bond dissociation energies of the bonds broken and the bonds formed in the process, respectively, and $IE_{(fragment)}$ is the ionization energy of the neutral parent fragment of the cationic fragment observed.

In general, the total dissociation cross-section for a given DI process shows a smooth increase with increasing electron energy and a maximum at around 50–100 eV. At higher energies, the interaction time of the electron with the molecule decreases, and consequently, the total DI cross-section decreases [37]. It has been demonstrated that DI is effective for many FEBID precursors (see, e.g., [39–41]) and may thus play a significant role in the deposition process.

The current study investigated the production of Au structures with relatively high metallic content from $(CH_3)AuP(CH_3)_3$ as a precursor using an SEM setup in UHV. This was carried out in combination with a corresponding gas-phase DI study with the same precursor, yielding important insights into fundamental aspects of the FEBID process. A previous FEBID study on this precursor under HV conditions led to promising results with 19–25 at.% Au from $(CH_3)AuP(CH_3)_3$ [25]. The use of an ultra-high vacuum (UHV) setup is suitable to reduce unwanted deposits from residual gases and thus reduce contamination effects in the FEBID structures. Therefore, the UHV approach was expected to enable better controlled deposition. This has been demonstrated previously for the precursors $Fe(CO)_5$ and $Co(CO)_3NO$. Under UHV, these precursors yielded metallic contents higher than 90 at.% and 80 at.%, respectively [18,42]. These values were compared to HV studies which yielded up to 70–85 at.% Fe [7,43] and 40–50 at.% Co [44–46] from these precursors, respectively. Therefore, we aimed to test and perform FEBID with this gold precursor, using a UHV-SEM setup with the combination of mass spectrometry (MS) and local Auger electron spectroscopy (AES). To provide a deeper understanding of the underlying electron-induced reaction pathway(s) in the deposition, DI of $(CH_3)AuP(CH_3)_3$ was also studied in the gas phase under single-collision conditions. Quantum chemical calculations of the threshold energies for selected ion fragments observed in DI were also presented and compared to the respective experimental appearance energies to identify the most probable fragmentation pathways.

2. Materials and Methods

Precursor synthesis. Methylgold(I) trimethylphosphine ($(CH_3)AuP(CH_3)_3$) was synthesized by following the steps as described in the literature [47]. The synthesis was performed under nitrogen atmosphere, using pre-dried solvents and standard Schlenk techniques. The starting material was $H[AuCl_4]\cdot3H_2O$, which was obtained in the form of orange crystals by dissolving gold metal in aqua regia, evaporating all liquids, adding concentrated HCl, and evaporating all liquids again. The quality of the compound was checked and confirmed via ^1H and ^{31}P NMR spectroscopy and via elemental analysis (C, H, and N values showed a maximum deviation of 0.5%).

Precursor handling. The $(CH_3)AuP(CH_3)_3$ precursor was kept at 253 K in a refrigerator inside a glove box ($O_2 < 0.1$ ppm) and later filled into a stainless-steel precursor storage holder at room temperature under nitrogen atmosphere in the glove box. The precursor holder had a small glass window to enable the precursor quality to be checked visually. The filled storage holder was wrapped in aluminum foil to avoid photodecomposition during the experiments and attached to the analysis chamber.

Deposition. FEBID structures were fabricated in a modified commercial UHV system (Scienta Omicron GmbH, Taunusstein, Germany) with a base pressure of $p < 2 \times 10^{-10}$ mbar. For the mass spectrometry (MS) of the $(CH_3)AuP(CH_3)_3$ precursor in the gas phase, a quadrupole mass spectrometer (Prisma QMS 200 M, Pfeiffer Vacuum GmbH, Aßlar, Germany) that was mounted to the UHV chamber was used, and the precursor was sublimed into the chamber at room temperature (298 K). The system included a UHV-compatible scanning electron microscopy (SEM) column (Leo Gemini, nominal resolution better than 3 nm); the latter was also used for FEBID. In addition, a hemispherical electron energy analyzer (EA125, Scienta Omicron GmbH, Taunusstein, Germany) enabled local Auger

electron spectroscopy (AES). The electron beam settings during FEBID were a primary electron beam energy of 5 keV and a beam current of 3 nA. The lithographic processes were controlled through custom-developed software based on LabVIEW 8.6 (National Instruments, Austin, TX, USA) and a high-speed DAC PCIe-card (M2i.6021-exp, Spectrum Elektrotechnik GmbH, München, Germany) [48]. The lithographic processes were performed with a step size of 6.2 nm and a sweep number of 100. SEM images were acquired at a beam energy of 15 keV and a current of 400 pA with SmartSEM (Zeiss, Oberkochen, Germany). Minor contrast and brightness adjustments were applied. A commercially available SiO_2 (230 nm)/Si (111) substrate was used as delivered to create FEBID structures.

The precursor gas was allowed to effuse into the system through a nozzle in close proximity to the sample surface. Based on simulations using GIS Simulator (version 1.5) [49], the local pressure increase at the sample surface was estimated to be a factor of 30, and the chamber pressure was kept at 1.3×10^{-7} mbar, which corresponded to a local pressure of $\sim 4.0 \times 10^{-6}$ mbar at the substrate's surface.

Gas-Phase Study. The DI experiments were carried out with a crossed electron/molecular beam apparatus that has been described in detail elsewhere [50], and only a brief description is given here. Electrons were emitted from a tungsten filament and guided with a stack of electrical lenses through a trochoidal electron monochromator to generate a quasi-monoenergetic electron beam. The full width at half maximum (FWHM) of the electron energy spread was about 140 meV during the experiments. The temperature of the monochromator was kept at 393 K with two halogen lamps to avoid the condensation of precursor molecules or background contaminations on its electronic lens components. In the interaction section of the instrument, the electron beam crossed a molecular beam of $(CH_3)AuP(CH_3)_3$, generated by sublimation at room temperature (298 K) through an effusion stainless-steel capillary inlet. The background pressure in the chamber was in the order of 2–3×10^{-8} mbar, and the working pressure was in the range of 7–9×10^{-7} mbar. Ionic fragments formed, as a result of the collision of the electrons with the precursor molecules, were extracted into a quadrupole mass spectrometer (EPIC 1000, Hiden Analytical Warrington, UK) and analyzed and detected with a channelton electron multiplier. Mass spectra were recorded at fixed electron energy by scanning through the relevant m/z range, and ion yield curves were recorded at fixed m/z by scanning through the relevant electron energy range. The positive ion yields were normalized relative to the cross-section of the formation of Ar^+ from Ar at 50 eV recorded after all fragment ion measurements [51]. The appearance energies for positive ion fragments were evaluated by fitting a Wannier-type model function to the onset region of the respective ion yields, as has been described in detail [52], and the energy scale was calibrated with reference to the first ionization energy of Ar [51].

Quantum chemical calculations. The current calculations were carried out with the ab initio quantum chemistry program package ORCA, version 4.1 [53]. Geometry optimizations were carried out at the density functional level of theory (DFT) using the meta-generalized gradient approximation (meta-GGA) TPSS functional and the valence triple-zeta polarization basis set def2-TZVP. The D3(BJ) dispersion correction by Grimme et al. was included in the calculations [54]. For closed-shell systems, the restricted Kohn–Sham (RKS) formalism was used, and the unrestricted Kohn–Sham (UKS) formalism was used for open-shell systems. The geometry optimizations were conducted with tight SCF settings, and the single-point energies, at the TPSS/def2-TZVP level of theory, were calculations with normal SCF settings. The TPSS/def2-TZVP approach was chosen based on studies conducted by Kepp [55] and Goel et al. [56], where they found the TPSS/def2-TZVP level of theory to give more reliable bond energies and structures of gold clusters compared to other functionals such as B3LYP, M06, and PBE0. Positive values of harmonic vibrational frequencies were confirmed at the same level of theory and were used to derive zero-point energies and thermal energy corrections at 298 K for the neutral parent molecule and all fragments. Additionally, single-point energies of the optimized geometries were calculated at the coupled cluster level of theory. The coupled cluster calculations were

performed using domain-based local pair natural orbitals with single, double, and perturbative triple excitations, DLPNO-CCSD(T) [57–59]. These calculations were carried out with normal PNO settings and the valence quadruple-zeta basis set QZVPP, with two sets of polarization functions.

The threshold energy for each fragment was calculated from the single-point energies of the relaxed structures, both at the DFT and DLPNO-CCSD(T) level of theory. This was conducted by subtracting the total energy of all fragments formed in the respective processes from the total energy of the parent molecule. The respective ZPVEs and thermal energy corrections were included in all cases.

3. Results and Discussion

3.1. UHV-FEBID Study

3.1.1. Promotion of the Intact Precursor into the Gas Phase and Its Stability

To characterize the precursor prior to the FEBID experiment, $(CH_3)AuP(CH_3)_3$ was dosed into the UHV chamber via the gas-injection system (GIS) and monitored with a mass spectrometer. Figure 1 depicts a positive ion mass spectrum recorded under FEBID conditions, i.e., at a chamber background pressure of 1.3×10^{-7} mbar. Below m/z 40, the mass spectrum exhibited contributions of CH_n and C_2H_n with an admix of nitrogen- and oxygen-containing fragments. The significant contribution at and around m/z 28 may in part have been derived from ethane as a decomposition product, and for comparison, the relative intensities from the NIST DI spectra of ethane are shown as green triangles in Figure 1. The relative intensities around m/z 28 agreed well with the respective DI products from ethane, considering that m/z 28 may have drawn additional intensity from nitrogen originating from the precursor filling process (see the Experimental Section).
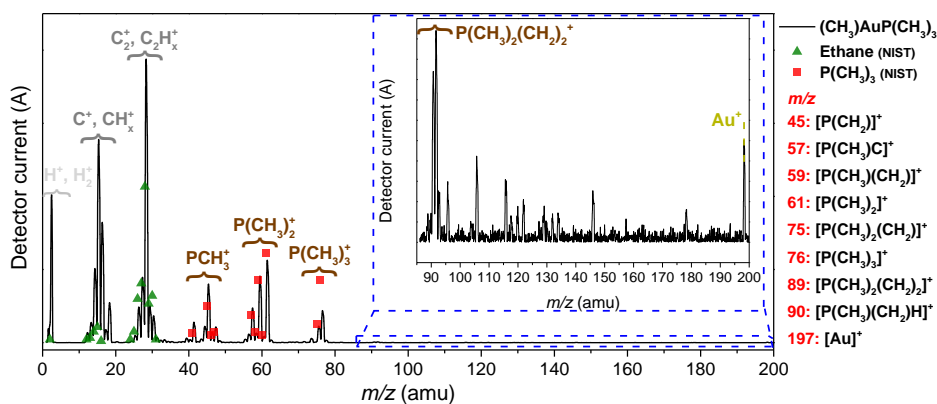
Figure 1. Mass spectrum of $(CH_3)AuP(CH_3)_3$, recorded at room temperature and a precursor pressure of 1.3×10^{-7} mbar (black line). The reference spectrum for trimethylphosphine $(P(CH_3)_3)$ from the NIST database is shown as red squares, and that for ethane as green triangles. A $60\times$ magnified region from m/z 85 to 200 is shown in the inset within the blue dashed lines. The observed precursor-related fragments, along with their m/z, are listed at the right-side of the graph.

This was consistent with the proposed ethane formation in the thermal decomposition of $(CH_3)AuP(CH_3)_3$ [60] and upon its decomposition on active surfaces. However, as the CH_n^+ intensities around m/z 15 were considerably higher than what was to be expected from DI of ethane, we considered these contributions to stem mainly from direct CH_n^+ loss from the precursor. Furthermore, both the contributions around m/z 28 and m/z 15 most likely contained admixtures of residual gases. In good agreement with the NIST electron impact mass spectra of trimethylphosphine [61] (Figure 1, red-colored squares), clear contributions from the trimethylphosphine group were present in the mass spectrum. These were at m/z 45 (PCH_2^+), m/z 57, 59, and 61 (reflecting $P(CH_3)_2$ along with the loss of

one and two hydrogens) as well as at m/z 75 and 76 (reflecting $P(CH_3)_3$ along with the loss of one hydrogen). Additionally, Au^+ (m/z 197) was clearly observable in the mass spectrum, indicating the promotion of the intact precursor into the gas phase at room temperature. This was confirmed in the gas-phase experiments discussed in the DI section. With reference to m/z 61, the DI peak ratios for the m/z ratios of 61, 75, 76, and 197 (Au^+) reported in the literature [47] were 100:33:74:1. The corresponding relative intensity reported for the parent ion ([$(CH_3)AuP(CH_3)_3$]$^+$, m/z 288) and the parent after the loss of one methyl group ([$AuP(CH_3)_3$]$^+$, m/z 273) were found to be about 30 and 200, respectively. This was a clear sign of a significant presence of the intact precursor in the gas phase in this experiment. Similarly, from the peak heights of the mass spectrum shown in Figure 1, we derived the relative intensity ratios 100:20:39:0.4 for these fragments (m/z 61:75:76:197). The literature data cited here were recorded with a sector field mass spectrometer, while the current mass spectra from the UHV chamber were recorded with a quadrupole with the higher m/z limit 200; notably, the transmission properties of these instruments were very different. Further, Au^+, m/z 197, was at the m/z limit of this quadrupole, where the transmission efficiency was comparatively low and the parent cation, [$(CH_3)AuP(CH_3)_3$]$^+$, m/z 288 was outside its m/z range. Considering this, the relative intensities of the m/z ratios observed were in good agreement. The relatively high contribution of the parent ion and the parent ion after the loss of one methyl group in the sector field experiments [47] confirmed the delivery of the intact precursor molecule into the gas phase in this experiment. From the comparison of the intensity ratios, we anticipated that that was also the case in the current experiment. This was further supported by the deposition and gas-phase DI experiments discussed below. With respect to volatility and stability, $(CH_3)AuP(CH_3)_3$ at room temperature was found to be sufficiently volatile to sublime and establish a chamber background pressure of 1.3×10^{-7} mbar (equivalent to ~4.0×10^{-6} mbar at the surface; see Experimental Section). Compared to earlier FEBID studies with this setup [18,42], using other precursors, this chamber pressure was low (1.3×10^{-7} mbar, this study, vs. 3.0×10^{-7} mbar, earlier FEBID studies). However, as is discussed in the deposition section, it was found to be sufficient to create the respective deposits. No change in color or in other aspects of appearance of the precursor was visible in the container of the GIS after one week of operation at room temperature, though the gold content of the deposits was found to drop already after three days (Figure S1a,e). The gold content of the deposits could be re-established by increasing the sublimation temperature to 313 K while maintaining the same chamber pressure of 1.3×10^{-7} mbar. However, a further increase in the sublimation temperature to 323 K resulted in a significant drop in the gold content of the deposits, and degradation was visible upon inspection after these experiments. Moreover, directly after the heating process, the precursor color was changed from shiny-white to pink/black, which we attributed to the thermal decomposition of the precursor (Figure S1b,c). The autocatalytic decomposition of $(CH_3)AuP(CH_3)_3$ on active metal surfaces such as copper has been reported to take place already at room temperature [60] and may have played a role in the current setup, where copper sealings were used in the GIS. In fact, the contact surface of these copper sealings was found to be clearly discolored and darkened when the degradation of the precursor was observed (Figure S1d). It is thus clear that this precursor is sufficiently volatile for FEBID, but the temperature window is narrow, and potentially, the material composition of the gas inlet system plays a role in the decomposition process. Further ex situ stability testing and vacuum thermogravimetry would be valuable in establishing these parameters.

3.1.2. FEBID

In the first step, focused-electron-beam-induced deposition experiments were performed on a commercially available SiO_2 (230 nm)/Si (111) substrate kept at room temperature. Banaszak et al. [62] reported that a thin (40 Å) silicon oxide surface on Si (111) leads to the spontaneous deposition of gold on surface defect sites at 298 K with $(CH_3)AuP(CH_3)_3$ as a precursor in chemical vapor deposition (CVD) experiments in UHV. In the same study, however, the authors demonstrated that a thicker silicon dioxide film of 5000 Å is

not reactive towards the decomposition of $(CH_3)AuP(CH_3)_3$ at room temperature. It can thus be concluded that a silicon surface with a too-thin silicon oxide layer can be reactive towards the $(CH_3)AuP(CH_3)_3$ precursor, while thicker layers are inert. Accordingly, the wafer used in the study at hand was selected with a 230 nm silicon oxide layer, which we expected to be inert with respect to the surface-promoted decomposition of the precursor at room temperature. Aligned with the pre-testing, the $(CH_3)AuP(CH_3)_3$ precursor was sublimed into the chamber from the sample container at room temperature. The corresponding precursor dosage was adjusted for deposition such that a chamber pressure of 1.3×10^{-7} mbar was set (local pressure at the sample: ~4.0×10^{-6} mbar; see Experimental Section). The chamber pressure was about half the pressure compared to previous FEBID studies performed in the same UHV setup [18,42,63,64]. The relatively low pressure was due to the low volatility of the precursor compared to the well-studied $Fe(CO)_5$ and $Co(CO)_3NO$ precursors [18,42], and correspondingly, a lower deposition rate was expected. It is worth mentioning that due to the thermal instability of the compound, discussed in the previous section, no external heating was applied to the precursor container to increase the vapor pressure. To compensate for the low precursor pressure, a relatively low SEM acceleration voltage of 5 keV was selected to increase the secondary electron yield for the deposition of $(CH_3)AuP(CH_3)_3$. Using this acceleration voltage, 4×4 μm^2 squares were written using a comparably high beam current of 3 nA. The fabricated FEBID structures were examined with SEM and AES. Figure 2a,b depict SEM images of the FEBID deposits fabricated with electron area exposures of 4.68 and 7.80 C/cm^2, respectively. Auger spectra were acquired with an acceleration voltage of 15 kV and a beam current of 3 nA. The centers of these rectangles, where the AES spectra were recorded, are marked by green- and blue-colored stars in the corresponding SEM images (Figure 2a and 2b, respectively), and the AES spectra acquired of the bare substrate and the deposited structures are shown in Figure 2c. From the pristine SiO_2 surface as a reference (black spectrum), only two main AES elements are visible, oxygen and carbon. The low-intensity peak at 272 eV was attributed to C_{KLL} Auger transitions of carbon [65], and the dominating peaks at 468, 483, and 503 eV were assigned to O_{KLL} Auger transitions of SiO_2 [66]. After deposition with a 4.68 C/cm^2 electron dose, the O_{KLL} Auger transitions of SiO_2 vanished, and AES signals appeared at kinetic energies of 69, 120, and 265 eV. These were assigned to Au_{NOO}, P_{LMM}, and C_{KLL} Auger transitions [66], respectively (Figure 2c, green and blue spectra).
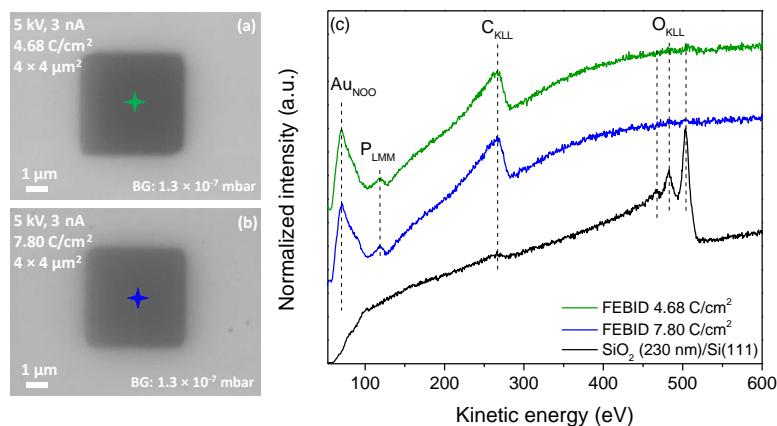
Figure 2. (**a**) SEM image of a 4×4 μm^2 FEBID structure deposited on SiO_2 from $(CH_3)AuP(CH_3)_3$ with an electron dose of 4.68 C/cm^2 and (**b**) with an electron dose of 7.80 C/cm^2. In both cases, the electron beam parameters are 5 keV and 3 nA, and (**c**) AES of the SiO_2 substrate prior to deposition (black line) and AES from FEBID structures (green and blue lines). The colored stars in (**a**,**b**) indicate the position where the spectra were acquired.

The elemental compositions of the FEBID structures were calculated according to the relative sensitivity factors (*S*) of characteristic AES peaks for each element. To obtain the elemental composition from AES, the following equation was used:

$$C_x = \frac{I_x}{S_x d_x} / \sum_i \left(\frac{I_i}{S_i d_i} \right) \tag{4}$$

where *C* is the atomic concentration, *I* is the integrated spectral intensity, *d* is a scaling factor, and *S* is the relative sensitivity factor [66]. The subscript *x* denotes all values corresponding to the investigated peak, whereas the subscript *i* "counts" through every peak in the spectrum. In the work at hand, peak areas were only compared within one spectrum. As a result, the scaling factor *d*, which was introduced to compensate for errors caused by the different intensity in two different Auger spectra, stayed constant for every peak and could be neglected. The integrated spectral peaks after linear baseline correction of the spectra were used for quantitative evaluation. The atomic concentrations for the FEBID structures shown in Figure 2 were calculated using Equation (4) and the relative sensitivity factors (*S*) [67]; 0.21 for Au_{NOO} at 69 eV, 0.30 for P_{LMM} at 120 eV, and 0.08 for C_{KLL} at 272 eV. These were found to be 31 at.% Au, 67 at.% C, and 2 at.% P (green spectrum), and 34 at.% Au, 65 at.% C and 1 at.% P (blue spectrum).

In previous FEBID studies of the same precursor, $CH_3AuP(CH_3)_3$, in HV [22,25], the deposit's composition was determined via EDX spectroscopy and found to be 19–25 at.% Au, 54–62 at.% C, 12–16 at.% P, and 2−7 at.% O. The underlying reaction path determining this composition was suggested to be the removal of one single methyl ligand. Clearly, more significant gold content was observed in the UHV deposits compared to those made in HV. However, in the structures deposited from the $CH_3AuP(CH_3)_3$ compound in UHV, unexpectedly, more significant carbon content and significantly lower phosphorus content were also observed. However, we note that caution should be taken when comparing the composition of the deposits in the HV study and the current UHV, as EDX is much less surface-sensitive than the here-applied AES. With this information, one might also speculate that the distribution of carbon in the UHV-FEBID structure is not even within the deposit but is enhanced in the surface region.

From the results of this study, however, the very low phosphorus content indicated the efficient removal of the trimethylphosphine ligand during the deposition, while the predominant removal of a single methyl group was more consistent with the HV-FEBID results. In fact, judging from the close to 1:2 Au:C composition of the current deposits, a dimethylphosphine group was dissociated from the precursor and pumped away from the chamber. This may have proceeded through the further decomposition and co-deposition of carbon from dissociating trimethylphosphine ligands or in a concerted electron-induced rearrangement reaction such as:

$$(CH_3)AuP(CH_3)_3 \xrightarrow{e^-} Au(CH_3)_2 + P(CH_3)_2 \uparrow \tag{5}$$
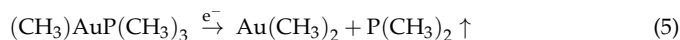
where $Au(CH_3)_2$ is the deposited species, and $P(CH_3)_2$ is the volatile part that is pumped away (note that the charge location is not considered here).

In FEBID, the deposit's composition results from the interaction of the precursor molecules with the primary electrons, back scattered electrons, and secondary electrons [7,34,68,69]. Hence, in FEBID experiments, the precursor molecules are subject to interaction with a broad energy range of electrons, from close to 0 eV up to the energy of the primary electrons. Thus, little information on individual fragmentation pathways can be gained from these experiments alone. To further explore these findings, we conducted a comprehensive gas-phase study in which we determined the average carbon and phosphor loss per DI incident and compared these with the current deposit compositions and those in the earlier HV FEBID study by Dorp et al. [25]. In addition, we determined the appearance energies for the dominating fragments and compared these with threshold calculations to identify the most probable processes behind individual fragment formation.

3.2. HV Gas-Phase Study

Dissociative Ionization in the Gas Phase

Figure 3 shows a positive ion, electron impact mass spectrum of $(CH_3)AuP(CH_3)_3$ in the m/z range from about 10 to 300. The spectrum was recorded at a 7×10^{-7} mbar target gas pressure and 50 eV incident electron energy. The mass spectrum was characterized by two progressions. The first was that of the decomposition of the trimethylphosphine ligand, with the most significant contributions at the m/z ratios of 45 (PCH_2^+), 59 $P(CH_3)CH_2^+$, 61 $P(CH_3)_2^+$, 75 ($P(CH_3)_2CH_2^+$), and 76 ($HP(CH_3)_2CH_2^+$). The second progression was that of CH_3 loss from the parent molecule, reflected in the m/z ratios of 273, 258, 243, and 228. These were assigned to the loss of methyl ligand(s) resulting in the formation of $[AuP(CH_3)_3]^+$, $[AuP(CH_3)_2]^+$, $[AuP(CH_3)]^+$, and $[AuP]^+$. Hence, the two main DI reaction pathways were methyl ligand(s) loss with charge retention on the gold holding fragment, dominated by the loss of a single methyl ligand (m/z 273), and the dissociation of the charge retaining trimethylphosphine ligand from the gold and its further fragmentation through methyl and hydrogen loss.
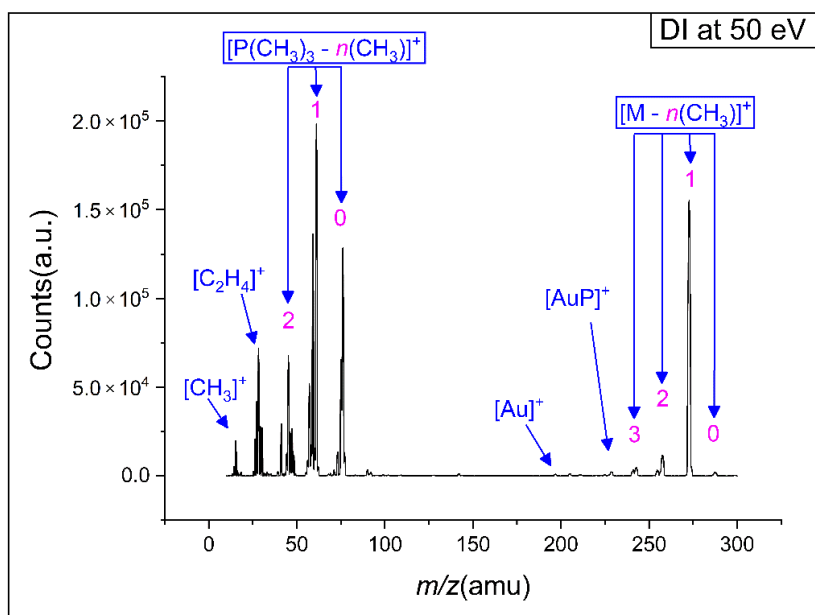
Figure 3. Positive ion mass spectrum of dissociative ionization to $(CH_3)AuP(CH_3)_3$ precursor at 50 eV incident electron energy.

As discussed in the study by Marashdeh et al. [22], the $(CH_3)AuP(CH_3)_3$ precursor is a good candidate for FEBID and CVD due to its comparably good stability at room temperature and volatility under high vacuum. These characteristics stem from the asymmetric crystal structure of $(CH_3)AuP(CH_3)_3$, which consists of six molecules in a unit cell, in which four molecules have strong aurophilic interactions, while the remaining two molecules are monomeric [22]. Consequently, some of the loosely bound molecules desorb from the crystal under high vacuum. The crystal structure degrades in this process and the now "freed" molecules can go into the gas phase [22,25]. This was reflected in the current gas-phase experiments, in which the intact precursor molecules were readily transported to the chamber at room temperature, as was clear from the significant contribution of the molecular ion after the loss of one methyl group (m/z 273).

Figure 4 shows the onset region of the ion yield curves of the most pronounced cations observed in DI of $(CH_3)AuP(CH_3)_3$. The onset region is shown for the ion yield curves of

the intact cation at m/z 288 and the loss of one methyl group at m/z 273 ($[AuP(CH_3)_3]^+$) as well as the $P(CH_3)_3$ rooted fragments: m/z 76 ($[P(CH_3)_3]^+$), 75 ($[P(CH_3)_2(CH_2)]^+$), 61 ($[HP(CH_3)(CH_2)]^+$), 59 ($[P(CH_2)_2]^+$), and 45 ($[PCH_2]^+$). The optimized ionic structures are also shown in the respective graphs. Further, the appearance energies (AEs) and their confidence limits are shown in the individual graphs, along with the respective Wannier-type fits used to determine these energies. The AEs are determined from the average of 3–4 independent measurements and the confidence limits reported are the standard deviations of the mean, rounded to the next 100 meV. In Table 1, the appearance energies are compared to the thermally corrected threshold energies for the respective processes calculated at the TPSS/def2-TZVP and DLPNO-CCSD(T)/QZVPP levels of theory.

For the appearance energy of the molecular cation, i.e., the ionization energy of $(CH_3)AuP(CH_3)_3$, we determined an experimental value of 7.5 ± 0.2 eV, in good agreement with the threshold values of 7.45 and 7.58 eV, calculated at the TPSS/def2-TZVP and DLPNO-CCSD(T)/QZVPP levels of theory, respectively. Considering the relative intensities in the mass spectrum in the m/z range of 197 to 288, it was clear that the loss of a single methyl group was the dominating fragmentation pathway leading to the observation of positively charged gold-containing fragments.

Table 1. Experimental AEs in DI of $(CH_3)AuP(CH_3)_3$ compared to the threshold values calculated at the TPSS/def2-TZVP and DLPNO-CCSD(T)/QZVPP levels of theory. The best agreements between experiment and theory and the respective reaction paths are signified in bold.

m/z	Product	TPSS-TZVP	DLPNO-CCSD-QZVPP	AE (eV)
288	**$[(CH_3)AuP(CH_3)_3]^+$**	**7.45**	**7.58**	**7.5 $\pm$ 0.2**
273	**$[AuP(CH_3)_3]^+ + (CH_3)$**	**8.59**	**8.38**	**8.1 $\pm$ 0.2**
	$[(CH_3)AuP(CH_3)_2]^+ + (CH_3)$	10.20	10.44	
76	**$[P(CH_3)_3]^+ + (CH_3)Au$**	**9.38**	**9.17**	**8.6 $\pm$ 0.2**
	$[HP(CH_3)_2(CH_2)]^+ + (CH_3)Au$	9.73	9.61	
	$[P(CH_3)_3]^+ + (CH_3) + Au$	12.04	11.54	
75	**$[P(CH_3)_2(CH_2)]^+ + (CH_3)AuH$**	**10.64**	**10.68**	**10.5 $\pm$ 0.2**
	$[P(CH_3)_2(CH_2)]^+ + (CH_3)Au + H$	12.12	11.86	
	$[HP(CH_3)(CH_2)_2]^+ + (CH_3)AuH$	12.62	12.90	
61	**$[HP(CH_3)(CH_2)]^+ + (CH_3)_2Au$**	**11.16**	**11.20**	**11.1 $\pm$ 0.2**
	$[HP(CH_3)(CH_2)]^+ + C_2H_6 + Au$	11.22	10.43	
	$[P(CH_3)_2]^+ + (CH_3)_2Au$	11.64	11.62	
59	**$[P(CH_2)_2]^+ + (CH_3)_2Au + H_2$**	**13.46**	**13.45**	**13.4 $\pm$ 0.3**
	$[P(CH_2)_2]^+ + (CH_3)AuH + CH_4$	13.18	12.93	
	$[P(CH_2)_2]^+ + H_2Au + C_2H_6$	13.56	13.07	
	$[HP(CH_2)CH]^+ + (CH_3)_2Au + H_2$	15.22	15.61	
45	$[PCH_2]^+ + (CH_3)AuH + 2(CH_3)$	17.50	17.04	13.6 $\pm$ 0.4
	$[PCH_2]^+ + (CH_3)AuH + C_2H_6$	**13.84**	**13.20**	
	$[PCH_2]^+ + Au(CH_3) + C_2H_6 + H$	15.32	14.38	
	$[PCH_2]^+ + (CH_3)Au(CH_3) + CH_4$	**13.50**	**13.06**	
	$[PCH_2]^+ + Au + (CH_3) + C_2H_6 + H$	17.98	16.76	
	$[HPCH]^+ + (CH_3)AuH + C_2H_6$	16.19	15.97	
	$[PCH_2]^+ + AuH + (CH_3) + C_2H_6$	14.85	13.75	
	$[HPCH]^+ + AuH + (CH_3) + C_2H_6$	17.19	16.52	
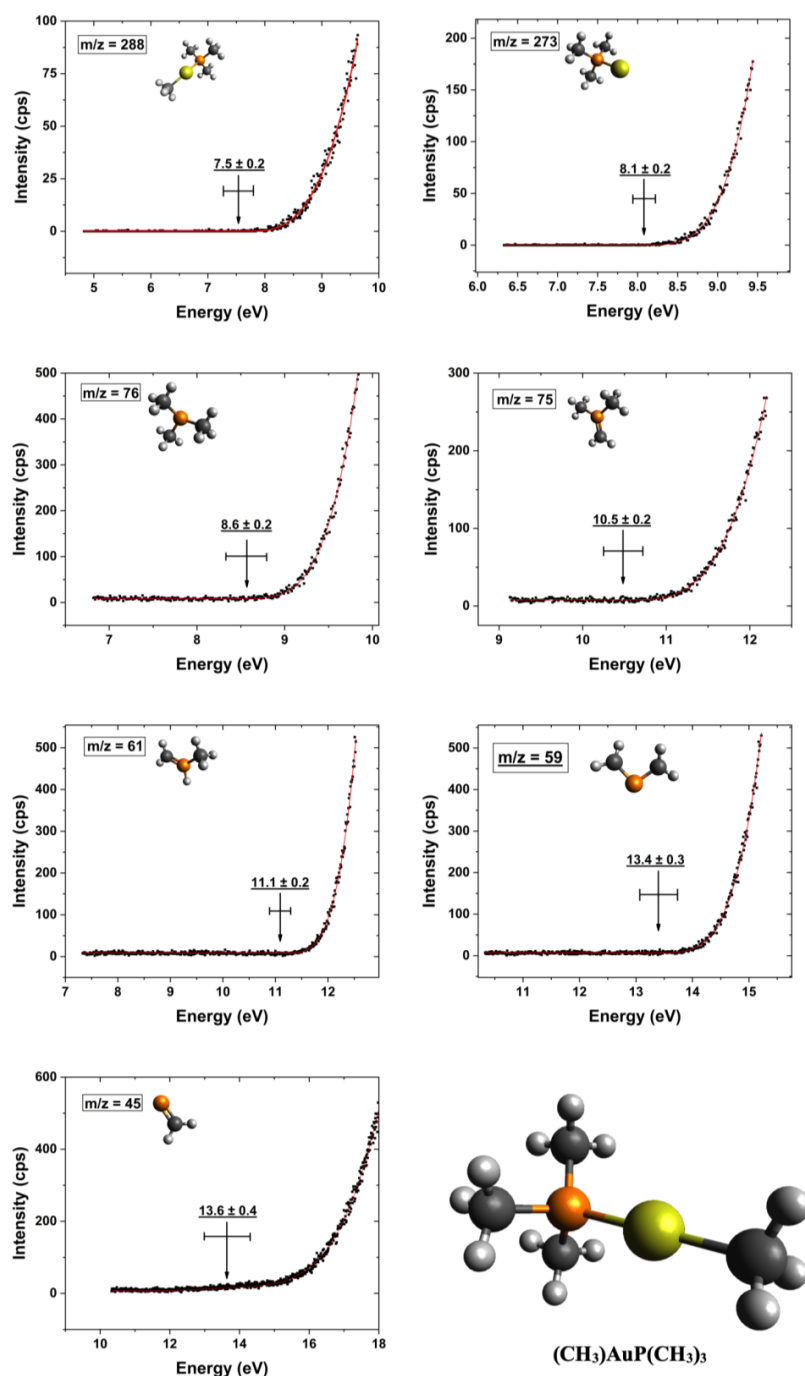
Figure 4. Representative fits to the onset region of the DI ion yield curves for the parent cation and the most dominant positively charged fragments from the $(CH_3)Au(CH_3)_3$ precursor. The respective Wannier-type fits, appearance energies, and their confidence limits for each ion yield curve are shown, and the respective chemical structure of the intact parent molecule is shown in the right corner.

In principle, this methyl group could be cleaved directly from the gold by rupture of the Au–CH$_3$ bond or from the trimethylphosphine ligand, i.e., rupture of one of the P–CH$_3$ bonds. We found the experimentally determined AE for this fragment to be 8.1 ± 0.2 eV, in relatively good agreement with the threshold values of 8.59 (TPSS/def2-TZVP) and 8.38 eV (DLPNO-CCSD(T)/QZVPP), for the loss of the methyl group from the gold, i.e., the formation of AuP(CH$_3$)$_3$$^+$. On the other hand, the calculated threshold values for methyl loss from the trimethylphosphine group were 10.20 and 10.44 eV at the same levels of theory, respectively.

For the dominating trimethylphosphine fragments *m/z* 76 and 61, we considered a direct cleavage of the (CH$_3$)Au–P(CH$_3$)$_3$ bond, leaving the neutral (CH$_3$)Au moiety with charge retention on the phosphor-containing fragment. For *m/z* 75, 59, and 45, which constituted additional hydrogen loss from P(CH$_3$)$_3$$^+$, P(CH$_3$)$_2$$^+$, and PCH$_3$$^+$, respectively, further neutral fragments were considered.

For the direct dissociation and ionization of P(CH$_3$)$_3$, *m/z* 76, we calculated threshold values of 9.38 and 9.17 eV (TPSS/def-TZVP and DLPNO-CCSD(T)/QZVPP, respectively). These were higher than our experimentally determined AE of 8.6 ± 0.2 eV. Considering hydrogen transfer to the phosphor and the formation of [HP(CH$_3$)$_2$CH$_2$]$^+$, as suggested by Bodi et al. [70] for the formation of *m/z* 61 ([HP(CH$_3$)CH$_2$]$^+$) in DI of trimethylphosphine, raised the respective threshold values to 9.73 and 9.61 eV, respectively. Considering the formation of the methyl radical and Au, rather than AuCH$_3$ as the neutral counterpart to this fragment, increased the respective thresholds further by about 2 eV. For additional hydrogen loss from this fragment, i.e., the *m/z* ratio 75, we determined an AE of 10.5 ± 0.2 eV in good agreement with the calculated values of 10.64 and 10.68 eV when considering the formation of HAuCH$_3$ as the neutral counterpart. Considering the formation of AuCH$_3$ and the hydrogen radical or the formation of [HP(CH$_2$)$_2$CH$_3$]$^+$ through hydrogen migration within the cation led to threshold values that were significantly higher (about 1 to 2 eV).

As an alternative to direct methyl loss for the formation of the *m/z* ratio 61 in DI of trimethylphosphine, Bodi et al. [70] considered the formation of [HP(CH$_3$)(CH$_2$)]$^+$ through hydrogen migration from one of the methyl groups to the phosphor. At both the G3 and CBS-QB3 levels of theory, they showed a stabilization of about 0.43 eV through this process. Further supported by their kinetic analyses and reaction path calculations, they inferred that this was the dominating channel in the loss of one methyl group from P(CH$_3$)$_3$ upon DI. This is in good agreement with our calculations, in which we found a stabilization of 0.48 and 0.42 eV, through hydrogen migration, at the TPSS/def2-TZVP and DLPNO-CCSD(T)/QZVPP levels of theory, respectively. The experimental AE for *m/z* 61 was 11.1 ± 0.2 eV, and considering (CH$_3$)$_2$Au as the neutral counterpart; this was in agreement with the threshold energies of 11.16 and 11.20 eV calculated for the [HP(CH$_3$)(CH$_2$)]$^+$ formation at the TPSS/def2-TZVP and DLPNO-CCSD(T)/QZVPP levels of theory, respectively. For direct methyl loss, i.e., the formation of [P(CH$_3$)$_2$]$^+$ without hydrogen migration to the phosphor, we found the respective threshold values to be 11.64 and 11.62, which was in both cases about 0.2 eV above the confidence limits for the AE of *m/z* 61. Additionally, we considered the formation of ethane (C$_2$H$_6$) and Au as neutral counterparts in this process. This led to threshold values of 11.22 and 10.43 eV at the TPSS/def2-TZVP and DLPNO-CCSD(T)/QZVPP levels of theory, respectively. We attribute this difference between the two approaches to the DFT meta-GGA TPSS functional overestimating the atomic energy of Au, and as the CCSD threshold was considerably lower than the experimental AE, we considered (CH$_3$)$_2$Au to be the neutral counterpart to *m/z* 61 instead. The *m/z* ratio 59 constituted an additional loss of two hydrogens from *m/z* 61 and may have been associated with the neutral counterparts (CH$_3$)$_2$Au + H$_2$, (CH$_3$)AuH + CH$_4$ or H$_2$Au + C$_2$H$_4$ and the positive fragment P(CH$_2$)$_2$$^+$. The threshold values for these processes at the DLPNO-CCSD(T)/QZVPP level of theory were 13.45 eV for H$_2$ formation, 12.93 eV for CH$_4$ formation, and 13.07 eV for C$_2$H$_6$ formation. While the CH$_4$ and C$_2$H$_6$ formation paths were both slightly below the experimental 13.4 ± 0.3 eV

AE, there was good agreement with the formation of $H_2 + (CH_3)_2Au$ as the counterparts to the $P(CH_2)_2^+$ cation.

Finally, the m/z ratio 45, i.e., PCH_2^+, was observed with appreciable intensity. There was a significant number of neutral fragment combinations that could be associated with the formation of this fragment. The preferred assignment through comparison with the calculated thresholds was thus not straightforward. The situation was further complicated as m/z 45 also showed a quasi-linear rise in the threshold already from about 10 eV. We expected this contribution to stem from the background gas from which m/z 45 is a common DI contribution, and we accounted for this by replacing the baseline (d) in the Wannier-type function with a linear function $a + bx$. This approach was previously practiced by Fiegele et al. [52] in their determinations of DI thresholds of carbon tetrafluoride, trifluoromethane, methane, and propane. Using this approach, we derived an AE of 13.6 ± 0.4 eV for the formation of this fragment. Within the confidence limits, this agreed with the threshold values for the formation of the neutral counterparts $(CH_3)AuH + C_2H_6$ and $(CH_3)Au(CH_3) + CH_4$, which were 13.84 and 13.50 eV, respectively, at the TPSS/def2-TZVP level of theory. The threshold values calculated for other possible reactions were all found to be above the confidence limit, as can be seen in Table 1. Similar to the MS recorded in the UHV-FEBID chamber, we also observed appreciable contributions around m/z 28 and m/z 15 in the gas phase HV experiments. Due to the admix of contributions from residual background gases and the potential manifold of different reaction pathways in these m/z ranges, we did not determine the AEs of these fragments and refer to their discussion above.

For better comparison with the deposit composition in FEBID and assessment of the energy dependence of individual reaction channels, Figure 5 shows the ion yield curves for the main fragments observed in the DI mass spectra of $(CH_3)AuP(CH_3)_3$. These are shown from below the lowest threshold up to about 50 eV and normalized to the pressure and signal intensity of Ar^+ from Ar at 50 eV incident electron energy.
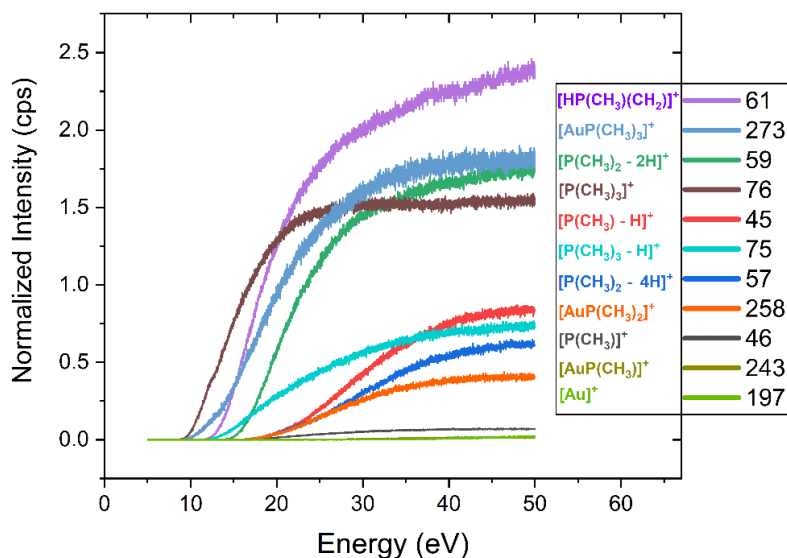
Figure 5. Ion yields for the main positively charged fragments in DI of $(CH_3)AuP(CH_3)_3$. The ion yields are shown in the incident electron energy range from below the respective thresholds up to 50 eV. All ion yields are normalized with respect to the pressure and the signal intensity of Ar^+ from Ar at 50 eV incident electron energy.

Table 2 compares the relative contributions of individual fragments integrated over the energy range from threshold to 50 eV with those determined from the peak heights in the mass spectrum shown in Figure 3. In both cases, the intensities reported are normalized to the highest intensity contribution of m/z 61, set as 100. At the bottom of Table 2, the average carbon and phosphor loss per ionization incident is reported, as well as the respective values from the current UHV-FEBID experiments and the previous HV experiments [25]. For the gas phase, the average carbon and phosphor loss per incident was calculated from the sum of all fragment contributions weighted by the respective carbon and phosphor losses and divided by the total intensity of all DI events. For the $[P(CH_n)_m]^+$ fragments, the average carbon loss was taken to be what was reflected in the gold-containing neutral counterpart of the respective reactions, shown in bold in Table 1. Other fragments were considered to desorb from the surface. For the deposition experiments, the carbon and phosphor losses were calculated from the difference between the elemental composition of the respective deposits and the stoichiometric ratios of the elements in the intact precursor. Noticeably, in Table 2, the relative integral intensity from the ion yield curves differs from those determined from the peak intensity in the mass spectrum. This is due to the lower integral contribution of the higher threshold fragments as compared to the intensities at 50 eV incident energy. Nevertheless, in both cases, the average carbon loss per ionization incident was about 2, and the average phosphor loss was about 0.8. The Au:P:C composition of the intact parent molecule was 1:1:4, and thus, assuming the desorption of all DI fragments that do not contain gold would result in a deposit ratio of 1:0.2:2 if DI is the dominating fragmentation mechanism.

Table 2. Relative peak intensities of $(CH_3)AuP(CH_3)_3$ fragments at 50 eV electron impact energy observed in the DI mass spectrum (Figure 3) and relative integral intensities from thresholds to 50 eV derived from the ion yield curves shown in Figure 5. The FEBID deposits compositions from the current UHV and the previous HV experiments are shown at the bottom of the table.

Fragment	m/z	Relative DI Yield (Intensity)	Relative DI Yield (Integration)
$[AuP(CH_3)_3]^+$	273	78.41	79.07
$[AuP(CH_3)_2]^+$	258	5.64	13.30
$[AuP(CH_3)]^+$	243	2.36	0.36
$[Au]^+$	197	0.51	0.29
$[P(CH_3)_3]^+$	76	64.78	78.98
$[P(CH_3)_3 - H]$	75	33.12	28.47
$[HP(CH_3)(CH_2)]^+$	61	100	100
$[P(CH_3)_2 - 2H]^+$	59	68.8	68
$[P(CH_3)_2 - 4H]^+$	57	26.19	17.98
$[P(CH_3)]^+$	46	14.1	2.54
$[P(CH_3) - H]^+$	45	33.7	24.7
Avrg. C loss per incident		1.94	2.01
Avrg. P loss per incident		0.80	0.76
UHV deposit composition	31–34 at.% Au	65–67 at.% C	1–2 at.% P
HV deposit composition	19–25 at.% Au	54–62 at.% C	12–16 at.% P	2–7 at.% O

3.3. Dissociative Ionization, UHV, and HV FEBID Composition

With respect to the Au:C ratio, the average carbon loss observed in the gas-phase DI experiments agreed well with the current UHV-FEBID experiments, in which it was also found to be close to 1:2. However, while the phosphor was as good as quantitatively desorbed in the UHV-FEBID experiments, the average phosphor loss per dissociation incident in the gas-phase DI experiments was about 0.8. Hence, in 20% of the DI incidents, the Au-P bond remained intact. This was predominantly due to the stability of the $AuP(CH_3)_3^+$

ion (m/z 273) in the gas phase, i.e., loss of the methyl group directly bound to the central gold atom.

In the HV-FEBID experiment, the Au:C ratio was determined by EDX to be about 1:2.5 to 1:2.8, and the Au:P ratio was found to be 1:0.63 to 1:0.64. While the slightly higher carbon content of the deposit may have been due to background gas contributions under HV conditions, the significantly higher phosphor content had to be rooted in different decomposition/desorption dynamics in these two experiments [25]. Both experiments were conducted at 5 keV electron energy, and electron current and deposition time did not influence the composition significantly in the HV-FEBID experiments. This difference thus had to be rooted in the different substrates used in the UHV- and HV-FEBID experiments or the difference in background gas partial pressure. The UHV experiments were conducted on a SiO_2 substrate, a material commonly used for passivation, and it clearly allowed for free desorption of the dissociated phosphor-containing ligands. Moreover, the close to 1:2 Au:C ratio of the deposit indicated that the neutral $(CH_3)_2Au$ fragmentation dominated in the electron-induced decomposition of $(CH_3)Au(CH_3)_3$ at the SiO_2 surface. This was also the characteristic fragment for the $P(CH_n)_2{}^+$ loss channels in DI. The $AuP(CH_3)_2{}^+$ fragment was, however, also a significant contribution to the total DI ion yield but was not apparent in the electron-induced decomposition at the SiO_2 surface, as was perceived from the close to quantitative removal of the phosphor. This close to quantitative removal of the phosphor and the 1:2 Au:C ratio in the UHV deposes was consistent with the deposition mechanism, as depicted schematically in Figure 6. In this scheme, electron impact led to a short-lived positive ion that fragmented to form $[P(CH_n)_2]^+$ and $[(CH_3)_2Au]$, and while $[(CH_3)_2Au]$ stayed on the surface, $[P(CH_n)_2]$ desorbed.
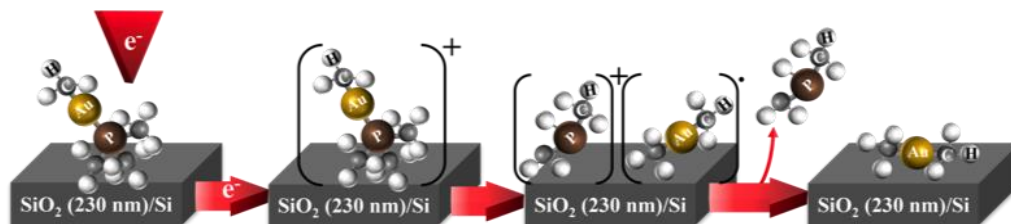
Figure 6. Proposed deposition scheme for the reaction steps of $(CH_3)Au(CH_3)_3$ in the UHV FEBID. After electron-induced ionization of $(CH_3)AuP(CH_3)_3$, a positively charged short-lived ion is produced $[(CH_3)Au(CH_3)_3]^+$ and fragments to form $[P(CH_n)_2]^+$ and $[(CH_3)_2Au]$. In the last step, $[P(CH_n)_2]$ desorbs from the surface, and $[(CH_3)_2Au]^{\cdot}$ stays as a deposited fragment.

This mechanism, however, cannot be dominant in the HV FEBID deposition with $CH_3AuP(CH_3)_3$ on a Si wafer surface. In this experiment, the Au:C:P:O deposit composition was reported to be in the range of 19–25 at.%, Au, 54–62 at.% C, 12–16 at.% P, and 2–7 at.% O. The authors point out that, though not conclusive, this composition may be consistent with a predominant single methyl loss from CH_3–Au–$P(CH_3)_3$, i.e., loss of the (CH_3)–Au methyl group [25]. This is in strong contradiction with the UHV FEBID experiments. We cannot offer a conclusive explanation of this marked difference between deposit compositions in the UHV and HV experiments. However, such a significant difference in FEBID composition is not uncommon when comparing deposition under HV and UHV conditions, even on identical substrates [18,42–45,71]. Most noticeably, in a recent comparative study on FEBID of $Pt(CO)_2Br_2$ and $Pt(CO)_2Cl_2$ [71], as good as quantitative desorption of the halogen was observed under HV conditions while the Pt:Cl and Pt:Br composition of the deposit under UHV conditions remained close to 1:1.56 and 1:1.65, respectively. This has been attributed to reactions with surface water always present in the HV experiments and has been discussed in analogy to the electron-induced decomposition of $Pt(NH_3)_2Cl_2$, where effective Cl removal through intramolecular reductive HCl formation is observed. Similarly, reductive HCl formation is achieved from surface-adsorbed $(\eta^3\text{-}C_3H_5)Ru(CO)_3Cl$ [72,73],

through in situ exposure to ammonia during electron irradiation. Post and in situ, the oxidative purification of deposits by electron irradiation in the presence of water was also proven efficient in a number of cases, and under HV conditions, a 75% increase in the gold purity of deposits from dimethylgold (III) trifluoroacetylacetonate was attained, reaching 91 at.% Au through oxidative carbon removal in the presence of water [33].

In the HV-FEBID experiment on the present precursor, van Dorp et al. [25] suggested that the presence of O_2 in the chamber might be responsible for the formation of $OP(CH_3)_3$ fragments. Similarly, it may be speculated that non-volatile $OP(CH_3)_3$ is formed in electron-induced reactions of $(CH_3)AuP(CH_3)_3$ in the presence of water. This might in part explain the higher amount of phosphor in their experiment as compared to the UHV experiment, but as the oxygen content of the deposits is significantly lower than the phosphor content, this alone cannot account for the observed difference. Notwithstanding the reason for the very different deposit compositions in these experiments, the current UHV study rather supports the conclusion that $P(CH_3)_3$ is a suitable Au(I) ligand in FEBID precursors, while the HV study points towards the contrary.

4. Conclusions

In the current study, the suitability of $(CH_3)AuP(CH_3)_3$ as a precursor for gold deposition in FEBID was explored under UHV conditions, and gas-phase DI experiments and quantum chemical calculations were performed to aid the interpretation of the underlying electron-induced reactions. This potential precursor was found to have sufficient volatility and sufficient stability to be practical as an Au precursor in FEBID, and under the current UHV conditions, 31–34 at.% Au content was achieved at 5 keV electron energy. The Au:C compositing of the deposits was close to 1:2 and in good agreement with the average carbon loss per incident observed in the gas-phase DI experiments, where a significant contribution of the neutral counterparts was found to be $(CH_3)_2Au$. The phosphor, on the other hand, was found to be as good as quantitatively removed in the UHV FEBID experiments, while the average phosphor loss per DI incident in the gas phase was found to be about 0.8. The remaining 0.2 average phosphor per DI incident in the gas, however, could at large be attributed to the loss of the CH_3–Au methyl group and the formation of $AuP(CH_3)_2^+$. This reaction channel was clearly not active in the UHV FEBID of $(CH_3)AuP(CH_3)_3$ on SiO_2.

While the Au:C:P deposit composition in the current UHV FEBID was found to be about 1:2:0, with as good as quantitative removal of the phosphor, a previous HV FEBID study reported an approximate Au:C:P:O composition of 1:2.6:0.6:0.2. The conclusions of these studies contrast with respect to the suitability of trimethylphosphine as Au(I) ligand in FEBID. Potentially, a part of the phosphor content in the HV experiment may be explained through the electron-induced oxidative formation of trimethylphosphine oxide in reactions with surface water or through reactions with residual oxygen in the chamber. However, other significant factors must also play a role. Compositions of deposits formed under UHV and HV are often significantly different, and like in the current case, the reason(s) for these differences are not obvious. Using a systematic comparison of UHV and HV deposition experiments in deciphering the root(s) of these differences may offer a valuable approach to tailoring better-suited precursors and gaining better control of the compositions of the deposits. From a more general perspective, the approach to combine different methods, namely UHV-FEBID, gas-phase DI experiments, and calculations on a quantum mechanical level proved to be powerful and yielded detailed insights into the mechanisms of electron-induced precursor dissociation and the resulting deposition process.

Author Contributions: T.X.G. synthesized the (CH$_3$)AuP(CH$_3$)$_3$ precursor; G.B. participated in the synthesis of the precursor; E.B. prepared and characterized the samples for UHV FEBID deposition and AES analysis, prepared the figures (Figures 1, 2, 6 and S1), drafted the manuscript, and managed the references; A.W. participated in the UHV FEBID deposition and AES analysis; A.K. performed the HV gas-phase experiment, conducted the quantum chemical calculations, prepared Figures 3–5 and tables, participated in the UHV FEBID deposition and AES analysis, and drafted the manuscript; S.H. supervised the synthesis of the precursor and contributed in the editing of the manuscript; H.M. supervised the UHV FEBID experiment and edited the drafted manuscript; O.I. supervised the HV gas-phase study and edited the drafted manuscript; E.B. and A.K. contributed equally to this and share the first co-authorship. All authors have read and agreed to the published version of the manuscript.

Institutional Review Board Statement: Not applicable.

Informed Consent Statement: Not applicable.

Data Availability Statement: Data presented in this study are available on request from the corresponding authors.

Conflicts of Interest: The authors declare no conflict of interest.

References

1. Winkler, R.; Schmidt, F.P.; Haselmann, U.; Fowlkes, J.D.; Lewis, B.B.; Kothleitner, G.; Rack, P.D.; Plank, H. Direct-Write 3D Nanoprinting of Plasmonic Structures. *ACS Appl. Mater. Interfaces* **2017**, *9*, 8233–8240. [CrossRef] [PubMed]
2. Drost, M.; Tu, F.; Berger, L.; Preischl, C.; Zhou, W.; Gliemann, H.; Wöll, C.; Marbach, H. Surface-Anchored Metal-Organic Frameworks as Versatile Resists for Gas-Assisted E-Beam Lithography: Fabrication of Sub-10 Nanometer Structures. *ACS Nano* **2018**, *12*, 3825–3835. [CrossRef] [PubMed]
3. van Dorp, W.F.; Beyer, A.; Mainka, M.; Gölzhäuser, A.; Hansen, T.W.; Wagner, J.B.; Hagen, C.W.; De Hosson, J.T.M. Focused Electron Beam Induced Processing and the Effect of Substrate Thickness Revisited. *Nanotechnology* **2013**, *24*, 345301. [CrossRef]
4. Prima, G.D.; Sachser, R.; Trompenaars, P.; Mulders, H.; Huth, M. Direct-Write Single Electron Transistors by Focused Electron Beam Induced Deposition. *Nano Futur.* **2019**, *3*, 25001. [CrossRef]
5. Marbach, H. Electron Beam Induced Surface Activation: A Method for the Lithographic Fabrication of Nanostructures via Catalytic Processes. *Appl. Phys. A Mater. Sci. Process.* **2014**, *117*, 987–995. [CrossRef]
6. Huth, M.; Porrati, F.; Schwalb, C.; Winhold, M.; Sachser, R.; Dukic, M.; Adams, J.; Fantner, G. Focused Electron Beam Induced Deposition: A Perspective. *Beilstein J. Nanotechnol.* **2012**, *3*, 597–619. [CrossRef] [PubMed]
7. Utke, I.; Hoffmann, P.; Melngailis, J. Gas-Assisted Focused Electron Beam and Ion Beam Processing and Fabrication. *J. Vac. Sci. Technol. B Microelectron. Nanom. Struct.* **2008**, *26*, 1197–1276. [CrossRef]
8. Heil, T.; Waldow, M.; Capelli, R.; Schneider, H.; Ahmels, L.; Tu, F.; Schöneberg, J.; Marbach, H. Pushing the Limits of EUV Mask Repair: Addressing Sub-10 Nm Defects with the next Generation e-Beam-Based Mask Repair Tool. *J. Micro/Nanopatterning, Mater. Metrol.* **2021**, *20*, 1–12. [CrossRef]
9. Edinger, K.; Becht, H.; Bihr, J.; Boegli, V.; Budach, M.; Hofmann, T.; Koops, H.W.P.; Kuschnerus, P.; Oster, J.; Spies, P.; et al. Electron-Beam-Based Photomask Repair. *J. Vac. Sci. Technol. B Microelectron. Nanom. Struct.* **2004**, *22*, 2902–2906. [CrossRef]
10. Liang, T.; Frendberg, E.; Lieberman, B.; Stivers, A. Advanced Photolithographic Mask Repair Using Electron Beams. *J. Vac. Sci. Technol. B Microelectron. Nanom. Struct.* **2005**, *23*, 3101–3105. [CrossRef]
11. Fernández-Pacheco, A.; Serrano-Ramón, L.E.; Tyliszczak, T.; Chou, K.W.; Córdoba, R.; Szkudlarek, A.; Brien, L.O.; Kapusta, C.; Ibarra, M.R.; De Teresa, J.M. Correlation between the Magnetic Imaging of Cobalt Nanoconstrictions and Their Magnetoresistance Response. *Nanotechnology* **2012**, *23*, 105703. [CrossRef] [PubMed]
12. Wendel, M.; Lorenz, H.; Kotthaus, J.P. Sharpened Electron Beam Deposited Tips for High Resolution Atomic Force Microscope Lithography and Imaging. *Appl. Phys. Lett.* **1995**, *67*, 3732–3734. [CrossRef]
13. Utke, I.; Friedli, V.; Michler, J.; Bret, T.; Multone, X.; Hoffmann, P. Density Determination of Focused-Electron-Beam-Induced Deposits with Simple Cantilever-Based Method. *Appl. Phys. Lett.* **2006**, *88*, 31906. [CrossRef]
14. Plank, H.; Winkler, R.; Schwalb, C.H.; Hütner, J.; Fowlkes, J.D.; Rack, P.D.; Utke, I.; Huth, M. Focused Electron Beam-Based 3D Nanoprinting for Scanning Probe Microscopy: A Review. *Micromachines* **2020**, *11*, 48. [CrossRef] [PubMed]
15. De Teresa, J.M.; Fernández-Pacheco, A. Present and Future Applications of Magnetic Nanostructures Grown by FEBID. *Appl. Phys. A* **2014**, *117*, 1645–1658. [CrossRef]

16. Höflich, K.; Yang, R.B.; Berger, A.; Leuchs, G.; Christiansen, S. The Direct Writing of Plasmonic Gold Nanostructures by Electron-Beam- Induced Deposition. *Adv. Mater.* **2011**, *23*, 2657–2661. [CrossRef]

17. Utke, I.; Swiderek, P.; Höflich, K.; Madajska, K.; Jurczyk, J.; Martinović, P.; Szymańska, I.B. Coordination and Organometallic Precursors of Group 10 and 11: Focused Electron Beam Induced Deposition of Metals and Insight Gained from Chemical Vapour Deposition, Atomic Layer Deposition, and Fundamental Surface and Gas Phase Studies. *Coord. Chem. Rev.* **2022**, *458*, 213851. [CrossRef]

18. Lukasczyk, T.; Schirmer, M.; Steinrück, H.P.; Marbach, H. Electron-Beam-Induced Deposition in Ultrahigh Vacuum: Lithographic Fabrication of Clean Iron Nanostructures. *Small* **2008**, *4*, 841–846. [CrossRef]

19. Klein, K.L.; Randolph, S.J.; Fowlkes, J.D.; Allard, L.F.; Meyer III, H.M.; Simpson, M.L.; Rack, P.D. Single-Crystal Nanowires Grown via Electron-Beam-Induced Deposition. *Nanotechnology* **2008**, *19*, 345705. [CrossRef]

20. Chien, M.H.; Shawrav, M.M.; Hingerl, K.; Taus, P.; Schinnerl, M.; Wanzenboeck, H.D.; Schmid, S. Analysis of Carbon Content in Direct-Write Plasmonic Au Structures by Nanomechanical Scanning Absorption Microscopy. *J. Appl. Phys.* **2021**, *129*. [CrossRef]

21. Kuhness, D.; Gruber, A.; Winkler, R.; Sattelkow, J.; Fitzek, H.; Letofsky-Papst, I.; Kothleitner, G.; Plank, H. High-Fidelity 3D Nanoprinting of Plasmonic Gold Nanoantennas. *ACS Appl. Mater. Interfaces* **2021**, *13*, 1178–1191. [CrossRef] [PubMed]

22. Marashdeh, A.; Tiesma, T.; van Velzen, N.J.C.; Harder, S.; Havenith, R.W.A.; De Hosson, J.T.M.; van Dorp, W.F. The Rational Design of a Au(I) Precursor for Focused Electron Beam Induced Deposition. *Beilstein J. Nanotechnol.* **2017**, *8*, 2753–2765. [CrossRef] [PubMed]

23. Carden, W.G.; Thorman, R.M.; Unlu, I.; Abboud, K.A.; Fairbrother, D.H.; McElwee-White, L. Design, Synthesis, and Evaluation of CF$_3$AuCNR Precursors for Focused Electron Beam-Induced Deposition of Gold. *ACS Appl. Mater. Interfaces* **2019**, *11*, 11976–11987. [CrossRef] [PubMed]

24. Carden, W.G.; Lu, H.; Spencer, J.A.; Fairbrother, D.H.; McElwee-White, L. Mechanism-Based Design of Precursors for Focused Electron Beam-Induced Deposition. *MRS Commun.* **2018**, *8*, 343–357. [CrossRef]

25. Van Dorp, W.F.; Wu, X.; Mulders, J.J.L.; Harder, S.; Rudolf, P.; De Hosson, J.T.M. Gold Complexes for Focused-Electron-Beam-Induced Deposition. *Langmuir* **2014**, *30*, 12097–12105. [CrossRef]

26. Mulders, J.J.L.; Veerhoek, J.M.; Bosch, E.G.T.; Trompenaars, P.H.F. Fabrication of Pure Gold Nanostructures by Electron Beam Induced Deposition with Au(CO)Cl Precursor: Deposition Characteristics and Primary Beam Scattering Effects. *J. Phys. D. Appl. Phys.* **2012**, *45*, 475301. [CrossRef]

27. Utke, I.; Hoffmann, P.; Dwir, B.; Leifer, K.; Kapon, E.; Doppelt, P. Focused Electron Beam Induced Deposition of Gold. *J. Vac. Sci. Technol. B Microelectron. Nanom. Struct.* **2000**, *18*, 3168–3171. [CrossRef]

28. Wnuk, J.D.; Gorham, J.M.; Rosenberg, S.G.; van Dorp, W.F.; Madey, T.E.; Hagen, C.W.; Fairbrother, D.H. Electron Beam Irradiation of Dimethyl-(Acetylacetonate) Gold(III) Adsorbed onto Solid Substrates. *J. Appl. Phys.* **2010**, *107*, 54301. [CrossRef]

29. Jenke, M.G.; Lerose, D.; Niederberger, C.; Michler, J.; Christiansen, S.; Utke, I. Toward Local Growth of Individual Nanowires on Three-Dimensional Microstructures by Using a Minimally Invasive Catalyst Templating Method. *Nano Lett.* **2011**, *11*, 4213–4217. [CrossRef]

30. Koops, H.W.P.; Kretz, J.; Rudolph, M.; Weber, M.; Dahm, G.; Lee, K.L. Characterization and Application of Materials Grown by Electron-Beam-Induced Deposition. *Jpn. J. Appl. Phys.* **1994**, *33*, 7099–7107. [CrossRef]

31. Folch, A.; Tejada, J.; Peters, C.H.; Wrighton, M.S. Electron Beam Deposition of Gold Nanostructures in a Reactive Environment. *Appl. Phys. Lett.* **1995**, *66*, 2080–2082. [CrossRef]

32. Botman, A.; Mulders, J.J.L.; Weemaes, R.; Mentink, S. Purification of Platinum and Gold Structures after Electron-Beam-Induced Deposition. *Nanotechnology* **2006**, *17*, 3779–3785. [CrossRef]

33. Shawrav, M.M.; Taus, P.; Wanzenboeck, H.D.; Schinnerl, M.; Stöger-Pollach, M.; Schwarz, S.; Steiger-Thirsfeld, A.; Bertagnolli, E. Highly Conductive and Pure Gold Nanostructures Grown by Electron Beam Induced Deposition. *Sci. Rep.* **2016**, *6*, 34003. [CrossRef] [PubMed]

34. Thorman, R.M.; Ragesh Kumar, T.P.; Howard Fairbrother, D.; Ingólfsson, O. The Role of Low-Energy Electrons in Focused Electron Beam Induced Deposition: Four Case Studies of Representative Precursors. *Beilstein J. Nanotechnol.* **2015**, *6*, 1904–1926. [CrossRef] [PubMed]

35. Unlu, I.; Spencer, J.A.; Johnson, K.R.; Thorman, R.M.; Ingólfsson, O.; McElwee-White, L.; Fairbrother, D.H. Electron Induced Surface Reactions of (η^5-C$_5$H$_5$)Fe(CO)$_2$Mn(CO)$_5$, a Potential Heterobimetallic Precursor for Focused Electron Beam Induced Deposition (FEBID). *Phys. Chem. Chem. Phys.* **2018**, *20*, 7862–7874. [CrossRef]

36. Ragesh Kumar, T.P.; Weirich, P.; Hrachowina, L.; Hanefeld, M.; Bjornsson, R.; Hrodmarsson, H.R.; Barth, S.; Howard Fairbrother, D.; Huth, M.; Ingólfsson, O. Electron Interactions with the Heteronuclear Carbonyl Precursor H$_2$FeRu$_3$(CO)$_{13}$ and Comparison with HFeCo$_3$(CO)$_{12}$: From Fundamental Gas Phase and Surface Science Studies to Focused Electron Beam Induced Deposition. *Beilstein J. Nanotechnol.* **2018**, *9*, 555–579. [CrossRef]

37. Ingólfsson, O. *Low-Energy Electrons Fundamentals and Applications*; Pan Stanford Publishing Pte. Ltd.: Singapore, 2019.

38. Märk, T.D.; Dunn, G.H. *Electron Impact Ionization*; Springer Science & Business Media: Berlin/Heidelberg, Germany, 1985.

39. Cipriani, M.; Thorman, R.M.; Brewer, C.R.; McElwee-White, L.; Ingólfsson, O. Dissociative Ionization of the Potential Focused Electron Beam Induced Deposition Precursor π-Allyl Ruthenium(II) Tricarbonyl Bromide, a Combined Theoretical and Experimental Study. *Eur. Phys. J. D* **2019**, *73*, 227. [CrossRef]

40. Thorman, R.M.; Unlu, I.; Johnson, K.; Bjornsson, R.; McElwee-White, L.; Fairbrother, D.H.; Ingólfsson, O. Low Energy Electron-Induced Decomposition of (η^5-Cp)Fe(CO)$_2$Mn(CO)$_5$, a Potential Bimetallic Precursor for Focused Electron Beam Induced Deposition of Alloy Structures. *Phys. Chem. Chem. Phys.* **2018**, *20*, 5644–5656. [CrossRef]

41. Bjarnason, E.H.; Ómarsson, B.; Jónsdóttir, N.R.; Árnason, I.; Ingólfsson, O. Dissociative Electron Attachment and Dissociative Ionization of 1,1-Dichloro-1-Silacyclohexane and Silacyclohexane. *Int. J. Mass Spectrom.* **2014**, *370*, 39–43. [CrossRef]

42. Vollnhals, F.; Drost, M.; Tu, F.; Carrasco, E.; Späth, A.; Fink, R.H.; Steinrück, H.P.; Marbach, H. Electron-Beam Induced Deposition and Autocatalytic Decomposition of Co(CO)$_3$NO. *Beilstein J. Nanotechnol.* **2014**, *5*, 1175–1185. [CrossRef]

43. Gavagnin, M.; Wanzenboeck, H.D.; Shawrav, M.M.; Belic, D.; Wachter, S.; Waid, S.; Stoeger-Pollach, M.; Bertagnolli, E. Focused Electron Beam-Induced CVD of Iron: A Practical Guide for Direct Writing. *Chem. Vap. Depos.* **2014**, *20*, 243–250. [CrossRef]

44. Gazzadi, G.C.; Mulders, H.; Trompenaars, P.; Ghirri, A.; Affronte, M.; Grillo, V.; Frabboni, S. Focused Electron Beam Deposition of Nanowires from Cobalt Tricarbonyl Nitrosyl (Co(CO)$_3$NO) Precursor. *J. Phys. Chem. C* **2011**, *115*, 19606–19611. [CrossRef]

45. Gazzadi, G.C.; Mulders, J.J.L.; Trompenaars, P.; Ghirri, A.; Rota, A.; Affronte, M.; Frabboni, S. Characterization of a New Cobalt Precursor for Focused Beam Deposition of Magnetic Nanostructures. *Microelectron. Eng.* **2011**, *88*, 1955–1958. [CrossRef]

46. Mulders, J.J.L.; Belova, L.M.; Riazanova, A. Electron Beam Induced Deposition at Elevated Temperatures: Compositional Changes and Purity Improvement. *Nanotechnology* **2010**, *22*, 55302. [CrossRef]

47. Schmidbaur, H.; Shiotani, A. Organogold-Chemie, VI Darstellung Komplexer Organogold-Verbindungen Durch Liganden-Substitutionsreaktionen. *Chem. Ber.* **1971**, *104*, 2821–2830. [CrossRef]

48. Vollnhals, F. Exploring Electron Beam Induced Surface Activation for the Fabrication of Well-Defined Nanostructures: On the Role of Catalytic Processes, Substrates and Precursors. Master's Thesis, Friedrich-Alexander-Universität Erlangen-Nürnberg, Erlangen, Germany, 2015.

49. Friedli, V.; Utke, I. Optimized Molecule Supply from Nozzle-Based Gas Injection Systems for Focused Electron- and Ion-Beam Induced Deposition and Etching: Simulation and Experiment. *J. Phys. D. Appl. Phys.* **2009**, *42*, 125305. [CrossRef]

50. Bjarnason, E.H.; Ómarsson, B.; Engmann, S.; Ómarsson, F.H.; Ingólfsson, O. Dissociative Electron Attachment to Titatinum Tetrachloride and Titanium Tetraisopropoxide. *Eur. Phys. J. D* **2014**, *68*, 121. [CrossRef]

51. Wetzel, R.C.; Baiocchi, F.A.; Hayes, T.R.; Freund, R.S. Absolute Cross Sections for Electron-Impact Ionization of the Rare-Gas Atoms by the Fast-Neutral-Beam Method. *Phys. Rev. A* **1987**, *35*, 559–577. [CrossRef]

52. Fiegele, T.; Hanel, G.; Torres, I.; Lezius, M.; Märk, T.D. Threshold Electron Impact Ionization of Carbon Tetrafluoride, Trifluoromethane, Methane and Propane. *J. Phys. B At. Mol. Opt. Phys.* **2000**, *33*, 4263–4283. [CrossRef]

53. Neese, F. Software Update: The ORCA Program System, Version 4.0. *WIREs Comput. Mol. Sci.* **2018**, *8*, e1327. [CrossRef]

54. Grimme, S.; Ehrlich, S.; Goerigk, L. Effect of the Damping Function in Dispersion Corrected Density Functional Theory. *J. Comput. Chem.* **2011**, *32*, 1456–1465. [CrossRef] [PubMed]

55. Kepp, K.P. Benchmarking Density Functionals for Chemical Bonds of Gold. *J. Phys. Chem. A* **2017**, *121*, 2022–2034. [CrossRef] [PubMed]

56. Goel, S.; A. Velizhanin, K.; Piryatinski, A.; Tretiak, S.; Ivanov, S.A. DFT Study of Ligand Binding to Small Gold Clusters Satyende. *J. Phys. Chem. Lett.* **2010**, *1*, 927–931. [CrossRef]

57. Riplinger, C.; Neese, F. An Efficient and near Linear Scaling Pair Natural Orbital Based Local Coupled Cluster Method. *J. Chem. Phys.* **2013**, *138*, 34106. [CrossRef] [PubMed]

58. Riplinger, C.; Sandhoefer, B.; Hansen, A.; Neese, F. Natural Triple Excitations in Local Coupled Cluster Calculations with Pair Natural Orbitals. *J. Chem. Phys.* **2013**, *139*, 134101. [CrossRef]

59. Riplinger, C.; Pinski, P.; Becker, U.; Valeev, E.F.; Neese, F. Sparse Maps—A Systematic Infrastructure for Reduced-Scaling Electronic Structure Methods. II. Linear Scaling Domain Based Pair Natural Orbital Coupled Cluster Theory. *J. Chem. Phys.* **2016**, *144*, 24109. [CrossRef]

60. Griffiths, M.B.E.; Dubrawski, Z.S.; Bačić, G.; Japahuge, A.; Masuda, J.D.; Zeng, T.; Barry, S.T. Controlling the Thermal Stability and Volatility of Organogold(I) Compounds for Vapor Deposition with Complementary Ligand Design. *Eur. J. Inorg. Chem.* **2019**, *2019*, 4927–4938. [CrossRef]

61. Wallace, W.E. Mass Spectra. In *NIST Chemistry WebBook, NIST Standard Reference Database Number 69*; Linstrom, P.J., Mallard, W.G., Eds.; National Institute of Standards and Technology: Gaithersburg, MD, USA, 2021; p. 20899. [CrossRef]

62. Banaszak Holl, M.M.; Seidler, P.F.; Kowalczyk, S.P.; McFeely, F.R. Surface Reactivity of Alkylgold(I) Complexes: Substrate-Selective Chemical Vapor Deposition of Gold from RAuP(CH3)3 (R = CH2CH3, CH3) at Remarkably Low Temperatures. *Inorg. Chem.* **1994**, *33*, 510–517. [CrossRef]

63. Schirmer, M.; Walz, M.M.; Vollnhals, F.; Lukasczyk, T.; Sandmann, A.; Chen, C.; Steinrück, H.P.; Marbach, H. Electron-Beam-Induced Deposition and Post-Treatment Processes to Locally Generate Clean Titanium Oxide Nanostructures on Si(100). *Nanotechnology* **2011**, *22*, 085301. [CrossRef]

64. Preischl, C.; Le, L.H.; Bilgilisoy, E.; Vollnhals, F.; Gölzhäuser, A.; Marbach, H. Controlled Electron-Induced Fabrication of Metallic Nanostructures on 1 Nm Thick Membranes. *Small* **2020**, *16*, 2003947. [CrossRef]

65. van Staden, M.J.; Roux, J.P. The Superposition of Carbon and Ruthenium Auger Spectra. *Appl. Surf. Sci.* **1990**, *44*, 259–262. [CrossRef]

66. Davis, L.E.; MacDonald, N.C.; Palmberg, P.W.; Riach, G.E.; Weber, R.E. *Handbook of Auger Electron Spectroscopy*; Perkin·Elmer Corporation, Physical Electronics Division: Eden Prairie, MN, USA, 1976.

67. Mathieu, H.J. Auger Electron Spectroscopy. In *Surface Analysis—The Principal Techniques*; Vickerman, J.C., Gilmore, I.S., Eds.; Wiley Online Books; John Wiley & Sons: Hoboken, NJ, USA, 2009; pp. 9–45.

68. van Dorp, W.F.; Hagen, C.W. A Critical Literature Review of Focused Electron Beam Induced Deposition. *J. Appl. Phys.* **2008**, *104*, 81301. [CrossRef]

69. Böhler, E.; Warneke, J.; Swiderek, P. Control of Chemical Reactions and Synthesis by Low-Energy Electrons. *Chem. Soc. Rev.* **2013**, *42*, 9219–9231. [CrossRef] [PubMed]

70. Bodi, A.; Kercher, J.P.; Baer, T.; Sztáray, B. On the Parallel Mechanism of the Dissociation of Energy-Selected $P(CH_3)^{3+}$ Ions. *J. Phys. Chem. B* **2005**, *109*, 8393–8399. [CrossRef]

71. Mahgoub, A.; Lu, H.; Thorman, R.M.; Preradovic, K.; Jurca, T.; McElwee-White, L.; Fairbrother, H.; Hagen, C.W. Electron Beam-Induced Deposition of Platinum from $Pt(CO)_2Cl_2$ and $Pt(CO)_2Br_2$. *Beilstein J. Nanotechnol.* **2020**, *11*, 1789–1800. [CrossRef] [PubMed]

72. Warneke, J.; Rohdenburg, M.; Zhang, Y.; Orszagh, J.; Vaz, A.; Utke, I.; De Hosson, J.T.M.; van Dorp, W.F.; Swiderek, P. Role of NH_3 in the Electron-Induced Reactions of Adsorbed and Solid Cisplatin. *J. Phys. Chem. C* **2016**, *120*, 4112–4120. [CrossRef]

73. Rohdenburg, M.; Boeckers, H.; Brewer, C.R.; McElwee-White, L.; Swiderek, P. Efficient NH_3-Based Process to Remove Chlorine from Electron Beam Deposited Ruthenium Produced from $(\eta 3-C_3H_5)Ru(CO)_3Cl$. *Sci. Rep.* **2020**, *10*, 10901. [CrossRef]

Supporting Information

On the Electron-Induced Reactions of (CH₃)AuP(CH₃)₃: A Combined UHV Surface Science and Gas-Phase Study

Ali Kamali [1,†], Elif Bilgilisoy [2,†], Alexander Wolfram [2], Thomas Xaver Gentner [3], Gerd Ballmann [3], Sjoerd Harder [3], Hubertus Marbach [2,4,*] and Oddur Ingólfsson [1,*]

[1]   Department of Chemistry and Science Institute, University of Iceland, Dunhagi 3, 107 Reykjavik, Iceland
[2]   Physikalische Chemie II, Friedrich-Alexander Universität Erlangen-Nürnberg, 91058 Erlangen, Germany
[3]   Inorganic and Organometallic Chemistry, Universität Erlangen-Nürnberg, 91058 Erlangen, Germany
[4]   Carl Zeiss SMT GmbH, 64380 Roßdorf, Germany
*   Correspondence: hubertus.marbach@fau.de (H.M.); odduring@hi.is (O.I.)
†   These authors contributed equally to this work.

Figure S1. (**a**) Gold content of FEBID deposits on SiO₂ (230 nm)/Si(111) substrate over the timeline of three consecutive experiment runs. Between experiment-run#1 and -run#2 is a pause of three days, and between run#2 and run#3 is one day. (**b**) The color of freshly filled (CH₃)AuP(CH₃)₃ precursor, and (**c**) the color of the precursor at the end of experiment-run#3. (**d**) The color change on copper sealing after the experiment run#3. (**e**) AES results obtained from the experiments run#1 and run#2.

Paper II

A combined gas phase dissociative ionization, dissociative electron attachment and deposition study on the potential FEBID precursor $[(CH_3)_2AuCl]_2$

Elif Bilgilisoy[a]‡, Ali Kamali[b]‡, Thomas Xaver Gentner[c], Gerd Ballmann[c], Sjoerd Harder[c],

Hubertus Marbach[a], [d], Oddur Ingólfsson[b]*, Hans-Peter Steinrück[a]*

Ali Kamali carried out the gas-phase experiment using HV equipment, performed quantum chemical calculations, contributed to the UHV FEBID deposition and AES analysis, and wrote the manuscript in collaboration with Dr. Elif Bilgilisoy.

A Combined Gas Phase Dissociative Ionization, Dissociative Electron Attachment and Deposition Study on the Potential FEBID Precursor [(CH$_3$)$_2$AuCl]$_2$
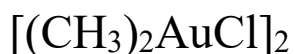
Elif Bilgilisoy[a]‡, Ali Kamali[b]‡, Thomas Xaver Gentner[c], Gerd Ballmann[c], Sjoerd Harder[c], Hubertus Marbach[a], [d], Hans-Peter Steinrück[a]*, Oddur Ingólfsson[b]*

[a] Physikalische Chemie II, Friedrich-Alexander Universität Erlangen-Nürnberg, 91058 Erlangen, Germany

[b] University of Iceland Science Institute and Department of Chemistry, Dunhagi 3, 107 Reykjavík, Iceland

[c] Inorganic and Organometallic Chemistry, Universität Erlangen-Nürnberg, 91058 Erlangen, Germany

[d] Carl Zeiss SMT GmbH, 64380 Roßdorf, Germany

‡ **Elif Bilgilisoy and Ali Kamali contributed equally to this work**

Abstract

Motivated by the potential of focused electron beam-induced deposition (FEBID) in the fabrication of functional gold nanostructures for application in plasmonic and detector technology, we have conducted a comprehensive study on $[(CH_3)_2AuCl]_2$ as a potential precursor for such depositions. Fundamental electron induced dissociation processes were studied under single collision conditions and the composition and morphology of FEBID deposits fabricated in an UHV chamber were explored on different surfaces and at varying beam currents. In the gas phase, dissociative ionization is found to lead to significant carbon loss from this precursor and about 50% of the chlorine is on average removed per DI incident. In dissociative electron attachment on the other hand, no chlorine is removed from the parent molecule. Contrary to these observations FEBID in the UHV setup is found to yield quantitative loss and desorption of the chlorine from the deposits, an effect that we attribute to electron induced secondary reactions in the deposition process. We find this precursor to be stable at ambient conditions and to have sufficient vapor pressure to be suitable for HV instruments. More importantly, in the UHV setup, FEBID with $[(CH_3)_2AuCl]_2$ yields deposits with high gold content, ranging from about 45 to 61 at.% depending on the beam current and the cleanliness of the substrates surface.

Introduction

In recent years, gold nanostructures have received much attention owing to their dielectric properties[1], their biocompatibility[2], and their electrical properties[3,4], properties that enable a multitude of exciting applications in the field of nanotechnology. These include, but are not limited to electronic interconnects[5], metamaterials[6], growth substrates for nanowires and nanotubes[7] and complex plasmonic structures[8,9]. For the latter application, mastery over the shape as well as accurate control of the distribution of the nanostructures is critical for enhancement of adsorption and controlled scattering of light.[10] Focused Electron Beam-Induced Deposition (FEBID) is a direct writing method for controlled deposition/fabrication of nanostructures on either flat or non-flat surfaces. It offers excellent shape control and thus the potential to widen the scope of applicable nanomaterials. In FEBID a focused electron beam is directed onto a substrate's surface in close proximity to a gas inlet, through which a precursor compound is supplied to deliver the material for the nanostructures to be build. For metallic structures, these precursor molecules are commonly organometallics that adsorb on the substrate and are decomposed by the electron beam irradiation. Ideally a pure metal is deposited while fragmented volatile ligands are pumped away.[11–13]

Several parameters affect the FEBID process, including the electron beam energy and current, the substrate material, the environment inside the deposition chamber, and the composition of the precursor.[14–17] Heretofore, various CVD precursors have been applied for FEBID deposition. For gold nanostructures these include for example, dimethylgold[III] acetylacetonate ($Me_2Au(acac)$), dimethylgold[III] trifluoroacetylacetonate ($Me_2Au(tfac)$), and dimethylgold[III] hexafluoroacetylacetonate ($Me_2Au(hfac)$).[18] Though these precursors have proven suitable for CVD, in FEBID their application has mainly resulted in amorphous matrixes of carbon with

embedded metal crystallites and a gold content of 2-3 at.%,[19] 10-40 at.%,[20] and 8-20 at.%,[21] respectively. This is most likely due to the fact that the CVD process is thermally-driven, while in FEBID, the precursor fragmentation is primarily electron driven. This may partly explain the insufficient metal content achieved when using CVD precursors in FEBID.[18] In this context, effort has been given to design gold precursors optimized for FEBID. Arguably the most noticeable of these are chloro(carbonyl)gold(I) (ClAu^I(CO))[22] and chloro(trifluorophosphine)gold(I) (ClAu^I(PF$_3$))[23] precursors that have enabled depositions of ~ 95 at.% Au and a resistivity of Au grains as low as 22 μΩ, respectively. However, the short lifetime of both precursors, which results from their moisture sensitivity and thermal instability has limited their applicability.

In FEBID, the irradiation of the substrate with a high-energy focused electron beam results in elastic and inelastic electron scattering, including ionizing events. The latter lead to the production of numerous reactive, low-energy scattered and secondary electrons. These play a significant role in the precursor decomposition and thus the deposit formation.[16] Hence, the decomposition of the precursor molecules is not only effectuated by the primary electron beam. In fact, the reactivity of these low energy electrons[24] may even determine the fragmentation of the precursor molecules, which in turn is critical with respect to the resulting purity of the FEBID deposits. In general, electron-induced fragmentation processes are categorized as dissociative ionization (DI), dissociative electron attachment (DEA), dipolar dissociation (DD), and neutral dissociation (ND).[25] To fully comprehend the electron-molecule interactions in FEBID, it is critical to understand the extent and nature of these processes and how they are reflected in the deposit formation at substrate surfaces from individual precursors or specific ligand structures. One approach in this direction is to combine ultra-high-vacuum (UHV) surface science studies and high-vacuum (HV) gas phase investigations.[26,27] In this context, the surface science experiments allow for electron-dose-dependent studies of the elemental composition of the deposit and

desorbing ligands may be monitored by means of mass spectrometry. Gas phase studies, using controllable, quasi mono-energetic electron beams under single collision conditions, on the other hand, provide information on the electron energy dependence and extent of the individual fragmentation processes.[27] A number of such comparative gas phase and surface science studies have been carried out in the past using a 500 eV flood gun in the deposition studies[28,29] and also in combination with higher energy FEBID studies.[29,30] In a recent study[31], we took a similar approach and investigated $(CH_3)AuP(CH_3)_3$ as a potential gold precursor for FEBID, using gas phase experimrnts under single collision conditions and quantum mechanical calculations to aid the interpretation of that data, in combination with FEBID in an UHV setup. The results of this study demonstrated that at 5 keV electron energy, FEBID deposits with 31-34 at.% Au content were attainable with this precursor in the UHV setup. A close to complete phosphor removal was observed and the Au:C ratio of the deposit was found to be 1:2. This corresponds to the average carbon loss per incident found in the DI gas-phase experiment and was consistent with the dominating reaction pathways as determined by the quantum chemical calculations. However, in one specific channel in the DI gas phase study, a significant retention of the phosphor at the gold was found indicating significant surface effects.

In the current study we extent this approach to investigate the deposition of Au using $[(CH_3)_2AuCl]_2$ as a potential FEBID precursor. FEBID in an UHV setup is conducted, in conjunction with a gas phase study on the electron energy dependence of the fragmentation of this compound through DI and DEA; moreover, quantum chemical calculations are used to determine the dominating reaction pathways. The UHV FEBID results are discussed in the context of the observed DI and DEA fragmentation processes, and also in the context of a previous FEBID study of this precursor under HV, conducted by van Dorp *et al.*[32] In that study a promising Au content of 29-41 at.% was achieved without additional purifications. In the current study, we find the Au

content to be further improved to reach about 50 at% in the UHV setup without pretreatment of the substrate surface and with a pretreated surface a gold content of 61 at% is reached.

Results and Discussion

FEBID on SiO$_2$ (500 nm) / Si (111).

In this experiment, 4×4 μm^2 FEBID structures were written with [(CH$_3$)$_2$AuCl]$_2$ as precursor using an acceleration voltage of 5 keV and a beam current of 1.5 nA. The fabricated structures were examined with SEM and AES. Figure 1a depicts a SEM image of the FEBID deposit created with an electron exposure of 7.80 C/cm^2. The position of the corresponding AES analysis is marked in Figure 1a by a green-colored star. AES spectra acquired on the bare substrate and the deposit are shown in Figure 1b. On the pristine SiO$_2$ (500 nm) /Si (111) substrate (black spectrum), only two main AES signals are visible: The peak at 272 eV is attributed to C$_{KLL}$ Auger transitions of carbon,[46] and the peaks at 468, 483 and 503 eV to O$_{KLL}$ the Auger transitions of SiO$_2$.[46] After deposition, AES signals at 69, 181, 272 and 430 eV are present. These are assigned to the Au$_{NOO}$, Cl$_{LMM}$, C$_{KLL}$, and Sn$_{MNN}$ Auger transitions,[46] respectively (Figure 1b, green spectrum). The broad and small peak at approximately 367 eV can also be attributed to an Sn signal.[46] The contamination with Sn is from the synthesis process of the [(CH$_3$)$_2$AuCl]$_2$ precursor, which involves SnMe$_4$ as a methylation agent.[33] The elemental composition of the FEBID structure was calculated using the relative sensitivity factors (S),[47] that is, S$_{Au}$: 0.21; S$_{Cl}$: 0.69; S$_C$: 0.08; S$_{Sn}$: 0.53. The atomic concentration of the deposit was found to be 51 at.% Au, 2 at.% Cl, 42 at.% C, and 5 at.% Sn. A magnification of a selected area of the SEM image shown in Figure 1a is depicted in Figure 1c, where nanoparticles in the deposition are noticeable, though the picture is somewhat blurry. To better visualize the observed nanoparticles, a background subtraction was performed with the image enhancement program ImageJ.[48] The image after the background subtraction is shown in

Figure 1d, where the particles can be distinguished more clearly. Through careful examination of Figure 1d, nanoparticles of different shapes with different sizes can be identified on the surface. Some of them appear to be triangular (depicted in a yellow-colored circle), some are rod-shaped (green-colored circle), and some are hexagonal (red-colored circle); however, the majority of the nanostructures observed are spherical (blue-colored circle). These different shapes are similar to
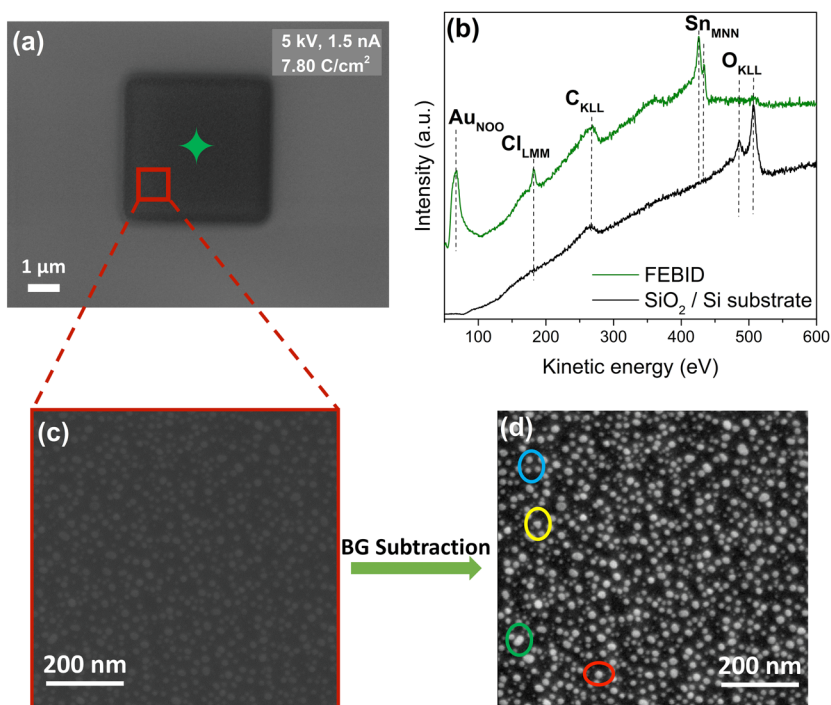
Figure 1. (a) SEM image of a 4 x 4 μm^2 FEBID structure deposited on SiO_2 from $[(CH_3)_2AuCl]_2$ with an electron dose of 7.80 C/cm^2 using the electron beam parameters of 5 keV and 1.5 nA. (b) AES of the SiO_2 substrate prior to deposition (black line) and from the FEBID structure (green line); the green-colored star in (a) indicates the position where the spectrum was acquired. (c) Magnified image from area within the red colored square shown in (a). (d) The same image as shown in (c) after the background subtraction process was applied using the ImageJ program.[48] Different shapes of nanoparticles are illustrated with red, yellow, green, and blue circles in (d) (see text).

that of gold nanoparticles produced by solution-based synthesis (seed-mediated growth) in order to control the shape and crystal structure of gold nanoparticles.[49,50] These nanoparticles have been mainly examined by STEM and/or TEM.[51]

HAADF-STEM on FEBID (SiO$_2$ (500 nm) / Si (111)).

As a next step, high-angle annular dark field scanning transmission electron microscopy (HAADF-STEM) was performed to analyze the morphology of the deposited nanoparticles. For this purpose, several FEBID structures were prepared on the SiO$_2$ substrate with the size of 4 × 4 μm^2 and an electron dose of 7.80 C/cm^2. For the HAADF-STEM measurements, a lamella was prepared with a thickness of around 100 nm and a width of approximately 4 μm (Figure S1). In Figure 2a, the HAADF-STEM image of deposited nanoparticles is shown, revealing a nearly uniform spatial distribution of nanoparticles with a size that is lower than 5 nm, but also non-uniformly distributed nanoparticles with larger sizes (~ 15 – 20 nm). The magnified image of a selected larger nanoparticle from Figure 2a is shown in Figure 2b. The determined fringe spacing of that particle is ~ 0.23 nm, which is consistent with the spacing between the (111) planes of a face-centered cubic (FCC) gold nanoparticle.[52,53] The crystallinity of the gold nanoparticles was also investigated by using selected area electron diffraction (SAED) pattern shown in Figure 2c. The relatively bright circular patterns indicate polycrystallinity of the deposits. Furthermore, the lattice spacings (d-spacings) of 2.30, 2.07, 1.42, 1.23, and 1.17 Å,[54] (Figure 2c) correspond to the (111), (200), (220), (133), and (222) growth planes, respectively, of the close-packed, face-centered cubic crystal structure of gold.
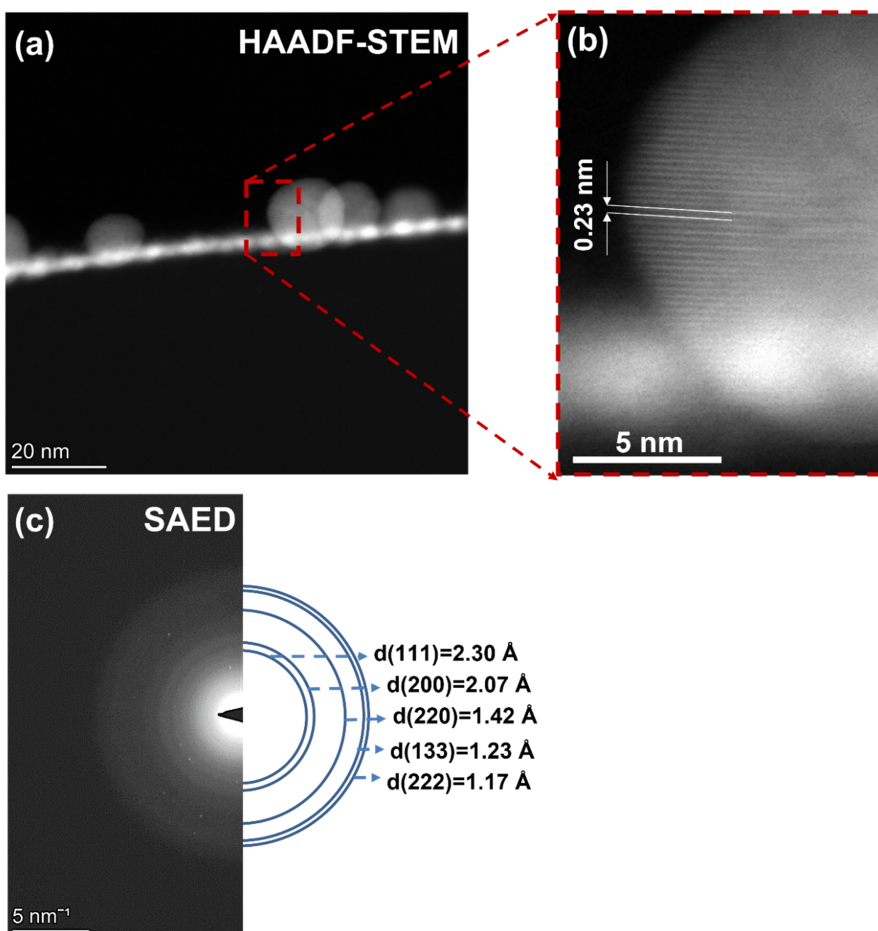
Figure 2. (a) HAADF-STEM image of a FEBID gold nanoparticle. (b) Enlarged image of the area depicted with red-dashed lines in (a), showing the interplanar distance of 0.23 nm between the {1, 1, 1} planes of the fcc lattice. (c) SAED of the FEBID gold nanoparticles, corresponding to fcc gold.

FEBID on SiO_2 (500 nm) / Si (111) at different beam currents.

FEBID deposits were also prepared with $[(CH_3)_2AuCl]_2$ using beam currents of 0.4 nA (deposit size: 2×2 μm^2), 1.5 nA (deposit size: 4×4 μm^2), and 3 nA (deposit size: 4×4 μm^2). The other

deposition parameters (electron dose: 7.80 C/cm^2, and acceleration voltage: 5 keV) were the same in all three experiments. The FEBID structures were investigated by SEM and non-contact AFM. Figure 3a shows the SEM images of the deposits along with the respective deposition parameters. Magnified sections from these SEM images are shown in Figure 3b. Auger electron spectroscopy was performed on these structures to determine their composition and better understand the effect of different beam currents on the compositions. The respective spectra are shown in Figure 3c.
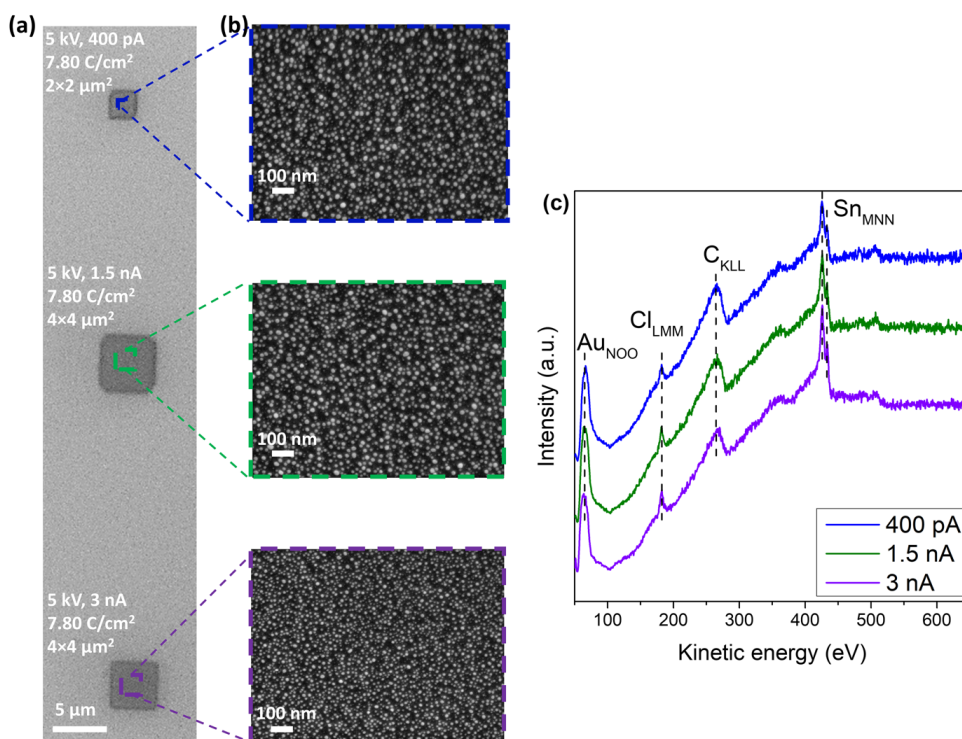
Figure 3. (a) SEM image of FEBID structures deposited on SiO$_2$ from [(CH$_3$)$_2$AuCl]$_2$ with an electron dose of 7.80 C/cm^2 using a 5 keV electron beam and different beam currents of 0.4 nA, 1.5 nA, and 3 nA. (b) Magnified images of FEBID structures from (a), (c) AES of the FEBID structures deposited with 0.4 pA, 1.5 nA, and 3 nA depicted with blue, green, and purple line, respectively.

A careful investigation of the SEM images reveals that the particle size is getting smaller when the current is increased, as is clearly discernible from Figure 3b. For detailed particle analysis, the ImageJ software[48] was used to obtain the numbers of nanoparticles and their mean diameter. As mentioned before, the observed gold nanoparticles (Figure 1d) have irregular shapes. Therefore, the mean Feret diameter, which gives the average value over all possible orientations (see Supporting Information, Figure S2), was used. The average particle sizes were found to be 9.8 nm at a beam current of 400 pA, 10.1 nm at 1.5 nA, and 8.2 nm at 3 nA. From the AES data shown in Figure 3c, the atomic concentrations of the structures were calculated: At 0.4 nA, the composition was found to be 45 at.% Au, 1 at.% Cl, 49 at.% C, 5 at.% Sn, at 1.5 nA it was found to be 50 at.% Au, 2 at.% Cl, 42 at.% C, 6 at.% Sn, and at 3 nA, it was found to be 52 at.% Au, 2 at.% Cl, 38 at.% C, 8 at.% Sn. Clearly, the increase in gold content with increasing deposition current is correlated with the decrease in carbon content. This is most evident from the reduction of the carbon peak areas in the AES, which is ~36% when comparing the depositions at 0.4 nA and 3 nA, and ~14% when comparing the depositions at 0.4 nA and 1.5 nA. We thus attribute the observed size reduction of the deposited gold particles with increasing deposition current to the decrease in carbon content. Similar size reduction of gold nanoparticles has been reported for post deposition oxidative purification of FEBID deposits, where carbon removal led to ~ 18% height reduction of the respective nanoparticles.[55]

AFM of FEBID on (SiO$_2$ (500 nm) / Si (111)) at different beam currents.

In order to obtain complementary information on the structures deposited with different beam currents, non-contact AFM was used to investigate the height of the deposits and their particle size. Figures 4a and 4b depict the 2D AFM images and magnified sections of these, respectively. The corresponding height profiles are shown in Figure 4c. The magnified sections of the 2D AFM

images (Fig. 4b) show the same trend as observed in the SEM images shown in Figure 3b, that is, the size of the gold nanoparticles is approximately the same for the FEBID structures written with 0.4 nA and 1.5 nA, while they are smaller in the deposit written with 3 nA beam current. The average particle sizes obtained from the AFM images are around 10.4 nm for 0.4 nA, 9.5 nm for 1.5 nA, and 7.0 nm for 3 nA (Figure S3b). These values are in good agreement with the values obtained from the SEM images (9.8 nm – 0.4 nA; 10.1 nm – 1.5 nA; 8.2 nm – 3 nA). Notably, the
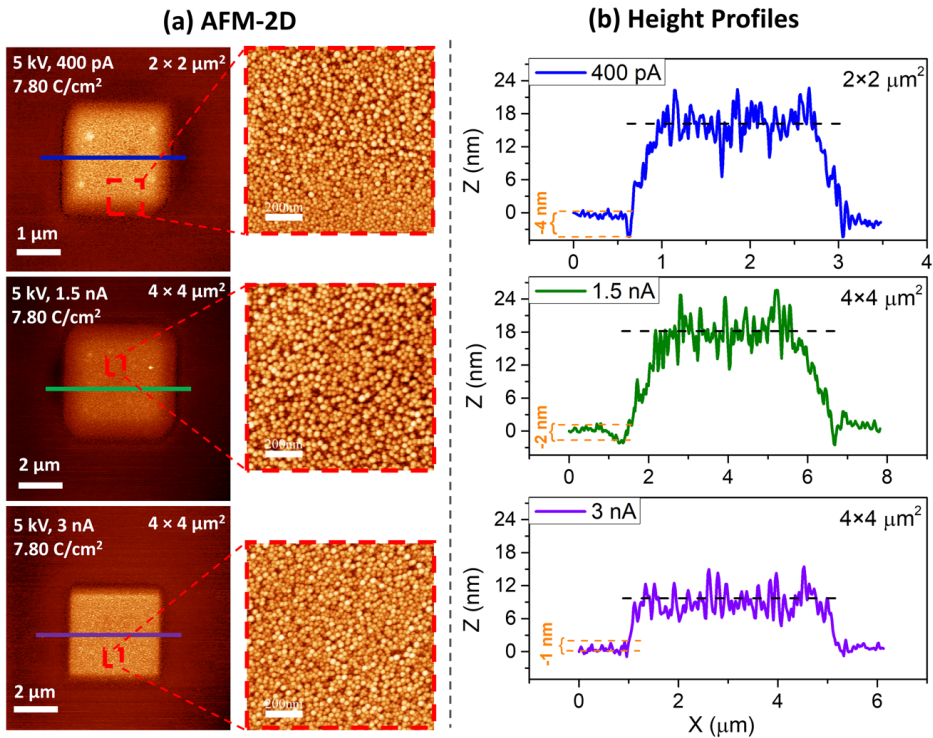
Figure 4. (a) 2D AFM images and magnified AFM images (red-dashed squares), (b) corresponding line profiles for the FEBID structures produced with electron dose of 7.80 C/cm^2 using the beam currents of 0.4 nA (blue line), 1.5 nA (green line), and 3 nA (purple line).

line profiles in Figure 4b for the structures created with 0.4 nA and 1.5 nA reveal thicknesses of the deposits of ~ 17 nm, while the thickness of the deposit written with 3 nA is only ~ 9 nm.

Most interestingly, the height profiles of depositions also change according to the applied beam current (Figure 4b). For example, especially in the height profile of the 0.4 nA deposition (Figure 4b, blue line), there is a negative dip at the edge of the deposit, indicated by the orange dashed lines. It is important to note that this negative dip is also observed for other line profiles throughout the deposit. Therefore, the negative dips is present in the entire structure (Figure S4). This negative dip can also be seen for the depositions created with 1.5 nA and 3 nA beam currents, depicted in Figure 4b with green and purple lines, respectively, but the depth of the dip decreases with increasing the applied beam current. This indicates that an etching process occurs simultaneously with the deposition process, wherein the etching effect being less pronounced than the deposition for the all-beam currents. Similar etching effects were observed in the literature, where it was reported that one of the expected effects when working with halogen-based precursors is the observation of etching as well as deposition.[22,56] In these studies, the release of halogen ligands was indicated as the main reason of the etching process. As shown in the AES results in Figure 3c, the Cl peak for the structure deposited with 0.4 nA (blue line) is around 30% less than that for the structures deposited with 1.5 and 3nA.

The combination of SEM and AFM to analyze the FEBID structures created with different beam currents reveals that the etching process is related to the change in Cl content, and the particle-size change is related to the difference in the C content.

FEBID on thermally cleaned Si (111).

In several UHV-FEBID studies,[56–58] it has been shown that an UHV setup alone is not sufficient to produce FEBID structures with relatively low organic contaminations. In addition, a comparably clean and well-defined substrate also helps to increase the metals content. Thus, the SiO_2 substrate was sputtered using Ar^+ for 45 minutes ($V_{(Ar^+)}$= 1 keV, $P_{(Ar^+)}$= 4 × 10^{-6} mbar) and subsequently annealed up to 823 K under an oxygen atmosphere for 90 minutes to demonstrate the effect of surface preparation (reduction of C and O contaminants) on the quality of deposition. After preparation, AES was performed to check the surface cleanliness and to compare with the uncleaned surface (Figure S5). Figure S5, clearly shows that the carbon (C_{KLL} at 272 eV) and oxygen peaks (O_{KLL} at 508 eV) were reduced (by ~17% for C, ~67% for O), and thus the Si_{LMM} peak at 92 eV became observable. Using the cleaned sample, a FEBID experiment with the $[(CH_3)_2AuCl]_2$ precursor was performed to create 4×4 μm^2 structures using same parameters as in
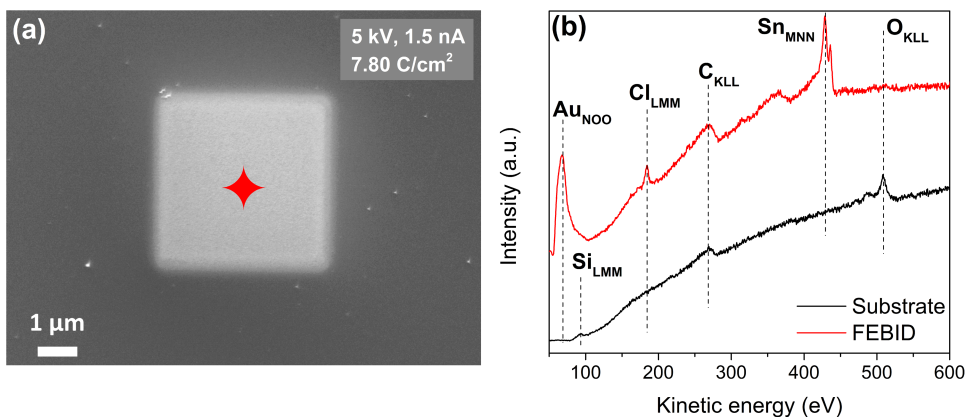
Figure 5. (a) SEM image of a 4 x 4 μm^2 FEBID structure deposited on SiO_2 from $[(CH_3)_2AuCl]_2$ with an electron dose of 7.80 C/cm² using the electron beam parameters of 5 keV and 1.5 nA. (b) AES of the SiO_2 substrate prior to deposition (black line) and the result from the FEBID structure (red line). The red-colored star in (a) indicates the position where the spectrum was acquired.

Figure 1. The results were analyzed with SEM and AES, see Figure 5. The red-colored star indicates the AES-measured point. AES (red-colored line) shows the following peaks: Au_{NOO} at 69 eV, Cl_{LMM} at 181 eV, C_{KLL} at 272 eV, and Sn_{MNN} at 430 eV peaks were observed,[46] yielding atomic concentrations of 61 at.% Au, 1 at.% Cl, 35 at.% C, and 3 at.% Sn, respectively. Comparison to Figure 1b reveals an increase of Au content by 10%, while the C content decreased by 10%.

In a previous study, the same precursor, $[(CH_3)_2AuCl]_2$, was used to create FEBID deposits on a SiO_2 substrate by using 5 keV and 0.1 / 0.4 nA in an HV atmosphere.[32] The composition of the structures was checked with EDX and reported to be 29 – 41 at.% Au, 2 – 6 at.% Cl, and 53 – 68 at.% C. The SEM images of the FEBID deposits also revealed grainy structures. These concentrations, reported in the reference study, support the idea of complete Cl ligand desorption and incorporation of both (CH_3) ligands into the deposit. The main difference between the work at hand and the aforementioned study in HV, is that this study was carried out in UHV with a higher electron beam current of 1.5 nA. However, it should be mentioned that AES used here is surface-sensitive as compared to EDX, which is bulk-sensitive. The reason for the detection of Sn peak in AES results (Figures 1b and 5b) is most likely due to the usage of different characterization tools. From both the UHV and HV FEBID results, one has to conclude that the Cl-ligands are completely removed and desorbed under the impact of the electron beam. The ease of Cl ligand desorption during electron beam deposition has also been addressed in several previous studies.[22,23] Notably, the UHV-FEBID results yield 10 – 20 at.% higher Au content than reported in the HV study. Therefore, the reaction pathway of $[(CH_3)_2AuCl]_2$ can be suggested as;

$$[(CH_3)_2AuCl]_2 + e^- \rightarrow Au_2(CH_3)_x + 2Cl \uparrow + (4-x)(CH_3) \uparrow$$

where $Au_2(CH_3)_x$ is the deposited material, while $2Cl$ and $(4-x)(CH_3)$ are desorbed from each molecule. According to the AES depicted in Figures 1b and 5b, x can be inferred to be 1 – 2.

Figure 6a shows a positive ion mass spectrum of $[(CH_3)_2AuCl]_2$, recorded for the m/z range from 10 to 550 at 50 eV electron impact energy. A rich fragmentation pattern, characterized by progressive loss of methyl groups, is observed. The first progression is that of the molecular cation at m/z 524 followed by sequential loss of methyl ligands, appearing at m/z 509, 494, 479, and 464, with the most significant contribution being from the loss of all four methyl ligands at m/z 464.

The second progression shows the loss of one chlorine atom and two, three and four methyl ligands at m/z 458, 444, and 429, respectively. From these m/z 458 has lost an additional hydrogen and m/z 444 overlaps with lesser contributions from m/z 443, which we also attribute to additional hydrogen loss. Like in the preceding progression, the loss of all four methyl ligands, m/z 429, is also the dominating contribution here. The third progression shows the loss of both chlorines in combination with the sequential loss of two three and four methyl ligands at m/z 422, 408 and 394, respectively. Here, the contributions are of similar intensity, though the loss of three methyl ligands, m/z 408, is slightly more apparent. Lesser contribution is also observed at m/z 407 and is
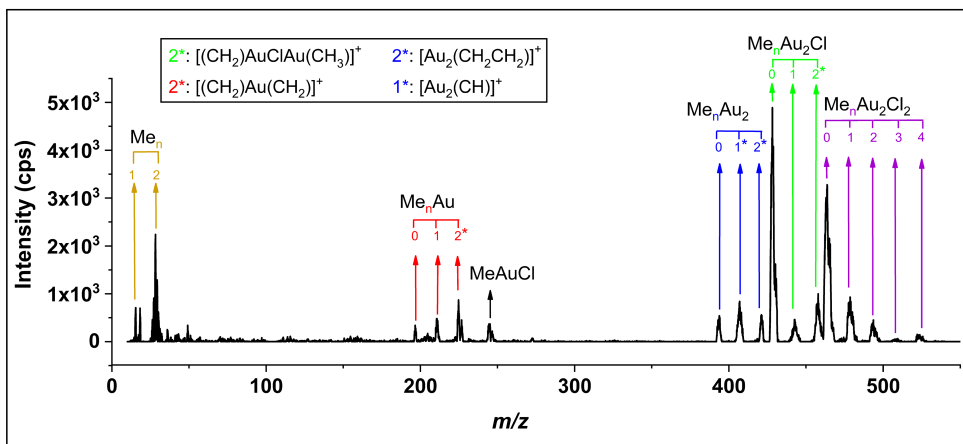
Figure 6. Positive ion mass spectrum of electron impact ionization and dissociation of $[(CH_3)_2AuCl]_2$ recorded at incident electron energy of 50 eV.

attributed to additional hydrogen loss as compared to *m/z* 408. The last progression is from the loss of both chlorine atoms along with one gold atom and two and three methyl groups and is observed at *m/z* 227 and 225, 212 and 197, respectively. From these, *m/z* 225 is ascribed to the loss of two methyl groups and two additional hydrogen and 197 represents Au^+, i.e., the elemental gold. Additionally, *m/z* 247 is observed with fair intensity and we attribute this fragment to the loss of three methyl ligands in combination with the loss of one chlorine and one gold atom, i.e., $[(CH_3)AuCl]^+$. There are also some contributions at and around *m/z* 28 and 15. While the contributions at and around *m/z* 28 are predominantly from the background gas in the chamber, including N_2, *m/z* 15 is in part attributed to CH_3^+ resulting from DI of $[(CH_3)_2AuCl]_2$.

For most of the observed *m/z* ratios, the assignment of the underlying fragmentation process is not straight forward as the neutral fragments, complementary to the *m/z* ratios observed, may be assigned to more than one composition. Thus, to better understand the underlying fragmentation process the respective AEs are determined using a Wannier-type threshold function (see the method section) and compared to calculated threshold energies for a variety of potential reaction pathways. A full list of all optimized geometries (Cartesian coordinates) of the parent and positively charged ions at the PBE0-TZVP level of theory are provided with the supporting materials in section (S6).

Figure 7 shows the fitted onset-region of representative ion yield curves for the individual fragments along with their average AEs determined from fits to 3-4 ion yield curves recorded on different days. Also shown are the respective confidence limits and the structures of the respective positive ions optimized at the PBE0-TZVP level of theory. Table 1 compares the individual AEs with calculated thresholds for different potential reactions leading to the respective fragments.
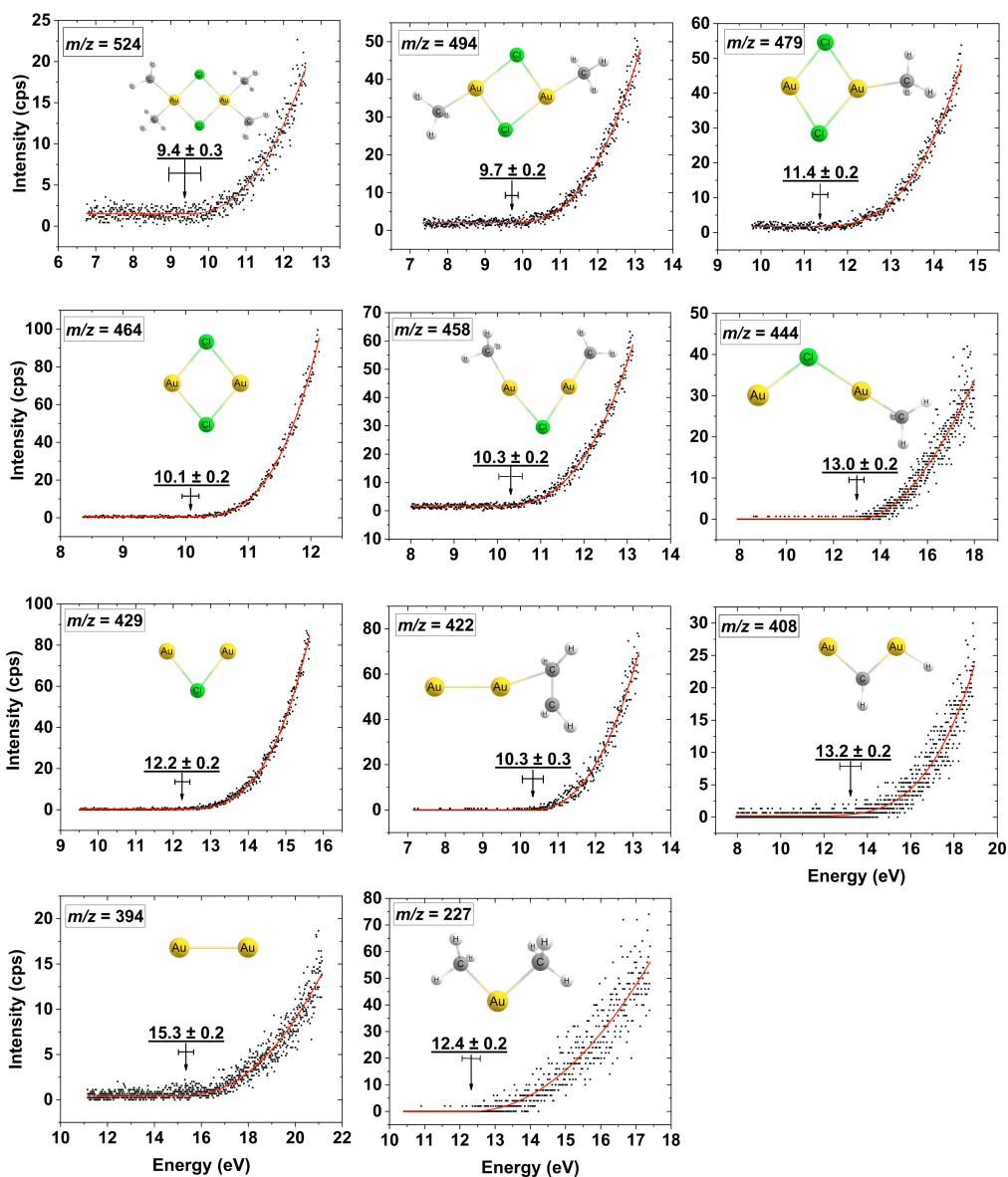
Figure 7. Representative fits to the onset region of the DI ion yield curves for the parent cation and the most dominant positively charged fragments from [(CH$_3$)$_2$AuCl]$_2$. The appearance energies and their confidence limits for each ion are shown along with the respective chemical structure optimized at the PBE0-TZVP level of theory.

Here the values for single bond ruptures without new bond formations are shown along with the best matches of the AEs with the respective threshold values. For comparison, threshold values for selected processes that are next to the assigned processes are also shown in Table 1, but a complete set of all threshold values calculated, and the respective processes are shown in Table S7 with the supporting material. The thresholds are calculated at both the PBE0-TZVP and DLPNO-CCSD(T)-TZVP levels of theory as is discussed in the method section, and the assigned fragmentation reactions shown in Table 1 are highlighted bold. In the assignment we primarily compare to the DLPNO-CCSD(T)-TZVP values. We note, that as activation barriers may shift the AEs to higher values as compared to the respective thermochemical thresholds, the true thermochemical threshold may in some cases be lower than the respective AE. Where the current comparison does not allow assignment to one combination of neutral fragments, the closest matches are highlighted bold in Table 1.

For the AE of the parent cation $[Au_2Cl_2(CH_3)_4]^+$, i.e., the ionization energy of $[(CH_3)_2AuCl]_2$, we determine a value of 9.4 ± 0.3 eV. Within the confidence limit, this agrees well with the calculated thresholds of 9.23 eV found at the PBE0-TZVP level of theory. However, at the DLPNO-CCSD(T)-TZVP levels of theory, we calculate a threshold of 9.92 eV, which is about 0.2 eV above the upper confidence limit for the experimental AE.

For the loss of one methyl group, *m/z* 509, we find the intensity too low to determine the AE. However, for the loss of two methyl groups, *m/z* 494 we find an AE of 9.7 ± 0.3 eV. Considering only single bond ruptures, i.e., the formation of two CH_3 radicals in this process, results in threshold values of 13.51 and 14.06 eV at the PBE0-TZVP and DLPNO-CCSD(T)-TZVP levels of theory, respectively. These values are about 4 eV above the respective AE which is significantly higher than the confidence limits of the experiment.

Table 1. Comparison of the experimental AE's with the respective calculated threshold values.

m/z	Products	AE (eV)	PBE0-TZVP (eV)	DLPNO-CCSD(T)-TZVP (eV)
524	**[Au$_2$Cl$_2$(CH$_3$)$_4$]$^+$**	**9.4 ± 0.3**	<u>**9.23**</u>	**9.92**
494	[Au$_2$Cl$_2$(CH$_3$)$_2$]$^+$ + 2(CH$_3$) **[Au$_2$Cl$_2$(CH$_3$)$_2$]$^+$ + CH$_3$CH$_3$** [Au$_2$Cl$_2$(CH$_3$)$_2$]$^+$ + CH$_2$CH$_2$ + H$_2$	**9.7 ± 0.2**	13.51 <u>**9.67**</u> 11.28	14.06 **10.29** 11.65
479	[Au$_2$Cl$_2$(CH$_3$)]$^+$ + 3(CH$_3$) **[Au$_2$Cl$_2$(CH$_3$)]$^+$ + (CH$_3$) + CH$_3$CH$_3$** [Au$_2$Cl$_2$(CH$_3$)]$^+$ + CH$_2$CH$_2$ + H$_2$ + (CH$_3$)	**11.4 ± 0.2**	15.01 <u>**11.18**</u> 12.78	15.04 **11.27** 12.64
464	[Au$_2$Cl$_2$]$^+$ + 4(CH$_3$) **[Au$_2$Cl$_2$]$^+$ + 2(CH$_3$CH$_3$)** [Au$_2$Cl$_2$]$^+$ + CH$_3$CH$_3$ + 2(CH$_3$) [Au$_2$Cl$_2$]$^+$ + CH$_2$CH$_2$ + H$_2$ + CH$_3$CH$_3$	**10.1 ± 0.2**	17.32 <u>**9.65**</u> 13.48 11.25	17.65 **10.12** 13.89 11.49
458	[Au$_2$Cl(CH$_2$CH$_3$)]$^+$ + 2CH$_3$ + Cl + H **[Au$_2$Cl(CH$_2$CH$_3$)]$^+$ + CH$_3$CH$_3$ + HCl** **[Au$_2$Cl(CH$_2$CH$_3$)]$^+$ + (CH$_4$) + CH$_3$Cl** [Au$_2$Cl(CH$_2$CH$_3$)]$^+$ + CH$_3$CH$_3$ + Cl + H	**10.3 ± 0.2**	18.72 <u>**10.46**</u> **10.64** 14.88	18.50 **10.41** **10.60** 14.73
444	[Au$_2$Cl(CH$_3$)]$^+$ + Cl + 3(CH$_3$) **[Au$_2$Cl(CH$_3$)]$^+$ + Cl + CH$_3$CH$_3$ + (CH$_3$)** **[Au$_2$Cl(CH$_3$)]$^+$ + Cl(CH$_3$) + 2(CH$_3$)** [Au$_2$Cl(CH$_3$)]$^+$ + Cl(CH$_3$) + CH$_3$CH$_3$	**13.0 ± 0.2**	17.42 **13.58** **13.72** 9.88	17.29 **13.52** **13.76** 9.99
429	[Au$_2$Cl]$^+$ + 4(CH$_3$) + Cl **[Au$_2$Cl]$^+$ + HCl + 2(CH$_4$) + CHCH$_2$** **[Au$_2$Cl]$^+$ + (CH$_3$) + CH$_3$Cl + CH$_3$CH$_3$** [Au$_2$Cl]$^+$ + 2 (CH$_3$CH$_3$) + Cl	**12.2 ± 0.2**	19.11 <u>**12.54**</u> **11.57** 11.44	18.84 **12.33** **11.54** 11.30
422	[Au$_2$(CH$_2$CH$_2$)]$^+$ + 2(CH$_3$) + 2Cl + 2H **[Au$_2$(CH$_2$CH$_2$)]$^+$ + 2Cl(CH$_3$) + H$_2$** [Au$_2$(CH$_2$CH$_2$)]$^+$ + CH$_3$CH$_3$ + 2HCl	**10.3 ± 0.3**	22.20 <u>**10.53**</u> 9.51	21.84 10.46 9.44
408	[Au(CH)AuH]$^+$ + 3(CH$_3$) + 2Cl + H **[Au(CH)AuH]$^+$ + CH$_2$CH$_2$ + 2HCl + CH$_4$** **[Au(CH)AuH]$^+$ + CH$_3$CH$_3$ + HCl + Cl(CH$_3$)**	**13.2 ± 0.2**	24.57 **13.35** **12.60**	24.14 **13.06** **12.54**
394	[Au$_2$]$^+$ + 4(CH$_3$) + 2Cl **[Au$_2$]$^+$ + 2(CH$_3$) + 2(CH$_3$Cl)** **[Au$_2$]$^+$ + CH$_2$CH$_2$ + 2(CH$_3$) + 2HCl** **[Au$_2$]$^+$ + 2(CH$_3$CH$_3$) + 2Cl** [Au$_2$]$^+$ + 2(CH$_3$CH$_3$) + Cl$_2$ [Au$_2$]$^+$ + CH$_3$CH$_3$ + 2(CH$_3$Cl)	**15.3 ± 0.2**	22.39 <u>**14.99**</u> <u>**15.56**</u> **14.71** 11.99 11.15	22.09 **15.05** **15.39** **14.56** 12.14 11.28
227	[(CH$_3$)Au(CH$_3$)]$^+$ + 2(CH$_3$) + 2Cl + Au **[(CH$_3$)Au(CH$_3$)]$^+$ + CH$_3$CH$_3$ + Cl$_2$ + Au** **[(CH$_3$)Au(CH$_3$)]$^+$ + AuCl + CH$_3$CH$_3$ + Cl** [(CH$_3$)Au(CH$_3$)]$^+$ + 2Cl(CH$_3$) + Au [(CH$_3$)Au(CH$_3$)]$^+$ + CH$_2$CH$_2$ + 2HCl + Au	**12.4 ± 0.2**	17.81 **11.24** **12.46** 10.41 10.98	18.72 **12.54** **12.20** 11.68 12.01

However, considering the formation of ethane CH_3CH_3 in this process results in threshold values of 9.67 and 10.29 eV at the respective levels of theory. Similar to the parent ion, the DFT value agrees well with the experimental AE while the DLPNO-CCSD(T)-TZVP value is about 0.3 eV above its higher confidence limit. We also calculated the threshold values at the DLPNO-CCSD(T) level using the smaller SPV basis set and these values are given in table S7 with the supporting information. At that level, the agreement with the experimental ionization energy and the AE for the loss of two methyl groups is good. However, while the AEs for the more complex processes are generally well reproduced at the TZVP level we found these to be underestimated when using the SPV basis set.

For the loss of three methyl ligands, m/z 479 we derive an AE of 11.4 ± 0.2, while the calculated threshold for this process without new bond formation is found to be 15.01 and 15.04 eV at the, respectively levels of theory, hence also here new bonds must be formed for this process to be thermochemically possible at its AE.

Considering the formation of ethane from two of the methyl radicals, the threshold values are lowered to 11.18 and 11.27 eV, respectively, which agree well with the experimental AE at both levels of theory. For the final reaction in this progression, i.e., the loss of all four methyl ligands, m/z 464, we determine an AE of 10.1 ± 0.2 eV, while the threshold values without the consideration of new bond formations are about 7 eV higher at both levels of theory. Considering the formation of two ethane in this process lowers these threshold values to 9.65 and 10.12 eV. Here the value at the DFT level of theory is somewhat below the confidence limit of the AE, but the value at the DLPNO-CCSD(T)-TZVP level of theory agrees well with the experimental AE value.

The next progression observed in the mass spectrum; m/z 458, 444 and 429, constitutes a progressive loss of the methyl ligands along with the loss of one chlorine and partly additional hydrogen loss. We find the AEs for these channels to be 10.3 ± 0.2, 13.0 ± 0.2 and 12.2 ± 0.2 eV,

respectively, and considering only single bond ruptures and no new bond formations results also here in threshold values that are considerably higher than the respective AEs. We have considered several potential reaction paths leading to these fragments and for m/z 458 (AE = 10.3 ± 0.2 eV), the formation of ethane and HCl, where the threshold values are 10.46 and 10.41 eV at the PBE0-TZVP and DLPNO-CCSD(T)-TZVP levels of theory, respectively, is in good agreement with the experimental AE. The formation of methane and chloromethane is the next closest match with thresholds of 10.64 and 10.60 eV at the respective levels of theory. Similarly, for the loss of chlorine and three methyl groups, m/z 444 (13.0 ± 0.2 eV) we get the closest agreements when considering the formation of ethane, atomic chlorine, and the methyl radical where the threshold values are 13.58 and 13.52 eV at the respective levels of theory, and the formation of chloromethane and two methyl radicals where the respective threshold values are 13.72 and 13.76 eV. Considering the formation of chloromethane and ethane, on the other hand, brings the respective thresholds down to 9.88 and 9.99 eV, which is at both levels of theory about 3 eV below the experimental AE. Finally, for the formation of [Au$_2$Cl]$^+$, m/z 429 (12.2 ± 0.2 eV), we find the closest match with the experimental AE when considering significant rearrangements leading to the neutral counterparts HCl, 2CH$_4$ and C$_2$H$_3$. The threshold value for this reaction is 12.54 and 12.33 eV at the PBE0-TZVP and DLPNO-CCSD(T)-TZVP levels of theory, respectively. However, this reaction requires, in addition to new bond formations, the migration of three hydrogen between the respective ligands lost. The respective threshold values for the formation of ethane, chloromethane and the methyl radical as the neutral counterparts are 11.57 and 11.54 eV, i.e., 0.63 and 0.66 eV below the experimental AE, respectively. However, as discussed above, such extensive rearrangement reactions are likely to be associated with non-negligible activation barriers and may also be subject to kinetic shift of the AEs,[44,45,59] making them appear at higher energies. We thus also consider the formation of ethane and chloromethane to be a potential

reaction path for the formation of $[Au_2Cl]^+$. Considering the formation of two ethane molecules and the chlorine radical as the neutral counterparts, on the other hand, lowers these threshold values further, to 11.44 and 11.30 eV, respectively, i.e., about 1 eV below the experimental AE. The next progression is that of the loss of both chlorine ligands and 2, 3 and 4 methyl ligands and is partly associated with additional loss of hydrogen. The resulting positive ion fragments appear at m/z 422, 408 and 394, and are assigned to $[Au_2(C_2H_4)]^+$, $[Au_2(CH_2)]^+$ and $[Au_2]^+$, respectively. The AE for m/z 422; $[Au_2(C_2H_4)]^+$, is found to be 10.3 ± 0.3 eV, which agrees with the threshold values of 10.53 and 10.46 eV calculated at the respective levels of theory when assuming the formation of two chloromethanes and one hydrogen molecule as the neutral counterparts. The threshold for the formation of ethane and two HCl as the neutral counterparts is, however, found to be 9.51 and 9.44 eV, respectively, i.e., 0.79 and 0.86 eV below the experimental AE. The m/z 408 constitutes the formation of $[Au_2(CH_2)]^+$, that is, the loss of three methyl groups and one hydrogen. We derive an AE of 13.2 ± 0.2 eV for this fragment, which agrees well with the threshold values of 13.35 and 13.06 eV, calculated at the DFT and coupled cluster level of theory (TZVP), respectively for the formation of ethene (CH_2CH_2), 2 HCl and methane as the neutral counterparts. Considering the formation of ethane (CH_3CH_3), HCl and chloromethane as the neutral counterparts, lowers the respective threshold values 12.60 to 12.54 eV, i.e., 0.40 and 0.46 eV below the lower confidence limit, respectively. Under the same considerations of potential activation barriers on these reaction paths, we do not exclude this reaction as potential rout for the formation of $[Au_2(CH_2)]^+$. Finally, for the formation of $[Au_2]^+$, m/z 394, we derive an AE of 15.3 ± 0.2 eV. Similar to the formation of $[Au_2(CH_2)]^+$, considering the ethene (CH_2CH_2), two HCl and two methyl radicals as the neutral counter parts, results in threshold values of 15.56 and 15.39 eV, at the respective levels of theory. From these, the coupled cluster value agrees well with the experimental AE ant the DFT value is only marginally above its higher confidence limit. Considering the formation of chloromethane

and two methyl radicals gives threshold values of 14.99 and 15.05 eV, respectively, which also agrees with the AE at the coupled cluster level and is only slightly below the confidence limits at the DFT level. The formation of two ethane and two atomic chlorine, on the other hand, gives values of 14.56 and 14.71 eV, respectively, which is about 0.5 and 0.4 eV below the lower limit of the AE for $[Au_2(CH_2)]^+$ and the formation of two ethane and Cl_2 or ethane and two chloromethanes as the neutral counterparts brings the threshold values around 3 eV below the experimental AE at both levels of theory. The last methyl loss progression constitutes the loss of one of the gold atoms, both chlorine and two, three and four methyl ligands appearing in the mass spectrum at m/z 227/225, 212 and 197, respectively. From these, m/z 225 is attributed to additional loss of two hydrogen as compared to m/z 227, and 197 is attributed to Au^+. The intensities of these ion signals are comparatively low and the number of combinations of neutral fragments is large. We have nonetheless determined the AEs for m/z 227 and 225 (see supporting material for m/z 225). For m/z 227 we find the AE to be 12.4 ± 0.2 which agrees at the coupled cluster level of theory with the formation of ethane, Cl_2 and atomic chlorine (12.54 eV) and with the formation of ethane, AuCl and atomic chlorine (12.20 eV). At the coupled cluster level, however, the thresholds for the formation of ethene, 2 HCl and atomic gold and for the formation of two chloromethanes and atomic gold are only 0.2 and 0.5 eV below the lower confidence limit of the experimental AE.

Several other possible combinations of neutral fragments were considered for all m/z ratios and a complete list of these can be found in Table S7 of the supporting material.

It is clear from these considerations that DI of $[(CH_3)_2AuCl]_2$ is dominated by rearrangement reactions with multiple bond ruptures and new bond formations. For the loss of the methyl groups, without chlorine loss, the assignment of the neutral counterparts is fairly straight forward and is dominated by ethane formation from the respective methyl groups. For the additional loss of one or two chlorine, which is also in part associated with hydrogen loss, the assignment of the neutral

counterparts is more complex. This is especially true as activation barriers are likely to influence the experimentally determined AEs of the respective cationic fragments, and considering the extent of these processes, kinetic shift may also play a role. Thus, reactions where the calculated thresholds are somewhat lower than the respective AEs cannot be excluded, and we can in many cases not offer a conclusive assignment to one single set of neutral counterparts. Notwithstanding, it is clear, that the formation of ethane and hydrochloric acid and/or chloromethane plays an important role in these fragmentation processes.
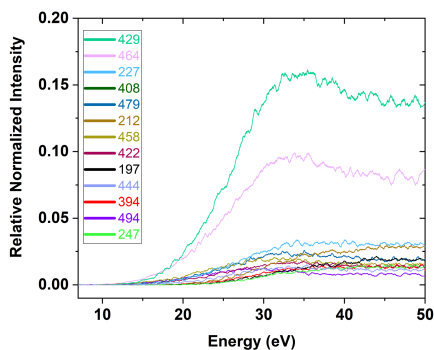
Figure 8. Positive ion yields for the most significant DI fragments in the incident electron energy range from below their threshold up to 50 eV. The ion yields are normalized with respect to the pressure and the signal intensity of Ar^+ from Ar at 50 eV.

In FEBID the effective damage yield[27,60] for a specific precursor will be a convolution of the energy distribution of the electrons involved, i.e., of the primary, secondary and inelastic scattered electrons, and the energy dependence of the cross sections for the respective electron induced processes. For more quantitative comparison with the UHV FEBID experiments presented here and the earlier HV experiments on this precursor, Figure 8 shows the energy dependence of the relative cross sections for the most significant DI processes from below their thresholds to 50 eV.

The intensities are normalized to the pressure and the signal intensity of Ar^+ from Ar at 50 eV electron energy.

Table 2 show the integral intensities of these fragments over the presented energy range, along with their relative peak intensities as observed in the mass spectrum shown in Figure 6. These are normalized with respect to the highest intensity fragment m/z $[Au_2Cl]^+$ (set as 100). At the bottom of the table the relative intensities are translated to average carbon and chlorine loss by summing the contributions from all fragments weighted by their respective carbon and chlorine losses and dividing by the total intensity of all DI fragments. Finally, the expected average elemental composition of a deposit that would form, if only these DI fragmentation processes were operational is shown. This is calculated from the relative intensities and composition of the gold containing positive ions and the neutral fragments, while desorption of all other fragments is assumed in this *Gedankenexperiment*. From the integrated intensity in the ion yield curves we derive an average chlorine loss of 0.96 and average carbon loss of 3.42, and from the mass spectra these values are 0.92 and 3.39, respectively. This marginal difference reflects the lesser contribution of the higher threshold fragments to the integral intensities as well as the shape of the respective ion yield curves. In the hypothetic deposition experiment this would lead to a deposit composed of about 55 at% Au, 29 at% Cl and 16 at % C. With respect to the high gold content, this is in line with the UHV FEBID deposits, however, the carbon content is significantly lower than observed in FEBID, and most noticeably, in both the UHV and HV depositions, chlorine is as good as quantitatively removed, while on average only half of the chlorine is cleaved from parent molecule in DI. It is thus clear that the unaltered DI processes, as they are observed in the gas phase under single collision conditions cannot explain the deposits composition observed in FEBID.

Table 2. Relative intensities of DI fragments from $Au_2(CH_3)_2Cl_2$ calculated from the peak intensities at 50 eV as they appear in the mass spectrum (Fig. 6) and from the areas under the respective ion yield curves shown in Fig. 7. The intensities are normalized with respect to the highest intensity fragment m/z $[Au_2Cl]^+$, that is set as 100. Also shown is the composition of a hypothetical deposit that would be formed if its formation would be governed by DI as observed in the gas phase. For comparison, the composition of the FEBID deposits from the current UHV and the previous HV experiments are shown at the bottom of the table.

m/z	Fragment	Relative DI Yield (Integration)	Relative DI Yield (intensity)		
494	$[Au_2Cl_2(CH_3)_2$	7.20	9.2		
479	$[Au_2Cl_2(CH_3)]$	15.13	19.02		
464	$[Au_2Cl_2]^+$	62.36	67.08		
458	$[Au_2Cl(C_2H_5)]$	12.46	20.45		
444	$[Au_2Cl(CH_3)]^+$	8.24	9.41		
429	$[Au_2Cl]^+$	100	100		
422	$[Au_2(C_2H_4)]^+$	10.78	11.45		
408	$[Au_2(CH_2)]^+$	15.69	17.18		
394	$[Au_2]^+$	7.62	11.04		
247	$[(CH_3)AuCl]^+$	6.58	7.57		
227	$[(CH_3)_2Au]^+$	19.97	17.8		
212	$[(CH_3)Au]^+$	13.65	9.82		
197	$[Au]^+$	8.49	6.95		
Chlorine loss		0.96	0.92		
Carbon loss		3.42	3.39		
Expect. comp. from DI	55 at. % Au	29 at. % Cl	16 at. % C		
UHV-FEBID composition	45-61 at. % Au	1-2 at. % Cl	38-49 at. % C	5-8 at. % Sn	
HV-FEBID composition	29-41 at. % Au	2-6 at. % Cl	53-68 at. % C		

To explore the potential role of DEA in the deposition formation, Figure 9a shows negative ion mass spectrum in the m/z range from 10 to 550.
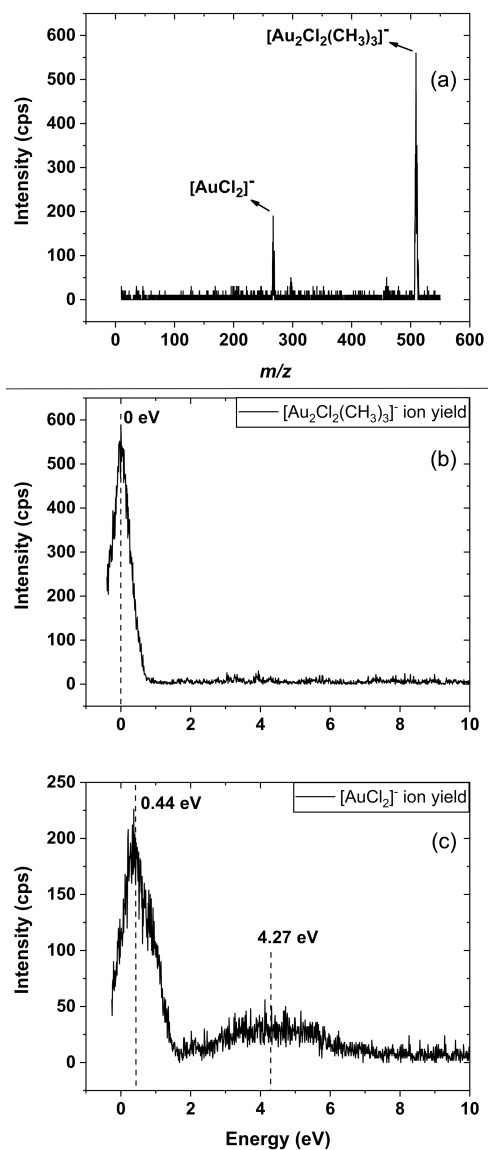
Figure 9. a) Cumulative negative ion mass spectrum composed of the sum of individual mass spectra recorded at 1 eV intervals in the energy range from 0 to 8 eV and covering the *m/z* range from about 10 to 550. b) and c) Negative ion yield curves of the most significant fragments observed in DEA to $Au_2Cl_2(CH_3)_4$ in the energy range from about 0 to 10 eV. b) $[Au_2Cl_2(CH_3)_3]^-$, *m/z* 509 and c) $AuCl_2^-$, *m/z* 267.

As DEA is a resonant process it proceeds within distinct energy ranges. Thus, to cover the relevant energy, the mass spectrum shown in Fig 9a is the sum of individual mass spectra recorded in the electron energy range from about 0 to 10 eV at 1 eV intervals. Figures 9b and c show the respective ion yield curves for the dominating fragments in this energy range.

It is clear from figure 9 that fragmentation through DEA is significantly less extensive than what is observed in DI. In fact, only two significant channels are observed; the loss of a single methyl group leading to the formation of $[Au_2Cl_2(CH_3)_3]^-$, m/z 509, which appears through a comparatively narrow contribution peaking at the 0 eV threshold, and the formation of $AuCl_2^-$, m/z 267, which low energy contribution peaks at about 0.4 eV. In addition, a broader and lower intensity contribution to the $AuCl_2^-$ signal is observed at around 4 eV. In DEA the cross section for the attachment process is inversely proportional to the square root of the incident electron energy[25] and the attachment cross sections are highest at the 0 eV threshold. Consequently, exothermic DEA processes that proceed at the 0 eV threshold are generally the most efficient. This is also the case here, and we find the single methyl loss leading to the formation of $[Au_2Cl_2(CH_3)_3]^-$ to be exothermic by 0.96 and 0.88 eV at the PBE0-TZVP and DLPNO-CCSD(T)-TZVP levels of theory, respectively. Similarly, we find the formation of $[AuCl_2]^-$ to be exothermic by about 2 eV at both levels of theory when presuming the formation of two neutral ethane molecules and elemental gold in the process. We also calculated the thresholds for the formation of $Au(CH_3)_2$ and one ethane molecule as well as $AuCH_3$, ethane and methane as the neutral counterparts in this process and we also find these channels to be exothermic at both levels of theory. The calculated thresholds for the negative ion formation are shown in Table S7 with the supporting material. From the width of the $[Au_2Cl_2(CH_3)_3]^-$ and $AuCl_2^-$ contributions in their ion yield curves, we anticipate that these are from overlapping resonances associated with single electron occupation of the lowest lying molecular orbitals. And, while the presumably faster loss of a single methyl group dominates

at threshold, $AuCl_2^-$ is only produced through the high energy flank. Applying the same considerations here as for the positive ions, we can calculate an expected elemental composition for a deposit that would be formed if only the unaltered DEA channels, as they proceed in the gas phase under single collision conditions, were active. By using the integrated intensities from the ion yield curves shown in figure 9 and presuming that the elemental gold stays on the surface, the expected composition would be about 32 at% gold, 32 at% chlorine and 36 at% carbon. Hence, in DEA no chlorine loss is observed as compared to as good as quantitative chlorine loss in the FEBID experiments, under HV as well as UHV.

Gas phase, UHV and HV FEBID.

When comparing FEBID deposits produced from $[(CH_3)_2AuCl]_2$ under UHV and HV conditions it is apparent that the compositions are qualitatively the same, i.e., high gold content, close to quantitative removal of the chlorine and predominantly carbon residues. In the UHV experiments, however, the residual carbon is as expected less, and though not as markedly, the chlorine removal is also more complete under UHV. Despite the fact that both UHV and HV deposits offer qualitatively the same picture, it is clear that significantly higher gold content is achievable under UHV. It is also apparent, that the composition of the deposit is dependent on the deposition current and the cleanliness of the substrate. Though we have not considered neutral dissociation up on electron excitation in the current gas phase experiments, it is clear, that the electron induced fragmentation of $[(CH_3)_2AuCl]_2$ is strongly influenced in the FEBID experiments as compared to the single collision conditions in the gas phase. Interestingly, more extensive fragmentation is observed in the FEBID experiment, while from energy dissipation considerations alone, one would rather expect stabilization and thus the opposite. In DI, rearrangement reactions are found to be dominant among the fragmentation processes, rather than direct dissociation without new bond

formation. Such rearrangement reactions generally proceed along convoluted paths on the respective potential energy surfaces that are likely to be altered in the condensed phase or on a substrates surface. Furthermore, considering the current electron dose of about 5×10^{19} e$^-$/cm^2 and the volume of the resulting deposits, electron induced secondary reactions may also play a role. Assuming dense pacing and a molecular diameter of 1 nm, a deposit of 4×4 µm^2 area and 20 nm high, consists of about 3×10^8 molecules. The number of electrons in this volume has been exposed to is about 8×10^{12}. Respectively, a monolayer consists of 1.5×10^7 molecules has been exposed to 4×10^{11} electrons. This corresponds to about 35,000 electrons per molecule. Assuming a generic cross section of 10^{-16} cm^2, which is on the order of magnitude for DI and DI of the FEBID precursor Co(CO)$_3$(NO)[60][61] and Pt(PF$_3$)$_4$,[62] the reactive area of this mono layer is 0.15 µm^2. Statistically this implies about 300 reactive incidents per molecule if the cross section is assumed to stay unchanged. This is clearly not a quantitative assessment but shows that multiple electron collisions may play a role in FEBID, while the gas phase experiments are conducted under single collisions conditions. In the last decade, interest in organometallic FEBID precursors containing the higher halogens, chlorine, bromine and iodine, has increased and in addition to the gold(I) precursors XAuL (L = P(NMe$_2$)$_3$, PMe$_3$, CNMe, CN^{t}Bu, P(OCH$_2$CF$_3$)$_3$; X = Cl, Br, I),[63] FEBID related studies on Ru(CO)$_4$I$_2$,[30] (η^3-C$_3$H$_5$)Ru(CO)$_3$X (X = Cl, Br),[44,64,65] Pt(NH$_3$)$_2$Cl$_2$,[66][67] and Pt(CO)$_2$X$_2$ (X = Cl, Br)[43,68–71] have been published. These include post deposition purification studies,[72][73] thin layer exposure to electrons at around 500 eV,[74,75] gas phase studies under single collision condition[27,76] and FEBID under HV and UHV conditions.[29,71] Most noticeably, the platinum precursors Pt(CO)$_2$X$_2$ (X = Cl, Br) have been studied with respect to their low energy electron interaction in the gas phase,[70][43] in thin layers under non-steady state conditions,[68] in comparative FEBID experiments under HV and UHV conditions[71] and with respect to post deposition purification through electron exposure and through reductive halogen removal using

atomic hydrogen.[69] In an early study by Spencer *et al.*[68], 0.7 nm layers of $Pt(CO)_2Cl_2$ were exposed to 500 eV electrons and desorbing ligands were monitored by mass spectrometry, while the development of the deposit was monitored using XPS. It was found that the initial decomposition, up to an electron dose of about 10^{-16} was characterized by a rapid CO loss, leaving a deposit of about 1:2 Pt:Cl ratio. However, a prolonged exposure up to doses around 10^{19} e$^-$/cm^2, which is the order of magnitude applied here, led to as good as complete removal of the halogen. While the first step was in good agreement with the observations in the gas phase under single collision conditions, the second step indicated that pure deposits were achievable through prolonged electron exposure of the deposit formed in the first step. This was further explored in a post deposition purification study where two approaches were taken; prolonged electron exposure and reductive halogen removal using atomic hydrogen. While atomic hydrogen was found to effectively remove the halogen, prolonged electron exposure was only found to have significant influence at the deposits surface. The halogen content in the bulk, on the other hand, was not markedly reduced. Interestingly, a recent comparative deposition study using a SEM under HV and an Auger spectrometer under UHV showed significant differences in the deposit's composition.[71] While the deposits fabricated in the UHV chamber contained primarily halogen contamination and comparatively low carbon content, carbon was the main component in the deposits under HV, while the halogen content was as low as 7.5-8 at%. It was pointed out that this might be due to reductive removal of the halogen through reactions with background water, which is of considerably higher concentration in the HV chamber than the UHV chamber. While HCl formation is apparently significant in DI of $[(CH_3)_2AuCl]_2$ in the current experiment and may in part be responsible for the etching effects observed, there are no indications that the higher background water content in the HV experiments influences the composition of the deposits. Electron induced secondary reactions, on the other hand, may play a role, especially as the growth

rate of the deposits are comparatively low, and correspondingly the electron exposure of each monolayer is high. This could be probed in a non-steady state experiment similar to those reported for Pt(CO)$_2$X$_2$ (X = Cl, Br) and several other potential FEBID precursors.[68]

Conclusions

In the current study we have evaluated the performance of [(CH$_3$)$_2$AuCl]$_2$ as a precursor for gold deposition in FEBID in an UHV setup, at different beam currents but constant dose, and on different substrates. The elemental composition of the deposits was determined by AES and their morphology and crystal structure was examined using SEM, AFM, HAADF-STEM and SAED. Complementary DI and DEA experiments were carried out under single collision conditions in the gas phase to better understand the underlying electron induced processes and quantum chemical threshold calculations were used to aid the interpretation of the gas phase data.

Generally, we find [(CH$_3$)$_2$AuCl]$_2$ suitable for FEBID, both with respect to its volatility and stability, and no indication of decomposition is observed in the DI experiments. Interestingly, a complete chlorine removal is observed in the FEBID experiments and a gold content as high as 61 at.% Au was obtained with 1.5 nA beam current on a Si(111) substrate pre-cleaned by Ar$^+$ sputtering.. On an untreated SiO$_2$(500 nm)/Si(111) surface at 0.4, 1.5 and 3 nA. the gold content of the deposits was found to be 45, 50 and 52 at.% Au, respectively. In a previous FEBID study under HV conditions,[32] these were found to be 29 and 41 at% Au at beam currents of 0.1 and 0.4 nA, respectively, but also here a close to quantitative removal of the chlorine was observed. It is thus clear that the gold content is dependent on the cleanliness of the substrate and the deposition environment in general, but also on the electron beam current. With respect to the morphology, the deposits were found to be composed of a bimodal size distribution of predominantly spherical nanoparticles with the dominant component being uniformly distributed particles of less than 5 nm

diameter but also a non-uniform distribution of larger particles (10-15 nm) is observed. The deposit was found to be polycrystalline, with the close-packed, face-centered cubic crystal structure of bulk gold. In the gas phase we find DEA to be at large limited to single methyl loss leading to the observation of $[M - CH_3]^-$, and the formation of $AuCl_2^-$. Hence, no chlorine loss is observed in DEA. Dissociative ionization, on the other hand, is found to be extensive and governed by rearrangement reactions and new bond formations. These are to a large extent associated with neutral ethane formation. HCl formation is also likely to be significant, though definite distinction between channels where HCl is formed and where CH_3Cl is formed is not always provided. Notwithstanding, on average only 50% of the chlorine is lost from the central gold atoms in DI and none in DEA, as compared to the close to quantitative chlorine loss in FEBID. Contrarily, more efficient methyl loss is observed in DI than is reflected in the FEBID deposits. We note that neutral dissociation up on electron excitation was not probed here, but it is nonetheless clear that chlorine loss through electron induced fragmentation in the FEBID experiments is considerably more extensive than what may be accounted for under single collision conditions in the gas phase. We anticipate that this is due to electron induced secondary reactions, and that the initial step in the fragmentation process is rather dominated by DI than DEA. This is a hypothesis that can readily be probed in non-steady state experiments, similar to those conducted by Spencer *et al.*[68] for $Pt(CO)_2Cl_2$. In such experiments, electron-dose dependence of the composition of thin layers of *cis*-$Pt(CO)_2Cl_2$ can be monitored by means of XPS and neutral desorbing fragments may be detected by means of mass spectrometry. This would also allow definite distinction between fragmentation channels where HCl is formed and where CH_3Cl is formed. The latter being an important parameter due to potential etching effects through HCl formation and generally as HCl outgassing may also cause instrumental problems.

Overall, $[(CH_3)_2AuCl]_2$ is found to have good potential for the fabrication of high gold content deposits in FEBID, but as has been observed for other FEBID precursors, aliphatic ligands are generally not good leaving groups. Thus, to reduce the carbon content of depositions from $[(CH_3)_2AuCl]_2$, in situ or postdeposition purification protocols would need to be incorporated into the deposition process. Furthermore, it would be advantageous to better understand the mechanism of the halogen removal as that might be critical with respect to the growth rates achievable.

Methods

Precursor synthesis and Precursor handling.

$[(CH_3)_2AuCl]_2$ was synthesized by following the steps described by Paul and Schmidbauer.[33] The synthesis was performed under a nitrogen atmosphere using pre-dried solvents and standard Schlenk techniques. The starting material was $H[AuCl_4]\cdot 3H_2O$, which was obtained in the form of orange crystals by dissolving gold metal in aqua regia, evaporating all liquids and, after the addition of concentrated HCl, evaporating all liquids again. The quality of the compound was checked and confirmed by ^1H NMR spectroscopy.

The so synthesized $[(CH_3)_2AuCl]_2$ precursor was kept at 253 K and filled into a stainless-steel precursor reservoir under nitrogen atmosphere (glove box). The reservoir with a small glass-window was chosen to be able to check the precursor quality and possible degradation visually. The filled reservoir was directly attached to the analysis chamber and wrapped in aluminum foil to avoid photodecomposition during the experiments.

Deposition and Characterization.

FEBID structures were fabricated in a commercial UHV system (Multiscanlab, Omicron Nanotechnology, Germany) with a base pressure of $p < 2 \times 10^{-10}$ mbar. The system consists of a UHV compatible electron column (Leo Gemini) for scanning electron microscopy (SEM, nominal resolution better than 3 nm), electron beam-based lithography (EBL, FEBID), and local Auger electron spectroscopy (AES) using a hemispherical electron energy analyzer with a resolution better than 10 nm. The Auger spectra (magnification: 100 kX; spectra area: 1.2×0.9 μm^2) were recorded with an acceleration voltage of 15 kV and a beam current of 3 nA. Electron exposures for FEBID were performed at a beam energy of 5 keV and beam currents of 0.4, 1.5, and 3 nA. A quadrupole mass spectrometer (Pfeiffer / Prisma QMS 200M) is integrated in the system and was used to acquire mass spectra (MS) of the gas phase $[(CH_3)_2AuCl]_2$ precursor at room temperature (298 K). The lithographic processes were controlled through a custom-developed software, based on LabVIEW 8.6 (National Instruments) and a high-speed DAC PCIe-card (M2i.6021-exp, Spectrum GmbH, Germany).[34] The lithographic parameters were a step size of 6.2 nm and a sweep number of 10. SEM images were acquired at a beam energy of 15 keV and a current of 0.4 nA with a SmartSEM (Zeiss). Minor contrast and brightness adjustments were applied.

The precursor gas was dosed onto the sample surface through a nozzle. During the FEBID process, the precursor container was held at room temperature as the precursor, $[(CH_3)_2AuCl]_2$, was found to be sufficiently volatile to transfer from the container into the UHV chamber via the gas-injection system. For the experiments, the precursor pressure in the chamber was adjusted to $6.0\text{-}9.0 \times 10^{-7}$ mbar. Based on simulations using GIS Simulator (version 1.5)[35], the local pressure at the sample surface was estimated to be about 30 times that of the chamber pressure, resulting in a local pressure at the substrate surface of about $2.0\text{-}3.0 \times 10^{-5}$ mbar.

FEBID structures were deposited and investigated on two different substrates, that is SiO$_2$ (500 nm) / Si(111) and thermally cleaned Si(111). No specific preparation was applied to clean the SiO$_2$

(500 nm) / Si(111) sample. Atomic force microscopy (AFM) was performed with a JPK NanoWizard 4 by using the noncontact mode and an FEI Titan Themis³ 300 transmission electron microscope was used to obtain HAADF-STEM and SAED results.

Gas Phase experiments.

The gas phase DI and DEA experiments were conducted under single collision conditions in a crossed electron-molecular beam instrument that has been described in detail elsewhere[36] and only a short description is given here. It consists of an effusive stainless-steel capillary gas inlet system, a trochoidal electron monochromator and a quadrupole mass spectrometer (Hiden EPIC 1000) with a channelton detection system and can be operated in positive or negative ion mode. The system is housed in a HV chamber with a typical base pressure of 2×10^{-8} mbar. In the interaction section of the chamber the electron beam crosses the effusive molecular beam and charged products generated in the respective electron-molecule interactions are extracted into a quadrupole mass spectrometer that is orthogonal to both the molecular beam and the electron beam. The working pressure during the current experiments was maintained at around 4×10^{-7} mbar and the TEM is kept at 393 K with two halogen lamps to prevent condensation of precursor molecules or background contaminations on the electrical lens components. The electron energy resolution was around 140 meV, as determined from the full width at half maximum (FWHM) of the SF_6^- formation from SF_6 at 0 eV incident energy. Mass spectra are recorded at fixed electron energies by scanning through the relevant m/z range, and ion yields are recorded at a fixed m/z ratio by scanning through the respective electron energy range. Positive ion MS were recorded at 50 eV incident electron energy and negative ion MS at 0, 1, 2,…10 eV incident electron energies. In negative ion mode the electron energy scale was calibrated by the SF_6^- formation from SF_6 at 0 eV, and in positive ion mode by the ionization energy of Ar.[37] The positive ion yields were

normalized relative to the target gas pressure and the Ar^+ signal intensity from Ar at 50 eV and the negative ion yields to the target pressure and the signal intensity of SF_6^- from SF_6 at 0 eV. Appearance energies of positive ions were calculated by fitting the onset of the respective ion yields with a Wannier type[38] function of the form:

$$f(x) = \begin{cases} b & , \quad E \leq AE \\ b + a(E - AE)^d, & \quad E > AE \end{cases}$$

where AE denotes the appearance energy, E the incident electron energy, b accounts for constant background signal, a is a scaling coefficient, and d an exponential factor describing the onset region. The AE values reported are the average from fits to 3 ion yield curves recorded on different days and the standard deviation reported is that of the respective averages rounded up to the nearest 100 meV. The confidence limits reported are set by visual inspection to bracket the onset of the individual curves and are equal to or higher than the standard deviations from the fittings.

Quantum chemical calculations.

The ORCA program, version 4.1, was used as the platform for all quantum chemical computations.[39] For all geometry optimization we used the hybride GGA fuctional PBE0 with the def2-TZVP basis set and the D3BJ dispersion correction developed by Grimme.[40] This was based on an evaluation of DFT functionals for gold(I) and gold(III) hydrocarbon by Kang et al.[41] who found the hybrid GGA functional PBE0 with a TZ basis set to be the best for geometry optimisation and a later study by Kepp et al.[42] who found PBE and TPSS functionals with dispersion corrections to generally perform well for evaluation of gold bond dissociation enthalpies. The restricted Kohn-Sham (RKS) formalism was used for closed-shell systems and the unrestricted (UKS) for open-shell systems. Tight SCF settings were aplied in the geometry optimizations and the TPSS/def2-TZVP single point energies were calculated with normal SCF settings. Positive harmonic vibrational frequencies derived at the PBE0/def2-TZVP level of theory demonstrated that all

structures of the parent molecule and its fragments were stationary points on the respective potential energy surfaces. These frequencies were then used to compute zero-point vibrational energies and thermal corrections. For a variety of FEBID precursors, the optimization of the geometry at the DFT level of theory and the determination of the energy of the system using post-HF approaches such as CCSD(T) have been reported earlier.[43–45] In the current study, single point coupled-cluster computations were also done on the optimized geometries. These were done at the DLPNO-CCSD(T)/TZVP level of theory using the TZVP/c auxiliary basis set and were carried out with normal PNO settings.

Threshold energies for individual processes were calculated at both levels of theory by substracting the single point energies of the optimized geometries of the respective fragments formed from those of the parent molecule, including the respective ZPVEs and thermal energy corrections in all cases. Several alternative reaction paths, including rearrangement reactions were calculated for all fragmentation processes considered.

Supporting Information

Additional details on preparation of lamella for STEM and SAED experiments (S1); the particle size analysis by Feret diameter method (S2); the comparison of particle numbers versus particle diameters with respect to the different beam currents (S3); the line profiles of AFM image (S4); the AES results on SiO_2 substrate before and after surface treatment by Ar^+ sputtering (S5); the Cartesian coordinates (Å) of optimized geometries and their respective Gibbs free energy (Eh) calculated at the PBE0/def2-TZVP level of theory (S6); and full table of calculated threshold values for potential reaction pathways leading to the observed cations and anions due to DI and

DEA processes at the PBE0/def2-TZVP, DLPNO-CCSD(T)-SVP, and DLPNO-CCSD(T)-TZVP levels of theory (S7).

Author Information

Corresponding Authors

*Oddur Ingólfsson - Science Institute and Department of Chemistry, University of Iceland, Dunhagi 3, 107 Reykjavík, Iceland; Email: odduring@hi.is

*Hans-Peter Steinrück - Physikalische Chemie II, Friedrich-Alexander Universität Erlangen-Nürnberg, 91058 Erlangen, Germany; Email: Hans-Peter.Steinrueck@fau.de

Author Contributions

Elif Bilgilisoy: Investigation, Formal analysis, Visualization, Writing – Original Draft. **Ali Kamali:** Investigation, Formal analysis, Visualization, Writing – Original Draft. **Thomas Xaver Gentner:** Investigation, Resources. **Gerd Ballmann:** Investigation, Resources. **Sjoerd Harder:** Supervision. **Hubertus Marbach:** Supervision, Conceptualization, Project administration, Methodology, Funding acquisition, Writing – Review & Editing. **Oddur Ingólfsson:** Supervision, Conceptualization, Project administration, Methodology, Funding acquisition, Writing – Review & Editing. **Hans-Peter Steinrück:** Supervision, Funding acquisition, Writing – Review & Editing. Elif Bilgilisoy and Ali Kamali have contributed equally to this work and share the first co-authorship (indicated by the symbol ‡).

Notes

The authors declare no conflict of interest.

References

(1)   Sharifi, M.; Attar, F.; Saboury, A. A.; Akhtari, K.; Hooshmand, N.; Hasan, A.; El-Sayed, M. A.; Falahati, M. Plasmonic Gold Nanoparticles: Optical Manipulation, Imaging, Drug Delivery and Therapy. *Journal of Controlled Release*. Elsevier B.V. October 1, 2019, pp 170–189. https://doi.org/10.1016/j.jconrel.2019.08.032.

(2)   Shukla, R.; Bansal, V.; Chaudhary, M.; Basu, A.; Bhonde, R. R.; Sastry, M. Biocompatibility of Gold Nanoparticles and Their Endocytotic Fate inside the Cellular Compartment: A Microscopic Overview. *Langmuir* **2005**, *21* (23), 10644–10654. https://doi.org/10.1021/la0513712.

(3)   Fraga, F.; Torres, C.; Rodríguez-Núñez, E.; Martínez-Ageitos, J. M.; Vázquez-Barreiro, E. C.; Suárez-Pereiro, F.; Miragaya, J. Characterization of an Epoxy Network with Gold Nanoparticles Using Dielectric Analysis. *Adv. Polym. Technol.* **2018**, *37* (3), 850–856. https://doi.org/10.1002/adv.21730.

(4)   Zhang, Y.; Schwartzberg, A. M.; Xu, K.; Gu, C.; Zhang, J. Z. Electrical and Thermal Conductivities of Gold and Silver Nanoparticles in Solutions and Films and Electrical Field Enhanced Surface-Enhanced Raman Scattering (SERS). *Phys. Chem. Interfaces Nanomater. IV* **2005**, *5929*, 592912. https://doi.org/10.1117/12.614499.

(5)   Takakuwa, M.; Fukuda, K.; Yokota, T.; Inoue, D.; Hashizume, D.; Umezu, S.; Someya, T. Direct Gold Bonding for Flexible Integrated Electronics. *Sci. Adv.* **2021**, *7* (52), 1–9. https://doi.org/10.1126/sciadv.abl6228.

(6)   Park, W.; Emoto, K.; Jin, Y.; Shimizu, A.; Tamma, V. A.; Zhang, W. Controlled Self-

Assembly of Gold Nanoparticles Mediated by Novel Organic Molecular Cages. *Opt. Mater. Express* **2013**, *3* (2), 205. https://doi.org/10.1364/ome.3.000205.

(7)   Mbenkum, B. N.; Schneider, A. S.; Schütz, G.; Xu, C.; Richter, G.; Van Aken, P. A.; Majer, G.; Spatz, J. P. Low-Temperature Growth of Silicon Nanotubes and Nanowires on Amorphous Substrates. *ACS Nano* **2010**, *4* (4), 1805–1812. https://doi.org/10.1021/nn900969y.

(8)   Scheeler, S. P.; Ullrich, S.; Kudera, S.; Pacholski, C. Bottom-up Fabrication of Ordered 2D and 3D Gold Nanoparticle Assemblies Showing Collective or Individual Plasmon Resonances. In *2013 7th International Congress on Advanced Electromagnetic Materials in Microwaves and Optics*; 2013; pp 313–315. https://doi.org/10.1109/MetaMaterials.2013.6809037.

(9)   Kasani, S.; Curtin, K.; Wu, N. A Review of 2D and 3D Plasmonic Nanostructure Array Patterns: Fabrication, Light Management and Sensing Applications. *Nanophotonics* **2019**, *8* (12), 2065–2089. https://doi.org/10.1515/nanoph-2019-0158.

(10)   Ali, A.; El-Mellouhi, F.; Mitra, A.; Aïssa, B. Research Progress of Plasmonic Nanostructure-Enhanced Photovoltaic Solar Cells. *Nanomaterials* **2022**, *12* (5), 788. https://doi.org/10.3390/nano12050788.

(11)   Höflich, K.; Yang, R. Bin; Berger, A.; Leuchs, G.; Christiansen, S. The Direct Writing of Plasmonic Gold Nanostructures by Electron-Beam- Induced Deposition. *Adv. Mater.* **2011**, *23* (22–23), 2657–2661. https://doi.org/10.1002/adma.201004114.

(12)   Winkler, R.; Schmidt, F. P.; Haselmann, U.; Fowlkes, J. D.; Lewis, B. B.; Kothleitner, G.;

Rack, P. D.; Plank, H. Direct-Write 3D Nanoprinting of Plasmonic Structures. *ACS Appl. Mater. Interfaces* **2017**, *9* (9), 8233–8240. https://doi.org/10.1021/acsami.6b13062.

(13) Seniutinas, G.; Balčytis, A.; Reklaitis, I.; Chen, F.; Davis, J.; David, C.; Juodkazis, S. Tipping Solutions: Emerging 3D Nano-Fabrication/-Imaging Technologies. *Nanophotonics* **2017**, *6* (5), 923–941. https://doi.org/10.1515/nanoph-2017-0008.

(14) Huth, M.; Porrati, F.; Dobrovolskiy, O. V. Focused Electron Beam Induced Deposition Meets Materials Science. **2017**. https://doi.org/10.1016/j.mee.2017.10.012.

(15) Huth, M.; Porrati, F.; Schwalb, C.; Winhold, M.; Sachser, R.; Dukic, M.; Adams, J.; Fantner, G. Focused Electron Beam Induced Deposition: A Perspective. *Beilstein J. Nanotechnol.* **2012**, *3* (1), 597–619. https://doi.org/10.3762/bjnano.3.70.

(16) Utke, I.; Hoffmann, P.; Melngailis, J. Gas-Assisted Focused Electron Beam and Ion Beam Processing and Fabrication. *J. Vac. Sci. Technol. B Microelectron. Nanom. Struct.* **2008**, *26* (4), 1197–1276. https://doi.org/10.1116/1.2955728.

(17) Van Dorp, W. F.; Hagen, C. W. A Critical Literature Review of Focused Electron Beam Induced Deposition. *J. Appl. Phys.* **2008**, *104* (8). https://doi.org/10.1063/1.2977587.

(18) Carden, W. G.; Lu, H.; Spencer, J. A.; Fairbrother, D. H.; McElwee-White, L. Mechanism-Based Design of Precursors for Focused Electron Beam-Induced Deposition. *MRS Commun.* **2018**, *8* (2), 343–357. https://doi.org/10.1557/mrc.2018.77.

(19) Folch, A. High-Vacuum versus '"Environmental"' Electron Beam Deposition. *J. Vac. Sci. Technol. B Microelectron. Nanom. Struct.* **1996**, *14* (4), 2609. https://doi.org/10.1116/1.588994.

(20) Koops, H. W. P. High-Resolution Electron-Beam Induced Deposition. *J. Vac. Sci. Technol. B Microelectron. Nanom. Struct.* **1988**, *6* (1), 477. https://doi.org/10.1116/1.584045.

(21) Mulders, J. J. L.; Belova, L. M.; Riazanova, A. Electron Beam Induced Deposition at Elevated Temperatures: Compositional Changes and Purity Improvement. *Nanotechnology* **2011**, *22* (5). https://doi.org/10.1088/0957-4484/22/5/055302.

(22) Mulders, J. J. L.; Veerhoek, J. M.; Bosch, E. G. T.; Trompenaars, P. H. F. Fabrication of Pure Gold Nanostructures by Electron Beam Induced Deposition with Au(CO)Cl Precursor: Deposition Characteristics and Primary Beam Scattering Effects. *J. Phys. D. Appl. Phys.* **2012**, *45* (47), 1–8. https://doi.org/10.1088/0022-3727/45/47/475301.

(23) Utke, I.; Hoffmann, P.; Dwir, B.; Leifer, K.; Kapon, E.; Doppelt, P. Focused Electron Beam Induced Deposition of Gold. *J. Vac. Sci. Technol. B Microelectron. Nanom. Struct.* **2000**, *18* (6), 3168. https://doi.org/10.1116/1.1319690.

(24) Swiderek, P. Electron-Induced Chemical Reactions for Surface Functionalization. In *Encyclopedia of Interfacial Chemistry: Surface Science and Electrochemistry*; Elsevier, 2018; pp 702–710. https://doi.org/10.1016/B978-0-12-409547-2.13876-4.

(25) Ingólfsson, O. *Low-Energy Electrons Fundamentals and Applications*; Pan Stanford Publishing Pte. Ltd.: Singapore, The Republic of Singapore, 2019.

(26) Utke, I.; Swiderek, P.; Höflich, K.; Madajska, K.; Jurczyk, J.; Martinović, P.; Szymańska, I. B. Coordination and Organometallic Precursors of Group 10 and 11: Focused Electron Beam Induced Deposition of Metals and Insight Gained from Chemical Vapour Deposition, Atomic Layer Deposition, and Fundamental Surface and Gas Phase Studies. *Coord. Chem.*

Rev. **2022**, *458*, 213851. https://doi.org/https://doi.org/10.1016/j.ccr.2021.213851.

(27)   Thorman, R. M.; Ragesh Kumar, T. P.; Howard Fairbrother, D.; Ingólfsson, O. The Role of Low-Energy Electrons in Focused Electron Beam Induced Deposition: Four Case Studies of Representative Precursors. *Beilstein J. Nanotechnol.* **2015**, *6* (1), 1904–1926. https://doi.org/10.3762/bjnano.6.194.

(28)   Ingólfsson, O.; Thorman, R. M.; Unlu, I.; Spencer, J.; Johnson, K. R.; McElwee-White, L.; Fairbrother, H. A Combined Gas Phase and Surface Study on Electron Induced Decomposition of the Heteronuclear FEBID Precursor; CpFe(CO)2Mn(CO)5. *J. Phys. Conf. Ser.* **2017**, *875* (7), 62039. https://doi.org/10.1088/1742-6596/875/7/062039.

(29)   Ragesh Kumar, T. P.; Weirich, P.; Hrachowina, L.; Hanefeld, M.; Bjornsson, R.; Hrodmarsson, H. R.; Barth, S.; Howard Fairbrother, D.; Huth, M.; Ingólfsson, O. Electron Interactions with the Heteronuclear Carbonyl Precursor H2FeRu3(CO)13 and Comparison with HFeCo3(CO)12: From Fundamental Gas Phase and Surface Science Studies to Focused Electron Beam Induced Deposition. *Beilstein J. Nanotechnol.* **2018**, *9* (1), 555–579. https://doi.org/10.3762/bjnano.9.53.

(30)   Thorman, R. M.; Jensen, P. A.; Yu, J. C.; Matsuda, S. J.; McElwee-White, L.; Ingólfsson, O.; Fairbrother, D. H. Electron-Induced Reactions of Ru(CO)4I2: Gas Phase, Surface, and Electron Beam-Induced Deposition. *J. Phys. Chem. C* **2020**, *124* (19), 10593–10604. https://doi.org/10.1021/acs.jpcc.0c01801.

(31)   Kamali, A.; Bilgilisoy, E.; Wolfram, A.; Gentner, T. X.; Ballmann, G.; Harder, S.; Marbach, H.; Ingólfsson, O. On the Electron-Induced Reactions of (CH3)AuP(CH3)3: A Combined UHV Surface Science and Gas-Phase Study. *Nanomaterials*. 2022.

https://doi.org/10.3390/nano12152727.

(32)   Van Dorp, W. F.; Wu, X.; Mulders, J. J. L.; Harder, S.; Rudolf, P.; De Hosson, J. T. M. Gold Complexes for Focused-Electron-Beam-Induced Deposition. *Langmuir* **2014**, *30* (40), 12097–12105. https://doi.org/10.1021/la502618t.

(33)   Paul, M.; Schmidbaur, H. A New Synthesis of Dimethylgold(III) Chloride Using Tetramethyltin. *Zeitschrift fur Naturforsch. - Sect. B J. Chem. Sci.* **1994**, *49* (5), 647–649. https://doi.org/10.1515/znb-1994-0513.

(34)   Vollnhals, F. R.; Naturwissenschaftlichen, D.; Vollnhals, F. R. Exploring Electron Beam Induced Surface Activation for the Fabrication of Well-Defined Nanostructures: On the Role of Catalytic Processes, Substrates and Precursors., Master's Thesis, Friedrich-Alexander-Universität Erlangen-Nürnberg, Erlangen, Germany, 2015.

(35)   Friedli, V.; Utke, I. Optimized Molecule Supply from Nozzle-Based Gas Injection Systems for Focused Electron- and Ion-Beam Induced Deposition and Etching: Simulation and Experiment. *J. Phys. D. Appl. Phys.* **2009**, *42* (12). https://doi.org/10.1088/0022-3727/42/12/125305.

(36)   Bjarnason, E. H.; Ómarsson, B.; Jónsdóttir, N. R.; Árnason, I.; Ingólfsson, O. Dissociative Electron Attachment and Dissociative Ionization of 1,1-Dichloro-1-Silacyclohexane and Silacyclohexane. *Int. J. Mass Spectrom.* **2014**, *370*, 39–43. https://doi.org/https://doi.org/10.1016/j.ijms.2014.06.020.

(37)   Wetzel, R. C.; Baiocchi, F. A.; Hayes, T. R.; Freund, R. S. Absolute Cross Sections for Electron-Impact Ionization of the Rare-Gas Atoms by the Fast-Neutral-Beam Method.

Phys. Rev. A **1987**, *35* (2), 559–577. https://doi.org/10.1103/PhysRevA.35.559.

(38)   Fiegele, T.; Hanel, G.; Torres, I.; Lezius, M.; Märk, T. D. Threshold Electron Impact Ionization of Carbon Tetrafluoride, Trifluoromethane, Methane and Propane. *J. Phys. B At. Mol. Opt. Phys.* **2000**, *33* (20), 4263–4283. https://doi.org/10.1088/0953-4075/33/20/306.

(39)   Neese, F. Software Update: The ORCA Program System, Version 4.0. *Wiley Interdiscip. Rev. Comput. Mol. Sci.* **2018**, *8* (1). https://doi.org/10.1002/wcms.1327.

(40)   Grimme, S.; Neese, F. Double-Hybrid Density Functional Theory for Excited Electronic States of Molecules. *J. Chem. Phys.* **2007**, *127* (15). https://doi.org/10.1063/1.2772854.

(41)   Kang, R.; Chen, H.; Shaik, S.; Yao, J. Assessment of Theoretical Methods for Complexes of Gold(I) and Gold(III) with Unsaturated Aliphatic Hydrocarbon: Which Density Functional Should We Choose? *J. Chem. Theory Comput.* **2011**, *7* (12), 4002–4011. https://doi.org/10.1021/ct200656p.

(42)   Kepp, K. P. Benchmarking Density Functionals for Chemical Bonds of Gold. *J. Phys. Chem. A* **2017**, *121* (9), 2022–2034. https://doi.org/10.1021/acs.jpca.6b12086.

(43)   Cipriani, M.; Svavarsson, S.; da Silva, F. F.; Lu, H.; McElwee-White, L.; Ingólfsson, O. The Role of Low-Energy Electron Interactions in Cis-Pt(Co)2 Br2 Fragmentation. *Int. J. Mol. Sci.* **2021**, *22* (16). https://doi.org/10.3390/ijms22168984.

(44)   Cipriani, M.; Thorman, R. M.; Brewer, C. R.; McElwee-White, L.; Ingólfsson, O. Dissociative Ionization of the Potential Focused Electron Beam Induced Deposition Precursor π-Allyl Ruthenium(II) Tricarbonyl Bromide, a Combined Theoretical and Experimental   Study.   *Eur.   Phys.   J.   D*   **2019**,   *73*   (10),   1–7.

https://doi.org/10.1140/epjd/e2019-100151-9.

(45)   Cipriani, M.; Bjornsson, R.; Barclay, M.; Terfort, A.; Fairbrother, D. H.; Ingólfsson, O. Relative Cross Sections and Appearance Energies in Electron Impact Ionization and Dissociation of Mono-Halogenated Biphenyls. *Int. J. Mass Spectrom.* **2021**, *459*. https://doi.org/10.1016/j.ijms.2020.116452.

(46)   Davis, L. E.; MacDonald, N. C.; P.W., P.; Riach, G. E.; Weber, R. E. *Handbook of Auger Electron Spectroscopy*; Physical Electronics Division, Perkin·Elmer Corporation: Minnesota, USA, 1976.

(47)   JOHN C. VICKERMAN. Front Matter. In *Surface Analysis– The Principal Techniques*; John Wiley & Sons, Ltd, 2009; pp i–xix. https://doi.org/10.1002/9780470721582.fmatter.

(48)   Schneider, C. A.; Rasband, W. S.; Eliceiri, K. W. NIH Image to ImageJ: 25 Years of Image Analysis. *Nat. Methods* **2012**, *9* (7), 671–675. https://doi.org/10.1038/nmeth.2089.

(49)   Grzelczak, M.; Pérez-Juste, J.; Mulvaney, P.; Liz-Marzán, L. M. Shape Control in Gold Nanoparticle Synthesis. In *Colloidal Synthesis of Plasmonic Nanometals*; Liz-Marzán, L. M., Ed.; Jenny Stanford Publishing: New York, 2020; p 24. https://doi.org/https://doi.org/10.1201/9780429295188.

(50)   Chen, Y.; Gu, X.; Nie, C.-G.; Jiang, Z.-Y.; Xie, Z.-X.; Lin, C.-J. Shape Controlled Growth of Gold Nanoparticles by a Solution Synthesis. *Chem. Commun.* **2005**, No. 33, 4181–4183. https://doi.org/10.1039/B504911C.

(51)   Georgiev, P.; Bojinova, A.; Kostova, B.; Momekova, D.; Bjornholm, T.; Balashev, K. Implementing Atomic Force Microscopy (AFM) for Studying Kinetics of Gold

Nanoparticle's Growth. *Colloids Surfaces A Physicochem. Eng. Asp.* **2013**, *434* (Complete), 154–163. https://doi.org/10.1016/j.colsurfa.2013.05.064.

(52)   Yu, H.; Chen, M.; Rice, P. M.; Wang, S. X.; White, R. L.; Sun, S. Dumbbell-like Bifunctional Au−Fe3O4 Nanoparticles. *Nano Lett.* **2005**, *5* (2), 379–382. https://doi.org/10.1021/nl047955q.

(53)   Belić, D.; Shawrav, M. M.; Gavagnin, M.; Stöger-Pollach, M.; Wanzenboeck, H. D.; Bertagnolli, E. Direct-Write Deposition and Focused-Electron-Beam-Induced Purification of Gold Nanostructures. *ACS Appl. Mater. Interfaces* **2015**, *7* (4), 2467–2479. https://doi.org/10.1021/am507327y.

(54)   Weng, C.-H.; Huang, C.-C.; Yeh, C.-S.; Lei, H.-Y.; Lee, G.-B. Synthesis of Hexagonal Gold Nanoparticles Using a Microfluidic Reaction System*. *J. Micromechanics Microengineering* **2008**, *18* (3), 35019. https://doi.org/10.1088/0960-1317/18/3/035019.

(55)   Wnuk, J. D.; Gorham, J. M.; Rosenberg, S. G.; Madey, T. E.; Hagen, C. W.; Fairbrother, D. H. Atomic Radical Abatement of Organic Impurities from Electron Beam Deposited Metallic Structures. *J. Vac. Sci. Technol. B* **2010**, *28* (3), 527–537. https://doi.org/10.1116/1.3378142.

(56)   Bilgilisoy, E.; Yu, J.-C.; Preischl, C.; McElwee-White, L.; Steinrück, H.-P.; Marbach, H. Nanoscale Ruthenium-Containing Deposits from Ru(CO)4I2 via Simultaneous Focused Electron Beam-Induced Deposition and Etching in Ultrahigh Vacuum: Mask Repair in Extreme Ultraviolet Lithography and Beyond. *ACS Appl. Nano Mater.* **2022**, *5* (3), 3855–3865. https://doi.org/10.1021/acsanm.1c04481.

(57) Lukasczyk, T.; Schirmer, M.; Steinrück, H. P.; Marbach, H. Electron-Beam-Induced Deposition in Ultrahigh Vacuum: Lithographic Fabrication of Clean Iron Nanostructures. *Small* **2008**, *4* (6), 841–846. https://doi.org/10.1002/smll.200701095.

(58) Lukasczyk, T.; Schirmer, M.; Steinrück, H.-P.; Marbach, H. Generation of Clean Iron Structures by Electron-Beam-Induced Deposition and Selective Catalytic Decomposition of Iron Pentacarbonyl on Rh(110). *Langmuir* **2009**, *25* (19), 11930–11939. https://doi.org/10.1021/la901612u.

(59) Shih, P. Y.; Tafrishi, R.; Cipriani, M.; Hermanns, C. F.; Oster, J.; Gölzhäuser, A.; Edinger, K.; Ingólfsson, O. Dissociative Ionization and Electron Beam Induced Deposition of Tetrakis(Dimethylamino)Silane, a Precursor for Silicon Nitride Deposition. *Phys. Chem. Chem. Phys.* **2022**, *24* (16), 9564–9575. https://doi.org/10.1039/d2cp00257d.

(60) Engmann, S.; Stano, M.; Papp, P.; Brunger, M. J.; Matejčík, Š.; Ingólfsson, O. Absolute Cross Sections for Dissociative Electron Attachment and Dissociative Ionization of Cobalt Tricarbonyl Nitrosyl in the Energy Range from 0 EV to 140 EV. *J. Chem. Phys.* **2013**, *138* (4), 0–7. https://doi.org/10.1063/1.4776756.

(61) Engmann, S.; Stano, M.; Matejčík, Š.; Ingólfsson, O. The Role of Dissociative Electron Attachment in Focused Electron Beam Induced Processing: A Case Study on Cobalt Tricarbonyl Nitrosyl. *Angew. Chemie - Int. Ed.* **2011**, *50* (40), 9475–9477. https://doi.org/10.1002/anie.201103234.

(62) May, O.; Kubala, D.; Allan, M. Dissociative Electron Attachment to Pt(PF3)4—a Precursor for Focused Electron Beam Induced Processing (FEBIP). *Phys. Chem. Chem. Phys.* **2012**, *14* (9), 2979–2982. https://doi.org/10.1039/C2CP23268E.

(63)   Carden, W. G.; Pedziwiatr, J.; Abboud, K. A.; McElwee-White, L. Halide Effects on the
         Sublimation Temperature of X-Au-L Complexes: Implications for Their Use as Precursors
         in Vapor Phase Deposition Methods. *ACS Appl. Mater. Interfaces* **2017**, *9* (46), 40998–
         41005. https://doi.org/10.1021/acsami.7b12465.

(64)   Rohdenburg, M.; Boeckers, H.; Brewer, C. R.; McElwee-White, L.; Swiderek, P. Efficient
         NH3-Based Process to Remove Chlorine from Electron Beam Deposited Ruthenium
         Produced   from   (H3-C3H5)Ru(CO)3Cl.   *Sci.   Rep.*   **2020**,   *10*   (1),   10901.
         https://doi.org/10.1038/s41598-020-67803-y.

(65)   Thorman, R. M.; Brannaka, J. A.; McElwee-White, L.; Ingólfsson, O. Low Energy
         Electron-Induced Decomposition of (H3-C3H5)Ru(CO)3Br, a Potential Focused Electron
         Beam Induced Deposition Precursor with a Heteroleptic Ligand Set. *Phys. Chem. Chem.
         Phys.* **2017**, *19* (20), 13264–13271. https://doi.org/10.1039/c7cp01696d.

(66)   Rohdenburg, M.; Martinović, P.; Ahlenhoff, K.; Koch, S.; Emmrich, D.; Gölzhäuser, A.;
         Swiderek, P. Cisplatin as a Potential Platinum Focused Electron Beam Induced Deposition
         Precursor: NH3 Ligands Enhance the Electron-Induced Removal of Chlorine. *J. Phys.
         Chem. C* **2019**, *123* (35), 21774–21787. https://doi.org/10.1021/acs.jpcc.9b05756.

(67)   Warneke, J.; Rohdenburg, M.; Zhang, Y.; Orszagh, J.; Vaz, A.; Utke, I.; De Hosson, J. T.
         M.; van Dorp, W. F.; Swiderek, P. Role of NH3 in the Electron-Induced Reactions of
         Adsorbed   and   Solid   Cisplatin.   *J.   Phys.   Chem.   C*   **2016**,   *120*   (7),   4112–4120.
         https://doi.org/10.1021/acs.jpcc.5b12184.

(68)   Spencer, J. A.; Wu, Y.-C.; McElwee-White, L.; Fairbrother, D. H. Electron Induced Surface
         Reactions of Cis-Pt(CO)2Cl2: A Route to Focused Electron Beam Induced Deposition of

Pure Pt Nanostructures. *J. Am. Chem. Soc.* **2016**, *138* (29), 9172–9182. https://doi.org/10.1021/jacs.6b04156.

(69)   Spencer, J. A.; Barclay, M.; Gallagher, M. J.; Winkler, R.; Unlu, I.; Wu, Y. C.; Plank, H.; McElwee-White, L.; Fairbrother, D. H. Comparing Postdeposition Reactions of Electrons and Radicals with Pt Nanostructures Created by Focused Electron Beam Induced Deposition. *Beilstein J. Nanotechnol.* **2017**, *8* (1), 2410–2424. https://doi.org/10.3762/bjnano.8.240.

(70)   Ferreira Da Silva, F.; Thorman, R. M.; Bjornsson, R.; Lu, H.; Mcelwee-White, L.; Ingólfsson, O. Dissociation of the FEBID Precursor: Cis-Pt(CO)2Cl2 Driven by Low-Energy Electrons. *Phys. Chem. Chem. Phys.* **2020**, *22* (11), 6100–6108. https://doi.org/10.1039/c9cp06633k.

(71)   Mahgoub, A.; Lu, H.; Thorman, R. M.; Preradovic, K.; Jurca, T.; McElwee-White, L.; Fairbrother, H.; Hagen, C. W. Electron Beam-Induced Deposition of Platinum from Pt(CO)2Cl2 and Pt(CO)2Br2. *Beilstein J. Nanotechnol.* **2020**, *11*, 1789–1800. https://doi.org/10.3762/BJNANO.11.161.

(72)   Botman, A.; Mulders, J. J. L.; Weemaes, R.; Mentink, S. Purification of Platinum and Gold Structures after Electron-Beam-Induced Deposition. *Nanotechnology* **2006**, *17* (15), 3779–3785. https://doi.org/10.1088/0957-4484/17/15/028.

(73)   Frabboni, S.; Gazzadi, G. C.; Spessot, A. TEM Study of Annealed Pt Nanostructures Grown by Electron Beam-Induced Deposition. *Phys. E Low-dimensional Syst. Nanostructures* **2007**, *37* (1), 265–269. https://doi.org/https://doi.org/10.1016/j.physe.2006.06.018.

(74)   Landheer, K.; Rosenberg, S. G.; Bernau, L.; Swiderek, P.; Utke, I.; Hagen, C. W.; Fairbrother, D. H. Low-Energy Electron-Induced Decomposition and Reactions of Adsorbed Tetrakis(Trifluorophosphine)Platinum [Pt(PF3)4]. *J. Phys. Chem. C* **2011**, *115* (35), 17452–17463. https://doi.org/10.1021/jp204189k.

(75)   Rosenberg, S. G.; Barclay, M.; Fairbrother, D. H. Electron Induced Surface Reactions of Organometallic Metal(Hfac)2 Precursors and Deposit Purification. *ACS Appl. Mater. Interfaces* **2014**, *6* (11), 8590–8601. https://doi.org/10.1021/am501457h.

(76)   Thorman, R. M.; Unlu, I.; Johnson, K.; Bjornsson, R.; McElwee-White, L.; Fairbrother, D. H.; Ingólfsson, O. Low Energy Electron-Induced Decomposition of (H5-Cp)Fe(CO)2Mn(CO)5, a Potential Bimetallic Precursor for Focused Electron Beam Induced Deposition of Alloy Structures. *Phys. Chem. Chem. Phys.* **2018**, *20* (8), 5644–5656. https://doi.org/10.1039/c7cp06705d.

For Table of Contents Only
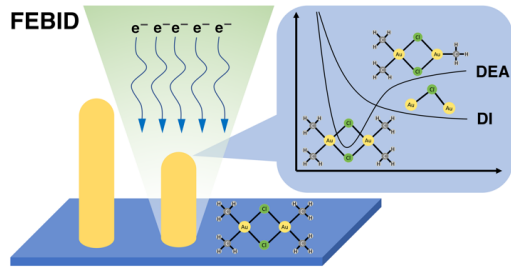
Supporting Information

A combined gas phase dissociative ionization, dissociative electron attachment and deposition study on the potential FEBID precursor [(CH$_3$)$_2$AuCl]$_2$

Elif Bilgilisoy[a]‡, Ali Kamali[b]‡, Thomas Xaver Gentner[c], Gerd Ballmann[c], Sjoerd Harder[c], Hubertus Marbach[a], [d], Oddur Ingólfsson[b]*, Hans-Peter Steinrück[a]*

[a] Physikalische Chemie II, Friedrich-Alexander Universität Erlangen-Nürnberg, 91058 Erlangen, Germany

[b] Science Institute and Department of Chemistry, University of Iceland, Dunhagi 3, 107 Reykjavík, Iceland

[c] Inorganic and Organometallic Chemistry, Universität Erlangen-Nürnberg, 91058 Erlangen, Germany

[d] Carl Zeiss SMT GmbH, 64380 Roßdorf, Germany
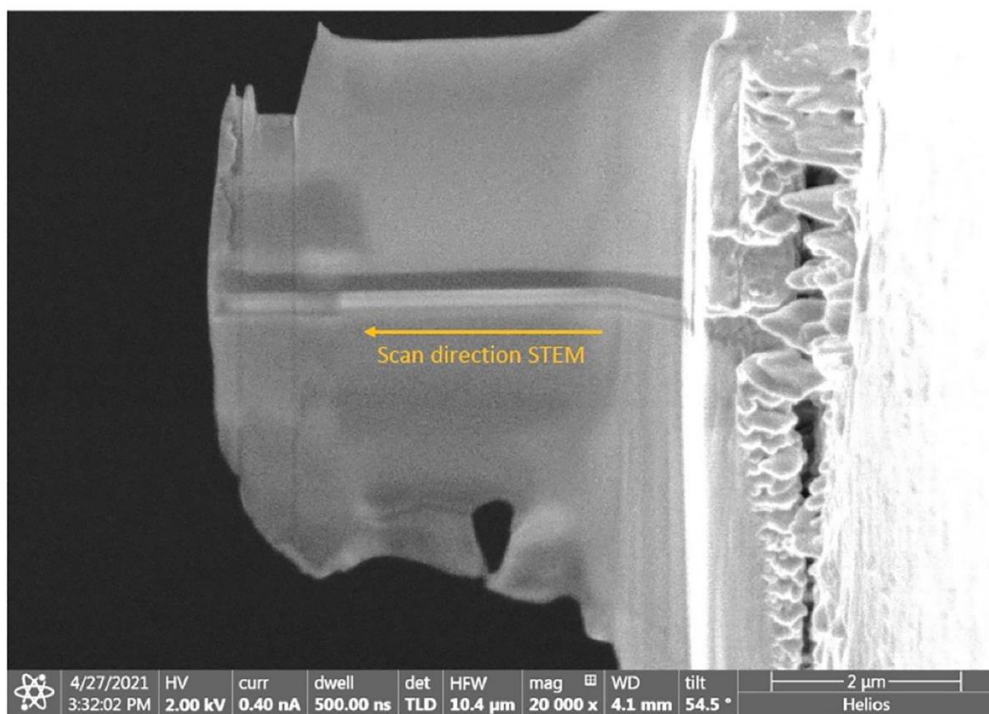
Figure S1. Prepared lamella for STEM, and SAED experiments.

The observed gold nanoparticles (Figure 1d) have irregular shapes. Therefore, the diameter of the selected particle was defined by considered the perpendicular distance between two parallel tangent lines of the particle at an arbitrary angle. This particle size analysis method is known as Feret diameter or caliper diameter. Beside the diameter of the particles, their approximate amount in one SEM image were also acquired by firstly removing the background from the SEM image, then applying the image threshold, and finally counting the numbers automatically (Figure S2).

(e)

	Area	Feret	FeretX	FeretY	FeretAngle	MinFeret
1	113.575	14.194	93.023	0	124.992	11.628
2	29.746	10.720	124.419	2.326	12.529	3.488
3	95.998	16.649	312.791	6.977	24.775	9.302
4	6.760	4.193	345.349	2.326	33.690	2.326
5	56.787	11.452	370.930	4.651	23.962	8.140
6	186.587	22.367	453.488	3.488	8.973	11.628
7	95.998	13.258	540.698	8.140	37.875	11.628
8	29.746	10.720	561.628	2.326	12.529	3.488
9	251.487	24.667	37.209	18.605	45.000	14.744
10	179.827	17.711	236.047	17.442	66.801	13.953
11	6.760	4.193	153.488	8.140	33.690	2.326
12	135.208	14.708	343.023	9.302	108.435	12.791
13	255.544	25.502	374.419	12.791	133.152	14.449
14	110.871	14.383	208.140	12.791	104.036	10.465
15	274.473	21.723	255.814	15.116	105.524	17.442
16	229.854	23.168	62.791	38.372	72.474	13.693
17	281.233	22.457	132.558	37.209	68.749	17.442

Figure S2. (a) SEM image of FEBID gold nanoparticles. (b) BG subtracted SEM image of (a) using ImageJ. (c) After automatic threshold was applied in ImageJ program. (d) and (e) results of automatic particle count in the program. (f) illustration of the feret, min. feret, max. feret, and feret angle.

The comparative histogram graphs of particle numbers versus particle diameters with respect to the beam currents for 400 pA (blue bars), 1.5 nA (green bars) and 3 nA (purple bars) were obtained from SEM and AFM, and plotted in Figure S3.
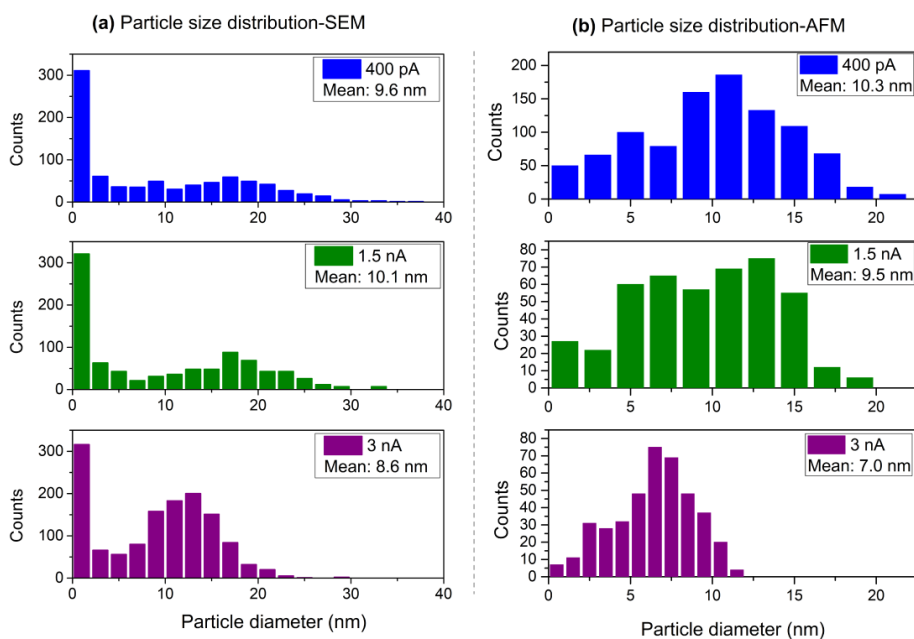
Figure S3. (a) and (b) The particle size distributions obtained from SEM and AFM, respectively for the FEBID gold nanoparticles with respect to the different applied beam currents.
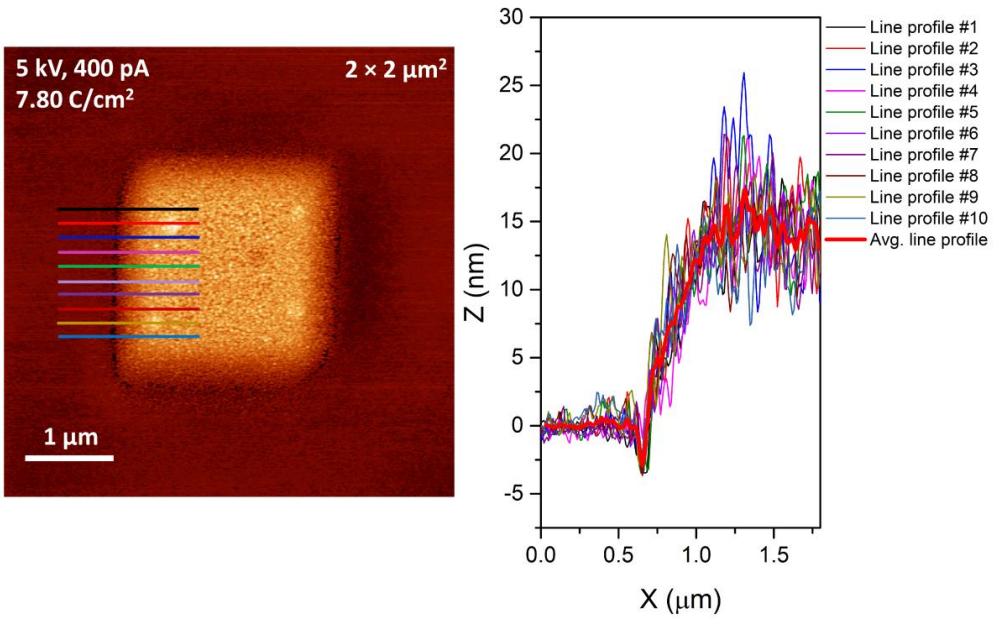
Figure S4. The AFM image of the FEBID deposit (5 kV, 400 pA) is shown on the left, and the line profiles from 10 different lines and their average line profile are shown on the right.

Figure S5. AES on SiO₂ before surface treatment (blue line) and after surface treatment (45 min. Ar⁺ sputtering + 90 min. annealing at 823 K under oxygen) on the same substrate (green line).

Table S6: All optimized geometries (parent molecule and cations) and their Gibbs free energy (Eh) at the PBE0/ def2-TZVP level of theory, expressed as Cartesian coordinates (Å).

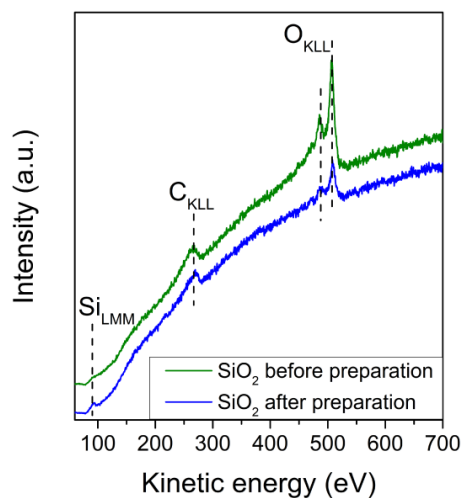| Molecule	Cartesian coordinates (Å)			Final Gibbs free energy (Eh)
[Au₂Cl₂(CH₃)₄]	Au	-2.072104	3.052679	-0.000000	-1351.07736325
	Au	-1.989186	-0.547564	0.000000	
	Cl	-3.700537	1.214412	-0.000000	
	Cl	-0.360753	1.290702	-0.000000	
	C	-0.673402	4.528115	0.000000	
	H	-1.112834	5.522029	0.000000	
	H	-0.068504	4.373457	-0.893801	
	H	-0.068504	4.373457	0.893801	
	C	-3.481400	4.517269	0.000000	
	H	-4.446950	4.013642	0.000000	
	H	-3.365518	5.129161	-0.893266	
	H	-3.365518	5.129161	0.893266	
	C	-3.387887	-2.023002	0.000000	
	H	-2.948454	-3.016916	0.000008	
	H	-3.992779	-1.868350	-0.893805	
	H	-3.992789	-1.868340	0.893796	
	C	-0.579889	-2.012155	0.000000	
	H	0.385662	-1.508527	-0.000000	
	H	-0.695771	-2.624047	-0.893266	
	H	-0.695770	-2.624046	0.893267	
[Au₂Cl₂(CH₃)₄]⁺	Au	-2.035627	2.919475	-0.027570	-1350.73933480
	Au	-2.017481	-0.444636	-0.010941	
	Cl	-3.788694	1.232543	0.016664	
	Cl	-0.261716	1.250851	-0.054282	
	C	-0.669548	4.439482	-0.345837	
	H	-1.190608	5.274419	-0.803414	
	H	0.084423	4.008933	-1.000436	
	H	-0.281488	4.671763	0.645097	
	C	-3.414131	4.432888	0.268665	
	H	-4.246110	3.972802	0.796011	
	H	-3.684834	4.768818	-0.731350	
	H	-2.929968	5.205118	0.858956	
	C	-3.388970	-1.973133	-0.245290	
	H	-2.926816	-2.738725	-0.861040	
	H	-4.248317	-1.518273	-0.731478	
	H	-3.615120	-2.321717	0.761195	
	C	-0.632326	-1.956939	0.242645	
	H	0.172322	-1.510011	0.821366	
	H	-0.322947	-2.225852	-0.766396	
	H	-1.114845	-2.775127	0.767926	
[Au₂Cl₂(CH₃)₂]⁺	Au	-1.819984	2.875611	0.004036	-1271.03956804
	Au	-2.287517	-0.353586	0.107295	
	Cl	-3.785590	1.579411	0.201733	
	Cl	-0.320606	0.946395	-0.090320	
	C	-2.858006	4.635135	0.063053	
	H	-3.352792	4.697531	1.029611	
	H	-3.556767	4.643787	-0.770184	
	H	-2.043623	5.357541	-0.051498	
	C	-1.251219	-2.114009	0.047678	

	H	-0.553619	-2.123453	0.882026
	H	-0.754647	-2.175376	-0.918170
	H	-2.065026	-2.837038	0.159960
[Au₂Cl₂(CH₃)]⁺	Au	-2.710731	3.628260	1.202848
	Au	-0.876681	0.582329	-0.199154
	Cl	-2.761916	-1.062272	-0.912648
	Cl	-1.072379	2.990585	-0.250808
	C	-1.119442	-1.403061	-0.364717
	H	-1.118450	-1.935881	0.580988
	H	-0.527731	-1.861705	-1.150811
	H	0.579778	0.504658	0.312600
[Au₂Cl₂]⁺	Au	-2.056269	2.768478	0.000000
	Au	-2.005021	-0.263367	0.000000
	Cl	-3.870060	1.221887	-0.000000
	Cl	-0.191230	1.283232	-0.000000
[Au₂Cl(CH₂CH₃)]⁺	Au	-2.333092	3.153032	0.004622
	Au	-2.219375	-0.696612	0.077322
	Cl	-0.911089	1.215951	0.078406
	C	-3.533568	4.824477	-0.052434
	H	-3.801526	4.928425	-1.104208
	H	-4.372147	4.586128	0.601986
	H	-2.880646	5.612803	0.325635
	C	-3.225313	-2.301311	0.078777
	H	-2.770456	-3.294805	0.109287
	H	-4.316942	-2.343808	0.049542
[Au₂Cl(CH₃)]⁺	Au	-1.973262	2.076357	-0.883223
	Au	1.414636	0.775184	0.287775
	Cl	-0.345118	2.376157	0.689014
	C	2.984080	-0.502369	-0.097905
	H	3.660789	0.071733	-0.729953
	H	2.520563	-1.355607	-0.594045
	H	3.369621	-0.715024	0.900903
[Au₂Cl]⁺	Au	-1.995645	3.106475	0.000000
	Au	-1.918943	-0.598947	0.000001
	Cl	-0.602069	1.281921	0.000001
[Au₂(CH₂CH₂)]⁺	Au	-4.755924	0.426633	2.421132
	Au	-2.189804	-0.011332	1.982566
	C	-6.841047	1.019418	2.105349
	C	-6.728617	0.480247	3.374092
	H	-6.990154	-0.556436	3.562073
	H	-6.617365	1.122366	4.242251
	H	-7.193350	0.415805	1.274756
	H	-6.820579	2.094239	1.955491
[Au(CH)AuH]⁺	Au	-4.297039	1.251104	-0.422872
	C	-2.616996	0.259825	-0.471263
	Au	-1.544376	1.861455	-0.360334
	H	-2.365271	-0.655309	0.065992
	H	-0.076828	1.338935	-0.313894
[Au₂]⁺	Au	-0.191712	-0.032106	1.367387

[Au₂Cl₂(CH₃)]⁺	-1231.21077897
[Au₂Cl₂]⁺	-1191.35489549
[Au₂Cl(CH₂CH₃)]⁺	-731.29110113
[Au₂Cl(CH₃)]⁺	-771.12783263
[Au₂Cl]⁺	-731.29110113 Eh
[Au₂(CH₂CH₂)]⁺	-349.72187310
[Au(CH)AuH]⁺	-310.36432548
[Au₂]⁺	-271.50548729

	Au	-0.191712	-0.032106	-1.267660	
[(CH₃)Au(CH₃)]⁺	Au	-4.797108	0.324695	0.130111	-215.12577260
	C	-3.255948	1.646757	0.222182	
	H	-2.412115	0.993246	-0.015651	
	H	-3.236292	2.025981	1.240925	
	H	-3.425177	2.410875	-0.531572	
	C	-6.214769	1.781065	0.177246	
	H	-7.104844	1.195111	0.421352	
	H	-6.236158	2.210645	-0.821382	
	H	-5.947248	2.489221	0.956170	
[AuCl₂]⁻	Au	-1.936113	2.153547	0.000000	-1056.07074733
	Cl	-4.222798	2.061043	0.000000	
	Cl	0.350565	2.246094	0.000000	
[Au₂Cl₂(CH₃)₃]⁻	Au	-1.294616	3.653728	-1.120733	-1311.34276020
	Au	-1.721580	-0.240883	-0.919247	
	Cl	-1.767896	1.626343	-2.419054	
	Cl	0.273929	4.438163	-2.736831	
	C	-0.978834	5.308899	0.018036	
	H	-1.893686	5.902582	0.034097	
	H	-0.166180	5.863241	-0.446048	
	H	-0.720249	5.003606	1.032234	
	C	-2.641690	3.056969	0.300580	
	H	-3.530829	2.701840	-0.221069	
	H	-2.897767	3.863223	0.987765	
	H	-2.197334	2.222438	0.845948	
	C	-1.675251	-1.832857	0.344300	
	H	-0.649151	-2.187884	0.486364	
	H	-2.271075	-2.664314	-0.046302	
	H	-2.078061	-1.558642	1.325165	

Table S7. Full list of experimental DI and DEA threshold values compared to theoretically calculated threshold values at PBE0/def2-TZVP, DLPNO-CCSD(T)/TZVP, and DLPNO-CCSD(T)/SVP levels of theory for the $[(CH_3)_2AuCl]_2$.

m/z	Products	AE (eV)	PBE0-TZVP (eV)	DLPNO-CCSD(T)-SVP (eV)	DLPNO-CCSD(T)-TZVP (eV)
	Dissociative Ionization				
524	**$[Au_2Cl_2(CH_3)_4]^+$**	**9.4 ± 0.3**	<u>**9.23**</u>	**9.69**	**9.92**
494	$[Au_2Cl_2(CH_3)_2]^+ + 2(CH_3)$		13.51	13.69	14.06
	$[Au_2Cl_2(CH_3)_2]^+ + CH_3CH_3$	**9.7 ± 0.2**	<u>**9.67**</u>	**9.86**	**10.29**
	$[Au_2Cl_2(CH_3)_2]^+ + CH_2CH_2 + H_2$		11.28	11.36	11.65
479	$[Au_2Cl_2(CH_3)]^+ + 3(CH_3)$		15.01	14.59	15.04
	$[Au_2Cl_2(CH_3)]^+ + (CH_3) + CH_3CH_3$	**11.4 ± 0.2**	<u>**11.18**</u>	**10.76**	**11.27**
	$[Au_2Cl_2(CH_3)]^+ + CH_2CH_2 + H_2 + (CH_3)$		12.78	12.26	12.64
464	$[Au_2Cl_2]^+ + 4(CH_3)$		17.32	17.06	17.65
	$[Au_2Cl_2]^+ + 2(CH_3CH_3)$		<u>**9.65**</u>	**9.41**	**10.12**
	$[Au_2Cl_2]^+ + CH_3CH_3 + 2(CH_3)$	**10.1 ± 0.2**	13.48	13.23	13.89
	$[Au_2Cl_2]^+ + CH_2CH_2 + H_2 + CH_3CH_3$		11.25	10.91	11.49
458	$[Au_2Cl(CH_2CH_3)]^+ + 2CH_3 + Cl + H$		18.72	17.87	18.50
	$[Au_2Cl(CH_2CH_3)]^+ + CH_3CH_3 + Cl + H$		14.88	14.04	14.73
	$[Au_2Cl(CH_2CH_3)]^+ + CH_3CH_3 + HCl$		<u>**10.46**</u>	**9.88**	**10.41**
	$[Au_2Cl(CH_2CH_3)]^+ + (CH_4) + CH_3Cl$	**10.3 ± 0.2**	**10.64**	**10.23**	**10.60**
	$[Au_2Cl(CH_2CH_3)]^+ + 2(CH_3) + HCl$		15.46	16.01	15.41
	$[Au_2Cl(CH_2CH_3)]^+ + (CH_3) + CH_3Cl + H$		15.02	14.58	14.97
444	$[Au_2Cl(CH_3)]^+ + Cl + 3(CH_3)$		17.42	16.52	17.29
	$[Au_2Cl(CH_3)]^+ + Cl + CH_3CH_3 + (CH_3)$		**13.58**	**12.69**	**13.52**
	$[Au_2Cl(CH_3)]^+ + Cl(CH_3) + 2(CH_3)$	**13.0 ± 0.2**	**13.72**	**13.23**	**13.76**
	$[Au_2Cl(CH_3)]^+ + Cl(CH_3) + CH_3CH_3$		9.88	9.40	9.99
429	$[Au_2Cl]^+ + 4(CH_3) + Cl$		19.11	18.00	18.84
	$[Au_2Cl]^+ + (CH_3) + CH_3Cl + CH_3CH_3$		11.57	10.89	11.54
	$[Au_2Cl]^+ + HCl + 2(CH_4) + CHCH_2$		**12.54**	**11.60**	**12.33**
	$[Au_2Cl]^+ + 2 CH_3CH_3 + Cl$	**12.2 ± 0.2**	11.44	10.35	11.30
	$[Au_2Cl]^+ + Cl + CH_3CH_3 + 2(CH_3)$		15.27	14.18	15.07
	$[Au_2Cl]^+ + 3(CH_3) + CH_3Cl$		15.41	14.72	15.31

422	[Au$_2$(CH$_2$CH$_2$)]$^+$ + 2(CH$_3$) + 2Cl + 2H		22.20	20.87	21.84
	[Au$_2$(CH$_2$CH$_2$)]$^+$ + 2Cl(CH$_3$) + H$_2$		**<u>10.53</u>**	**10.09**	**10.46**
	[Au$_2$(CH$_2$CH$_2$)]$^+$ + CH$_3$CH$_3$ + 2HCl	10.3 ± 0.3	9.51	8.72	9.44
	[Au$_2$(CH$_2$CH$_2$)]$^+$ + 2CH$_3$ + 2HCl		13.34	12.55	13.21
	[Au$_2$(CH$_2$CH$_2$)]$^+$ + 2(CH$_3$) + Cl$_2$ + H$_2$		15.21	14.75	15.10
	[Au$_2$(CH$_2$CH$_2$)]$^+$ + CH$_3$CH$_3$ + Cl$_2$ + H$_2$		11.37	10.93	11.33
408	[Au$_2$(CH$_2$)]$^+$ + 3(CH$_3$) + 2Cl + H		24.57	23.42	24.14
	[Au$_2$(CH$_2$)]$^+$ + CH$_2$CH$_2$ + 2HCl + CH$_4$		**13.35**	**12.62**	**13.06**
	[Au$_2$(CH$_2$)]$^+$ + 3(CH$_3$) + HCl + Cl		20.14	19.26	19.83
	[Au$_2$(CH$_2$)]$^+$ + CH$_3$CH$_3$ + CH$_3$ + HCl + Cl	13.2 ± 0.2	16.30	15.43	16.06
	[Au$_2$(CH$_2$)]$^+$ + CH$_3$CH$_3$ + HCl + Cl(CH$_3$)		12.60	12.15	12.54
	[Au$_2$(CH$_2$)]$^+$ + 2(CH$_3$) + HCl + Cl(CH$_3$)		16.44	15.97	16.30
	[Au$_2$(CH$_2$)]$^+$ + CH$_2$CH$_2$ + HCl + Cl(CH$_3$) + H$_2$		14.20	13.64	13.90
	[Au$_2$(CH$_2$)]$^+$ + CH$_3$ + 2Cl(CH$_3$) + H		17.16	16.84	17.10
407	[Au$_2$(CH)]$^+$ + 3(CH$_3$) + 2H + 2Cl		28.82	27.63	28.40
	[Au$_2$(CH)]$^+$ + 3(CH$_3$) + 2HCl		19.96	19.32	19.76
	[Au$_2$(CH)]$^+$ + CH$_3$CH$_3$ + CH$_3$ + 2HCl		16.13	15.49	15.99
	[Au$_2$(CH)]$^+$ + (CH$_3$) + 2Cl(CH$_3$) + H$_2$	13.8 ± 0.2	17.15	15.97	16.13
	[Au$_2$(CH)]$^+$ + CH$_3$CH$_3$ + Cl + Cl(CH$_3$) + H$_2$		17.02	16.32	16.78
	[Au$_2$(CH)]$^+$ + CH$_2$CH$_2$ + Cl + Cl(CH$_3$) + 2H$_2$		18.62	17.82	18.14
	[Au$_2$(CH)]$^+$ + CH$_3$CH$_3$ + Cl$^-$ + Cl(CH$_3$) + H$_2$		**<u>13.75</u>**	**14.46**	**13.69**
	[Au$_2$(CH)]$^+$ + 2HCl + CH$_2$CH$_3$ + CH$_4$		15.92	15.35	15.85
394	[Au$_2$]$^+$ + 4(CH$_3$) + 2Cl		22.39	21.94	22.09
	[Au$_2$]$^+$ + 2[CH$_3$CH$_3$] + 2Cl		**<u>14.71</u>**	**14.28**	**14.56**
	[Au$_2$]$^+$ + 2(CH$_3$) + 2(CH$_3$Cl)		**<u>14.99</u>**	**15.36**	**15.05**
	[Au$_2$]$^+$ + CH$_2$CH$_2$ + 2(CH$_3$) + 2HCl		**<u>15.56</u>**	**15.48**	**15.39**
	[Au$_2$]$^+$ + 4(CH$_3$) + Cl$_2$	15.3 ± 0.2	19.66	20.02	19.68
	[Au$_2$]$^+$ + 2[CH$_3$CH$_3$] + Cl$_2$		11.99	12.36	12.14
	[Au$_2$]$^+$ + CH$_3$CH$_3$ + 2(CH$_3$Cl)		11.15	11.53	11.28
	[Au$_2$]$^+$ + CH$_2$CH$_2$ + H$_2$ + 2(CH$_3$Cl)		12.75	13.03	12.65
	[Au$_2$]$^+$ + CH$_2$CH$_2$ + CH$_3$CH$_3$ + 2HCl		11.72	11.66	11.62
227	[(CH$_3$)Au(CH$_3$)]$^+$ + 2(CH$_3$) + 2Cl + Au		17.81	17.90	18.72
	[(CH$_3$)Au(CH$_3$)]$^+$ + CH$_3$CH$_3$ + Cl$_2$ + Au	12.4 ± 0.2	**11.24**	**12.15**	**12.54**
	[(CH$_3$)Au(CH$_3$)]$^+$ + AuCl + CH$_3$CH$_3$ + Cl		**12.46**	**11.63**	**12.20**
	[(CH$_3$)Au(CH$_3$)]$^+$ + 2(CH$_3$) + Cl$_2$ + Au		15.08	15.98	16.31

m/z	Products	AE (eV)	PBE0-TZVP (eV)	DLPNO-CCSD(T)-SVP (eV)	DLPNO-CCSD(T)-TZVP (eV)
	$[(CH_3)Au(CH_3)]^+ + CH_3CH_3 + 2Cl + Au$		13.97	14.07	14.95
	$[(CH_3)Au(CH_3)]^+ + 2Cl(CH_3) + Au$		10.41	11.32	11.68
	$[(CH_3)Au(CH_3)]^+ + CH_2CH_2 + 2HCl + Au$		10.98	11.44	12.01
	$[(CH_3)Au(CH_3)]^+ + AuCl + HCl + CH_2CH_2 + H$		13.90	13.16	13.58
225	$[(CH_2)Au(CH_2)]^+ + AuCl + Cl + 2(CH_3) + H_2$	12.6 ± 0.4	16.45	15.52	16.04
	$[(CH_2)Au(CH_2)]^+ + CH_3CH_3 + Au + Cl_2 + H_2$		**<u>12.80</u>**	**12.22**	**12.61**
	$[(CH_2)Au(CH_2)]^+ + CH_3CH_3 + AuCl + H + HCl$		**<u>12.44</u>**	**11.73**	**12.28**
	$[(CH_2)Au(CH_2)]^+ + CH_3CH_3 + AuCl + Cl + H_2$		**<u>12.61</u>**	**11.69**	**12.27**
	$[(CH_2)Au(CH_2)]^+ + 2Cl(CH_3) + Au + H_2$		11.96	11.22	11.59
	$[(CH_2)Au(CH_2)]^+ + 2Cl(CH_3) + AuH + H$		13.39	12.76	13.24
Dissociative Electron Attachment					
m/z	Products	AE (eV)	PBE0-TZVP (eV)	DLPNO-CCSD(T)-SVP (eV)	DLPNO-CCSD(T)-TZVP (eV)
267	$[AuCl_2]^- + Au + 2CH_3CH_3$	0.1-0.45	-2.20	-2.24	-1.96
	$[AuCl_2]^- + Au(CH_3) + CH_3CH_3 + CH_3$		-0.80	-0.71	-0.67
	$[AuCl_2]^- + (CH_3)Au(CH_3) + CH_3CH_3$		-1.82	-1.39	-1.54
509	$[M - CH_3]^- + CH_3$	0-0.2	-0.96	-0.76	-0.88

Paper III

Dissociative Electron Attachment and Dissociative Ionization of CF$_3$AuCNC(CH$_3$)$_3$; A Potential FEBID Precursor for Gold Deposition

Ali Kamali[1], Will G. Carden[2], Jodie V. Johnson[2], Lisa McElwee-White[2], O. Ingólfsson[1]

1. Science Institute and Department of Chemistry, University of Iceland, Dunhagi 3, 107 Reykjavík, Iceland.
2. Department of Chemistry, University of Florida, Gainesville, Florida 32611-7200, USA.

Ali Kamali carried out the gas-phase experiment using HV equipment, performed quantum chemical calculations, and wrote the manuscript.

Dissociative Electron Attachment and Dissociative Ionization of CF$_3$AuCNC(CH$_3$)$_3$, A Potential FEBID Precursor for Gold Deposition

Ali Kamali[1], Will G. Carden[2], Jodie V. Johnson[2], Lisa McElwee-White[2], O. Ingólfsson[1*]

1. Science Institute and Department of Chemistry, University of Iceland, Dunhagi 3, 107 Reykjavík, Iceland.

2. Department of Chemistry, University of Florida, Gainesville, Florida 32611-7200, USA.

Topical Issue;

Electron and Positron Interactions and Their Applications: a tribute to Professor Michael Brunger

Reminiscence of good times

More than one article could be written about Michael Brunger, the Hippy, and they would all be a testimony of a memorable man, a good scientist and more importantly a humorous, tolerant, and a very good person, moreover, they would be fun to read. However, in his spirit, I´m going to keep it short.

I was so fortunate to enjoy Michael's friendship, and his support and collaboration in science, in science administration (politics :-) and in personal matters. He also became dear to my children, when he generously hosted me and my family in Adelaide during my sabbatical in 2012, an experience we still talk about at the dinner table, now more than 10 years later. In one of our more personal conversations about lost ones, Michal said „*...as long as you are still talked about, you are not gone. "*. With all the opportunities the Hippy has provided for reminiscence of good times, there is no doubt that many will talk kindly and of respect of him long time from now. In that sense, he will certainly outlive me.

Oddur

Abstract

Appreciable effort is currently committed to designing suitable organometallic precursors for fabrication of metallic nanostructures with focused electron beam induced deposition (FEBID) – a direct write method with high potential for 3D patterning. In this context, the initial interaction of the potential precursor with low energy electrons is critical and the extent of electron induced ligand loss determines the composition of the resulting deposits. Specifically of interest are gold-containing precursors, as the optoelectronic properties of gold provide potential for a variety of plasmonic and light enhancing applications of 3D nanostructures. Here we study low energy electron induced fragmentation of $CF_3AuCNC(CH_3)_3$ through dissociative ionisation (DI) and dissociative electron attachment (DEA) in the gas phase under single collision conditions and under conditions where collisional stabilisation is provided. We further compare the fragmentation patterns observed under these conditions with the composition of deposits formed from this precursor under FEBID conditions. In DI, a significant difference in relative intensities is found under single collision conditions as compared to conditions where collisional stabilisation is provided, while under both these conditions only the same DEA channel is open. Comparison with the composition of deposits formed under FEBID conditions shows that the initial electron-induced fragmentation processes are not directly reflected in the deposit's composition. Rather, we expect these to determine the initial composition of immobilised fragments, while the final composition of the deposit is determined by electron induced secondary and tertiary reactions caused by further irradiation after immobilisation.

1. Introduction

Gold nanomaterials are employed in a wide variety of applications due to their unique optoelectrical properties. This is most noticeable in the biomedical sector where these have found application in e.g., imaging, diagnostics, and cancer therapy[1–4], and a number of well controlled physical and chemical protocols have been developed for their fabrication[5–7]. Well defined 3D nanostructures also have high potential as passive and/or active elements in technological applications [8,9]. For gold specifically, these include optical and electric sensors [10], surface enhanced Raman spectroscopy (SERS) elements [11], and plasmonic devices in general [12]. For the functionality of such stationary 3D nanostructures, however, their positioning, size, shape, and elemental purity are critical.

Focused Electron Beam Induced Deposition (FEBID) [13–15] is a direct write approach that has the potential of such control in the fabrication of free-standing nanostructures. In FEBID, a precursor gas enters an electron microscope through a gas injection system (GIS) in close proximity to a substrate surface where the precursor molecules are physisorbed in dynamic equilibrium with their gas phase. For metal deposition, such precursors are typically organometallic compounds with the central metal atom being that of the desired deposit[16]. A tightly focused, high-energy electron beam is directed at the surface, close to the gas injection point, and ideally the precursor molecules dissociate volatile ligands that are pumped away while the central atom(s) stays on the surface to build a pure metal deposit [17]. The lateral control of the shape of the structures created in this way is achieved by moving the electron beam relative to the surface of the substrate and the vertical control is achieved by variation of the dwell time [13,14]. However, composition control has proven to be difficult in FEBID, and generally significant amounts of impurities are found to be co-deposited with the desired metal element [18]. This is mainly due to incomplete decomposition of the precursor molecules under the electron beam, but adsorption and further decomposition of dissociated ligands and co-deposition of impurities from the background gas also play a role.

The general criteria for good precursors are that they are sufficiently volatile to be introduced to the FEBID system, that they are stable under ambient conditions, easy to handle, preferably of low toxicity and commercially available [16,19]. Most importantly, however, to achieve high purity depositions, the precursor molecules need to dissociate efficiently under the electron beam and the dissociated ligands need to readily desorb from the surface. [16]. As a large variety of commercially available precursors for chemical vapor deposition (CVD) fulfil most of these criteria, most of the early reported FEBID experiments focused on depositions from these precursors. However, while CVD is thermally driven, in FEBID the fragmentation processes and thus the deposition are electron driven [16,17]. Moreover, significant numbers of secondary electrons are produced in inelastic

scattering of the primary electrons from the substrate and forming deposits. Thus, the actual energy of the electrons inducing the fragmentation processes in FEBID is not that of the primary electrons alone. Rather, it is a distribution also reflecting the energy spread of the inelastic scattered and secondary electrons [20]. This energy distribution generally peaks below 10 eV, has a significant contribution close to 0 eV and a tail towards higher energies[20,21]. To further complicate the situation, these electrons may cause dissociation of the precursor molecules through four distinct processes: dissociative ionization (DI), dissociative electron attachment (DEA) and neutral and dipolar dissociation (ND and DD) upon electronic excitation[20,21]. These processes all have different energy dependences and lead to different fragmentation products, making the effective damage yield dependent on both the electron energy distribution and the energy dependence of the cross sections for the individual processes[20,22,23]. With this in mind, it is clearly a challenging task to design precursors that fragment completely under electron exposure and leave behind high metal content deposits.

Until fairly recently, the bulk of the studies on FEBID of gold were conducted with commercially available β-diketonate-derived Au(III) complexes commonly used in CVD, i.e., Me$_2$Au(acac), Me$_2$Au(tfac) and Me$_2$Au(hfac) [24–27]. These are volatile and stable precursors, however, in FEBID without any purification steps, they generally deliver deposits with gold content ranging from 20 to 40 atom % and correspondingly high carbon content. This was addressed in a few studies by in situ or post-deposition oxidative removal of the carbon using oxygen or water, resulting in gold content as high as 81 to 92 atom %. [28]. In contrast to the Au(III) complexes, early experiments with the gold(I) complexes Cl-Au-PF$_3$ [29–31] and Cl-Au-CO [32] were found to produce high purity deposits without any purification measures. In these studies, 95 atom % Au was reported for Cl-Au-PF$_3$ [29–31] and the formation of gold grains with about 22 μΩ resistivity was reported for Cl-Au-CO [32]. However, these compounds are labile, and readily decompose under ambient conditions, making them unsuitable for practical applications. Stimulated by the high gold content of these precursors, efforts have been made to design stable and volatile gold(I) complexes that still maintain the high performance observed for Cl-Au-PF$_3$ and Cl-Au-CO in FEBID[16,19,33]. However, though these were generally found to be suitable FEBID precursors with respect to their volatility, stability and deposit growth rates, the achievable gold content was low (about 7 – 22%), with the highest gold content (22%) achieved for CF$_3$AuCNCH$_3$ in deposition using an Auger spectrometer under UHV conditions[34].

Evidently FEBID involves a complex interplay between the fundamental electron induced processes leading to the initial precursor fragmentation, electron induced secondary processes, and how these are altered at surfaces and in the deposition process. It is thus important in the effort to tailor

organometallic precursors for the use in FEBID, to understand the fundamental processes leading to their initial fragmentation and immobilization in the deposition process.

In this context we have studied DEA and DI of $CF_3AuCNC(CH_3)_3$, one of the precursors from the series of recently tested Au(I) precursors[34]. Electron induced fragmentation processes are studied in the gas phase under single collision conditions and under conditions where collisional stabilization is provided, i.e., conditions that should better reflect the effective energy dissipation that is in place at the surfaces in the FEBID process. Appearance energies are determined for selected DI processes and quantum chemical calculations are used to support the interpretation of the observed DEA and DI processes. The gas phase results are compared to the composition of deposits from this precursor generated in an UHV Auger spectrometer[34] and discussed in the context of the initial fragmentation processes and electron induced secondary decomposition.

2. Methods

2.1. Experimental setup

Electron-molecule interaction experiments under single collision conditions were carried out in a crossed beam instrument that has previously been described in detail[35]. A molecular beam of $CF_3AuCNC(CH_3)_3$ was generated by gas effusion through a stainless-steel capillary system that can be heated to achieve sufficient working pressure with low vapor pressure compounds. The effusive molecular beam crosses a quasi-monoenergetic electron beam that is generated with a trochoidal electron monochromator. Charged products that are formed in the interaction section are extracted into a quadrupole mass spectrometer (EPIC 1000, Hiden Analytical Warrington, UK) for m/z analyses and detection. The base pressure of the instrument was on the order of $2\text{-}4 \times 10^{-8}$ mbar and the electrostatic lens components are maintained at 393 K to avoid condensation of the target gas and background impurities. The working pressure during experiments was on the order of $2\text{-}4 \times 10^{-7}$ mbar. In negative ion mode, the energy scale was calibrated by the peak of the SF_6^- formation from SF_6 set as 0 eV. The full width at half maximum of the same signal was used to estimate the energy resolution of the electron beam, which was found to be around 190 meV during the current experiments. The monochromator settings were kept the same for the positive ion measurements and we assume the energy resolution to be the same. The energy scale in positive ion mode was calibrated by the first ionization energy of Ar, using the onset of the Ar^+ signal recorded in the beginning and end of each measurement day. Mass spectra were recorded at fixed incident electron energies by scanning through the relevant m/z range and ion yield curves were recorded at fixed m/z ratios by scanning through the relevant electron energy range. Appearance energies for the observed positive ions were determined by fitting a Wannier-type threshold function to the onset region of

the respective ion yields. The reported AEs are the average of three measurements taken on different days and the confidence limits are the standard deviations of the averages from these curves and are optical inspection to make sure that they bracket the onset of the individual curves. These are higher or equal to the. More information on the fitting procedure may be found in reference [36]. The intensities of the ion yields are normalized with respect to the working pressure and the ion signal from SF_6^- at 0 eV and Ar^+ at 70 eV for the negative and positive ions, respectively.

Direct insertion probe negative chemical ionization mass spectra (DIP NCI MS) and direct insertion probe electron ionization mass spectra (DIP EI MS) were recorded with a Thermo Scientific DSQ II with a Thermo Scientific direct insertion probe (DIP) with an ion source temperature of 60C (373 K), using Qual Browser, Thermo Xcalibur 2.2 SP1.48, August 12, 2011, for data reduction. After evacuation of the sample vessel, the probe was held at 30°C for 10 s before being ramped 1°C/sec to 60°C where the temperature was kept constant for 10 min. Electron ionization mass spectra were recorded at 70 eV electron energy and the negative ion spectra were also recorded with 70 eV initial electron energy, but in the presence of methane as moderation gas for thermalization of the electrons, i.e., these represent thermal electron attachment at 333 K. While recording the DIP NCI MS, the methane moderation gas was supplied to the ionization region to maintain a nominal pressure of 1 Torr. In this setup an approximately 1 mm^2 aperture allows gas flow into the main chamber where the pressure is about 4.4×10^{-6} Torr during the experiments. With the 3.8 Å kinetic diameter of methane, and at 1 Torr, the mean free path in the ionization region is about 53 nm, which translates to a collision frequency of about 5×10^8 s^{-1} at 333 K. During the DIP EI MS, on the other hand, the ionization region is open at the top, providing an approximately 100 mm^2 aperture connecting the ionization region with the main chamber. During these experiments the pressure measured at the ion gauge of the main chamber is about 3.3×10^{-7} Torr, and as the conductance of the ionization region to the main chamber is directly proportional to the area of aperture, we estimate the pressure in the ionization region during the acquisition of the DIP EI MS to be 0.75 mTorr. Assuming a 10 Å kinetic diameter of $CF_3AuCNC(CH_3)_3$, this translates to a mean free path of 10 μm and a collision frequency of 2.7×10^6 s^{-1} at 333 K. Though these considerations only give an estimate, it is clear that DIP EI experiments are not conducted under single collision conditions.

The subject molecule, $CF_3AuCNC(CH_3)_3$, was synthesized according to a previously published procedure [34]. It is a white coloured powder but was found to adapt a slight pinkish appearance after prolonged storage under ambient conditions, indicating minor decomposition and formation of gold nanoparticles. Thermogravimetric analysis, however, showed no sign of mass loss up to about 290 K, after which rapid mass loss is observed with 30% reduction reached at 310 K[37]. All samples were stored refrigerated at -20 °C.

2.2. *Quantum chemical calculations*

All quantum chemical calculations were performed using the ORCA computational chemistry software, version 4.1[38]. The geometry optimizations for all the neutral and charged fragments and parent molecules, were performed with tight SCF settings using the hybrid DFT functional PBE0 as well as the triple-zeta polarization basis set def2-TZVP, and the D3BJ dispersion correction by Grimme et al. [39]. In addition, for closed-shell and open-shell systems, the unrestricted Kohn-Sham (UKS) and restricted Kohn-Sham (RKS) formalisms were used, respectively. The PBE0 functional was chosen based on studies by Kepp et al. [40] and Kang et al. [41], where they, found it to be one of the most accurate functionals at predicting the binding energies and structures of gold complexes. Harmonic vibrational frequencies were confirmed to be positive at the PBE0/def2-TZVP level of theory and were used to calculate the zero-point vibrational energy and thermal corrections. In addition to the DFT calculations, single point calculations were also conducted at the coupled-cluster level of theory on the optimized PBE0-TZVP geometries[42]. These calculations were carried out with normal PNO settings at the DLPNO-CCSD(T) level, using the double-zeta basis set def2-TZVP and the valence quadrupole-zeta auxiliary basis set TZVP/c.

The threshold values reported were calculated by subtracting the energy of all generated fragments from the energy of the parent molecule, including the zero-point vibrational energy and thermal corrections for the parent molecule and all fragments. For comparison with the experimental AEs, the threshold values for alternative reaction paths, leading to the observed *m/z* ratios, were calculated.

2. Results and discussion.

Figures 1 and 2 show positive ion mass spectra of $CF_3AuCNC(CH_3)_3$ recorded at 70 eV electron ionization energy. The mass spectra in Figure 1 show the *m/z* range from around 10 to about 190, i.e., covering fragments that do not contain the central Au metal atom (*m/z* 197), and Figure 2 covers the *m/z* range from about 190 to about 360. In both figures the mass spectra shown in panels a), b) and c) are recorded in the crossed beam experiment with the capillary inlet system at 298, 333 and 353 K respectively. For comparison, a direct insertion probe electron ionization mass spectrum (DIP EI MS) covering the same *m/z* ranges is shown in panel d). Similarly, Figure 3 a), b) and c) show negative ion mass spectra recorded in the crossed beam experiment at about 0 eV incident electron energy with the inlet system at 298, 333 and 353 K, respectively, while panel d) shows a direct insertion probe chemical ionization negative ion mass spectrum (DIP NCI MS). Crossed beam MS for negative ions were also recorded at 1eV intervals up to 10 eV but no significant fragments were observed above 0 eV.

Most noticeably, the positive ion mass spectra (Figures 1 and 2) show a rich fragmentation pattern, while only the m/z ratios 292, [CF$_3$AuCN]$^-$ and m/z 335 are observed in the crossed beam negative ion mass spectra at 353K, and m/z 292 is the only significant contribution in the DIP NCI spectrum. In fact, m/z 335 originates from an impurity caused by minor decomposition of the sample during shipping of the batch used in the crossed beam experiment, and is attributed to the formation of [Au(CF$_3$)$_2$]$^-$. The same batch of material did not show this impurity before shipping as has been confirmed with DIP NCI MS performed at the University of Florida (Figure 3d). Thus, [CF$_3$AuCN]$^-$ is the only significant ion formed from CF$_3$AuCNC(CH$_3$)$_3$ upon electron attachment. For the positive ions it is apparent in the comparison of the crossed beam mass spectra with the DIP EI spectrum that the relative intensities of the low m/z fragments are significantly higher in the crossed beam experiment. At the lower temperatures, this is to a large extent due to background impurities in the crossed beam chamber and minor decomposition during shipping, as is apparent when comparing the crossed beam spectra recorded at room temperature, 333 K and 353 K. However, the most significant contributions in the spectra recorded at 353 K, m/z 39, 41, 57 and 69 are clearly from DI of CF$_3$AuCNC(CH$_3$)$_3$. And, though we can not exclude some contributions from thermal decomposition at 353 K we consider this to be unlikely as the decomposition temperature of CF$_3$AuCNC(CH$_3$)$_3$ as determined by thermogravimetri is 373 K and no significant changes in the MS were observed over several days of experiments. This is also
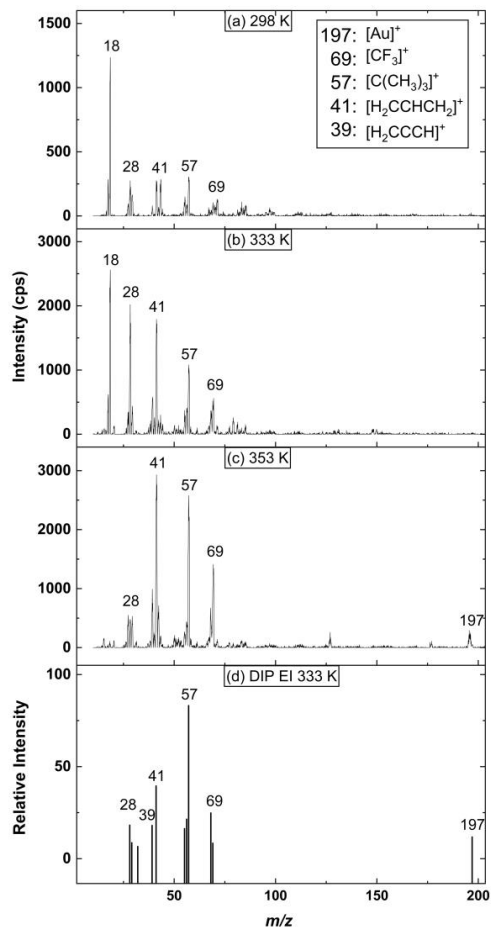

Figure 1. Positive ion mass spectra of CF$_3$AuCNC(CH$_3$)$_3$, recorded at 70 eV electron ionization energy. Panels a), b) and c) are recorded in the crossed beam experiment in the m/z range of from 10-200 with the inlet system at 298 K, 333 K, and 353 K, respectively. Panel. (d) is recorded in the m/z range from 25 to 200, using direct insertion probe electron ionization mass spectrometry (DIP EI MS) at a probe temperature of 333 K.

apparent from the relative intensity of the *m/z* 335 peak in the crossed beam negative ion mass spectra recorded at 333 as compared to 353 K. We thus attribute the difference in the relative intensities observed in the 353 K crossed beam spectrum and the DIP EI spectrum mainly to the fact that the local pressure in the ionization region of the DIP EI mass spectrometer is well beyond that for single collision conditions. Hence, that collisional stabilization influences the relative intensities in the positive DIP mass spectra. This effect may be further enhanced by the higher internal energy at 353 K as compared to 333.

Notwithstanding, with an estimated pressure in the ionization region of 0.75 mTorr, as discussed in the experimental section, the mean free path is on the order of 10 μm in the DIP EI MS experiment, hence, a number of collisions will take place on the ion's way from its site of ionization to the entrance of the mass spectrometer. The origin of the *m/z* 39, 41, 57 and 69 fragments from the intact parent molecule is further supported by comparing the experimental appearance energies (AEs) of these with the respective

Figure 2. Positive ion mass spectra of $CF_3AuCNC(CH_3)_3$, recorded at 70 eV electron ionization energy over the *m/z* range from 190 to 360. Panels a), b) and c) are recorded in the crossed beam experiment with the inlet system at 298 K, 333 K, and 353 K, respectively. Panel (d) is recorded with the direct insertion probe electron ionization mass spectrometer (DIP EI MS) at a probe temperature of 333 K.

calculated thresholds for their formation through dissociative ionization of $CF_3AuCNC(CH_3)_3$. Figure 4 shows the onset region of the ion yield curves for these fragments along with the respective Wannier-type threshold fits used to determine their appearance energies (AEs). The optimized structures of the ionic fragments are also shown in the respective panels along with their AEs and confidence limits as determined from three independent data sets (see method section). Table 1 compares these AEs with the thermally corrected threshold energies calculated at the PBE0-def2-TZVP and DLPNO-CCSD(T)-def2-TZVP levels of theory for potential processes leading to their
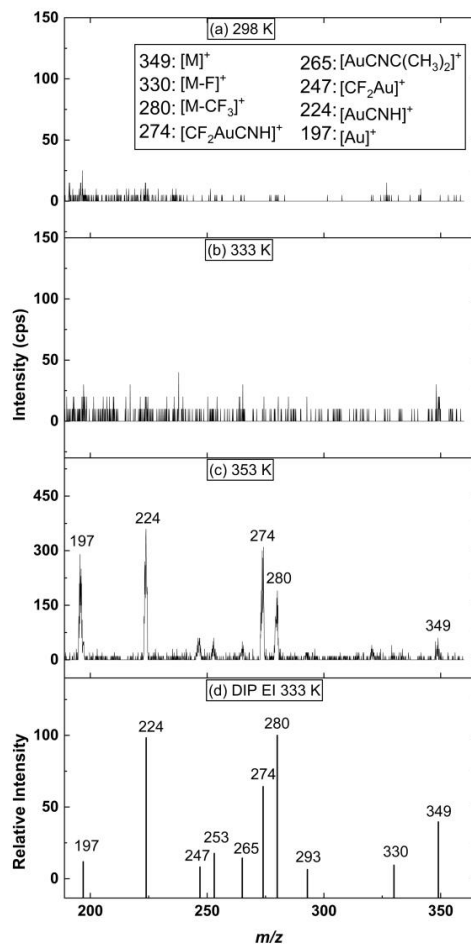
observation. In general, the DLPNO-CCSD(T)-def2-TZVP level of theory is considered to be the more accurate approach and in our assignments of the observed *m/z* ratios, we look for agreement with this method.

For *m/z* 39, the experimentally determined AE is found to be 15.0 ± 0.3 eV. This fragment must originate from partial fragmentation of the *t*-butyl isocyanide ligand, leading either to the elemental compositions C_3H_3 or NC_2H for the positive ion fragment. For this fragment, the best agreement with the threshold values are found for the formation of the $[H_2CCCH]^+$ cation and CF_3AuCN, CH_4 and H_2 as neutral fragments. At the PBE0-def2-TZVP and DLPNO-CCSD(T)/def2-TZVP levels of theory, the threshold for this reaction is found to be 15.32 and 14.87 eV, respectively. Assuming the formation of $[HCCHCH]^+$ rather than $[H_2CCCH]^+$ lowers the threshold values to 13.91 and 13.68 eV, respectively. This is in both cases more than 1 eV below the experimental AE. Considering the formation of $[CNCH]^+$ and the neutrals CF_3Au and propane ($CH_3CH_2CH_3$), on the
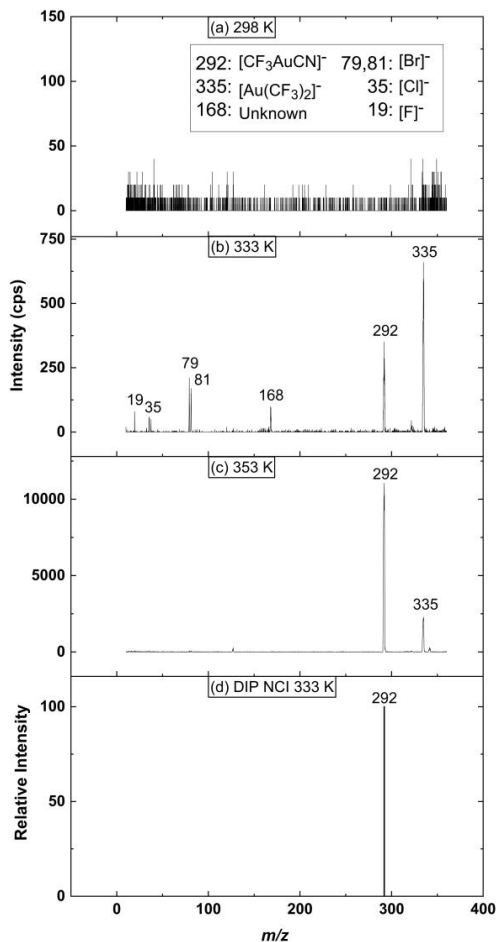

Figure 3. Negative ion mass spectra of $CF_3AuCNC(CH_3)_3$. Panels a), b) and c) are recorded in the crossed beam experiment at an incident electron energy of 0 eV in the *m/z* range from 10 to 360 with the inlet system at 298 K, 333 K, and 353 K, respectively. Panel. (d) is recorded using direct injection probe negative chemical ionization (DIP NCI MS) in the *m/z* range from 50 to 360, at a probe temperature of 333 K using methane at 1 torr nominal pressure as moderation gas.

other hand, results in threshold values of 15.65 and 15.48 eV at the respective levels of theory. These are both about 0.5 eV above the experimental value for the AE of *m/z* 39.

For *m/z* 41, the AE is found to be 12.1 ± 0.3 eV, and the best agreement with the calculated threshold at the DLPNO-CCSD(T)/def2-TZVP level of theory is found when considering the formation of $[H_2CCHCH_2]^+$ and the neutral counterparts CH_4 and CF_3AuCN, where we find the threshold to be 12.45 eV. At the PBE0-def2-TZVP level, the threshold for this reaction is found
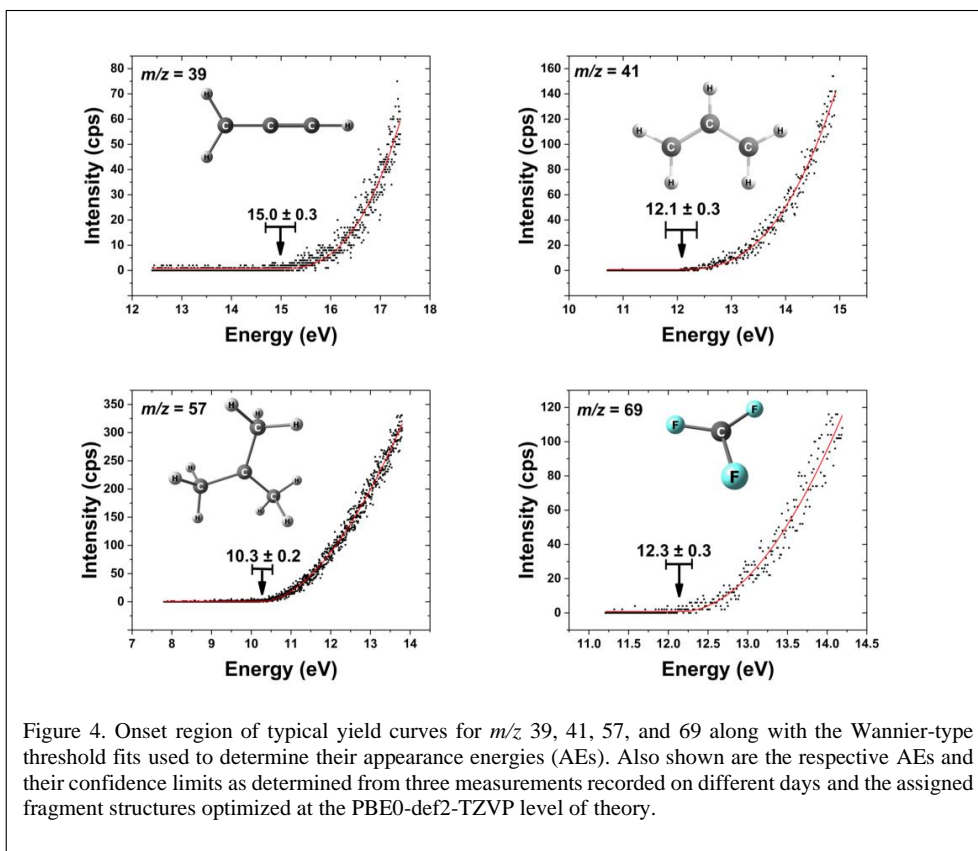
Figure 4. Onset region of typical yield curves for *m/z* 39, 41, 57, and 69 along with the Wannier-type threshold fits used to determine their appearance energies (AEs). Also shown are the respective AEs and their confidence limits as determined from three measurements recorded on different days and the assigned fragment structures optimized at the PBE0-def2-TZVP level of theory.

to be 12.65 eV, i.e., 0.25 eV above the higher confidence limit of the AE. However, considering the $[H_2CCCH_3]^+$ isomer as the positive fragment raises the threshold values to 12.85 and 12.82, respectively, i.e., about 0.4 eV above the higher confidence limit. Also, a number of isomers of C_2H_3N were considered for the positively charged fragment *m/z* 41, as is shown in Table 1. The threshold values for these were, generally found to be well above the experimental AE, with the exception of the formation of the $[HCNCH_2]^+$ ion and $CF_3AuC(CH_3)_2$ as the neutral counterpart. For this reaction we find the threshold to be 12.35 eV at the PBE0-def2-TZVP level of theory, hence in good agreement with the experimental value but at the coupled cluster level the threshold is found to be 12.52 eV, about 0.2 eV above the confidence limits of the AE. This reaction, however, constitutes significant rearrangements including rupture of the CN triple bond and exstensive rearrangement of the *t*-butyl group. We thus consider this cannel unlikely as compared to the formation of $[H_2CCHCH_2]^+ + CH_4 + CF_3AuCN$ which proceeds through single bond ruptures and hydrogen migration within the fragmenting *t*-butyl group.

Table 1. Appearance energies (AEs) for m/z 39, 41, 57 and 69 in dissociative ionization of CF$_3$AuCNC(CH$_3$)$_3$ under single collision conditions compared to the respective threshold energies calculated at the PBE0-TZVP and DLPNO-CCSD(T)-TZVP levels of theory. The threshold values are calculated for different reaction paths and the assigned reaction, based on the best match with the DLPNO-CCSD(T)-TZVP threshold values, are highlighted bold. Additionally, the AE and the threshold values for the formation of m/z 292, [CF$_3$AuCN]$^-$, through dissociative electron attachment to CF$_3$AuCNC(CH$_3$)$_3$ are shown in the last row.

	CF$_3$AuCNC(CH$_3$)$_3$			
m/z	Products	AE (eV)	PBE0-def2-TZVP (eV)	DLPNO-CCSD(T)-def2-TZVP (eV)
39	**[H$_2$CCCH]$^+$ + CF$_3$AuCN + CH$_4$ + H$_2$**	15.0 ± 0.3	**15.32**	**14.87**
	[CNCH]$^+$ + CF$_3$Au + CH$_3$CH$_2$CH$_3$		15.56	15.48
	[HCCHCH]$^+$ + CF$_3$AuCN + CH$_4$ + H$_2$		13.91	13.68
41	**[H$_2$CCHCH$_2$]$^+$ + CH$_4$ + CF$_3$AuCN**	12.1 ± 0.3	**12.65**	**12.45**
	[CNCH$_3$]$^+$ + CF$_3$Au + CH$_3$CCH$_3$		17.33	17.23
	[CNCH$_3$]$^+$ + CF$_3$AuC(CH$_3$)$_2$		14.67	14.47
	[HCNCH$_2$]$^+$ + CF$_3$Au + CH$_3$CCH$_3$		15.18	15.27
	[HCNCH$_2$]$^+$ + CF$_3$AuC(CH$_3$)$_2$		12.35	12.52
	[H$_2$CCCH$_3$]$^+$ + CH$_4$ + CF$_3$AuCN		12.85	12.82
57	**[C(CH$_3$)$_3$]$^+$ + CF$_3$AuCN**	10.3 ± 0.2	**10.61**	**10.82**
	[HCCH$_2$(CH$_3$)$_2$]$^+$ + CF$_3$AuCN		14.54	14.85
69	**[CF$_3$]$^+$ + AuCNC(CH$_3$)$_3$**	12.3 ± 0.3	**12.62**	**12.67**
292	**[CF$_3$AuCN]$^-$ + C(CH$_3$)$_3$**	0	**-1.20**	**-1.23**

For the *m/z* ratios 57 and 69 the assignment is more straight forward as these can unambiguously be assigned to [C$_4$H$_9$]$^+$ and [CF$_3$]$^+$, respectively. For *m/z* 57 the AE is found to be 10.3 ± 0.2 eV and for direct dissociation and the formation of [C(CH$_3$)$_3$]$^+$ and CF$_3$AuCN as the neutral counterpart the calculated threshold for this reaction is 10.61 and 10.82 eV at the PBE0-def2-TZVP and DLPNO-CCSD(T)/def2-TZVP levels of theory, respectively. Hence, 0.1 and 0.3 eV above the confidence limit, at the respective levels of theory. We additionally considered the formation of [HC(CH$_2$)(CH$_3$)$_2$]$^+$ through hydrogen transfer from one of the methyl groups to the central carbon, but at both levels of theory we find the threshold for this reaction to be more than 4 eV above the experimental AE. For *m/z* 69, i.e., the formation of [CF$_3$]$^+$ and AuCNC(CH$_3$)$_3$, the AE is found to be 12.3 ± 0.3 eV and threshold energies of 12.62 and 12.67 eV are calculated at the PBE0-def2-TZVP and DLPNO-CCSD(T)/def2-TZVP levels of theory, respectively. In both cases these are only marginally above the upper confidence limit of the AE, 12.3 ± 0.3 eV.

In general, the agreement between the experimental AEs and the calculated threshold values is good, though the threshold values tend to be somewhat higher than the AEs, and more so at the

DFT level of theory. This is likely, at least in part, to be due to the fact that the thermal correction is that of the average, and not the energy distribution at 353K. Thus, the high energy tail of the distribution may shift the observed AEs to lower energies with respect to the actual thermally corrected threshold.

As shown in Figure 2, the main gold containing fragments in the crossed beam experiment are observed at m/z 197, 224, 274 and 280, corresponding to the positive ions Au^+, $[AuCNH]^+$, $[CF_2AuCNH]^+$ and $[AuCNC(CH_3)_3]^+$. Lesser contributions are observed at m/z 247, 253 and 265, and based on their elemental composition, stability and extent of rearrangement required for their formation, they are assigned to $[AuCF_2]^+$, $[CH_3AuCNCH_3]^+$, and $[AuCNC(CH_3)_2]^+$. A minor contribution is also observed from the parent cation $[CF_3AuCNC(CH_3)_3]^+$ at m/z 349. Qualitatively, this agrees with the m/z ratios observed in the DIP EI spectra shown in panel d), however, the relative intensities differ markedly in these experiments. For further comparison, Table 2 compares the relative intensities of the main fragments observed in the crossed beam experiment with those observed in the DIP EI experiment. The intensities are normalized with respect to the highest intensity fragments set as 100 in both cases. In the crossed beam experiment this is m/z 41; $[H_2CCHCH_2]^+$ and in the DIP EI, m/z 280; $[AuCNC(CH_3)_3]^+$. Additionally, the relative intensities of the gold containing fragments observed in the crossed beam experiment experiments are shown in the last column, normalized to the highest intensity gold containing fragment, m/z 224. With respect to the gold containing fragments, it is most notable that the relative intensity of Au^+, m/z 197 is significantly higher in the crossed beam experiment as compared to the DIP EI MS. Conversely the relative intensity of the parent cation is significant in the DIP EI MS, while it is only a minor contribution to the mass spectra recorded under single collision conditions. We attribute this to the effect of collisional stabilization in the DIP EI MS experiment. This can also explain the absence of m/z 330, $[CF_2AuCNC(CH_3)_3]^+$ and the relatively low intensity of m/z 280 in the crossed beam experiment under single collision conditions as compared to DIP EI MS, as both these fragments may decay further to form m/z 274 $[CF_2AuCNH]^+$, 247 $[CF_2Au]^+$, 224 $[AuCNH]^+$ or 197 $[Au]^+$.

Table 2. Normalized peak intensities from the EI mass spectra of $CF_3AuCNC(CH_3)_3$ at 70 eV recorded under single collision conditions and in DIP EI MS. The intensities are normalized with respect to the highest intensity fragment set as 100 in both cases. This is m/z 41 in the crossed beam experiment and m/z 280 in the DIP EI experiment (columns three and four, respectively). For better comparison the last column also shows the relative intensities of gold-containing fragments observed in the crossed beam experiment normalized to the highest intensity gold containing fragment, m/z 224.

		Relative Intensity		
m/z	Fragment	Crossed beam	DIP	Au-Fragments Crossed beam
349	$[CF_3AuCNC(CH_3)_3]^+$	2	40	15
330	$[CF_2AuCNC(CH_3)_3]^+$	0	9	0
280	$[AuCNC(CH_3)_3]^+$	2	100	17
274	$[CF_2AuCNH]^+$	11	64	92
265	$[AuCNC(CH_3)_2]^+$	0	14	0
247	$[CF_2Au]^+$	2	8	17
224	$[AuCNH]^+$	12	98	100
197	$[Au]^+$	10	12	83
69	$[CF_3]^+$	48	8	-
57	$[C(CH_3)_3]^+$	88	83	-
41	$[H_2CCHCH_2]^+$	100	40	-
40	$[H_2CCCH_2]^+$	9	0	-
39	$[H_2CCCH]^+$	34	18	-
15	$[CH_3]^+$	5	-	-

A priori, one would expect that the DIP EI MS, where collisional stabilisation is provided, should better reflect the fragmentation as it is observed at surfaces where an effective energy dissipation is in place. It is thus interesting to compare the current experiments with the composition of actual deposits formed under FEBID conditions. In this context, Table 3 shows the average carbon, fluorine, and nitrogen loss per incident in the gas phase experiments, and the atomic composition of a hypothetical deposit that would result if these processes, unaltered and alone, would determine the composition of a deposit. For the average element loss, the contribution of all gold containing fragments is weighted with the respective number of carbons, fluorine or nitrogen lost, and divided by the total intensity of all fragments. For m/z 39, 41, 57 and 75 the neutral gold containing fragments as assigned in Table 2 provide the basis for this calculation for both experiments. At the bottom of the table is the elemental composition of a deposit formed from this precursor under FEBID conditions.[34] These deposition experiments were conducted under UHV in an Auger spectrometer at an electron-beam energy of 3 kV and a current of 1 μA on a silicon substrate that was pre-treated by sputtering with 4 keV Ar^+ ions to remove the oxide layer and residual carbon.

Table 3. Average carbon, fluorine, and nitrogen loss per incident observed in the crossed beam EI experiment, the DIP EI experiment and in DEA (crossed beam and DIP NCI). Also shown are the atomic compositions that would result from the respective average elemental losses and the deposits composition observed in EBID in an Auger spectrometer at an electron energy of 5 keV.[34]

Element loss	C	N	F	
Crossed beam (EI)	3.15	0.03	0.71	
DIP EI	3.30	0.04	1.71	
DEA (Crossed beam and DIP)	4	0	0	
Elemental composition calculated for EI and DEA and observed in EBID (Ref. [34])				
Crossed beam (EI)	14 at.% Au	40 at.% C	32 at.% F	14 at.% N	
DIP EI MS	17 at.% Au	45 at.% C	22 at.% F	16 at.% N	
DEA	14 at.% Au	29 at.% C	43 at.% F	14 at.% N	
EBID [34]	14 at.% Au	80 at.% C	0 at.% F	6 at.% N	<1 at.% O

With this approach, the average F, N and C loss per incident in the crossed beam experiment is found to be 0.71, 0.03, and 3.15, respectively, and in the DIP EI MS these are found to be 1.71, 0.04, and 3.30, respectively. Under the assumption that all fragments that do not contain gold would desorb, this translated to a deposit of 14 at.% Au, 40 at.% C, 32 at.% F, and 14 at.% N using the crossed beam data. The expected composition derived from the DIP EI MS data, where collisional stabilization potentially plays a role. would be 17 at.% Au, 45 at.% C, 22 at.% F, and 16 at.% N, respectively. Applying the same approach to the negative ion data, where the only significant fragment is [CF$_3$AuCN]$^-$ (*m/z* 292) in both experiments is straightforward and results in an expected Au:C:F:N deposit composition of 1:2:3:1, i.e., 14 at.% Au, 29 at.% C, 43 at.% F, and 14 at.% N. For comparison, the elemental composition of the deposit generated under FEBID conditions was found to be 14 at.% Au, 80 at.% C, 0 at.% F, 6 at.% N, as determined by EDX.[34] Most noticeably, fluorine is as good as quantitatively removed in the deposition experiments, while less than 1 fluorine is lost on average per incident through DI under single collision conditions, and 1.7 in the DIP EI experiments. Moreover, the fluorine loss in both the gas phase EI experiments is substantially through the loss of the CF$_3$ group from the central gold. This is clearly not the route for fluorine loss in the deposition experiment where no carbon removal is observed and the stoichiometric Au:C ratio of the precursor is retained in the deposit. Furthermore, in DEA, both under single collision conditions and in the DIP NCI experiment, no fluorine loss is observed. It is thus clear that the DEA and DI processes observed in the gas phase are not reflected in the deposit's composition, even if collisional stabilization is provided. However, this is in line with the interpretation of the deposition experiments, where sequential fluorine loss upon prolonged irradiation of the initial deposit was proposed[34]. Considering that the electron dose in the deposition experiment was about 1.15 x 10^{14} e$^-$/μm^2, electron induced secondary reactions are likely to play a significant role. Presuming, for

simplicity, dense packing and a 1 nm^2 area occupied by each molecule at the surface, 1 μm^2 is covered by a monolayer of 10^6 molecules. The thickness of the deposit in the Auger experiments was stated to be > 100 nm, and if we, for sake of argument, assume 200 nm thickness, each molecule has been exposed to more than 5×10^5 electrons. With a generic electron induced fragmentation cross section of 10^{-16} cm^2, which is on the order of magnitude determined for other FEBID precursors [22,43,44], the reactive area is of this 1 μm^2 coverage is about 0.01 μm^2. Thus, each molecule may have been subject to about 5,000 reactive incidences. In this consideration it is assumed that the cross section remains the same after each reactive incident and that the reactive cross section of the high energy primary beam is the same as measured with low energy electrons in the gas phase. These assumptions do not hold, and the cross sections for further electron induced decomposition of immobilized secondary and tertiary fragments may be orders of magnitude lower than those for the initial process. Nonetheless it is clear from these considerations that electron induced secondary reactions may play a significant, if not determining role in FEBID. It is also clear that the carbon containing ionic fragments do not desorb from the surface but are rather immobilised and subjected to further electron induced fragmentation. Secondary and tertiary electron induced reactions have been discussed in context to other FEBID precursors [23,45] and is in fact reflected in a number of non-steady state experiments where thin precursor layers are exposed to 500 eV electrons and the elemental composition change is monitored in dependence of the electron dose. Good examples are the precursors Ru(CO)$_4$I$_2$[46], cis-Pt(CO)$_2$Cl$_2$[47], and (η^3-C$_3$H$_5$)Ru(CO)$_3$Br[48], where initial electron induced carbonyl loss at low electron doses correlates well with low energy electron induced fragmentation as it is observed in the gas phase. Continued electron exposure, however, leads to further, secondary fragmentation, partly resulting in removal (desorption) of the halogens but also in decomposition of carbon containing ligands and integration of carbon in the deposit.

Turning back to the negative ion formation, Figure 5a shows the ion yield curve for [CF$_3$AuCN]$^-$ in the energy range from 0 to 10 eV, with an expanded insertion comparing the normalized [CF$_3$AuCN]$^-$ ion yield curve and that of SF$_6^-$ from SF$_6$, used for the respective energy calibration. Figure 5b compares contour plots of the LUMO of the neutral molecule with the HOMO (SOMO) of the ground state anion. The contour plots are generated with Chemcraft[49] for the respective equilibrium geometries optimized at the PBE0-def2-TZVP level of theory and visualized with a contour value of 0.05. Noticeably, the [CF$_3$AuCN]$^-$ signal shown in Figure 5a is slightly blue shifted (0.05 eV) and significantly broader (FWHM of 300 meV) than that of the SF$_6^-$ ion yield (190 meV), which in turn, reflects the energy distribution of the electron beam. As discussed above, the DEA spectra recorded in the crossed beam experiment under single collision conditions and in DIP NCI are nearly identical, with the dominating contribution being from *m/z* 292, i.e., loss of the *t*-butyl

group with the formation of [CF₃AuCN]⁻. The only difference is the additional observation of a fairly weak [M – H]⁻ signal (about 7%) in the DIP NCI spectra. This is not surprising as the DIP NCI experiments are recorded in the presence of methane as moderation gas at a pressure of about 1 torr (see the experimental section). The mean free path is thus on the order of 50 nm in these experiments, corresponding to a collisional frequency of about 5×10^8 s⁻¹ at 333 K. This in turn provides for efficient collisional stabilization and observation of the relaxed ground state anion is expected. Furthermore, at the PBE0-def2-TZVP level of theory, we find the adiabatic electron affinity (EA) of CF₃AuCNC(CH₃)₃ to be 0.63 eV and thus all prerequisites for the formation of the stable ground state anion should be provided. However, when comparing the vacant LUMO of the neutral with the HOMO of the anion (Figure 5b), it is clear that a single electron occupation of the LUMO of the neutral leads to strong coupling of this electronic state with the N–C(CH₃)₃ coordinate. While the neutral HOMO is

Figure 5. (a) Ion yield curve of [CF₃AuCN]⁻ formed in DEA to CF₃AuCNC(CH₃)₃ under single collision conditions in the incident electron energy range from about 0 to 10 eV. The inset shows an expansion of the energy range from about 0 to 1.5 eV, along with the respective [SF₆]⁻ calibration curve. (b) Isosurfaces of the LUMO of the neutral CF₃AuCNC(CH₃)₃ molecule and the HOMO (SOMO) of its ground state anion. These are generated with Chemcraft for the respective relaxed geometries optimized at the PBE0-def2-TZVP level of theory.

antibonding with π* character along the AuC–N coordinate of the linear ground state, a single electron occupation of this orbital leads to stabilization of the molecular anion through substantial bending of the C–N–C coordinate, leading to a change of the respective angle from 180° to 150°. Hence, the geometrical relaxation of the initially formed TNI to its ground state proceeds along a deformation coordinate, while the dissociation leading to the formation of [CF₃AuCN]⁻ is directly along the N–C(CH₃)₃ bond. It's also apparent, that strong orbital mixing is provided along the dissociation coordinate whereby the AuC–N antibonding π* character of the LUMO of the neutral is largely lost. In turn, it acquires an admix of σ* character along the N–C(CH₃)₃ bond with an
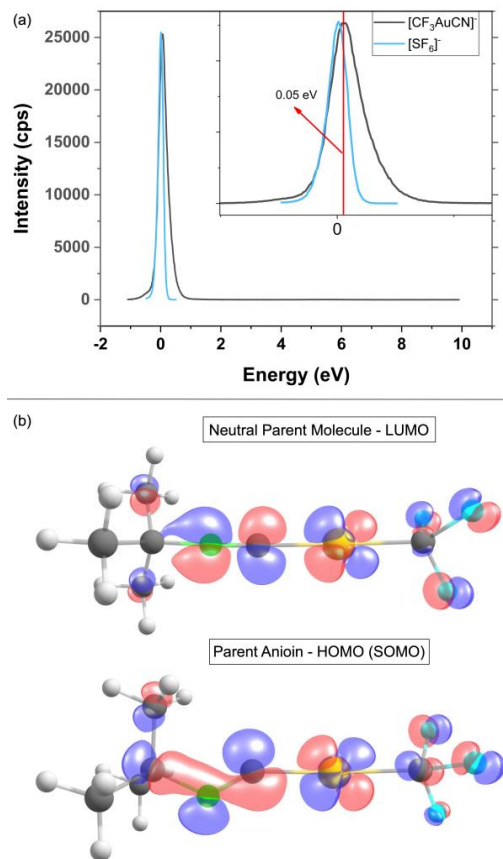
antibonding node at the C atom in the fully relaxed geometry. From these considerations, we anticipate that the initial TNI formed in the vertical transition is a strongly repulsive state with orbital mixing provided in the attachment process through the N–C(CH$_3$)$_3$ bending motion. In this picture, the extension along the N–C(CH$_3$)$_3$ coordinate is fast compared to the relaxing bending motion and proceeds on a timescale shorter than the collisional stabilization provided in the DIP NCI experiments. From the fundamental physical and chemical point of view, this is an interesting dynamic problem that is worthy of further studies, both from the experimental and theoretical side. Specifically, angular dependence measurements of the attachment process, such as velocity imaging would be of interest. Also, on the theory side non-adiabatic dynamic calculations would provide further insight. With respect to the deposition experiments discussed here above these dynamics may offer a rationale for the absence of carbon loss by dissociation and desorption of the *t*-butyl group through DEA. At the surface, the energy dissipation is direct, and the dissociation process is likely to be dampened in the presence of alternative relaxation paths such as the bending motion in the current case.

Conclusions

In the context of the development of precursor molecules suitable for the fabrication of gold nanostructures through focused electron beam induced deposition, we have studied low energy electron induced fragmentation of CF$_3$AuCNC(CH$_3$)$_3$. Dissociative electron attachment and dissociative ionization were studied both under single collision conditions and under conditions where collisional stabilization is provided. Dissociative ionization under single collision conditions was found to be more extensive than when collisional stabilization is provided and is dominated by charged organic ligand fragments, rather than charged gold containing fragments, as is the case in the DIP EI MS experiments. Interestingly the electron attachment spectra are identical under both conditions, and dissociation of the initially formed TNI to form [CF$_3$AuCN]$^-$ is the only significant channel. We find that the parent anion has positive electron affinity and would thus rather expect stabilization and its observation where intermolecular energy dissipation is provided. However, comparison of the distribution of the LUMO of the neutral parent molecule with that of the HOMO of the relaxed anion indicates a strong π*–σ* coupling in the attachment process, with the σ* antibonding character along the observed dissociation coordinate. We thus anticipate that dissociative relaxation along this coordinate proceeds significantly faster than collisional stabilization and relaxation of the anion to its ground state. When comparing the current gas phase results with the composition of deposits from this precursor generated in electron induced deposition in an UHV Auger spectrometer, marked differences are apparent. In the deposition experiments the

stoichiometric carbon and nitrogen content of the parent molecule is retained in the deposit while the fluorine is almost quantitatively removed. From the gas phase experiments on the other hand, significant carbon removal should be expected but only partial fluorine removal. Moreover, while the fluorine loss in the gas phase experiments is predominantly through dissociation of the CF_3 ligand, the fluorine removal in the deposit experiment is sequential through prolonged electron irradiation. In agreement with the deposition experiment, we attribute this to an initial fragmentation and immobilization on the surface through a first electron/molecule interaction. In this step, desorption, and in part also dissociation, is hindered through molecule surface interactions and efficient energy dissipation. Prolonged irradiation then leads to further fragmentation in electron-induced secondary and tertiary reactions that result in sequential fluorine loss, finally resulting in almost quantitative fluorine loss and carbonization of the remaining ligands.

Importantly, the consideration of the role of electron-induced secondary and tertiary reactions changes the parameter space that needs to be considered in the rational design of FEBID precursors, and also has consequences for the deposition strategies applied. Specifically, potential precursors need to be designed in such a way that the immobilized fragments from the initial electron-induced dissociation processes are still susceptible to further electron induced fragmentation, leading to desorption of the respective secondary ligand fragments.

Author contributions

Ali Kamali: Investigation, Calculations, Formal analysis, Validation, Writing – Original draft, Visualization. **Will G. Carden**: Resources, Investigation. **Jodie V. Johnson:** Resources, Investigation. **Lisa McElwee-White:** Funding acquisition, Conceptualization, Supervision,

Resources, Writing – Review & Editing. **Oddur Ingólfsson:** Project administration, Conceptualization, Funding acquisition, Supervision, Writing – Review & Editing, Methodology.

Data availability

The datasets generated during and/or analyzed during the current study are available from the corresponding author on reasonable request.

References

(1)   Saha, K.; Agasti, S. S.; Kim, C.; Li, X.; Rotello, V. M. Gold Nanoparticles in Chemical and Biological Sensing. *Chem. Rev.* **2012**, *112* (5), 2739–2779. https://doi.org/10.1021/cr2001178.

(2)   Dykman, L. A.; Khlebtsov, N. G. Gold Nanoparticles in Biology and Medicine: Recent Advances and Prospects. *Acta Naturae* **2011**, *3* (2), 34–55. https://doi.org/10.32607/20758251-2011-3-2-34-56.

(3)   Yang, X.; Yang, M.; Pang, B.; Vara, M.; Xia, Y. Gold Nanomaterials at Work in Biomedicine. *Chem. Rev.* **2015**, *115* (19), 10410–10488. https://doi.org/10.1021/acs.chemrev.5b00193.

(4)   Sondhi, P.; Lingden, D.; Bhattarai, J. K.; Demchenko, A. V; Stine, K. J. Applications of Nanoporous Gold in Therapy, Drug Delivery, and Diagnostics. *Metals*. 2023. https://doi.org/10.3390/met13010078.

(5)   Yeh, Y.-C.; Creran, B.; Rotello, V. M. Gold Nanoparticles: Preparation, Properties, and Applications in Bionanotechnology. *Nanoscale* **2012**, *4* (6), 1871–1880. https://doi.org/10.1039/C1NR11188D.

(6)   Hassan, H.; Sharma, P.; Hasan, M. R.; Singh, S.; Thakur, D.; Narang, J. Gold Nanomaterials – The Golden Approach from Synthesis to Applications. *Mater. Sci. Energy Technol.* **2022**, *5*, 375–390. https://doi.org/https://doi.org/10.1016/j.mset.2022.09.004.

(7)   Oliveira, B. B.; Ferreira, D.; Fernandes, A. R.; Baptista, P. V. Engineering Gold Nanoparticles for Molecular Diagnostics and Biosensing. *WIREs Nanomedicine and Nanobiotechnology* **2023**, *15* (1), e1836. https://doi.org/https://doi.org/10.1002/wnan.1836.

(8)   Huth, M.; Porrati, F.; Dobrovolskiy, O. V. Focused Electron Beam Induced Deposition Meets Materials Science. **2017**. https://doi.org/10.1016/j.mee.2017.10.012.

(9)   Hu, R.; Yu, L. Review on 3D Growth Engineering and Integration of Nanowires for

Advanced Nanoelectronics and Sensor Applications. *Nanotechnology* **2022**, *33* (22). https://doi.org/10.1088/1361-6528/ac547a.

(10) Zhang, Y.; Chu, W.; Foroushani, A. D.; Wang, H.; Li, D.; Liu, J.; Barrow, C. J.; Wang, X.; Yang, W. New Gold Nanostructures for Sensor Applications: A Review. *Materials (Basel).* **2014**, *7* (7), 5169–5201. https://doi.org/10.3390/ma7075169.

(11) Sackmann, M.; Bom, S.; Balster, T.; Materny, A. Nanostructured Gold Surfaces as Reproducible Substrates for Surface-Enhanced Raman Spectroscopy. *J. Raman Spectrosc.* **2007**, *38* (3), 277–282. https://doi.org/https://doi.org/10.1002/jrs.1639.

(12) Hu, M.; Chen, J.; Li, Z.-Y.; Au, L.; Hartland, G. V; Li, X.; Marquez, M.; Xia, Y. Gold Nanostructures: Engineering Their Plasmonic Properties for Biomedical Applications. *Chem. Soc. Rev.* **2006**, *35* (11), 1084–1094. https://doi.org/10.1039/B517615H.

(13) Utke, I.; Hoffmann, P.; Melngailis, J. Gas-Assisted Focused Electron Beam and Ion Beam Processing and Fabrication. *J. Vac. Sci. Technol. B Microelectron. Nanom. Struct.* **2008**, *26* (4), 1197–1276. https://doi.org/10.1116/1.2955728.

(14) Huth, M.; Porrati, F.; Schwalb, C.; Winhold, M.; Sachser, R.; Dukic, M.; Adams, J.; Fantner, G. Focused Electron Beam Induced Deposition: A Perspective. *Beilstein J. Nanotechnol.* **2012**, *3* (1), 597–619. https://doi.org/10.3762/bjnano.3.70.

(15) Huth, M. Focused Electron Beam Induced Deposition-Principles and Applications. *Proc. Beilstein Symp. Funct. ...* **2010**, 193–212.

(16) Carden, W. G.; Lu, H.; Spencer, J. A.; Fairbrother, D. H.; McElwee-White, L. Mechanism-Based Design of Precursors for Focused Electron Beam-Induced Deposition. *MRS Commun.* **2018**, *8* (2), 343–357. https://doi.org/10.1557/mrc.2018.77.

(17) Van Dorp, W. F.; Hagen, C. W. A Critical Literature Review of Focused Electron Beam Induced Deposition. *J. Appl. Phys.* **2008**, *104* (8). https://doi.org/10.1063/1.2977587.

(18) Ivo Utke, Stanislav Moshkalev, A. P. R. *Nanofabrication Using Focused Ion and Electron Beams*; 2018.

(19) Carden, W. G.; Pedziwiatr, J.; Abboud, K. A.; McElwee-White, L. Halide Effects on the Sublimation Temperature of X-Au-L Complexes: Implications for Their Use as Precursors in Vapor Phase Deposition Methods. *ACS Appl. Mater. Interfaces* **2017**, *9* (46), 40998–41005. https://doi.org/10.1021/acsami.7b12465.

(20) Thorman, R. M.; Ragesh Kumar, T. P.; Howard Fairbrother, D.; Ingólfsson, O. The Role of Low-Energy Electrons in Focused Electron Beam Induced Deposition: Four Case Studies of Representative Precursors. *Beilstein J. Nanotechnol.* **2015**, *6* (1), 1904–1926. https://doi.org/10.3762/bjnano.6.194.

(21)   Ingólfsson, O. *Low-Energy Electrons Fundamentals and Applications*; Pan Stanford Publishing Pte. Ltd.: Singapore, The Republic of Singapore, 2019.

(22)   Engmann, S.; Stano, M.; Papp, P.; Brunger, M. J.; Matejčík, Š.; Ingólfsson, O. Absolute Cross Sections for Dissociative Electron Attachment and Dissociative Ionization of Cobalt Tricarbonyl Nitrosyl in the Energy Range from 0 EV to 140 EV. *J. Chem. Phys.* **2013**, *138* (4), 0–7. https://doi.org/10.1063/1.4776756.

(23)   Kamali, A.; Bilgilisoy, E.; Wolfram, A.; Gentner, T. X.; Ballmann, G.; Harder, S.; Marbach, H.; Ingólfsson, O. On the Electron-Induced Reactions of (CH3)AuP(CH3)3: A Combined UHV Surface Science and Gas-Phase Study. *Nanomaterials*. 2022. https://doi.org/10.3390/nano12152727.

(24)   Wnuk, J. D.; Gorham, J. M.; Rosenberg, S. G.; Van Dorp, W. F.; Madey, T. E.; Hagen, C. W.; Fairbrother, D. H. Electron Beam Irradiation of Dimethyl-(Acetylacetonate) Gold(III) Adsorbed onto Solid Substrates. *J. Appl. Phys.* **2010**, *107* (5). https://doi.org/10.1063/1.3295918.

(25)   Jenke, M. G.; Lerose, D.; Niederberger, C.; Michler, J.; Christiansen, S.; Utke, I. Toward Local Growth of Individual Nanowires on Three-Dimensional Microstructures by Using a Minimally Invasive Catalyst Templating Method. *Nano Lett.* **2011**, *11* (10), 4213–4217. https://doi.org/10.1021/nl2021448.

(26)   Folch, A. High-Vacuum versus '"Environmental"' Electron Beam Deposition. *J. Vac. Sci. Technol. B Microelectron. Nanom. Struct.* **1996**, *14* (4), 2609. https://doi.org/10.1116/1.588994.

(27)   Koops, H. W. P.; Kretz, J.; Rudolph, M.; Weber, M.; Dahm, G.; Lee, K. L. Characterization and Application of Materials Grown by Electron-Beam-Induced Deposition. *Jpn. J. Appl. Phys.* **1994**, *33* (Part 1, No. 12B), 7099–7107. https://doi.org/10.1143/jjap.33.7099.

(28)   Shawrav, M. M.; Taus, P.; Wanzenboeck, H. D.; Schinnerl, M.; Stöger-Pollach, M.; Schwarz, S.; Steiger-Thirsfeld, A.; Bertagnolli, E. Highly Conductive and Pure Gold Nanostructures Grown by Electron Beam Induced Deposition. *Sci. Rep.* **2016**, *6*. https://doi.org/10.1038/srep34003.

(29)   Brintlinger, T.; Fuhrer, M. S.; Melngailis, J.; Utke, I.; Bret, T.; Perentes, A.; Hoffmann, P.; Abourida, M.; Doppelt, P. Electrodes for Carbon Nanotube Devices by Focused Electron Beam Induced Deposition of Gold. *J. Vac. Sci. Technol. B Microelectron. Nanom. Struct.* **2005**, *23* (6), 3174–3177. https://doi.org/10.1116/1.2130355.

(30)   Perentes, A.; Hoffmann, P.; Munnik, F. FOCUSED ELECTRON BEAM INDUCED

DEPOSITION OF GOLD AND RHODIUM. *23rd Eur. Mask Lithogr. Conf.* **2007**, *6533*, 65331Q. https://doi.org/10.1117/12.736918.

(31) Utke, I.; Hoffmann, P.; Dwir, B.; Leifer, K.; Kapon, E.; Doppelt, P. Focused Electron Beam Induced Deposition of Gold. *J. Vac. Sci. Technol. B Microelectron. Nanom. Struct.* **2000**, *18* (6), 3168. https://doi.org/10.1116/1.1319690.

(32) Mulders, J. J. L.; Veerhoek, J. M.; Bosch, E. G. T.; Trompenaars, P. H. F. Fabrication of Pure Gold Nanostructures by Electron Beam Induced Deposition with Au(CO)Cl Precursor: Deposition Characteristics and Primary Beam Scattering Effects. *J. Phys. D. Appl. Phys.* **2012**, *45* (47), 1–8. https://doi.org/10.1088/0022-3727/45/47/475301.

(33) Glessi, C.; Mahgoub, A.; Hagen, C. W.; Tilset, M. Gold(I) N-Heterocyclic Carbene Precursors for Focused Electron Beam-Induced Deposition. *Beilstein J. Nanotechnol.* **2021**, *12*, 257–269. https://doi.org/10.3762/bjnano.12.21.

(34) Carden, W. G.; Thorman, R. M.; Unlu, I.; Abboud, K. A.; Fairbrother, D. H.; McElwee-White, L. Design, Synthesis, and Evaluation of CF3AuCNR Precursors for Focused Electron Beam-Induced Deposition of Gold. *ACS Appl. Mater. Interfaces* **2019**, *11* (12), 11976–11987. https://doi.org/10.1021/acsami.8b18368.

(35) Bjarnason, E. H.; Ómarsson, B.; Engmann, S.; Ómarsson, F. H.; Ingólfsson, O. Dissociative Electron Attachment to Titatinum Tetrachloride and Titanium Tetraisopropoxide. *Eur. Phys. J. D* **2014**, *68* (5). https://doi.org/10.1140/epjd/e2014-50091-9.

(36) Fiegele, T.; Hanel, G.; Torres, I.; Lezius, M.; Märk, T. D. Threshold Electron Impact Ionization of Carbon Tetrafluoride, Trifluoromethane, Methane and Propane. *J. Phys. B At. Mol. Opt. Phys.* **2000**, *33* (20), 4263–4283. https://doi.org/10.1088/0953-4075/33/20/306.

(37) Carden, W. G. Ligand Effects in Gold Precursors for Focused Electron Beam Induced Deposition, Ph.D. Dissertation, University of Florida, 2020.

(38) Neese, F. The ORCA Program System. *Wiley Interdiscip. Rev. Comput. Mol. Sci.* **2012**, *2* (1), 73–78. https://doi.org/10.1002/wcms.81.

(39) Grimme, S.; Huenerbein, R.; Ehrlich, S. On the Importance of the Dispersion Energy for the Thermodynamic Stability of Molecules. *ChemPhysChem* **2011**, *12* (7), 1258–1261. https://doi.org/10.1002/cphc.201100127.

(40) Kepp, K. P. Benchmarking Density Functionals for Chemical Bonds of Gold. *J. Phys. Chem. A* **2017**, *121* (9), 2022–2034. https://doi.org/10.1021/acs.jpca.6b12086.

(41) Kang, R.; Chen, H.; Shaik, S.; Yao, J. Assessment of Theoretical Methods for

Complexes of Gold(I) and Gold(III) with Unsaturated Aliphatic Hydrocarbon: Which Density Functional Should We Choose? *J. Chem. Theory Comput.* **2011**, *7* (12), 4002–4011. https://doi.org/10.1021/ct200656p.

(42)   Riplinger, C.; Neese, F. An Efficient and near Linear Scaling Pair Natural Orbital Based Local Coupled Cluster Method. *J. Chem. Phys.* **2013**, *138* (3), 34106. https://doi.org/10.1063/1.4773581.

(43)   May, O.; Kubala, D.; Allan, M. Dissociative Electron Attachment to Pt(PF3)4—a Precursor for Focused Electron Beam Induced Processing (FEBIP). *Phys. Chem. Chem. Phys.* **2012**, *14* (9), 2979–2982. https://doi.org/10.1039/C2CP23268E.

(44)   Engmann, S.; Stano, M.; Matejčík, Š.; Ingólfsson, O. The Role of Dissociative Electron Attachment in Focused Electron Beam Induced Processing: A Case Study on Cobalt Tricarbonyl Nitrosyl. *Angew. Chemie - Int. Ed.* **2011**, *50* (40), 9475–9477. https://doi.org/10.1002/anie.201103234.

(45)   Shih, P. Y.; Tafrishi, R.; Cipriani, M.; Hermanns, C. F.; Oster, J.; Gölzhäuser, A.; Edinger, K.; Ingólfsson, O. Dissociative Ionization and Electron Beam Induced Deposition of Tetrakis(Dimethylamino)Silane, a Precursor for Silicon Nitride Deposition. *Phys. Chem. Chem. Phys.* **2022**, *24* (16), 9564–9575. https://doi.org/10.1039/d2cp00257d.

(46)   Thorman, R. M.; Jensen, P. A.; Yu, J. C.; Matsuda, S. J.; McElwee-White, L.; Ingólfsson, O.; Fairbrother, D. H. Electron-Induced Reactions of Ru(CO)4I2: Gas Phase, Surface, and Electron Beam-Induced Deposition. *J. Phys. Chem. C* **2020**, *124* (19), 10593–10604. https://doi.org/10.1021/acs.jpcc.0c01801.

(47)   Spencer, J. A.; Wu, Y.-C.; McElwee-White, L.; Fairbrother, D. H. Electron Induced Surface Reactions of Cis-Pt(CO)2Cl2: A Route to Focused Electron Beam Induced Deposition of Pure Pt Nanostructures. *J. Am. Chem. Soc.* **2016**, *138* (29), 9172–9182. https://doi.org/10.1021/jacs.6b04156.

(48)   Spencer, J. A.; Brannaka, J. A.; Barclay, M.; McElwee-White, L.; Fairbrother, D. H. Electron-Induced Surface Reactions of H3-Allyl Ruthenium Tricarbonyl Bromide [(H3-C3H5)Ru(CO)3Br]: Contrasting the Behavior of Different Ligands. *J. Phys. Chem. C* **2015**, *119* (27), 15349–15359. https://doi.org/10.1021/acs.jpcc.5b03775.

(49)   Chemcraft - graphical software for visualization of quantum chemistry computations. https://www.chemcraftprog.com.